DOCTORAL THESIS

Improvements in the numerical modelling of wake effects for wave energy converter farms

Author:
Nicolas TOMEY BOZO

Supervisor:
Dr. Jimmy MURPHY

Co-Supervisors:
Prof. Tony LEWIS
Dr. Gareth THOMAS

Head of School:
Prof. Liam MARNANE

A thesis submitted in fulfilment of the requirements for the degree of Doctor of Philosophy

in the

Offshore Renewable Energy Technology Group
MaREI Centre
School of Engineering
National University of Ireland, Cork

January 5, 2018

Contents

Declaration of Authorship

This is to certify that the work I am submitting is my own and has not been submitted for another degree, either at University College Cork or elsewhere. All external references and sources are clearly acknowledged and identified within the contents. I have read and understood the regulations of University College Cork concerning plagiarism.

Signed: 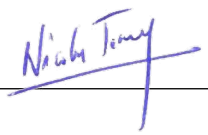

Date: 15/03/2019

Dedicated to my parents Veronique and Juan Carlos, as well as my partner Marguerite, who, in their own way, have been such an example to me of perseverance and dedication.

Acknowledgements

I would like to gratefully acknowledge the help from the following people and research groups throughout these years of knowledge, experiences and learning.

To my supervisors, Jimmy Murphy, Tony Lewis, and Gareth Thomas, for their support through this research work. A special thanks to Jimmy Murphy for his guide to find the path across this challenge and for his helpful and valuable corrections.

To the research group from the Civil Engineering Department in Ghent University, for providing me with the opportunity to learn from their expertise in their in-house software MILDwave, for their friendly welcome in Ghent, and for make me feeling part of their team from the beginning till the end of my secondment.

To the research group from the LHEEA in École Central de Nantes, for providing me with the opportunity to gain from their expertise in wave energy modelling, specially with the use of their open-source code NEMOH and the sharing of their mastery in hydrodynamics. A special thank you to the friends I made there, for the time they spent with me sharing their outside-work plans.

To the MaREI Centre and all the colleagues that have shared with me these three years at work. To the people I met in the Hydraulic and Maritime Resach Centre (HMRC) and the people I met later at the new facilities of the Beaufort Building. A special thank you to Cora and Grainne for their support in all the logistics.

To my friend and colleague Chris Wright for his time and energy dedicated to all the technical discussions we had, and for his enthusiasm and capacity to confront challenges.

To my friends and colleagues Pierre, Florent, Celia, and Mike, for their patience to listen to the ups and downs of a PhD candidate as I was, and for their warm embrace at home.

Finally I would like to acknowledge that the research leading to these results is part of the OceaNET project, which has received funding from the European Union's Seventh Framework Programme for research, technological development and demonstration under grant agreement no 607656.

NATIONAL UNIVERSITY OF IRELAND, CORK

Abstract

School of Engineering
MaREI Centre

Doctor of Philosophy

Improvements in the numerical modelling of wake effects for wave energy converter farms

by Nicolas TOMEY BOZO

Ocean Energy Europe has estimated that 100 GW of ocean energy capacity (wave and tidal) could be deployed in Europe by 2050. Along with these European targets it is expected that large farms of Wave Energy Converters (WECs) will be installed in the sea and as part of the consenting process it will be necessary to quantify their impact on the local environment. The physics of the wave field around the WEC farm is important since it affects coastal processes and potentially marine activities located near by. Thus it will be mandatory to accurately quantify the local changes generated by the presence of a WEC farm and assess the significance of its impact.

To address these concerns, the objective of this thesis is to improve the available numerical methodologies to assess wake effects for WEC farms in order to quantify their impact on the surrounding wave field. Two different methodologies have been developed in order to better represent WECs in wave propagation models (WPMs), the type of model to resolve wave transformation processes. The two methodologies use a WPM based on the mild-slope equations to solve the wave propagation across large domains and a wave-structure interaction Boundary Element Method (BEM) solver to assess the near-field wave-body interaction phenomenon. The first method is based on a representation of the WECs as obstacle cells that are tuned based on the wave field obtained from the BEM solver. The second method looks into the description of the wave perturbation generated by the WEC by coupling the results obtained from the BEM solver into the WPM as an internal boundary condition.

The methods accuracy is assessed together with case scenarios accounting for realistic environmental conditions such as irregular sea states and irregular bathymetries. Thus, as part of the accomplishments of this thesis two innovative numerical methodologies were developed, which include the main transformation processes surrounding a WEC farm for medium scale domains using realistic bathymetries.

List of Abbreviations

WEC	**W**ave **E**nergy **C**onverter
BEM	**B**oundary **E**lement **M**ethods
WPM	**W**ave **P**ropagation **M**odel
CFD	**C**omputational **F**luid **D**ynamics
PTO	**P**ower **T**ake **O**ff
AMETS	**A**tlantic **M**arine **E**nergy **T**est **S**ite
EIA	**E**nvironmental **I**mpact **A**ssessment
SPH	**S**moothed-**P**article **H**ydrodynamics

List of Symbols

Symbol	Name
$X(\omega)$	complex motion amplitude
A	wave amplitude
Γ	excitation force coefficient
A_r	added mass coefficient
ω	wave angular frequency
B_r	radiation damping coefficient
B_{pto}	PTO damping coefficient
K_{pto}	PTO spring coefficient
H	hydrostatic coefficient
P_{abs}	time-average power
P_{wave}	wave power resource per unit of wave front
C_w	capture width
C_r	capture width ratio
H_s	significant wave height
T_p	peak period
f_p	peak frequency
K_d	disturbance coefficient
η	surface elevation
φ	wave phase
k	wave number
λ	wave length
β	wave propagation direction angle respect to the x-axis
V	flow velocity
ϕ	velocity potential
h	vertical distance to the free-surface
d	water depth
g	gravitational acceleration
S	wave spectral density distribution
γ	peak enhancement factor
α	scaling parameter of JONSWAP spectrum
σ	spectral width parameter of JONSWAP plectrum
m_0	zeroth-moment of variance spectrum
H_{sd}	disturbed significant wave height

H_{su}	undisturbed significant wave height
A_{sd}	disturbed wave amplitude
S_d	disturbed wave spectrum
S_u	undisturbed wave spectrum
A_{inc}	incident wave amplitude
f_0	depth dependence for velocity potential
ϕ_p	perturbed wave potential
ϕ_{inc}	incident wave potential
ϕ_d	diffracted wave potential
ϕ_r	radiated wave potential
ϕ_t	total wave potential
U	body velocity vector
n	normal vector of the body surface
Φ	velocity potential at the free-surface
Δx	grid cell size along x-axis
Δy	grid cell size along y-axis
Δt	time step
Δb	angle interval discretisation for circular wave generation line
C	wave phase velocity
C_g	wave group velocity
C_e	wave energy velocity
η^*	additional surface elevation
η_p	perturbed surface elevation
η_{inc}	incident wave surface elevation
η_d	diffracted wave surface elevation
η_r	radiated wave surface elevation
η_t	total wave surface elevation
θ	pitch motion amplitude

List of Publications

Publications Appended to this Thesis

This thesis is presented as a collection of the following four papers included in the Appendix in a text-based manuscript format. The author of this thesis (first author in the papers) carried out the research work presented in the four publications and the rest of co-authors supervised the work and collaborated in the reviewing process.

- N. Tomey-Bozo, J. Murphy, P. Troch, T. Lewis, G. Thomas, "Modelling of a flap-type wave energy converter farm in a mild-slope equation model for a wake effect assessment", *IET Renew. Power Gener.* (2017) 1–11. doi:10.1049/iet-rpg.2016.0962.
- N. Tomey-Bozo, J. Murphy, P. Troch, A. Babarit, T. Lewis, G. Thomas, "The modelling of a flap type wave energy converter in a time-dependent mild-slope equation model", in: *Renew. Energies Offshore*, 2016: pp. 277–284.
- N. Tomey-Bozo, J. Murphy, A. Babarit, P. Troch, T. Lewis, G. Thomas, "Wake effect assessment of a flap type wave energy converter farm using a coupling methodology", in: *ASME 2017 36th Int. Conf. Ocean. Offshore Arct. Eng.*, 2017.
- N. Tomey-Bozo, J. Murphy, A. Babarit, P. Troch, T. Lewis, G. Thomas, "Wake effect assessment of a flap type wave energy converter farm under realistic environmental conditions by using a coupling methodology", Submitted to *Coastal Engineering*, Elsevier.

The appended papers do not contain reference lists, though the submitted versions do, and their references are contained within the common reference list of the thesis.

Publications Not Appended to this Thesis

Other publications carried out during the PhD research time that were not appended to this thesis are listed here. These publications were not appended since they represent preliminary research carried out before selecting the specific subject of the thesis (first publication) or similar applications of the work already presented in the appended publications (second and third publications).

In the first and second publications the author of this thesis carried out the research work and the rest of co-authors supervised the work and collaborated in the

reviewing process. In the third publication the author of this thesis collaborated by providing some of the results that are presented and the main research work was carried out by the first and second authors. The rest of co-authors supervised and reviewed the work.

- N. Tomey-Bozo, J. Murphy, T. Lewis, G. Thomas, "A review and comparison of offshore floating concepts with combined wind-wave energy", in: *11th Eur. Wave Tidal Energy Conf.*, 2015: pp. 1–8.
- N. Tomey-Bozo, J. Murphy, P. Troch, V. Stratigaki, T. Lewis, G. Thomas, "Wake Effect Of A Flap Type Wave Energy Converter Farm In A Time-Dependent Mild-Slope Equation Model", in: *Offshore Energy Storage Symp.*, 2016.
- G. Verao Fernandez, P. Balitsky, N. Tomey-Bozo, V. Stratigaki, P. Troch, "Far-field effects by arrays of oscillating wave surge converters and heaving point absorbers: a comparative case study", in: *12th Eur. Wave Tidal Energy Conf. Eur. Wave Tidal Energy Conf.*, 2017.

Chapter 1

Introduction

1.1 Context

The large increase in greenhouse gas emission trends over the past decades has led governments to decrease energy production from fossil fuel sources and transit towards renewable energy sources. Electricity and heat production were responsible for 25% of 2010 global greenhouse gas emissions, where oil was the largest single source [1]. As a response to these concerns, the European Commission has defined targets for renewable energy production for the coming decades. Well-established renewable sources, such as wind and solar energy, are the major players considered as part of the short term targets. Alternative energies, such as wave and tidal energy, are potentially an important contributor to the long-term targets. Ocean Energy Europe has estimated that 100 GW of ocean energy capacity (wave and tidal energy) could be deployed in Europe by 2050 making ocean energy a key component of the long term sustainable horizons.

The work within this thesis has been supported by the OceaNET project [2], a multinational Initial Training Network funded under the PEOPLE Programme (Marie Curie Actions) of European Union's FP7. The aim of the network was to train thirteen early stage researchers to support the emerging offshore renewable energy sector in the area of floating offshore wind and wave energies. The OceaNET project is part of the group of projects supported by the European Commission (EC) to contribute to the development of ocean energy and attain the long-term targets. The research and training programme has supported thirteen research positions, at different university groups and companies, and nine one-week-long courses on various topics related to wind and wave energy.

This thesis reflects the major findings of a study carried out in collaboration with two other European research institutions, the Department of Civil Engineering from Ghent University and the Research Laboratory in Hydrodynamics, Energy and Atmospheric Environment (LHEEA) from Ecole Central de Nantes. Ghent University has a strong expertise in coastal engineering and is the developer of MILDwave, a numerical tool to simulate the transformation of linear water waves over a mildly varying bathymetry. Ecole Centrale de Nantes is the developer of NEMOH, an open-source numerical tool to solve the interaction between waves and offshore structures

based on potential flow. Both solvers have been used extensively in this thesis and were the main tools employed for the calculations. As part of the collaborative work with both institutions, the candidate spent two visiting secondments of five months each in order to benefit from their expertise.

1.2 Objectives and Scope

This thesis aims to develop innovative numerical methods to assess the impact of Wave Energy Converters (WECs) on their surrounding wave climate. The deployment of WEC farms composed of many devices in the near-shore can have a significant impact on the local wave climate. WECs in a farm absorb and redistribute the incident wave power and consequently, transform the magnitude and direction of the incoming waves. These wave transformation processes will change the wave spectral distribution surrounding the WEC farm at each location and may affect local coastal processes and/or other marine activities located in the nearby area. It will be mandatory to assess this impact as part of the environmental impact assessment procedure for the future commissioning of WEC farms and thus the availability of numerical tools to assess this phenomenon will become very important.

The transformation of ocean waves that encounter a WEC farm, defined as the wake effect, relies on two important phenomena: the local wave-body interaction problem depending on the dynamics of the devices, and the transformation of waves when travelling across the sea-space before and after interaction with the farm. There exist numerical tools to assess each of these two phenomena independently but none of these tools are able to fully represent both phenomena together.

The main objective of the thesis is to develop a methodology that can incorporate the following features, in order to assess all phenomena that are present in a WEC farm wake effect assessment, and give a full consideration to realistic environmental conditions:

- The complete perturbation generated by the WECs in the incoming wave field, i.e. the wave diffraction due to the encountering of the incoming wave with a fixed body, the wave radiation phenomenon due to the WEC motion, and the wave interactions due to the surrounding WECs.
- The wave transformation induced by the water depth changes along the domain is represented including real bathymetry scenarios.
- The wake effect for irregular sea states scenarios can be computed based on an incoming wave spectra at the boundary of the domain.
- The computational demand remains acceptable in order to apply the method with an average desktop computer (no need of a cluster).
- A farm with multiple WECs can be modelled including all hydrodynamic interactions between devices.

1.3 Outline

Four publications have been included in the Appendices of this thesis, which are the main publications produced during this study and they summarise the main findings of the research work. They are referred in this document as Papers A, B, C, and D. Additional publications made during this time are not appended to the thesis since they represent preliminary research carried out before selecting the specific subject of the thesis or similar applications of the already presented work. A list of publications is provided at the beginning of the document where both, the appended and not appended publications, are enumerated.

Paper A was published in a peer-reviewed journal listed on the ISI WEb of Science, Papers B and C are conference publications where a strict peer-review process (double blind peer-review) was undertaken, and Paper D has been submitted to a peer-review journal also listed on the ISI Web of Science. The four publications are appended in a text-based format and in some cases additional sections are included at the end of each document.

Each paper presents a numerical methodology based on a specific technique to represent WECs in Wave Propagation Models (WPMs). Thus, the term "methodology" refers to the broad scope covering the full method applied along the corresponding paper to assess the wake effect for WEC farms, while the term "technique" refers only to the numerical representation of the WECs within the model.

Paper A describes the methodology that was developed as a first step to represent WECs in WPMs based on a linear wave representation. The methodology aimed at enhancing an already existing technique, referred to as the sponge layer technique, which is based on an inherent representation of WECs as obstacle cells (represented as absorbing sponge layers). The obstacle cells are attributed absorption coefficients that are tuned with reference to the wave pattern obtained from a wave-structure interaction Boundary Element Method (BEM) solver. The BEM solver was used to obtain the body motion response and the wave perturbation generated by the WEC on the incident wave climate composed of irregular waves, where reflection, absorption, transmission, and diffraction phenomena are considered. Then the obstacle cells from the WPM were tuned based on the wave pattern obtained from the BEM solution attempting to replicate the same impact on the incoming wave climate. Based on this representation WEC farms of several devices were modelled and wake effect assessments under irregular sea states were carried out considering a mild-slope bathymetry. Finally, the influence of several parameters in the wake effect was assessed, including the separating distance between devices, peak period of the sea state, and water depth changes.

Paper B represents the first stage of development of the second methodology, referred to as the coupling technique. The coupling technique is based on a representation of the WEC as an internal boundary condition that describes the wave pattern solution corresponding to the near-field surrounding the WEC and obtained

from a wave-structure interaction BEM solver. The wave generated by the presence of the WEC (perturbed wave) is described as a circular wave generation line that replicates the wave solution from the BEM solver at the location of the WEC in order to assess its propagation towards the rest of the domain. In this publication the method was applied to regular waves and single WECs and the results were compared to applications of the sponge layer technique in order to assess the benefits brought by the coupling technique.

Paper C presents a methodology based on an improved version of the coupling technique where the near-field solution from the BEM solver is described by means of a wave generation surface. The wave pattern solution (perturbed wave) obtained from the wave-structure BEM solver is imposed in the WPM at each grid cell located within the near-field, where the WECs are situated and then propagated towards the outer domain. The wave generation surface allows a much more consistent set up of the internal boundary, compared to the circular wave generation line of Paper B, and significantly improves the solution obtained. The technique was validated against BEM solver solutions for a single WEC and a WEC farm case, showing a good agreement for both applications. Then the technique was applied to a WEC farm exposed to regular waves and located on a mild-slope bathymetry, assessing its wake effect in the far-field.

Finally Paper D summarises the methodology based on the coupling technique providing a full description of the method and applying it to realistic environmental conditions. First the method is described, providing full details of the governing equations and validated for the single WEC and WEC farm cases, and then optimised through a convergence analysis that gives a recommendation of the main numerical parameter ratios to use. Irregular sea states were computed from the regular wave solution to assess the wake effect for a large WEC farm. The method was applied to a case scenario where a WEC farm was located on a real bathymetry. Finally a sensitivity analysis for several parameters was conducted, assessing the influence of the separation distance between WECs, the peak period of the incident sea state and the importance of considering changing depths for wake effect assessments.

The four publications are introduced by 5 chapters that provide the reader with a background of the subject assessed in the publications and a summary of the findings. Chapter 2 presents a literature review of the numerical models employed to assess WEC farm wake effects and their impact on the surrounding wave climate. Chapter 3 summarises the theory and equations describing the models employed in this thesis. Chapter 4 explains the different methods developed and describes the step-by-step approach followed to reach the objective of this thesis. Finally Chapter 5 summarises the results as well as presenting conclusions and recommend options for further work.

1.4 Wave Energy Review

1.4.1 History in Brief

The idea of inventing machines capable of extract the energy from ocean waves is not a modern concept. The earliest patent was filed in France in 1799 by a father and a son named Girard [3] and since then the number have been increasing significantly, with more than one thousand patents registered in 1980 [4]. Yoshio Masuda may be regarded as the father of modern wave energy technology with studies beginning in Japan in the 1940s. He developed a navigation buoy powered by wave energy, equipped with an air turbine, which was later named as a (floating) oscillating water column. The oil crisis in the 1970s resulted in a major change in how renewable energy was regarded and raised the interest from governments in large-scale energy production from the waves. A paper published in 1974 in the prestigious journal Nature by Stephen Salter [5], became a landmark and brought wave energy to the attention of the international scientific community [3].

Wave energy technologies have not yet matured to commercialisation even though a large number of concepts have been developed. The industry growth has oscillated up and down, generally remaining at low-medium technology readiness levels, because of technical and non-technical barriers. After a few of the most important companies became bankrupt in the early 2010s, investments in wave energy decreased significantly. However public and private funding for wave energy has recently increased again, with promising projects such as Wave Energy Scotland [6] or MaRINET2 [7], and promising developers such as Oceantec [8], Seabased [9], or Carnegie [10], that will help to raise wave energy at the level of the European targets.

1.4.2 Classification of Technologies

Wave energy converters have been classified in different ways depending on the aim of the classification. Falcão [3] arranged them according to their working principle and created groups of similar technologies. The main working principles are classified into three groups, defined as oscillating water columns, oscillating bodies and over-topping. These were then subdivided into sub-groups depending on if they are floating or fixed. Figure 1.1 shows the schematic of the classification together with example of concepts.

The oscillating water column is a technology composed of a chamber connected to the sea. Inside the chamber a water column moves up and down with the oscillating pressure from the incoming waves driving an air column, located above the water column, through an air turbine. Oscillating bodies are defined by a main moving body reacting against another body which is fixed and seabed anchored, or which has a much larger inertia than the main moving body. Then, between the relative movement of the two bodies, a Power Take-Off (PTO) system composed of

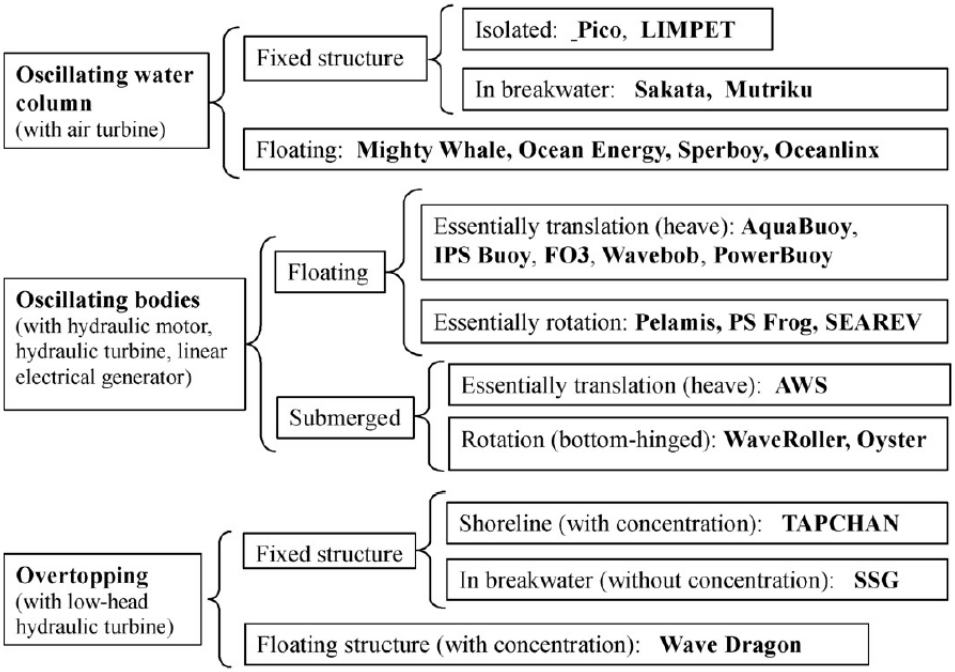

FIGURE 1.1: Classification of wave energy technologies by Falcão [3]

a hydraulic motor or turbine, or a linear electrical generator, extracts the kinetic energy of the motion. Finally over-topping devices are based on a structure located above the free-surface that waves overflow filling a tank from where the potential energy is extracted by means of a low-head hydraulic turbine.

Another type of classification is the one introduced by Falnes [11] based on the main dimension of the device exposed to the wave front. If the device dimension is very small compared to a typical wavelength or if its two horizontal dimensions are of similar size, the WEC is called a point absorber. If the horizontal dimension is comparable to or larger than a typical wavelength, the WEC is called attenuator and terminator. It is an attenuator or a terminator depending on parallel or normal alignment to the prevailing direction of wave propagation, respectively.

The type of WEC technology has a strong influence on the incoming waves transformation caused by the presence of a WEC farm, the so-called wake effect of the farm. Some technologies, such as point absorbers, have a relatively low impact on the wave field and other technologies such as terminators have a strong influence on the incoming wave field, usually due to their reflection and diffraction capacities. When WECs are deployed as arrays of several devices, then their impact may be strongly increased due to the interactions and accumulative effects. A number of examples of WEC farm layouts are modelled along this thesis where their wake effect is assessed, thus showing the influence of the number of devices on the wake.

1.4.3 Examples of WECs

Some examples of known technologies for the main types of WECs are shown to give an idea of the variety of devices that have been invented.

The OE Buoy is a wave power device developed by Ocean Energy that uses an oscillating water column design applied to a floating body [12]. The chamber inside the device is of L shape, being horizontal at its opening (connection with the sea) and then vertical at the connection with the turbine (top). The opening of the chamber is located on the lee-side of the device. It was deployed in quarter-scale test mode in Spiddal near Galway in Ireland for over two years between 2007 and 2009. During 2011 the model was redeployed at the same site, primarily as a data collector for the EU funded CORES Project.

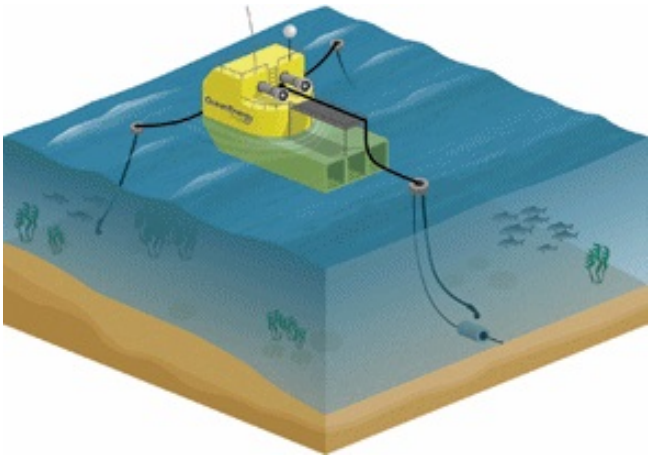

FIGURE 1.2: OEBuoy: Oscillating water column WEC developed by Ocean Energy.

The WaveRoller is a flap type WEC developed by AW Energy [13]. Figure 1.3 shows a sketch representation of the device. As the WaveRoller flap moves and absorbs the energy from ocean waves, the hydraulic piston pumps attached to the panel pump the hydraulic fluids inside a closed hydraulic circuit, and then the hydraulic circuit spins a generator. A platform with three WaveRoller technologies was deployed several times off the coast of Peniche (Portugal) between 2009 and 2013.

Figure 1.4 shows the Pelamis device, an attenuator type WEC composed of at most five cylindrical sections connected to each other with two degrees of freedom [14]. Hydraulic pistons are located in between each cylinder and generate electricity by means a hydraulic circuit connected to a generator. The Pelamis became the first offshore wave machine to generate electricity into the grid, when it was first connected in 2004 in the UK. Pelamis Wave Power then went on to build and test five additional Pelamis machines: three first-generation P1 machines, which were tested in a farm off the coast of Portugal in 2009, and two second-generation machines, the Pelamis P2, were tested off Orkney between 2010 and 2014.

WaveDragon is a terminator type WEC, which uses the principle of over-topping

FIGURE 1.3: WaveRoller: Oscillating flap WEC developed by AW Energy.

FIGURE 1.4: Pelamis: Attenuator WEC developed by Pelamis Wave Power.

to extract the energy [15]. It consists of two wave reflectors that direct the waves towards a ramp. Behind the ramp, a large reservoir collects the directed water, and temporarily stores the water. The reservoir is held above the sea level and the water leaves the reservoir through low-head hydro turbines. The first prototype was connected to the power grid in 2003 and since then many long-term offshore tests were carried out in Denmark.

Figure 1.6 shows the Seabased device, a WEC developed by a company of the same name [9]. The working principle of the device is a point absorber, composed of a floating body reacting against a gravity based seabed platform, where the PTO is usually located and therefore the electricity is generated. The floating device is linked to the base by a rope. Currently, several devices are deployed along the coast of Sweden at different pre-commercial wave energy test sites.

FIGURE 1.5: Wave Dragon: Terminator or over-topping WEC developed by Wave Dragon Aps.

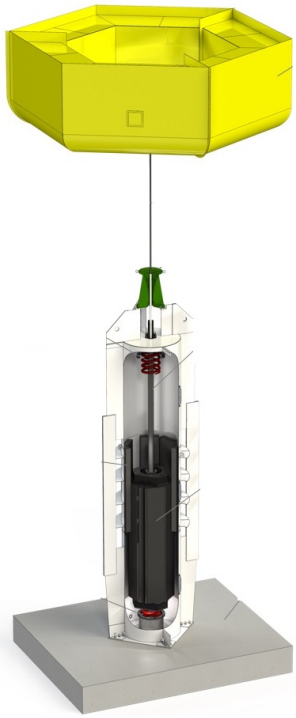

FIGURE 1.6: Point absorber WEC developed by Seabased.

Chapter 2

Literature Review

The aim of this chapter is to analyse the state-of-the-art of the different models employed to compute the wave field transformation while interacting with the WECs and their impact on the far-field. A number of models have been used across the studies presented; their adequacy depends on the aim of the study and the level of accuracy required. At the end of the chapter the shortcomings requiring resolution are highlighted.

2.1 General Aspects of Wave Field Modelling in a Wave Energy Farm

The large-scale commercial exploitation of WECs as arrays of multiple devices is the motivation that has led some previous investigations to study the wave field transformation in a WEC farm and the wake effect on the lee side. The interactions between the multiple devices influence the incoming wave field arriving at each WEC and therefore vary their energy production. An understanding of the hydrodynamic interactions in such arrays is essential to investigate optimum layouts of WEC farms.

The first numerical models of WEC arrays were developed in the late 1970s and were based on wave-structure interaction BEM solvers using potential flow models. Based on most recent publications, this numerical modelling technique still remains the most popular method for determining interactions between WECs and for assessing WEC farms power production. More recent numerical modelling techniques provide alternatives for assessing the WECs interaction as well as the wave field impact of a WEC farm. A review of a number of these models and methodologies was given by Folley et al. [16].

Some of these models are relevant when studying the dynamics of the devices themselves and the local wave-body interaction while others remain more relevant when the aim remains to represent the evolution of the wave field across large domains accounting for realistic environmental conditions. The most common assessments are based on the use of a single type of model although some recent works have coupled the results between two different models [17]. These coupling methods are based on the modelling of the local near-field surrounding the WECs in one model and the far-field propagation of waves in another model. In the following

sections a description of the three main groups of models used is first summarised and then the current development state of the coupling methods is described.

2.2 Boundary Element Methods

The most popular models employed to solve the wave-body interaction phenomena are the BEM solvers based on potential flow. These models solve the linear wave-body interaction scattering problem and offer the best ratio between accuracy and computational time demand compared to the rest of models. The scattering problem solves Laplace's equation for a set of given boundary conditions by dividing the solution in two, the diffraction and radiation solution (Section 3.3 for more detail). Among these codes, commercial versions such as WAMIT [18] and ANSYS Aqwa [19] or the recently available open source code NEMOH [20] developed by École Centrale de Nantes. They are theoretically able to deal with any number of devices but they rapidly become less suitable as the number of devices increase. The computational time increases with the square of the number of unknowns (number of degrees of freedom and devices). These codes are restricted to conditions where the assumptions of the linear water wave theory remains valid, described in detail in Section 3.2.

All three authors [21], obtained the wave pattern for arrays of heaving cylinders and surging barges using Aquaplus [22], the predecessor code of NEMOH. The heaving cylinder dimensions were 10 m diameter and 10 m draft, and the surging barge dimensions were 10 m width, 10 m draft, and 7.85 m length, all located in deep waters. The evolution of the wave field in the lee of arrays was investigated for far-field distances. Arrays formed by 8 and 18 devices of each type of WEC in addition to a combination of two clusters of 8 devices were considered. Based on the principle of superposition from the linear wave theory irregular sea states were computed from the regular wave results. Different sea states, with and without directional spreading through the arrays, were taken into account. An example of an 18 barge cluster under an irregular sea state of significant wave height $H_s = 1$ m and peak period $T_p = 6$ s is shown in figure 2.1. The plots show the disturbance coefficient $K_d = H_{sd}/H_s$ obtained along a 4000 x 2000 m domain where H_{sd} represents the significant wave height at each grid cell and H_s the incident significant wave height.

Durand et al. [23] and Thilleul et al. [24] have shown that assumptions related to linear potential theory apply very well for applications to WECs in small to moderate sea states. Comparison of numerical predictions with experiments or more complex Computational Fluid Dynamics (CFD) calculations were carried out and proved BEM solvers to give accurate results for low to moderate sea states. Nevertheless, for larger sea states significant discrepancies appear as the linearity assumptions do not remain valid and other non-linear effects as vortex shedding become important.

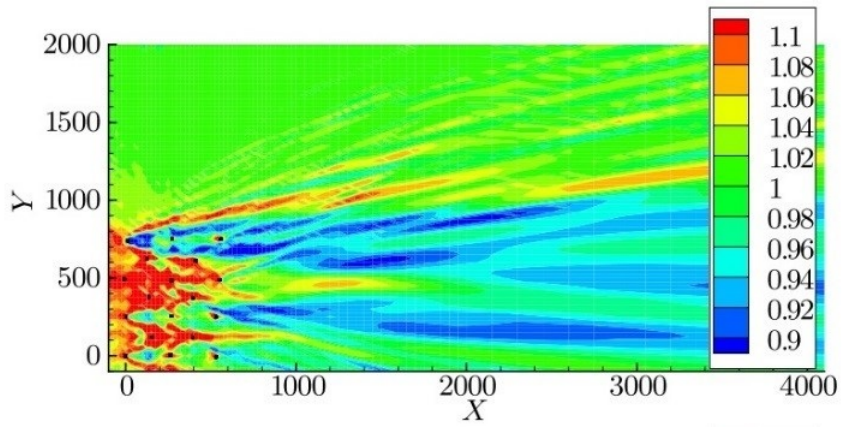

FIGURE 2.1: K_d for an 18-barges cluster under a sea state of $H_s = 1$ m and $T_p = 6$ [21].

A matrix method initially developed by Kagemoto and Yue [25] to compute interactions between multiple three-dimensional bodies subjected to partial cylindrical waves was applied to plane incident waves by McNatt, Venugopal, and Forehand [26] considering cylinder and attenuator type WECs and by Fàbregas, Babarit, and Clément [27] considering heaving buoy type WECs. The essential component of the method is the so-called diffraction transfer matrix, a linear operator defined for each unique geometry. The approach computing the diffraction transfer matrix from plane-waves (wave whose wavefronts, surfaces of constant phase, are infinite parallel planes) enabled the derivation of the interactions from standard wave-body software, i.e. BEM or experiments. This leads to a significant reduction in computational time compared to the direct method in which the linear wave-body scattering problem is solved for all bodies simultaneously. Figure 2.2 shows comparison plots between WAMIT results and the matrix method for regular wave cases with 16 WECs. The results confirmed the method to be accurate, especially in the far-field.

Direct methods with BEM solvers have been employed in many works [28]–[31] to investigate the layout optimisation of WEC arrays. These works looked mainly into the q-factor variation (power output per device in a farm with respect to the power output of the equivalent number of single devices) by changing the configuration and the distances between devices. Therefore these studies were focused on the array power production rather than the surrounding wave pattern. The number of devices considered remained small (typically 5-10 devices) as the computational time and memory requirement became a real issue with the increase in number of devices. A review of studies assessing the farm effect from the point of view of the energy efficiency was undertaken by Babarit [32].

As a summary, BEM solvers based on linear wave theory are highly suitable to study the wave-body interaction within the near field for low to moderate sea states and for relatively small amplitude body motions. Due to their constant water

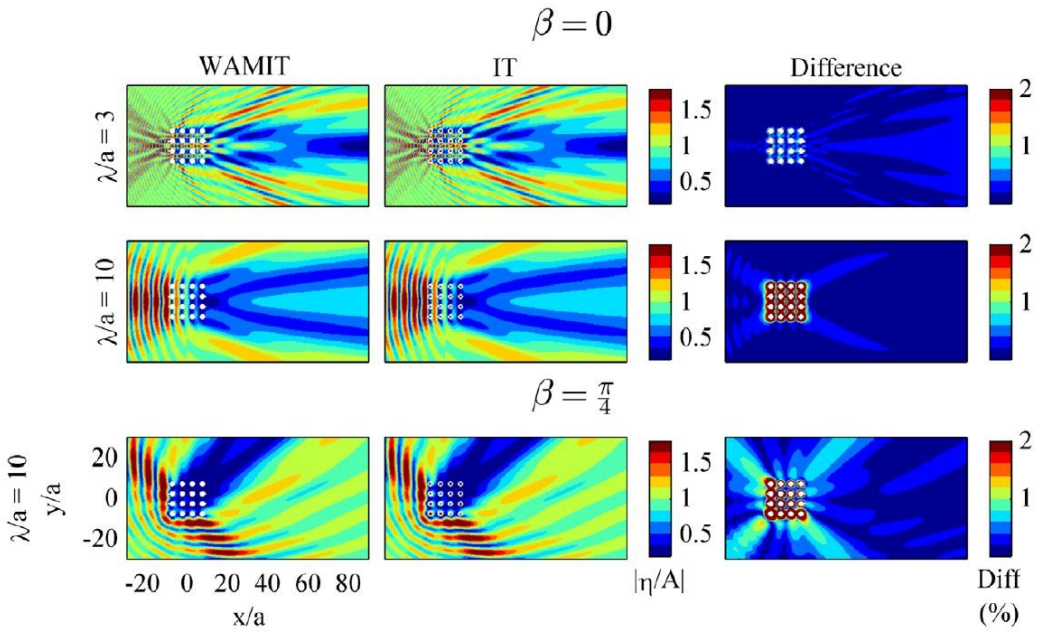

FIGURE 2.2: Wave amplitude for an array 16 cylinder type WECs under regular waves and two wave directions. Left: WAMIT results. Middle: Method based on the diffraction transfer matrix. Right: Difference between both methods [26].

depth assumption, these codes do not allow for the accurate computation of the far-field wave transformation. The transformation of waves induced by the water depth changes and by the dissipative processes becomes important when enlarging the domain, especially towards shallow waters (e.g. wave breaking or bottom friction); these solvers do not account for such phenomena.

2.3 Wave Propagation Models

The main feature of wave propagation models (WPMs) is their suitability to compute wave transformation processes across large domains with real bathymetries. Some of these models are capable of representing obstacles and their interaction with waves. They can be classified in two main groups, which are the phase-resolved models and the phase-averaged models. As their names suggests, their main difference is based on the first group solving the wave transformation in the time-domain by considering each wave phase individually while the second group computes the evolution of the wave field in terms of energy spectrum in the frequency domain. The latter models are also called spectral wave models.

The implementation of WECs is not a intrinsic feature of WPMs although several studies have attempted to improve the state-of-the-art on this subject. These models are not capable of modelling intrinsically the hydrodynamic behaviour specific to moving devices (i.e. wave radiation), however they may be used to model device characteristics such as wave transmission, reflection and absorption. Examples of

WEC implementations dealing with the limitations of these models are shown in the following subsections.

2.3.1 Phased-resolved models

Phase-resolved models can be subdivided into models based on the linear mild-slope equations and models based on the non-linear Boussinesq equations. The typical applications of phase-resolved models are near-shore or relatively local scale environments (e.g. harbours) using small to medium grid sizes (of the order of square kilometres). The mild-slope equation models are considered to be fast solvers describing the transformation of linear waves when propagating from deep to shallow water on a mild-slope bathymetry. The Boussinesq equation models have been shown to be accurate predictors of more complex near-shore hydrodynamic behaviour such as the propagation of non-linear waves in deep to shallow water. Nevertheless their complexity makes them computationally very demanding and restrictied to specific application where non-linear phenomena are predominant.

Mild-slope equation models

The first form of the mild-slope equation was developed by Eckart in 1952 [33] and thereafter many modified and extended forms have been proposed such as the equations of Berkhoff [34]. They describe the combined effects of diffraction and refraction for waves propagating over a mildly-varying bathymetry and due to lateral boundaries such as cliffs, beaches, seawalls and breakwaters. With the extended forms additional effects have been included such as; wave-current interaction, wave non-linearities, bed friction, wave breaking and even diffraction modules for surface waves have been developed. Velocity potential and surface elevations throughout the numerical domain can be calculated with a relatively low computational and accuracy cost and with a high stability performance. Their major limitation remains the inability to represent radiated waves generated by moving bodies. Commercial versions of these codes can be found such as the modules Elliptic Mild Slope Wave and Parabolic Mild Slope Wave from MIKE 21 [35] or the MILDwave model developed by Ghent University [36]. Open-source versions are available as well such as the ARTEMIS module from the Open TELEMAC-MASCARET model [37].

One of the first implementations of WECs in a mild-slope model was considered by Mendes et al. [38] where an energy dissipation coefficient was used to model the Pelamis type WEC, a device that was designed for water depths of 50 m. The wave climate was assessed considering the presence of a WEC farm composed of 3 and 6 devices. The applicability of these results to the real environment remained limited due to the assumptions considered: regular waves, diffraction limited to main propagation direction, and simple representation of the whole WEC farm as a group of energy dissipation terms.

Beels et al. [39], [40] assessed the performance of a WEC farm with devices based on the over-topping principle. The work was implemented in MILDwave, a linear mild-slope model based on the equations of Radder and Dingemans [41]. First, an exhaustive sensitivity analysis of the WEC representation was carried out by representing the devices as obstacle cells with a given absorption coefficient. The wake effects in the lee of multiple WECs was investigated by adapting the performance of each WEC to the incident wave power. The WECs were implemented as an array of cells (covering the spatial extensions of the WEC) that were assigned a given degree of absorption using the sponge layer technique. Since the amount of energy absorbed varies with the period of the incident wave, a frequency dependent absorption coefficient was implemented. An example of the disturbance coefficient for the wave field surrounding 9 WECs considering irregular long-crested waves of $T_p = 5.2\ s$ is shown in Figure 2.3. Then, as a continuation of the previous work, wake effects were assessed by Troch et al. [42] varying lateral and longitudinal spacing from the farm layout for the same type of WECs.

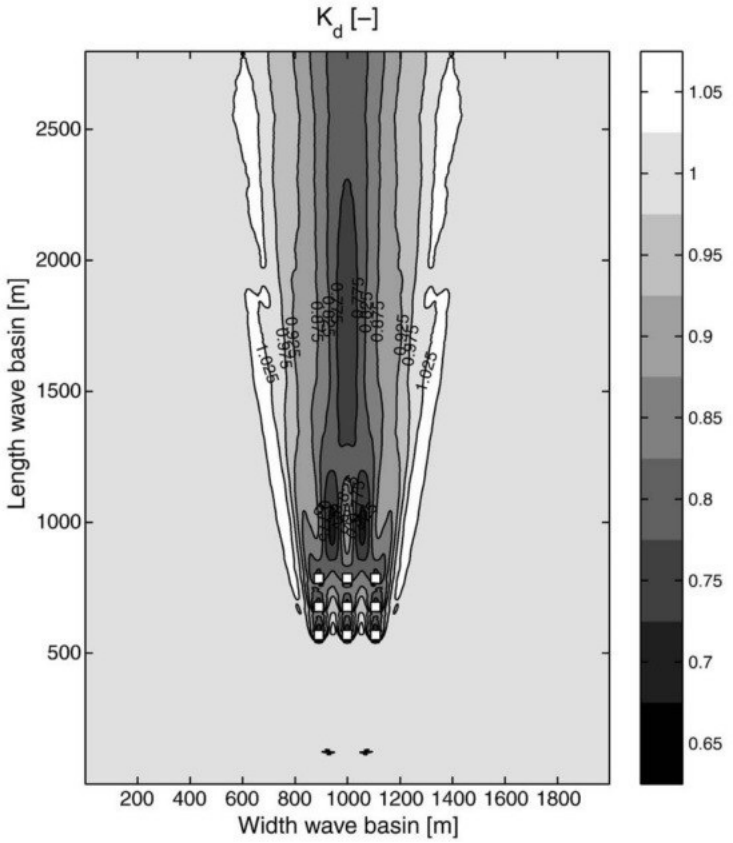

FIGURE 2.3: Kd values for a farm of over-topping principle WECs [39].

Boussinesq models

Boussinesq models are based on a set of non-linear partial differential equations known as the Boussinesq equations developed by Joseph Boussinesq [43] in 1872. Similar to the previous mild-slope equation models, their main difference is the inclusion of non-linear terms accounting for phenomena such as wave breaking, wave-wave interaction, or bottom friction. The Boussinesq approximation takes into account the vertical structure of the horizontal and vertical flow velocity, resulting in non-linear partial differential equations which incorporate frequency dispersion. These models are usually mathematically enhanced versions of the classic equations, allowing the consideration of all important wave transformation processes. One advantage of these models for modelling wave energy farms is the realistic representation of diffraction phenomena. Nevertheless, as for mild-slope equation models, the wave radiation generated by the motion of WECs can not be modelled intrinsically as part of the solver. Examples of these codes are the commercial MIKE 21 BW module [35] or the open-source TELEMAC-2D module of Open TELEMAC-MASCARET [37].

Due to their high computational time demand only a few works have attempted to model WEC arrays in these type of codes. Venugopal and Smith [44] studied the changes in the wave climate surrounding an hypothetical array of 5 individual bottom mounted WECs. This was achieved by modelling the WECs with partial transmitting and reflecting obstacles. Different porosity values were used to simulate varying degrees of reflection, absorption, and transmission ranging from 0 to 1. It was found that reductions in wave height vary greatly depending on the attributed values of porosity and attention is required to ensure that realistic device characteristics are modelled.

2.3.2 Phased-averaged models

Spectral wave models are phase-averaged wave propagation models which predict how the surface wave frequency and directional spectrum evolve as waves propagate through varying background currents, water depth, and additional natural processes. While the previous phase-resolved models determine the surface elevation of the waves, the spectral wave models solve an energy conservation equation. This means waves are solved in the frequency domain based on a wave energy spectrum representation instead of phase by phase in the time domain, as phase-resolved models do.

These models are capable of representing wave transformation processes such as depth and current induced refraction, shoaling, wind forcing, white-capping and bottom friction dissipation, and non-linear wave-wave interactions. Open-source codes are readily available such as the SWAN model [45], the TOMAWAC module as part of the Open TELEMAC-MASCARET model [37], or the WAVEWATCH model

[46]. There also exist commercial versions such as the Spectral Wave module from MIKE 21 [35].

Wave spectral models are unable to represent diffraction and radiation waves explicitly since they solve the transformation of phase-averaged sea states. However, a phase-decoupled refraction-diffraction representation has been developed attempting to address this deficiency. Holthuijsen, Herman and Booij [47] and Ilic et al. [48] have shown that a relatively good agreement (10-15%) can be found for the far-field results by implementing the refraction-diffraction technique for breakwaters in SWAN and comparing the results with experimental data. Nevertheless larger differences are found in the near-field situated immediate in the lee of the breakwater.

In spite of the complexity of representing WECs in these models, a small number of studies have attempted to model WEC arrays in spectral wave models by trying to account for the energy absorbed and radiated by the devices. These methods can be divided into two categories; the supra-grid modelling technique where the WEC array is represented over several computational grid points, and the sub-grid modelling technique in which each individual WEC is represented at a single computational grid point.

Supra-grid modelling

This technique is based on the implementation of the WECs using an obstacle feature for which an energy transmission coefficient can be set. Millar [49] assessed the transformation of the wave spectra in SWAN representing an entire wave farm as a single obstacle, while Posner, O' Sullivan and Murphy [50] applied the same method to a specific type of WEC representing each device individually as a transmission coefficient based on experimental results. A representation of the obstacles as frequency-dependent transmission coefficients and using SWAN was implemented by; Smith, Pearce and Millar [51], Alexandre, Stallard and Stansby [52], and Porter et al. [53]. This representation allowed for a more realistic modelling by representing the WEC impact on the wave field dependent on the incoming sea state. Figure 2.4 shows a representation of the work carried out by Smith [51] where a WEC array composed of two rows is implemented considering a frequency-dependent transmission coefficient. The results are expressed in terms of wave height difference, which is the difference between the incident wave height and the locally transformed wave height.

More recently several studies were conducted into the device WaveCat (a lateral over-topping WEC) in SWAN [54]–[58]. The devices are represented as transmission coefficients that were obtained from experimental testing. These works were focused on the impact of wave energy farms on the near-shore and the coastline by representing realistic coastal processes. Figure 2.5 shows some of the results of Abanades, Greaves and Iglesias [57] where the reduction in the significant wave height was assessed behind a farm by changing the distance to the coastline.

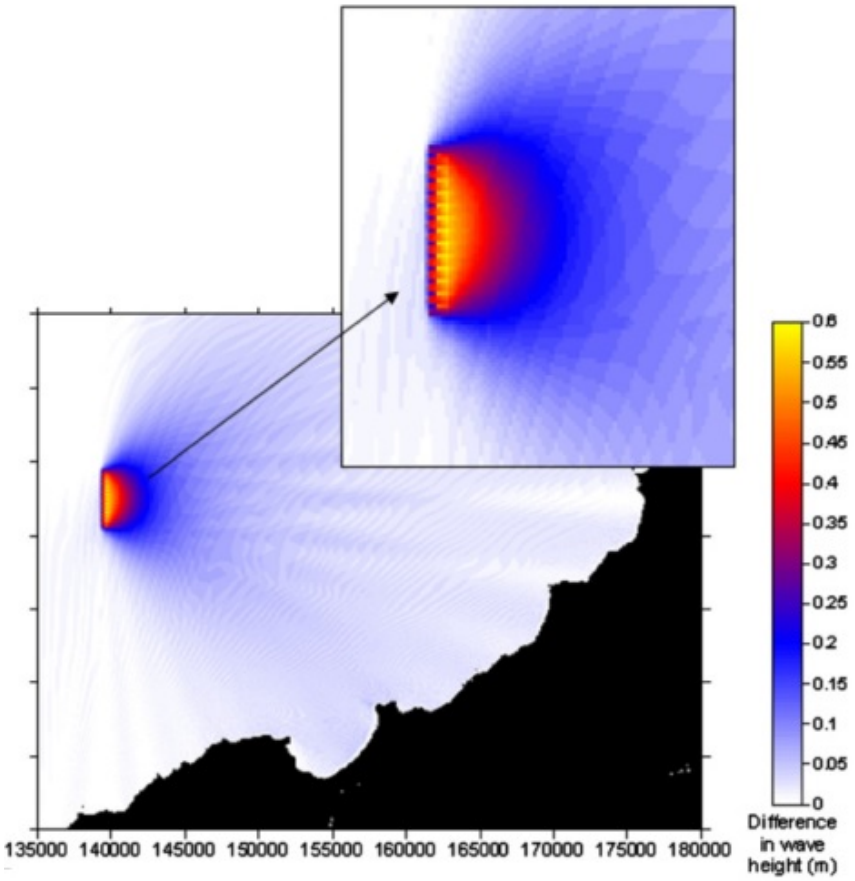

FIGURE 2.4: Difference on the wave height for a WEC array composed of 2 rows [51].

McNatt et al. [59] represented pitching flaps, points absorbers and hinged rafts WECs in SNL-SWAN, a modification of the well known SWAN. The devices were modelled parametrically as partially transmitting obstacles based on the WEC's power absorption characteristics. The devices were represented individually and the transformation of irregular sea states on the surrounding wave field was assessed for the different WEC types.

Sub-grid modelling

The sub-grid technique for modelling WECs seeks to represent the disturbance of the WEC in the wave climate by treating each device located at a computational grid point as a source and sink of wave energy. The energy absorption and radiation, which can be dependent on the incident wave, is therefore incorporated at each WEC location into the wave action conservation equation. This technique is similar to how the existing wave processes such as wind generation and wave dissipation are treated in spectral wave models.

Silverthorne and Folley [60] implemented WECs in TOMAWAC as independent source/sink terms and examined the importance of the frequency and directional

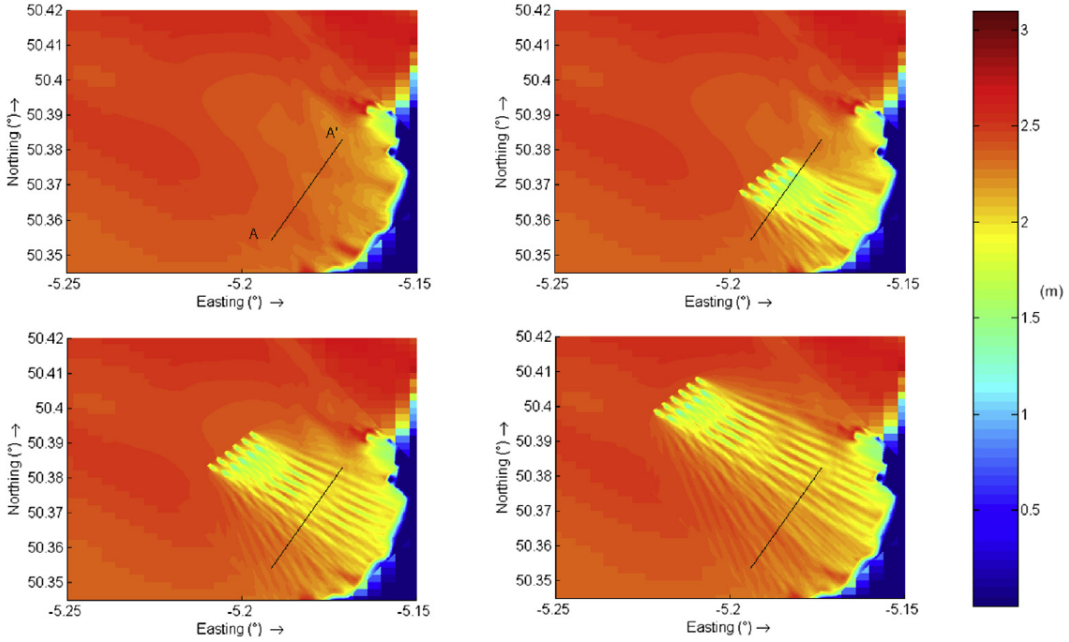

FIGURE 2.5: Significant wave height [m] in the baseline scenario and in the presence of the farm at distances of 2 km, 4 km and 6 km from the reference (clockwise from above left) [57].

dependence of the wave climate response to the presence of WECs. Figure 2.6 shows the significant wave height obtained for the case of a WEC farm composed of 40 devices. Folley and Whittaker [61] and Weywada, Child and Cruz [62] used the same approach to look into the performance of WEC arrays and validated their results against other models. The first one compared the results against time-domain models including non-linear forces while the second one carried out a comparison against frequency-domain results from BEMs. Both works found good agreement in the comparisons that were focusing on the performance of the array. However, because of the low accuracy to resolve phase-dependent processes, the near field effects around each individual device did not model properly. The same approach was applied by Greenwood, Christie and Venugopal [63] using the Spectral Wave Model from MIKE 21 to investigate the wave field transformation in the lee of an array of 30 devices.

2.4 CFD Models

The term "CFD model" is commonly used for numerical codes that solve the Navier-Stokes equations. The Navier-Stoke equations are a set of equations derived from the conservation laws (mass, energy, momentum, and angular momentum, all of which are conserved in a closed volume). These equations together with the continuity equation constitute what is often regarded as the fundamental set of fluid flow equations. CFD approaches can be based on finite element, finite difference, or

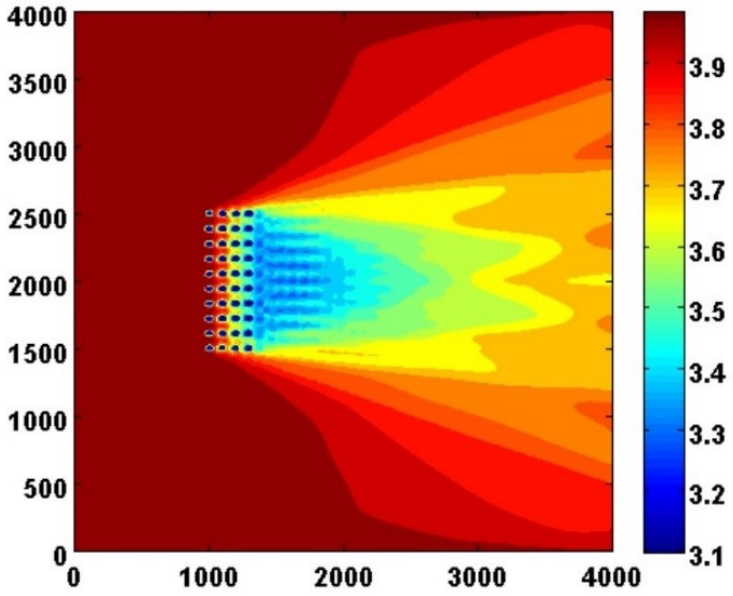

FIGURE 2.6: Significant wave height for a WEC farm composed of 40 devices [60].

finite volume representation and are often referred to as such. Their main difference from the potential flow models is the inclusion of viscous effect and two-phase flow (air entrainment in breaking waves) making them a good tool for the simulation of extreme wave loading and turbulence.

Due to their high computational demand only a few studies have attempted to represent WEC arrays in CFD models. Agamloh, Wallace and von Jouanne [64] considered an array of two heaving WECs using a unstructured finite volume CFD code, focusing on the power production of the devices and the interference between them. CFD models are often prone to internal over-dissipation when resolving gravity water waves, i.e. free surface flow, due to the presence of high viscosity effects. Therefore only the near field surrounding the WECs can be computed with accuracy before the wave dissipation become too significant. In addition their high demand in computational time makes them unsuitable to model an event of more than a few seconds long or a case scenario with several devices.

2.5 Coupling Methodologies

The wake effect assessment for a WEC farm depends on two important phenomena: the local wave-body interaction in the near field of the WEC and the wave propagation and transformation in the far-field. The limitation comes when the models described in the previous sections are only suitable for one of these two phenomena, being the BEM solvers the best solution to model the first phenomenon and the wave propagation models the best solution for the second phenomenon.

In consequence of the limitations of the previous models, methods attempting to put together the features of the BEMs and the phase-resolved type WPMs have been investigated in the studies mentioned within this section. The aim of the method is to assess the wave climate in the far-field accounting for real wave transformation processes while having an accurate representation of the wave perturbation caused by the interaction of the incoming wave field with the WECs. The technique consists of using the BEM solver wave pattern solution to properly represent the near-field wave perturbation of the WEC in the wave propagation model. An internal boundary condition surrounding the device is implemented within the WPM to describe the perturbed wave and assess its transformation in the far-field.

Phase-resolved models based on the mild-slope equations are the type of WPM that have been used to apply such methodologies based on coupling techniques. These models remain the best option in terms of balance between accuracy and computational time demand and are similar to BEM solvers in terms of governing theory. Both models, mild-slope equation WPM and BEM solvers, use a representation of the wave field based on the linear water wave theory which allows for the direct coupling between the two models from a theoretical point of view.

The first approach of the methodology was implemented by Beels [65] to heaving point absorber type WECs. In this case the coupling technique was applied between WAMIT as a BEM solver and MILDwave as WPM considering point absorbers type WECs. Regular waves were coupled for a single WEC case and the results of the coupling were validated against WAMIT predictions for constant depth bathymetries. In addition, a module to solve the diffracted wave pattern intrinsically in MILDwave was implemented using the obstacle cell representation feature from the model. Good agreements were found with the diffracted wave pattern obtained from WAMIT. Once the methodology was validated for a single WEC case, 9 WECs were modelled for three different regular waves cases. Figure 2.7 shows the wave amplitude obtained across a large domain for the latter case study considering a regular wave.

As a continuation of the work from Beels, Stratigaki [66] applied the same methodology to another type of heaving WEC. This time the method was only applied to a single device since the work was focused on the tuning of the internal boundary parametrisation. Figure 2.8 shows the wave amplitude obtained for a point absorber under regular waves by applying the coupling technique. Both works, [65] and [66], used a circular wave generation line and an inner sponge layer to describe the internal boundary generating the perturbed wave based on the BEM solver solution. Good agreements were found but the reflection caused by the inner sponge layer makes this type of set-up for the internal boundary difficult to implement.

Babarit et al. [67] and Charrayre et al. [68], [69] applied a coupling technique using Aquaplus (NEMOH) to obtain the perturbed wave for the near-field and ARTEMIS (module of the TELEMAC-MASCARET model) to propagate the waves towards the

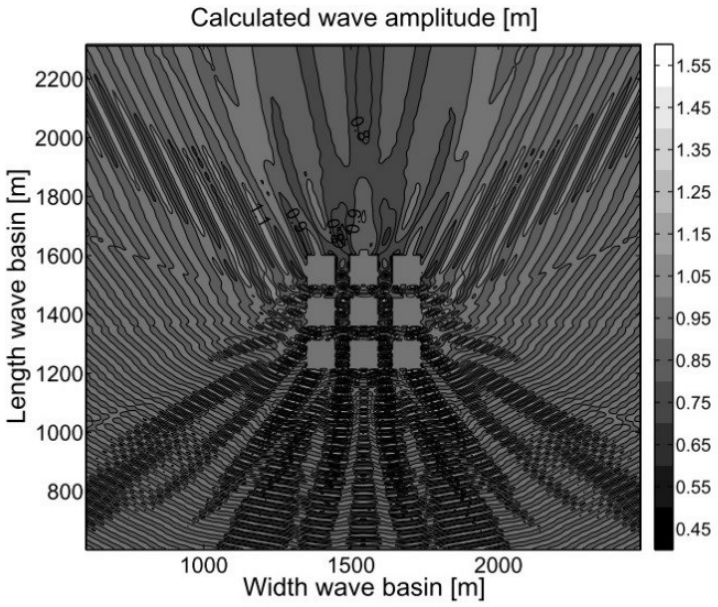

FIGURE 2.7: Wave amplitude for 9 heaving WECs under regular waves [65].

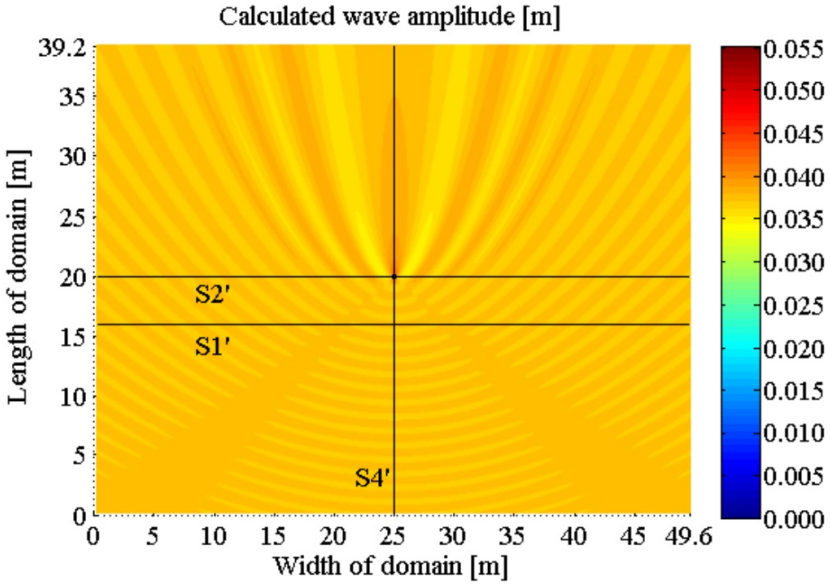

FIGURE 2.8: Wave amplitude for a heaving point absorber WEC under regular waves [66].

far-field. Both solvers are open-source code versions of BEM solver and WPM respectively. In this case the wave pattern surrounding the WEC was obtained from NEMOH by using a far-field approximation method based on the Kochin function [70]. The method allows the wave field surrounding the device to be obtained based on an angular discretisation, which is used then to describe the internal boundary in ARTEMIS. The technique was applied to a sea state composed of 5 regular wave components using a mild-slope bathymetry and proves the versatility of the method.

Figure 2.9 shows the wave height obtained for a WEC farm of 11 heaving buoy type devices.

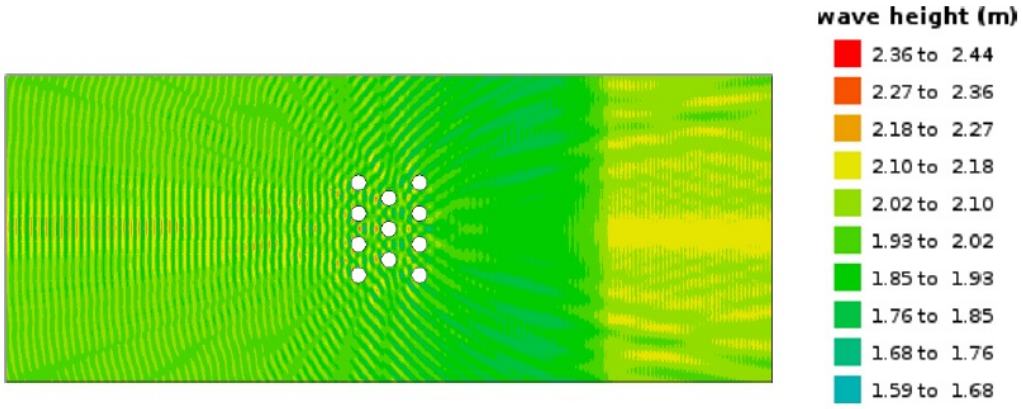

FIGURE 2.9: Wave height for a farm of 11 point absorber type WECs on a mild-slope bathymetry [68].

More recently Ruiz, Ferri and Kofoed [71] developed a similar method to the coupling techniques from above where the direct matrix method was adapted to the elliptic mild-slope equation. Utilising a finite-element implementation, the mild-slope equations were used to model the effect of the bottom on the waves while the effect of the bodies was represented by means of the diffraction transfer matrices. The method was applied to solve regular wave solutions surrounding truncated vertical cylinders and surging barges that were compared against analytical solutions. Figure 2.10 shows the wave amplitude obtained for the diffracted wave by an array of surging barges located over a flat bottom (left) and over a plateau (right) for three wave periods applying the methodology described in [71].

2.6 Discussion

For the wave-body interaction phenomena, BEM solvers based on potential flow are the best option to obtain the wave pattern surrounding a WEC in the near-field. While restricted by the limits of the linear water theory, the wave pattern can be computed with accuracy for relatively small domains. However, they are limited by the constant depth assumption, the increasing demand in computational time related to the number of devices, and the inability to consider dissipative processes of real environments such as wave breaking or bottom friction. Models based on Navier Stoke equations such as CFD models are only suitable for specific events highly governed by non-linearities. Extreme loads and viscous effects can be modelled with high accuracy but they remain unsuitable to compute gravity waves propagation across large distances, as the dissipation effects are overestimated due to the viscous forces. In addition, they are limited to short-time frames due to their high computational demand.

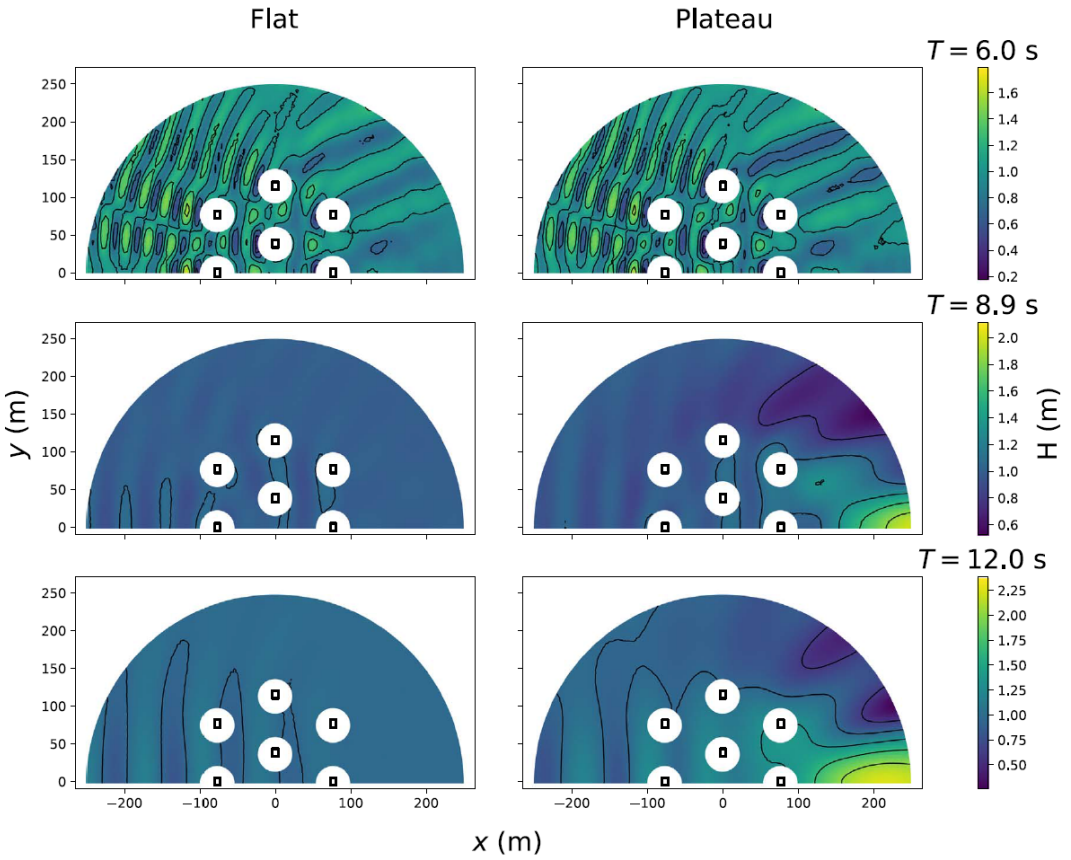

FIGURE 2.10: Free surface amplitude H of the wave diffracted by an array of barges over a flat bottom and a plateau for the three wave periods T = 6, 8.9 and 12 s [71].

Wave propagation models can not deal intrinsically with the full representation of WECs as they do not represent the radiation phenomena related to the motion of the device. However phase-resolved models offer the option of modelling WECs as energy absorbing obstacles and compute the diffraction with high accuracy for WEC technologies that cover the entire water column. Phase-averaged models are then even more limited to represent moving bodies even though a few studies have attempted to model them as source energy terms.

In terms of suitability to consider wave transformation processes, mild-slope equation models are generally the best option for small to medium scale domains (1 to 500 Km^2). They account for the most important transformation processes related to irregular bathymetries and their computational demand remains acceptable. Boussinesq equations models are more suitable to represent non-linear effects of the wave field propagation for the same domain size than mild-slope equations models. However they remain limited to specific applications due to their high demand in computing time. Wave spectral models are the most suitable option to model extensive domains and account for the wave transformation processes present in the real environment. A large amount of data representing years of climate can be processed

for extensive domains. Nevertheless as they are based on a phase-averaged resolution of the wave field it is not possible to use them to extract results for local single wave components.

All models presented in this chapter are appropriate to specific application cases but none of them can accurately cope with the full modelling of the wake effect for a WEC farm; this is why methodologies based on the coupling technique have the potential to provide the most complete solution. By combining the features from BEMs and phase-resolved type WPMs the two main phenomena are locally assessed with accuracy and then the coupling allows for a complete solution across the whole domain. The linear theory limitations need to be taken into account although accurate results are obtained for a range of cases covering most common applications (low to moderate sea states), even above the theoretical limits in some cases. The alternative of applying a coupling technique to non-linear models would be an option to address the case studies situated above the linear theory limits, even though it will require a remarkably high computational demand.

To date the coupling technique remains under development which means there are no available codes that allow the study of the full problem. At the current stage, the methodology is being applied by using in-house modified source codes for simple case scenarios and it is slowly but progressively being validated for more complex environments. Theoretically and once fully developed, the methodology can deal with the full representation of the disturbance generated by the WECs on the incoming wave climate and assess the most important processes occurring in real scenarios considering short-term time scales: irregular sea-states, irregular bathymetries, and some dissipative processes.

2.7 Shortcomings

A large number of studies have attempted to model the wave field transformation around wave energy farms as shown along this Chapter 2. The first attempts with WPMs started by representing WECs as obstacle cells (or as a source term) with a constant coefficient representing the absorption or transmission of the device. This coefficient was usually obtained from 2D experimental tests or from look-up tables given by the technology developers. Subsequent works incorporated a frequency dependent absorption coefficient that changed with the incident wave frequency. The accuracy of representing real WECs impact has been progressively improving but none of these methods include the full representation of the radiation component. In the last five years a few studies started to develop coupling techniques (Section 2.5) where the reflection-diffraction and radiation components of the WEC perturbation are solved with a BEM solver and then implemented as an internal boundary condition of a phase-resolved WPM, allowing for the full representation of the WEC perturbation.

It is based on these recent studies that the methods presented in publications appended to this theses were developed. The objective was to go a step further and bring the full representation of WECs to WPM applications where realistic environmental conditions are considered (irregular waves, real bathymetries, and large WEC farms). Two methods were developed based on the wave-structure interaction BEM solver to assess the wave field surrounding the WECs in their vicinity (near-field) and the phased-resolved type WPM based on the mild-slope equations to solve the wave transformation towards the far-field. The BEM solver provides a 3D solution of the WEC perturbation and the aim was to use this solution to improve the WEC representation in the WPM.

Chapter 3

Wave Field Modelling

In this chapter the numerical tools employed, together with the background theory underpinning the methodologies developed, are described. In addition, the WEC type chosen as a case study for the application of the methods is identified, together with an assessment of the wave energy absorption capacity for different types of WECs.

3.1 Wave Energy Absorption

This section presents a preliminary assessment of the energy absorption capacity of the main type of WECs; this is to justify the WEC type selected for the case studies to which the methods described in this thesis were applied. The methodologies are applicable to all types of WEC but, to validate them, it has been decided to chose a WEC type with a high energy absorption and thus a high impact on the surrounding wave field. Since the objective of the methods developed in this thesis is to evaluate the WEC farm impact on the surrounding wave field, WECs with a higher impact make the validation more reliable.

3.1.1 WEC dynamics

The energy absorbed by a WEC is defined by the dynamics of its PTO system which depends on the whole dynamics of the device. The forces to which a WEC is exposed include the hydrodynamic forces, the hydrostatic forces, the forces applied by the PTO system and additional forces that depend on the specific configuration of the device, such as mooring forces. In this thesis the dynamics of WECs under regular waves are analysed under the assumptions of linear wave theory, which are described in Section 3.2. This assumes linear WEC responses with small amplitudes of motion compare to the wavelength and therefore frequency domain equations were employed to solve the dynamics of the devices. The hydrodynamic forces were determined with a wave-structure interaction BEM solver based on potential flow that is detailed in Section 3.3.

The response motion of a WEC is calculated as a post-processing calculation and the motion amplitude x for a WEC under regular waves of frequency ω is calculated based on Equation (3.1) of [72]. The system analysis is based on the reference of the

incident wave phase being zero at the origin of the domain. The hydrodynamic coefficients Γ, A_r and B_r, are obtained from the BEM solver in a complex form, where Γ represents the excitation force coefficient non-dimensionalised by the amplitude A of the incident wave, and A_r, B_r are the radiation added inertia and damping coefficients respectively. The hydrostatic coefficient H and the inertia component I are calculated based on the geometry description of the device. A passive PTO composed of a linear damper was assumed and Equation (3.2) defines the optimum value of the PTO damping coefficient for a specific wave frequency, which is theoretically demonstrated in [73]. The PTO is modelled by a damping coefficient B_{pto} calculated in Equation (3.2).

$$X(\omega) = \frac{A\Gamma(\omega)}{-\omega^2(I + A_r) - i\omega(B_r + B_{pto}) + H} \tag{3.1}$$

$$B_{pto} = \sqrt{\left(\frac{H}{\omega} - \omega(I + A_r)\right)^2 + B_r^2} \tag{3.2}$$

In the case of WECs with multiple degrees of freedom (Section 1.4.3) or the case of a WEC farm where various devices are computed within the BEM solver, the terms composing (3.1) are expanded to j dimensions where j represents the number degrees of freedom (times the number of devices). The expanded form of the equation of motion computes all interactions between WECs and therefore determines the motion amplitude for each device accounting for the presence of the surrounding moving devices.

In the case of an irregular sea state, composed of many wave frequencies, a fixed value of the PTO damping coefficient was assigned considering the overall statistics of the sea state (based on the peak period) instead of an optimal value for each frequency that would be constantly changing in time. The peak period was chosen as a representative parameter of the sea state, being this the wave period having the largest impact on the dynamics of the device.

3.1.2 Energy absorption

It is straightforward to obtain the absorbed power once the amplitude of motion is determined. The time-average power P_{abs} absorbed by a WEC under regular waves is given by Equation (3.3) and only depends on the PTO damping coefficient B_{pto}, the motion amplitude x, and the wave frequency ω.

$$P_{abs} = \frac{1}{2} B_{pto} \omega^2 |X^2(\omega)| \tag{3.3}$$

The efficiency for wave energy conversion is usually defined by the capture width C_w or the capture width ratio C_r. Both parameters are defined by Equations (3.4) and (3.5) where P_{abs} represents the absorbed power [W], P_{wave} the available wave power per meter of wave front [W/m], and D [m] the main dimension of the device. The capture width describes the equivalent number of wave front meters

of energy extracted by the device and the capture width ratio describes the ratio of absorbed wave power with respect to the available power to which the main dimension of the WEC is exposed. Thus, the first definition is not related to a specific device dimension while the second definition is proportional to the main dimension of the WEC.

$$C_w = \frac{P_{abs}}{P_{wave}} \tag{3.4}$$

$$C_r = \frac{P_{abs}}{P_{wave} D} \tag{3.5}$$

3.1.3 Efficiency assessment for main type of WECs

The efficiency comparison between WECs is a complicated subject, the major challenge is to compare technologies that are still at a research and development stage, therefore where there is not a clear real device definition to chose. The comparison can be done based on the rated energy of the device, or based on its efficient respect to the energy to which the main dimension of the device is exposed. In this assessment is has been chosen to compare the device based on the second option. It is often difficult to define the main dimension of a WEC since they are three dimensional bodies where more than one dimension is exposed to the wave front and contributing to the energy extraction. Therefore an assessment of the energy absorption efficiency for various types of WEC is conducted based on the capture width definition and considering WECs that are comparable in terms of surface exposed to the wave front.

The hydrodynamic forces are determined with NEMOH and then the dynamics, the power absorption, and the capture width of the WECs are obtained from (3.1)-(3.4). Four types of WEC were assessed using the group classification defined by Falnes (point absorber, attenuator, and terminator) to which a fourth type defined as a flap type WEC was added. The flap-type WEC is a particular variation of the terminator type since it has a vertical wall where two dimensions are exposed to the wave front: the horizontal dimension parallel to the wave front and a vertical dimension covering the entire water column (or most of it).

Figure 3.1 shows a sketch representation of the four type of WECs that have been analysed based on a predominant wave direction. The dimensions of the devices were determined based on an equivalent surface defined by the two main dimensions exposed to the wave front and set equal to 200 m^2. This was stipulated to define an equivalent wave energy flux to which the devices are exposed. For the case of the point absorber, terminator, and attenuator the equivalent surface was the horizontal plane surface and the same draft of 4 m was defined for all. To simplify the comparison, the devices were each constrained to move only in one degree of freedom. The point absorber was defined as a vertical cylinder constrained to move

in heave, the terminator was defined as a barge parallel to the wave front and constrained to move in surge, and the attenuator was defined as barge perpendicular to the wave front and constrained to move in pitch. For the case of the flap type WEC the equivalent surface was its vertical surface parallel to the wave front. A thickness of 1 m was defined and the device was considered to be constrained to move only in pitch rotating around an axis located at its bottom end.

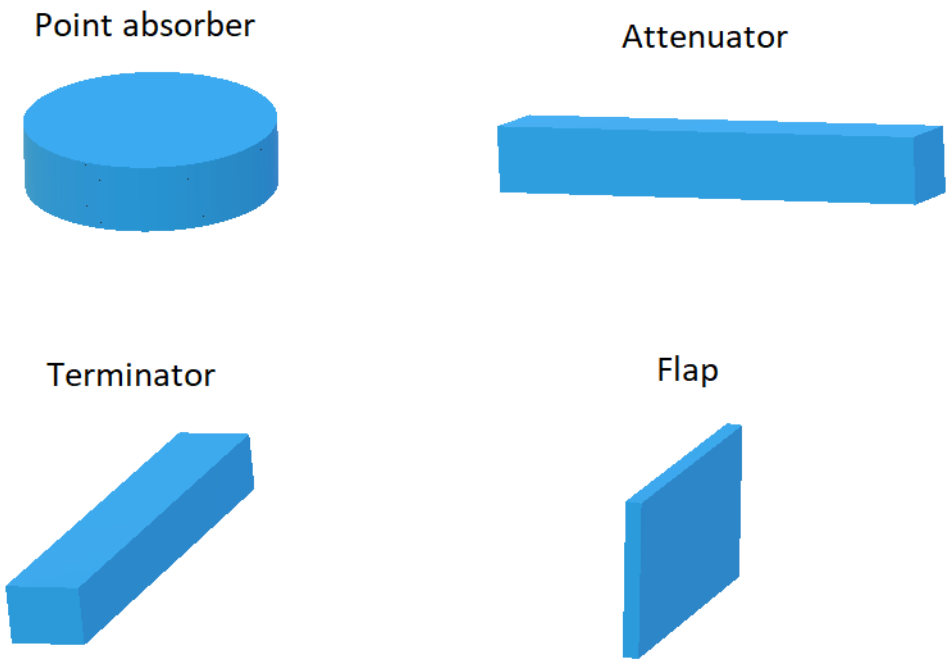

FIGURE 3.1: Sketch representation of four types of WECs. The waves propagate from left to right.

The capture width ratio was calculated along a range of 50 frequencies ($\Delta\omega = 0.1$) to assess the energy absorption capacity of the four types of WECs, assuming a constant water depth of 10 m. A constant damping coefficient tuned for a wave period of 8 s (based on Equation (3.2)) was selected for all frequencies, assuming a sea state of peak period $T_P = 8$ s being representative of common operational wave conditions for a WEC farm.

Figure 3.2 shows that the maximum capture width is obtained close to the optimum period with one peak for the point absorber, attenuator, and terminator types and a double peak for the flap. The flap has the highest capture width with values surrounding 1.6 m. The point absorber and terminator type have lower capture width distributions with maximum values at about 0.5, while the attenuator type capture width remain pretty low with values below 0.1. The results clearly show that the average capture width of the flap is much higher than the rest of technologies for the whole range of frequencies.

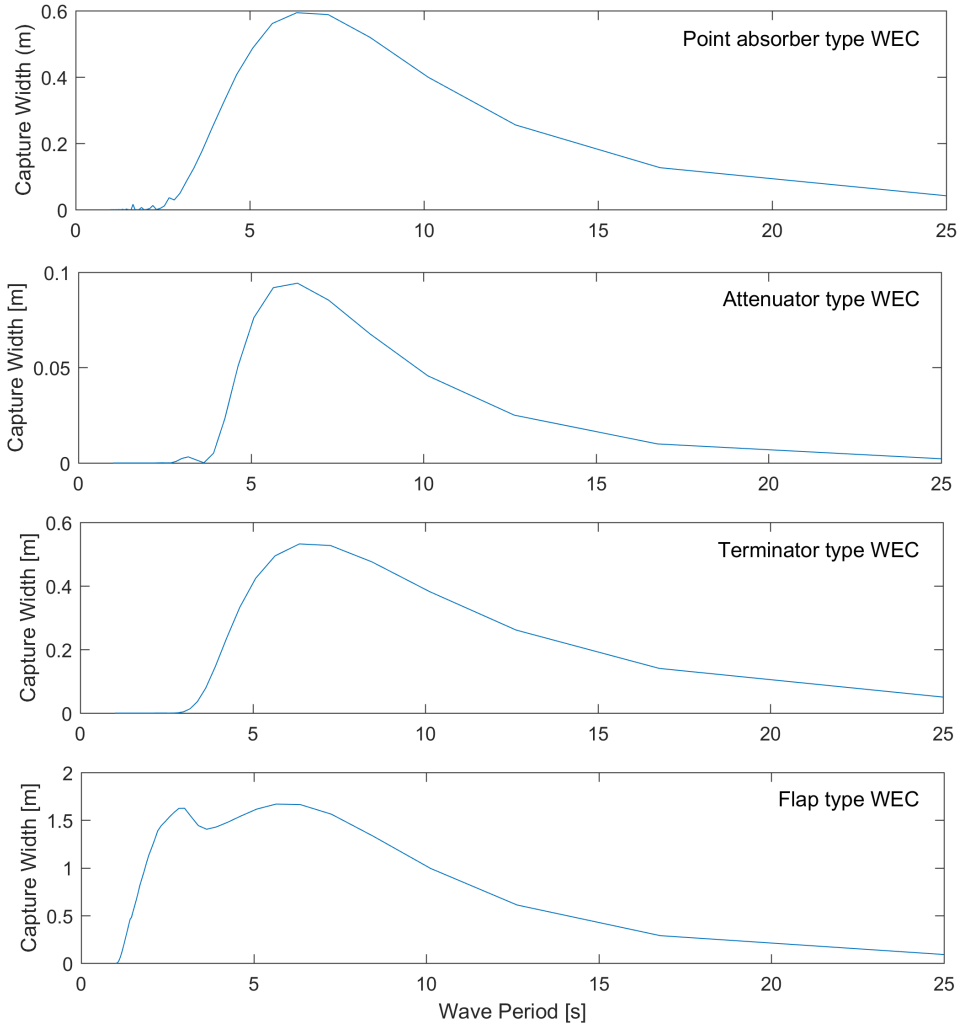

FIGURE 3.2: Capture width vs. wave period for different types of WECs.

3.1.4 Flap Type WEC

The flap WEC was chosen as the device type to apply the different methods developed in this thesis. Since the capture width results (Section 3.1.3) showed it is the most absorbing energy type of WEC, it was assumed therefore that it is the technology affecting the most the surrounding wave field. A technology having a stronger impact on the wave field facilitates the validation of numerical methods where the aim is to model the perturbation generated by a WEC in the wave field. In most of the case scenarios the flap is considered as a surface-piercing device hinged at the bottom of the seabed as shown in Figure 3.3.

The motion is restricted to pitch therefore the rest of degrees of freedom are constrained. The shaft about which the flap rotates is at the base of the device which is mounted on the sea bed. Table 3.1 shows the main characteristics of the flap that were used to describe the device in the numerical solvers.

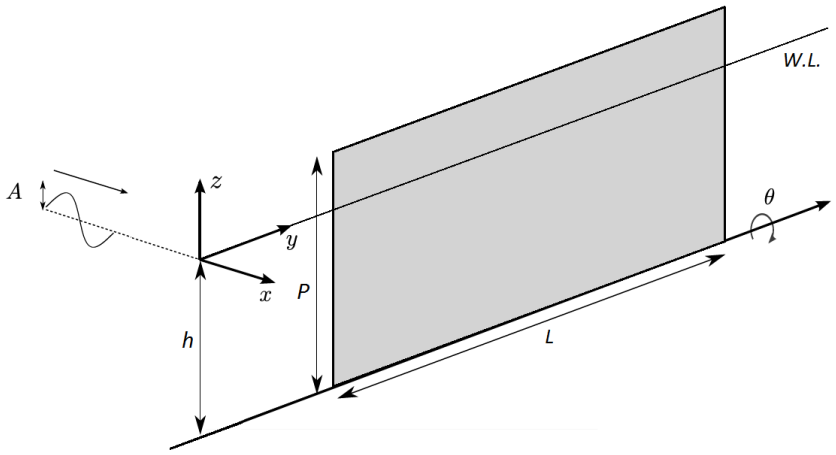

FIGURE 3.3: Flap type WEC sketch.

TABLE 3.1: Main characteristics of the flap type WEC.

Parameter	Coefficient	Value	Units
Length	L	20	m
Height	P	12	m
Thickness	t	1	m
Relative density	ρ_r	0.3	-

3.2 Linear Wave Theory

The two models used in this thesis are based on the linear wave theory and the applicability of this theory relies on the presumption that the case studies remain within its limits of application. In this section the main equations and assumptions defining the linear wave theory are summarised based on [74] and [75].

3.2.1 Surface elevation characterisation

The irregular oscillations of the surface elevation $\eta(t)$ over time t and across a free-surface can be regarded as being composed of a continuous spectrum of frequencies, each characterised by an amplitude density measure $A(\omega)$ and a phase function $\varphi(\omega)$. So the surface elevation can be represented as the linear sum of an infinite number of frequency components (Equation (3.6)).

$$\eta(t) = \sum_{n=0}^{\infty} A_n \cos(\omega_n t - \varphi_n) \tag{3.6}$$

If wave amplitudes A_n are considered to be small, (3.6) can be regarded as a series of individual sinusoidal waves where the influence of each wave component can be considered separately. Each wave component will lie within the linear regime provided that $A_n k_n << 1$ and $A_n/d << 1$, where k_n is the wave number vector

related to the wavelength λ by $k_n = 2\pi/\lambda_n$ and which represents the number of wavelengths per unit of distance for each wave component.

An expanded version of Equation (3.6) is obtained if directionality is included in the wave field. Equation (3.7) represents a superposition of a infinite number of long-crested wave components propagating in arbitrary directions where β_n is the angle between the direction of wave propagation and the x-axis.

$$\eta(x, y, t) = \sum_{n=0}^{\infty} A_n \cos(k_n(x \cos \beta_n + y \sin \beta_n) - \omega_n t - \varphi_n) \tag{3.7}$$

In the following sections starting from the assumptions of the potential flow theory a set of equations are derived in order to describe the flow with the form of Equation (3.7).

3.2.2 Potential flow theory

Potential flow theory describes an ideal fluid in the absence of viscous tensions allowing for the simplification of the mathematical expressions defining the fluid. The main assumptions of this are:

- The fluid is inviscid
- The flow is irrotational.
- The fluid is incompressible.

From the irrotationality condition, meaning the flow vorticity is zero, derive Equation (3.8)

$$\nabla \times \vec{V} = 0 \tag{3.8}$$

which allows describing the flow velocity $\vec{V}$ as the gradient of the velocity potential ϕ described by Equation (3.9),

$$\vec{V}(x, y, z) = \nabla\phi. \tag{3.9}$$

.

From the incompressibility condition the continuity equation can be simplified and expressed as

$$\nabla \cdot \vec{V} = 0 \tag{3.10}$$

that together with Equation (3.9) leads to Laplace's Equation,

$$\nabla^2\phi = 0. \tag{3.11}$$

3.2.3 Boundary conditions

Seeking a solution for the surface elevation η and velocity potential ϕ, a group of linearised boundary conditions for the free surface and the bottom are described, leading to the following additional assumptions

- The wave amplitude is small with respect to the wavelength.
- The wave amplitude is small with respect to the water depth.
- The water depth is assumed to be constant

Bottom boundary

The sea bed is considered as a fixed and rigid body. Therefore, in the absence of viscosity, the vertical component of velocity is zero at the bottom boundary to ensure that no fluid can flow through the boundary surface. Thus, the boundary condition at the sea bed can be described by (3.12) where the vertical component z is considered equal to the water depth h

$$\frac{\partial \phi}{\partial z} = 0. \tag{3.12}$$

Free-surface boundary

The free-surface boundary condition is defined by two boundary conditions: the kinematic boundary condition and dynamic boundary condition for the free-surface. The kinematic boundary condition states that the free surface is defined by $z = \eta(x, y, t)$ and this must hold at all times, giving a linear boundary condition defined by:

$$\frac{\partial \eta}{\partial t} = \frac{\partial \phi}{\partial z}. \tag{3.13}$$

Then the dynamic boundary condition assumes that the water pressure and the air pressure will be equal on the interface leading to the linearised boundary on $z = \eta$ described by:

$$\frac{\partial \phi}{\partial t} + g\eta = 0, \tag{3.14}$$

where g represents the gravitational acceleration. From (3.13) and (3.14) the function η can be eliminated deriving in (3.15) only depending on ϕ

$$\frac{\partial^2 \phi}{\partial t^2} + g\frac{\partial \phi}{\partial z} = 0. \tag{3.15}$$

3.2.4 Regular waves solution

Finally, considering the previous boundary conditions and looking for a solution of Laplace's equation (Equation 3.11) of the form given by Equation (3.16) where ($\hat{}$)

denotes the spatial component of the complex form of a variable, in this case the velocity potential:

$$\phi(x, y, z, t) = \Re\left\{\tilde{\phi}(x, y, z)e^{-i\omega t}\right\}. \tag{3.16}$$

The complete solution is given by (3.17) and (3.18),

$$\eta(x, y, t) = A\cos(k(x\cos\beta + y\sin\beta) - \omega t) \tag{3.17}$$

$$\phi(x, y, z, t) = \frac{Ag}{\omega}\frac{\cosh k(z+h)}{\cosh kh}\sin(k(x\cos\beta + y\sin\beta) - \omega t) \tag{3.18}$$

with h being the vertical distance to the free-surface and the frequency ω related to the wavenumber k by the dispersion relation from Equation (3.19). The mean of η is assumed to be at $z = 0$,

$$\omega^2 = gk\tanh kh. \tag{3.19}$$

3.3 BEM Solver NEMOH

NEMOH is an open-source Boundary Element Method (BEM) solver developed by Ecole Centrale de Nantes [20], written in Fortran programming language, and is used in this thesis to obtain the near-field surrounding WECs. As all BEM solvers are based on potential flow, NEMOH solves the perturbed velocity potential ϕ as a 3D solution in the frequency domain from the linear wave-body interaction boundary value problem (or scattering problem). In the following sections the main equations solved by NEMOH are detailed, together with the main consideration for the modelling of WECs.

3.3.1 Governing equations

The scattering problem solved by NEMOH seeks a solution of Laplace's equation (3.11) considering a set of boundary conditions for an incident regular wave described by:

$$\tilde{\phi}_{inc}(x, y, z) = -\frac{ig}{\omega}A_{inc}f_0(z)e^{i(k(x\cos\beta + y\sin\beta) - \omega t)} \tag{3.20}$$

where A_{inc} represent the incident wave amplitude and $f_0(z)$ the depth dependence. The set of boundary conditions is composed of the bottom and free-surface boundary conditions described earlier in (3.12), (3.13), and (3.14), and the body and scattering boundary conditions described by:

$$\frac{\partial\phi}{\partial n} = \vec{U}\cdot\vec{n} \tag{3.21}$$

$$\lim_{r \to +\infty} \phi_p = 0 \tag{3.22}$$

The body and scattering boundary conditions need to satisfy (3.21) and (3.22) respectively, where $r^2 = (x^2 + y^2)$, ϕ_p is the perturbed potential generated by the presence of the body, $\vec{U}$ is the velocity vector relative to the body assumed to be rigid, and $\vec{n}$ the normal vector of the body surface. The body boundary condition (3.21) needs to be satisfied at the wetted surface of the body and describes the non-porosity of the body surface. The scattering boundary condition (3.22) describes the complete dissipation of the perturbed potential at the infinity of the domain.

The problem is divided into a scattering-diffraction problem and a radiation problem per degree of freedom that are solved individually for each wave frequency using Green's function. The diffraction problem is defined by considering the body to be fixed under the presence of an incoming incident wave based on the boundary condition from (3.23) for the body surface.

$$\frac{\partial \phi_d}{\partial n} = -\frac{\partial \phi_{inc}}{\partial n} \tag{3.23}$$

where ϕ_d represents the diffracted potential. The radiation problem is solved by considering a forced motion of the body in calm conditions (absence of waves) assuming the boundary condition from (3.24) for the body surface

$$\frac{\partial \phi_r}{\partial n} = U_j \cdot n_j, \tag{3.24}$$

where ϕ_r represents the radiated potential and j represents the corresponding degree of freedom for each radiation problem. Figure 3.4 shows a sketch of the two problems solved by a BEM solver, where the body is meshed and a solution is found for the diffracted wave and the radiated wave at each node defining the body mesh.

From the resolution of these problems the diffracted and radiated potential are obtained, and the sum of the two solutions gives the perturbed potential ϕ_p (3.25). Using the principle of superposition the velocity potential for the total wave field ϕ_t is calculated in (3.26) as a sum of the perturbed wave potential and the incident wave potential ϕ_{inc} defined in Equation (3.20).

$$\tilde{\phi_p}(x, y, z) = \tilde{\phi_d} + \sum_{j=1}^{6} \tilde{\phi_{r,j}} \tag{3.25}$$

$$\tilde{\phi_t}(x, y, z) = \tilde{\phi_{inc}} + \tilde{\phi_p} \tag{3.26}$$

Then from the potential at the free surface condition $(z = 0)$ expressed as Φ it is then straightforward to obtain the surface elevation as described by (3.27)

$$\tilde{\eta}(x, y) = \frac{i\omega}{g} \tilde{\Phi}(x, y). \tag{3.27}$$

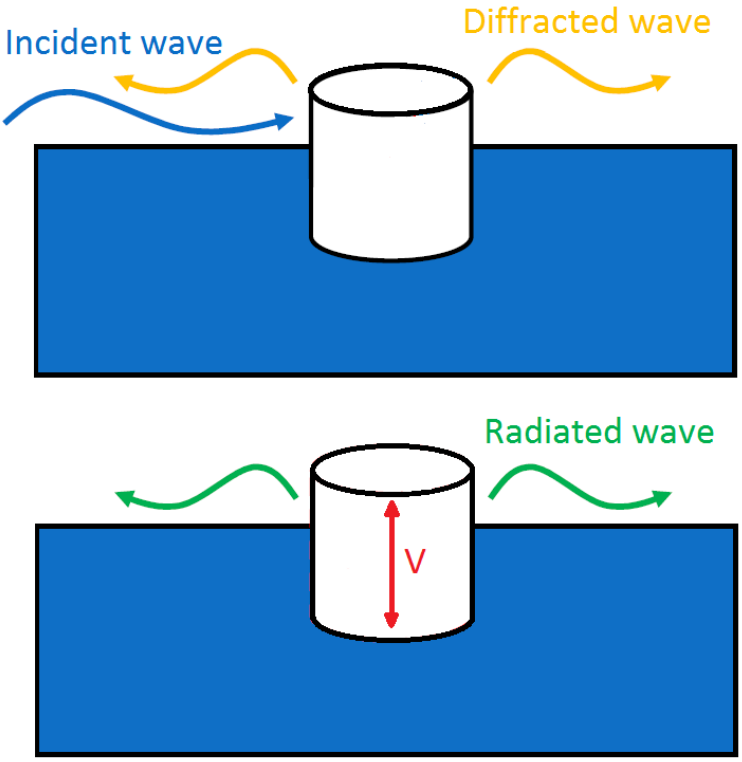

FIGURE 3.4: Sketch of the diffraction (top) and radiation (bottom) problem solved by a BEM solver.

3.3.2 Total wave field calculation

NEMOH was used across the publications presented in this thesis to compute near-field wave patterns for single devices or WEC farms composed of several devices. These solutions were used then to compute the wave perturbation caused by WECs in the WPM. In this section a step-by-step approach describes the solutions obtained from NEMOH and the post-processing to obtain the total wave field. As an illustrative example a farm composed of 9 flaps was modelled in order to represent the interaction between devices.

The diffracted and radiated wave field are obtained as an output from NEMOH, one diffracted wave where the flaps are considered to be fixed under the presence of an incoming regular wave (Figure 3.5), and one radiated wave representing the wave generated by the motion of the flap (Figure 3.6). One radiated wave is obtained for each degree of freedom and per device in a non-dimensional form relative to a unit of motion amplitude and then dimensionalised by the resultant motion amplitude obtained from (3.1). The results are output in terms of wave amplitude and phase, considering the incident wave phase is zero at the centre of the domain ($x = 0$, $y = 0$). For the sake of simplicity the solutions are plotted here in terms of wave amplitude normalised by meter of incident wave, and a domain on 400 x 400 m is considered as an illustrative example.

Figure 3.7 shows the amplitude for the perturbed and total waves, (3.25) and

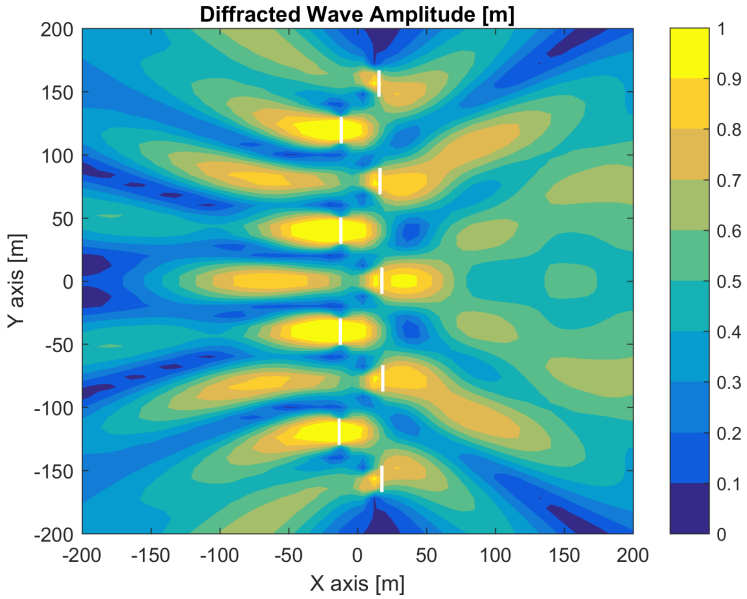

FIGURE 3.5: Diffracted wave amplitude for 9 flaps.

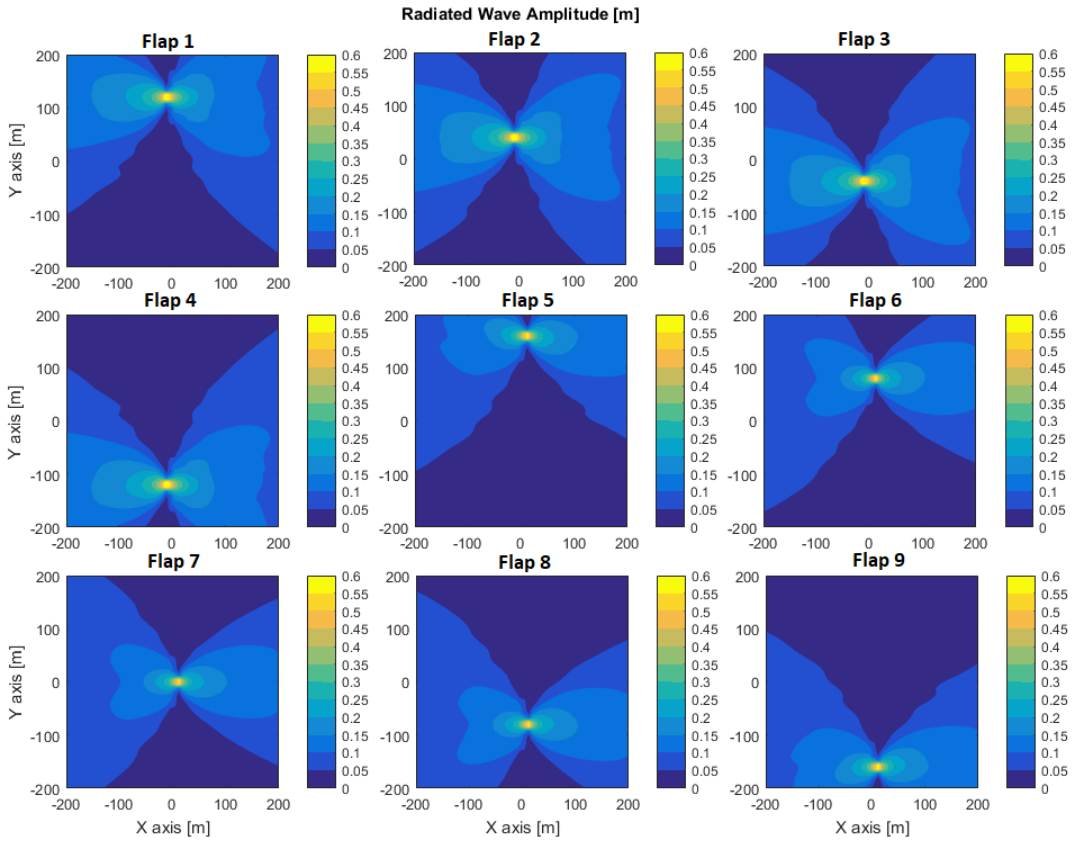

FIGURE 3.6: Radiated wave amplitude for each of the 9 flaps.

(3.26). Once the wave field outputs from NEMOH have been obtained, the perturbed and the total wave amplitude can be computed in the post-processing. The perturbed wave amplitude is obtained from the sum of the diffracted and all radiated waves amplitudes, and the total wave amplitude is obtained as the sum of the

perturbed and incident wave amplitudes.

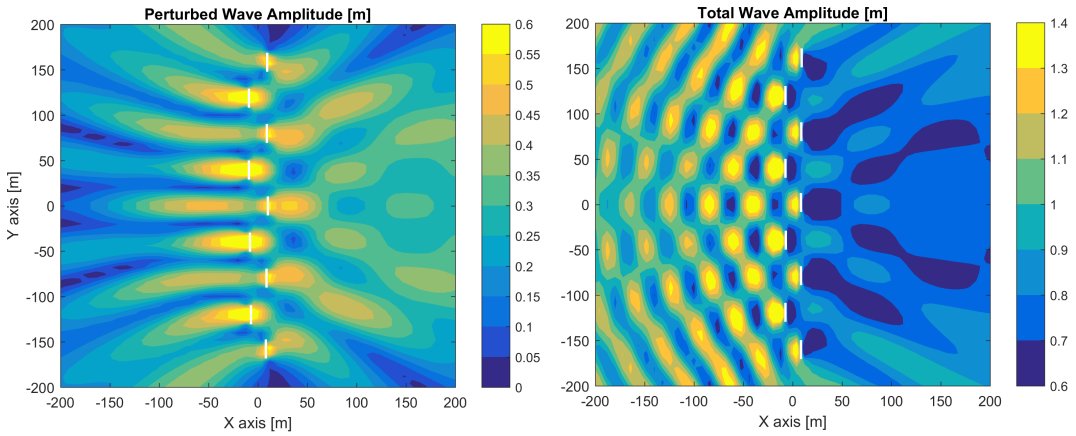

FIGURE 3.7: Perturbed and total wave amplitude for 9 flaps.

3.3.3 Mesh convergence

The flap is modelled in NEMOH as a vertical wall piercing the free-surface in most of the cases with its axis of rotation located at a water depth of 10 m. The mesh describing the device is composed of rectangular panels as the mesh described in Figure 3.8.

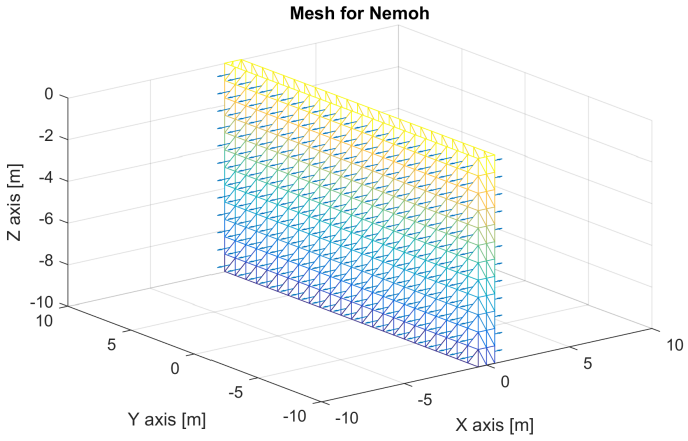

FIGURE 3.8: Flap mesh discretisation in NEMOH.

A convergence analysis was carried out in order to assess the optimal number of panels to use in the wave field computations. The wave field surrounding the flap was obtained for different mesh refinements ranging from 50 to 1000 panels for a regular wave of T = 7.85 s. Figure 3.9 shows the percentage error [%] obtained for each case compared to the 1000 panel case.

It is assumed that convergence is reached for the case of 500 panels since the error remains below 1% along the whole domain. The optimum panel size is directly proportional to the wavelength of the incident wave [20]. Thus this convergence

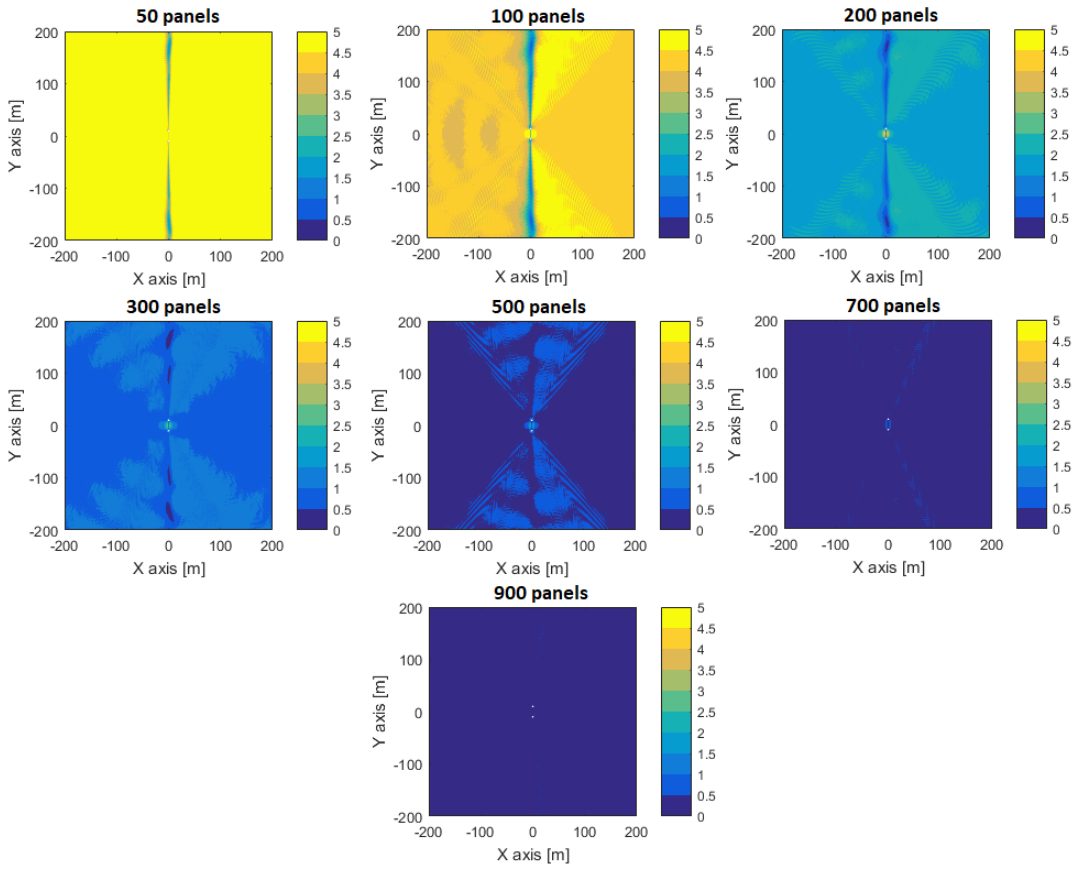

FIGURE 3.9: Perturbed wave amplitude error [%] for different mesh refinements.

analysis suggests that a maximum panel size of $\Delta x = \lambda/70$ should be used in all cases, which was equal to 1 m for the 500 panels case.

3.4 Wave Propagation Model MILDwave

MILDwave is used in this thesis to solve the wave transformation processes throughout large domains and obtain the far-field wave pattern to assess the wake effect for WEC farms. MILDwave is, as mentioned in Section 2.3.1, a time-dependent mild-slope equation model and a phase-resolved type Wave Propagation Model (WPM). MILDwave is written in C++ programming language and it solves the propagation of surface waves throughout the domain and the interaction with obstacles (previously defined) by solving the depth-integrated mild-slope equations of Radder and Dingemans [41].

3.4.1 Governing equations

Equations (3.28) and (3.29) describe the transformation of linear regular and irregular waves over a mild slope bathymetry (bed steepness up to 1/3 [76] for irregular

waves) and are the main equations solved by MILDwave at each time step,

$$\frac{\partial \eta}{\partial t} = B_c \Phi - \nabla \cdot (A_c \nabla \Phi), \tag{3.28}$$

$$\frac{\partial \Phi}{\partial t} = -g\eta. \tag{3.29}$$

The variables η and Φ represent respectively the surface elevation and velocity potential at the free surface level. The value of B_c and A_c are calculated using (3.30) and (3.31):

$$B_c = \frac{\omega^2 - k^2 C C_g}{g}, \tag{3.30}$$

$$A_c = \frac{C C_g}{g}, \tag{3.31}$$

where C is the phase velocity and C_g the group velocity for a wave with wave number k and angular frequency ω. The full derivation of these equations can be found in [65].

A finite difference scheme (Figure 3.10) as described in [77] is used to discretise and solve (3.28) and (3.29), which consists of a two-step space-centred and time-staggered computational grid [78]. The domain is divided in grid cells with dimensions Δx and Δy and central differences are used for spatial as well as time derivatives. Both η and Φ are calculated in the centre of each grid cell at different time levels, $(n+\frac{1}{2})\Delta t$ and $(n+1)\Delta t$ respectively, by using the discretised equations (3.32) and (3.33),

$$\begin{aligned}
\eta_{i,j}^{n+\frac{1}{2}} \simeq \eta_{i,j}^{n-\frac{1}{2}} &+ B_{i,j}\Phi_{i,j}^{n}\Delta t \\
&- \frac{A_{i+1,j} - A_{i-1,j}}{2\Delta x}\frac{\Phi_{i+1,j}^{n} - \Phi_{i-1,j}^{n}}{2\Delta x}\Delta t \\
&- A_{i,j}\frac{\Phi_{i-1,j}^{n} - 2\Phi_{i,j}^{n} + \Phi_{i+1,j}^{n}}{(\Delta x)^2}\Delta t \\
&- \frac{A_{i,j+1} - A_{i,j-1}}{2\Delta y}\frac{\Phi_{i,j+1}^{n} - \Phi_{i,j-1}^{n}}{2\Delta y}\Delta t \\
&- A_{i,j}\frac{\Phi_{i,j-1}^{n} - 2\Phi_{i,j}^{n} + \Phi_{i,j+1}^{n}}{(\Delta y)^2}\Delta t
\end{aligned} \tag{3.32}$$

$$\Phi_{i,j}^{n+1} \simeq \Phi_{i,j}^{n} - g\eta_{i,j}^{n+\frac{1}{2}}\Delta t \tag{3.33}$$

where A and B represent A_c and B_c given by (3.30) and (3.31). Subscripts index i, j represent the spatial grid cell at position $i\Delta x$ and $j\Delta y$ and superscript index n represents the time step $n\Delta t$.

The grid cell size $\Delta x = \Delta y$ is set so that $\frac{\lambda}{20} \leq \Delta x \leq \frac{\lambda}{10}$ where λ is the shortest wavelength for the case of irregular waves. The time step Δt has to meet the Courant-Friedrichs-Lewy criterion, $\Delta t \leq \frac{\Delta x}{C}$ where C is the phase velocity of the

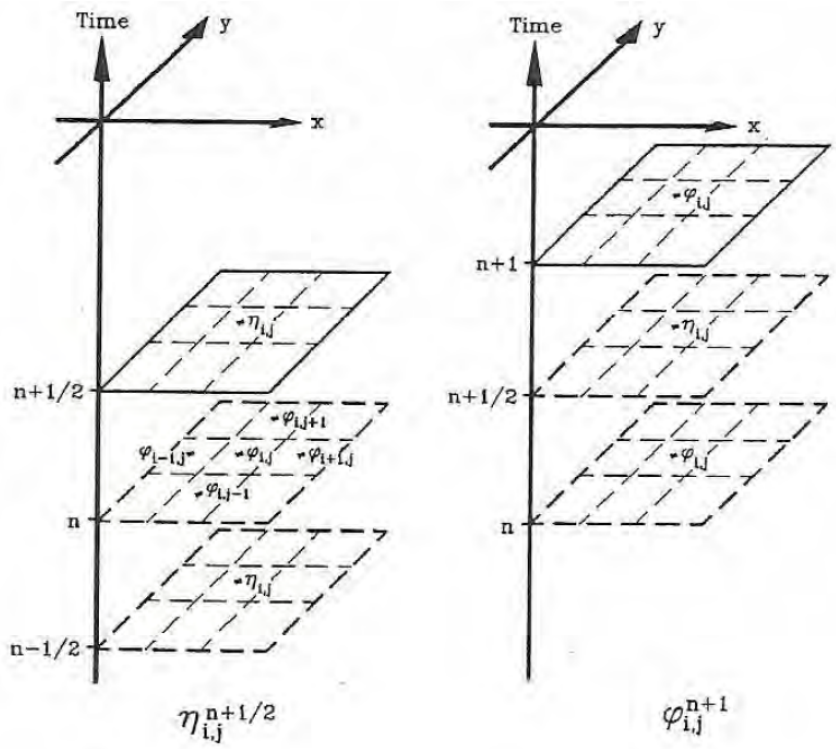

FIGURE 3.10: Finite difference scheme (computational space-centred, time-staggered grid)

lowest frequency (longest wavelength), in order to guarantee a stable and consistent result.

3.4.2 Wave generation

Incident waves are generated in MILDwave at the offshore boundary by using the source term addition method, i.e. by adding an additional surface elevation η^* given by (3.34) and described in [79] to the calculated value on a wave generation line for each time step,

$$\eta^* = 2\eta_{inc}\frac{C_g \Delta t}{\Delta x}\cos\beta \tag{3.34}$$

where η_{inc} the surface elevation of incident waves.

The incident wave generation line is assumed to be parallel to the y-axis generating waves in both directions, towards the positive and negative x-axis directions. The component of the wave propagated towards the negative direction is absorbed by the sponge layer located just next to the generation line and the second component propagates towards the domain replicating the desired incident wave across the domain.

The source term addition method means that any reflected waves (by obstacles) travelling across the generation line can cross the line without suffering any type of disturbance. Absorption sponge layers are set up in MILDwave at the open

boundaries of the domain to absorb the outgoing waves. It is recommended to use a minimum length of 2.5λ to ensure no reflection takes place, considering the longest wavelength for the case of irregular waves.

Figure 3.11 shows a sketch of the set up for a wave generated along y-axis and propagating parallel to the x-axis. In the case of a wave generated with a heading angle β different from 0 (wave propagation direction not parallel to the x-axis) waves are generated along x and y-axis and (3.34) becomes dependent on $\cos\beta$ and $\sin\beta$ respectively for each axis. Sponge layers may be added to the sides of the domain as well for the cases where waves do not propagate parallel to the x-axis, i.e. waves generated by the presence of obstacles (Paper A) or internal waves generated from the inner domain (Paper B, C, and D).

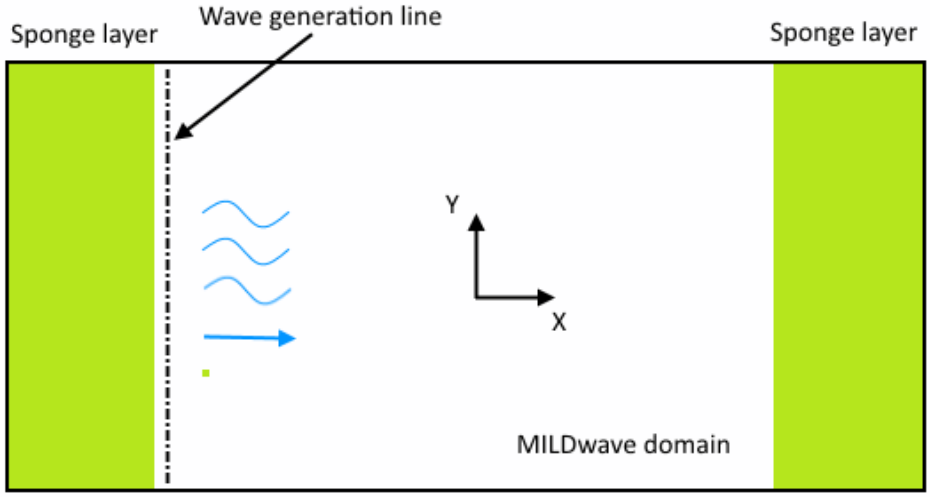

FIGURE 3.11: MILDwave wave generation set up.

MILDwave does not intrinsically represent the wave field perturbation generated by a moving WEC as a BEM solver does. However solutions attempting to represent moving bodies such as WECs in MILDwave are available [65], [66]. In next Chapter 4, two methodologies aiming at overcoming this gap are described.

3.5 Irregular waves

The representation of irregular waves is carried out in this thesis based on the superposition principle of linear waves presented in (3.7). The surface elevation of a complex sea state is assumed to be a superposition of a discrete number of regular sinusoidal waves with random phases along a range of frequencies representing a wave spectrum. The parametrised JONSWAP spectrum [80] is used to represent the wave spectral density distribution S at the input boundary where incident long-crested irregular waves are defined:

$$S(f) = \alpha H_s^2 f_p^4 f^{-5} \gamma^{\exp(-\frac{(f-f_p)^2}{2\sigma^2 f_p^2})} \exp.(\frac{-5}{4}(\frac{f_p}{f})^4) \tag{3.35}$$

Equation (3.35) defines the spectral density distribution for the JONSWAP spectrum where the peak enhancement factor $\gamma = 3.3$, the scaling parameter $\alpha = 0.2044$, the peak frequency $f_p = 1/T_p$, and the spectral width parameter $\sigma = 0.07$ for $f \leq f_p$ and $\sigma = 0.09$ for $f \geq f_p$. Therefore the wave spectral density distribution at the boundaries is described by a peak period T_p and a significant wave height H_s. In the thesis the wave frequency is expressed in terms of angular frequency ω which is related to the linear frequency f by $\omega = 2\pi f$.

The relation between the wave spectral density S and the wave amplitude A, corresponding to each frequency interval, is defined by:

$$S(\omega)\Delta\omega = \frac{1}{2}A^2(\omega), \tag{3.36}$$

where $\Delta\omega$ represents the increment between frequencies.

The incident wave spectrum will change locally along the domain due to the water depth changes and the disturbance generated by the presence of the WEC farm. Thus, in order to assess the wake effect of a farm, the spectral density distribution is obtained for the undisturbed sea state S_u (in the absence of the farm), and then for the disturbed sea state S_d (in the presence of the farm). Figure 3.12 shows an example of the change in the wave spectral density due to the presence of a WEC farm for a grid cell centrally located behind the farm where a decrease in the energy is found.

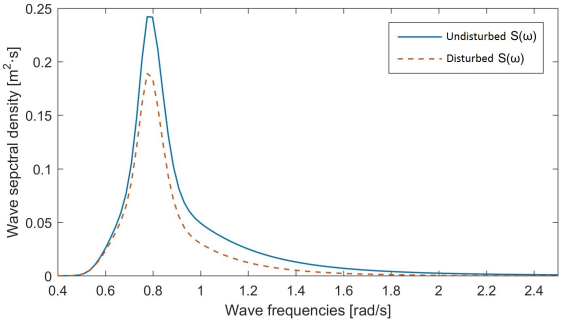

FIGURE 3.12: Undisturbed wave energy spectrum vs. disturbed wave energy spectrum (behind the WEC).

Finally the disturbance coefficient K_d defined by (3.37), quantifies using a single parameter the disturbance caused by the WEC farm at each grid cell along the domain. H_{sd} represents the significant wave height corresponding to the disturbed wave spectrum and H_{su} the significant wave height corresponding to the undisturbed wave spectrum. The significant wave height H_s is approximated here as $4\sqrt{m_0}$ where m_o is the zeroth-moment of the variance wave spectrum $S(\omega)$.

$$K_d = \frac{H_{sd}}{H_{su}} \tag{3.37}$$

The disturbance coefficient is the main parameter used in the publications appended to this thesis to quantify the wake effect generated by the WEC farms. The

wave reflection and transmission is quantifiable by means of this single parameter since each grid cell across the domain has its corresponding disturbance coefficient value, representing the local increase or decrease of significant wave height. This method based on the superposition principle relies on the limitations of the linear wave theory, so in practice it is limited to low-to-moderate sea states.

Chapter 4

Developed Methodologies

An overview of the different numerical methodologies developed in this PhD is summarised in this chapter, together with a description of the step-by-step approach followed during the research work.

4.1 Introduction

WPMs have been developed to assess the main wave transformation processes and to account for a variety of modules depending on the environmental conditions considered. However, the implementation of WECs and their effect on the wave climate is not an intrinsic feature of the existing versions. WECs are moving bodies, so they do not only diffract, reflect and absorb waves, as the common obstacles modelled in WPMs, but they also radiate waves generated by their motion affecting the surrounding wave climate environment. Thus, the inclusion of such radiated waves is a feature that still needs to be addressed to fully represent the wave climate impact of WECs.

4.1.1 Overview on the methodologies

Methodologies based on the so-called sponge layer technique and coupling technique have been developed as a step-by-step approach starting from the state-of-the-art and progressively adding features and complexity to the work. The final objective was to develop assessment tools to quantify wake effects for WEC farms considering realistic environmental conditions such as irregular waves and real bathymetries. A gap in the WPM needed to be addressed to fully represent the wave perturbation generated by WECs and, from the available literature, it was clear that potential flow BEM solvers were a good option to obtain the local near-field WEC perturbation.

The first methodology is based on the sponge layer technique initially implemented by Beels et al. in [39]. The method was developed in Paper A and is based on a representation of WECs as obstacle cells that are attributed an absorption coefficient. This technique is usually implemented by tuning the absorption coefficients using experimental tests or look-up tables providing the WEC transmission coefficients. It is difficult to provide an accurate representation of the 3D wave field

surrounding the WEC from either experimental tests or look-up tables, since they are primarily based on 2D assessments. In this application of the method, a new approach utilises absorption coefficients tuned against near-fields solutions obtained from a BEM solver that provide a 3D wave field representation. The method is presented in Paper A and applied to WEC farms under irregular sea states and mild-slope varying depths.

The second methodology is based on a coupling technique initially presented by [65] that was further developed through Paper B, Paper C and Paper D to be applied to real scenarios with greater complexity. The method merges the results obtained from a BEM solver into the WPM as an internal boundary condition. This boundary condition aims at describing the perturbed waves generated by the presence of WECs on the incoming waves, which together give the solution of the total wave field. As a consequence of the similarity in the governing equations between the two solvers, coupling the solution from the BEM solver into the WPM remained a feasible task. The methodology was further developed in Paper B and Paper C where improvements were progressively implemented until obtaining a fully developed method described in Paper D, which is applied to WEC farms subject to irregular sea states and a real bathymetry.

Both methodologies are described in detail in this chapter and the flap-type WEC described in Section 3.1.4 is employed in all the case studies presented. Therefore the device is always deployed at a water depth of 10 m according to its design conditions. An error definition based on a comparison with BEM solver solutions is used to define the accuracy of each methodology. The error is regularly used along the appended papers and is defined in Section 5.1 where an assessment for all methodologies is done. This error definition considers the solution obtained from NEMOH as the target solution to which the comparison is done, since in practice it is the best solution that can be obtained for the perturbed wave field generated by a WEC under an incoming regular wave.

4.2 Sponge Layer Technique

4.2.1 Overview

Irregular long-crested waves are generated in the time-domain in MILDwave to assess WEC farms wake effects using the sponge layer technique. Therefore, the same irregular waves for a single device need to be computed first from NEMOH to use them as a target to tune the WEC representation in MILDwave. Then the obstacle cells representing the WEC in MILDwave are tuned to the target waves computed from NEMOH. Once the accurate configuration of absorption coefficients is found for a single WEC, a farm of several devices can be represented by replicating the same obstacle cell configuration throughout the domain. It is important to consider

that each sea state has its own optimum configuration of obstacle cells and therefore a tuning of the absorption coefficients is needed for each case scenario.

4.2.2 Target irregular waves from NEMOH

Irregular waves are described based on the disturbance coefficient described as $K_d = H_{sd}/H_{su}$ (Section 3.5). The irregular waves from NEMOH are computed from a superposition of the total wave amplitude obtained for each wave frequency and assuming constant water depth conditions. Figure 4.1 shows the K_d values obtained from NEMOH along the a domain of 400 x 400 meters for a long-crested irregular sea state with peak period $T_p = 8\ s$ considering a discretisation of 50 frequencies. Section S, drawn by a dotted line, represents the region where the K_d values are used as a target to tune the absorption coefficients representing the WEC in MILDwave. The disturbance coefficient does not change with the significant wave height of the incident sea state since linear waves conditions are assumed. Therefore each sea state is only described by its peak period T_p.

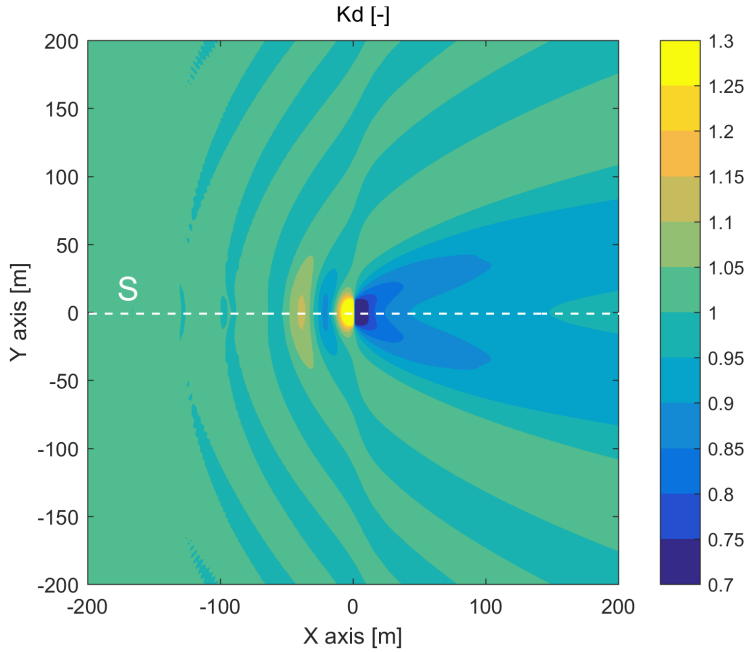

FIGURE 4.1: Disturbance coefficient from NEMOH for 1 flap and $T_p = 8$ s.

4.2.3 Tuning representation in MILDwave

The obstacle cells in MILDwave locally affect the surface elevation of the propagated wave which is multiplied by values in the range from 1 to 0. Values equal to 1 represent a water grid cell (no absorption) while values equal to 0 represent a grid cell of a fully reflective obstacle (100 % reflection). Therefore, the reflection, absorption, and transmission of the obstacle change depending on the distribution of the absorption coefficients through the set of obstacles cells. The absorption coefficients are tuned

in such a way that the near-field from MILDwave matches the results obtained from NEMOH along section S (Figure 4.1).

A grid cell size of 2 x 2 m is chosen as an intermediate value to obtain consistent results for a wide range of sea states based on the recommendations from [36] (Section 3.4.1). The flap type WEC is represented here by a group of grid cells occupying the length of the flap (20 m as shown in Table 3.1) and a thickness of two grid cells, which is the minimum number of grid cells to obtain consistent results. The thickness from the reference flap was originally 1 m, but due to the limitations of the obstacle cell representation a flap of 4 m thickness is defined here.

Figure 4.2 shows a sketch of the device grid discretisation where the empty grid cells have the absorption coefficient a set to 0 (fully reflective obstacle) and the coloured grid cells have absorption coefficients a set to a value different than 0 (energy absorbing obstacle). Different combinations of absorption coefficients (displayed in Table 4.1) are assigned to the coloured grid cells to assess the wave reflection and transmission as part of a sensitivity analysis to find the optimal configuration. The same configuration and number of empty and coloured grid cells was kept along the analysis in order to properly reproduce the reflection effect of the flap.

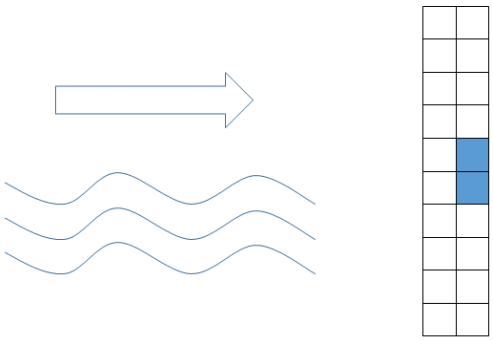

FIGURE 4.2: Flap discretised as obstacle cells.

TABLE 4.1: Absorption coefficients configurations

	Absorption coefficient a
Config. 1	0.2
Config. 2	0.3
Config. 3	0.4
Config. 4	0.5

Figure 4.3 shows the K_d values obtained from MILDwave along section S for the different configurations together with the target K_d values from NEMOH. Based on this assessment, configuration 2 was selected as the configuration most accurately representing the flap disturbance for this sea state, since it is the configuration adjusting the best to the results obtained from NEMOH. The same procedure has to be applied for every sea state since the absorption, reflection, and transmission of the WEC changes depending on the peak period. The K_d values distribution obtained

for configuration 2 are shown in Figure 4.4 for the whole domain showing the 3D disturbance generated by the flap in MILDwave.

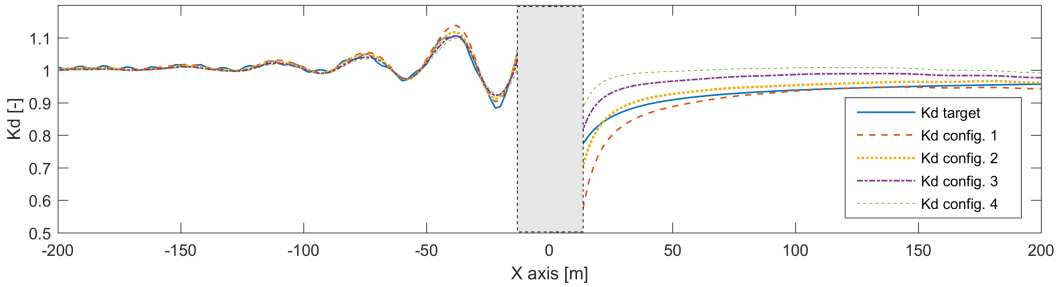

FIGURE 4.3: Tuning of the absorption coefficients attributed to the WEC grid cells.

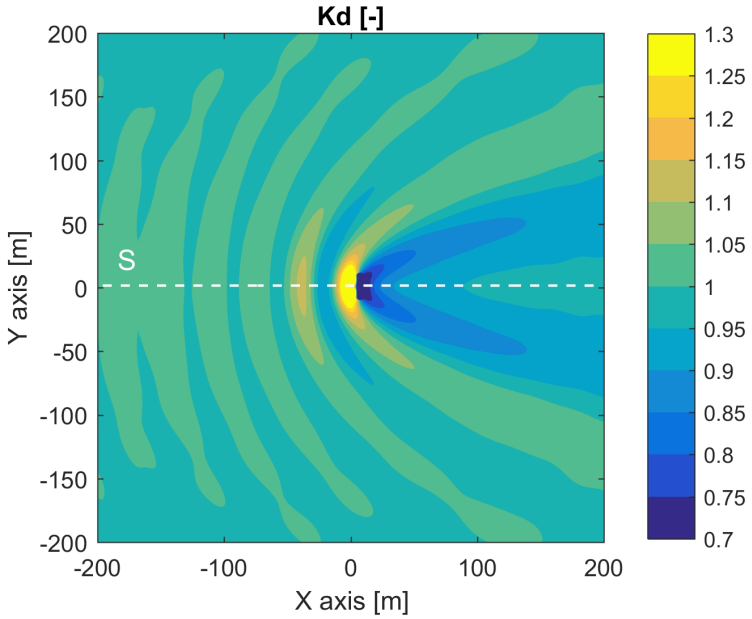

FIGURE 4.4: Disturbance coefficient from MILDwave for 1 flap and $T_p = 8$ s.

4.2.4 Wake effect for a WEC farm

The wake effect for a farm composed of several devices can be assessed by replicating the same representation of obstacle cells (configuration 2) at the location of each flap across the domain. As an illustrative example, Figure 4.5 shows the disturbance coefficient K_d obtained for a farm composed of 9 flaps along a domain of 2000 x 1000 m. The wake effect is affected by the multiple obstacles and therefore the reflection and absorption effect of the obstacles is much larger. The layouts of the WEC farms assessed along the thesis were defined based on a minimum spacing between flaps of $3L$ to run operation and maintenance works and staggered in order to expose the devices to a higher wave energy density.

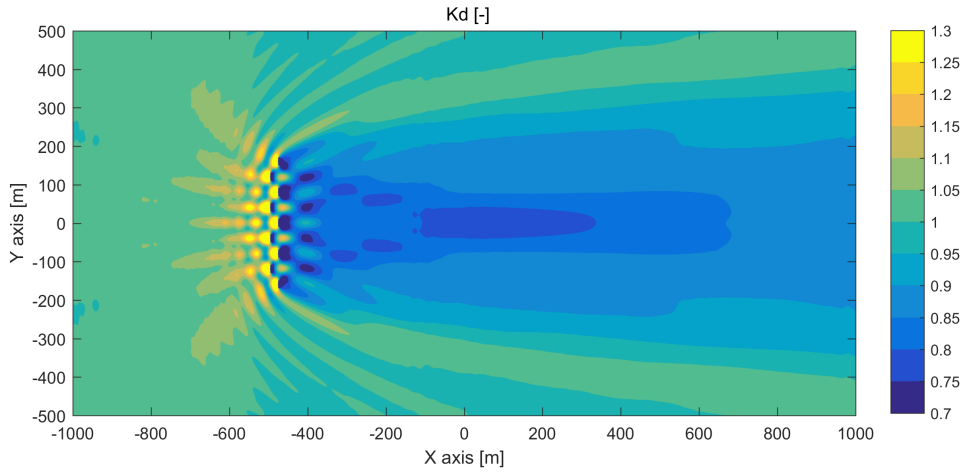

FIGURE 4.5: Disturbance coefficient from MILDwave for 9 flaps and $T_p = 8$ s.

4.2.5 Conclusion

The application of the sponge layer technique based on BEM solver solutions made possible to tune the obstacle cells in the WPM against a wave solution representing the full perturbation of the WEC, the reflected-diffracted wave and the radiated wave. However, the obstacle cell representation itself does not consider the full perturbation since the radiated wave is not intrinsically modelled. The obstacles only reflect, diffract and absorb the waves, and by playing with the absorption coefficient the three phenomena are tuned for the obstacle to have an impact on the wave field similar to the full perturbation from the BEM solver. In addition, the tuning of the absorption coefficients is implemented for an incoming wave propagating towards the x-axis, therefore the interaction effects due to the waves generated by the presence of surrounding WECs are not validated.

The wake effect is assessed by using this methodology in Paper A to different scenarios considering various WEC farm layouts and changing depths.

4.3 Coupling Technique

4.3.1 Overview

The coupling technique aims at overcoming the weaknesses of the sponge layer technique and bring the full representation of the perturbed wave in MILDwave by coupling to NEMOH as an internal boundary condition. This provides the option of representing the full perturbation of the WEC including the radiated wave and potentially considering all the interactions between devices, albeit within the linear wave regime.

Different versions were obtained in the development of the coupling technique based on different set-ups of the internal boundary conditions. A first technique was implemented, as presented in Paper B, to apply the coupling between the two

solvers for regular waves and a single flap based on the previous work of Beels [65] for a point absorber WEC. The results provided accurate solutions but were missing consistency in the parameters defining the internal boundary. Then the parametrisation of the internal boundary was improved in Paper C and extended to an array of several flaps which gave satisfactory results. Finally the methodology was further developed and applied to WEC farms under irregular sea states and irregular bathymetries in Paper D. The different versions of the coupling technique developed in this thesis are described in the following sections.

4.3.2 Methodology description

The coupling technique was developed to represent the perturbed wave in MILDwave by merging the results from NEMOH. Thus, in order to obtain the total wave component in MILDwave for each wave frequency two separate calculations need to be run: one for the incident wave that is intrinsically computed in MILDwave and one for the perturbed wave solution by applying a coupling between the two solvers. A total wave solution is obtained for each wave frequency and then irregular sea states are computed from the superposition of those regular wave solutions, considering the limits of the linear wave theory.

The incident wave is resolved by means of a wave generation line located at the up-wave side of the domain that allows the wave to propagate along the positive x-axis. Then the perturbed wave is considered by means of an internal boundary that generates the wave at the location of the WECs based on the NEMOH solution and propagates the wave in all directions towards the outer domain. Figure 4.6 shows a sketch of the method representing both calculations, the perturbed wave and the incident wave in MILDwave.

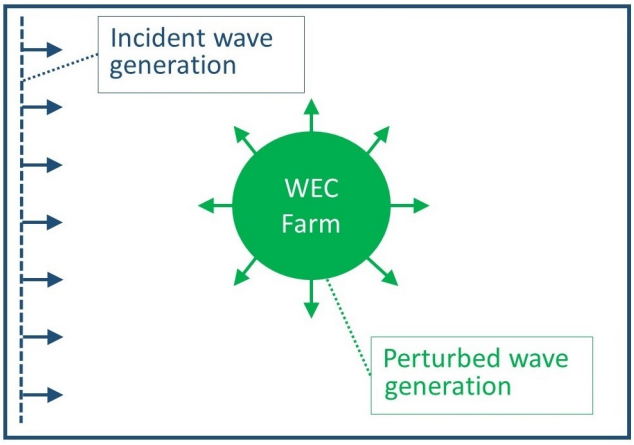

FIGURE 4.6: Methodology description sketch for the coupling technique.

The internal boundary was first implemented by using a circular wave generation line scheme based on the same set-up as the one used for the incident waves

generated at the offshore boundary. Due to some inconsistencies in the discretisation of the circular wave generation line, a second version of the method was developed where the perturbed wave was described by a wave generation surface of adaptable shape. The two ways of applying the coupling technique are described in Sections 4.3.3 and 4.3.4, where constant water depths of 10 m and a regular wave of T = 8 s and A = 1 m are assumed.

4.3.3 Circular wave generation line

A circular wave generation line was used in Paper B to couple the wave solution from NEMOH into MILDwave. This technique relies on the source term addition method implemented commonly in MILDwave to generate waves at the offshore boundaries (Section 3.4.2). To showcase the method the technique is applied in this section only to a radiated wave, even though exactly the same procedure applies to the diffracted or to the perturbed wave (sum of radiated and diffracted wave). Complementary applications of the technique to diffracted and radiated waves were conducted in Paper B (Section B.3.3) where additionally a comparison of the coupling technique with the previous sponge layer technique was additionally implemented (Section B.4 and B.7.2).

Set up of the generation line

The radiated wave was defined in MILDwave by setting up an internal circular wave generation line surrounding the device at a defined distance from its centre and an inner sponge layer covering the inner area inside the circular line, as shown in Figure 4.7. The generation line is defined based on the wave amplitude and phase obtained as a solution from NEMOH at the location of the circular line.

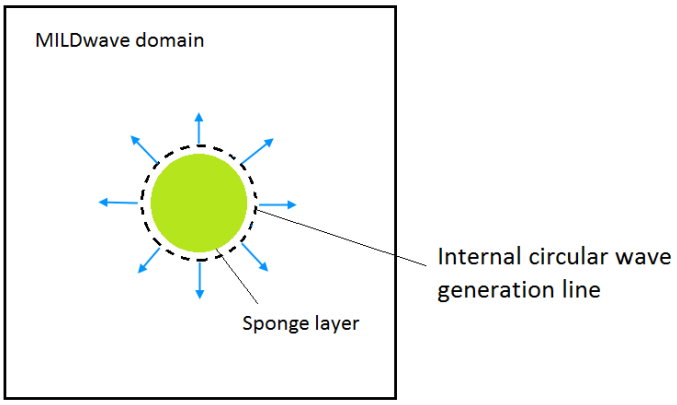

FIGURE 4.7: Definition sketch of the internal boundary condition.

To obtain the expected propagation of the radiated wave through the domain, a tuning of the circular generation line discretisation needs to be implemented as described in [65]. The generation line is defined by a discretisation of grid generation

points i determined by a radius distance r to the centre of the domain (x_c, y_c) and an angle interval Δb as presented in Figure 4.8.

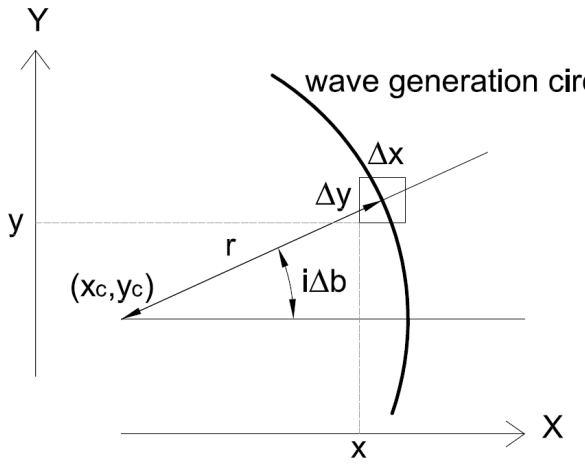

FIGURE 4.8: Definition sketch of the internal wave generation line set-up [65].

An additional surface elevation is imposed at each generation point based on the source term addition method but now applied to a circular wave generation line as described by (4.1) below,

$$\eta^* = 2\eta_N \frac{C_e \Delta t}{\Delta x} \tag{4.1}$$

where $|\tilde{\eta}_N|$ is the surface elevation modulus obtained from NEMOH.

From the generation line the wave is propagated towards both, the outward and inward directions of the circle, in the same way as happens with a generation line located at the offshore boundary to generate an incident wave. However, the sponge layer located inside the circle absorbs the inward directionality of the wave and only the outward directionality propagates towards the far-field. In practice, the sponge layer does not fully absorb the inward component of the wave and therefore part of the inner wave gets reflected and propagated towards the outer direction. This phenomenon means that, depending on the size of the inner sponge layer, the wave reflection also changes and the discretisation of the grid generation points i need to be readjusted for each value of the radius distance r.

Application to radiated wave by a flap

Figure 4.9 shows the radiated wave obtained for a generation line located at a 20 m distance from the centre together with the surface elevation obtained from NEMOH. Half a wave length distance from the WEC is needed to obtain a stable wave field due to the reflection of the inner sponge layer (Section B.7.1). Both the amplitude and phase obtained with the coupling technique match the results from NEMOH, even though slight discrepancies are found with error values below 6% at a distance

of 50 m from the device (Section B.7.2). The white circle in MILDwave represents the near-field where the internal boundary condition was implemented.

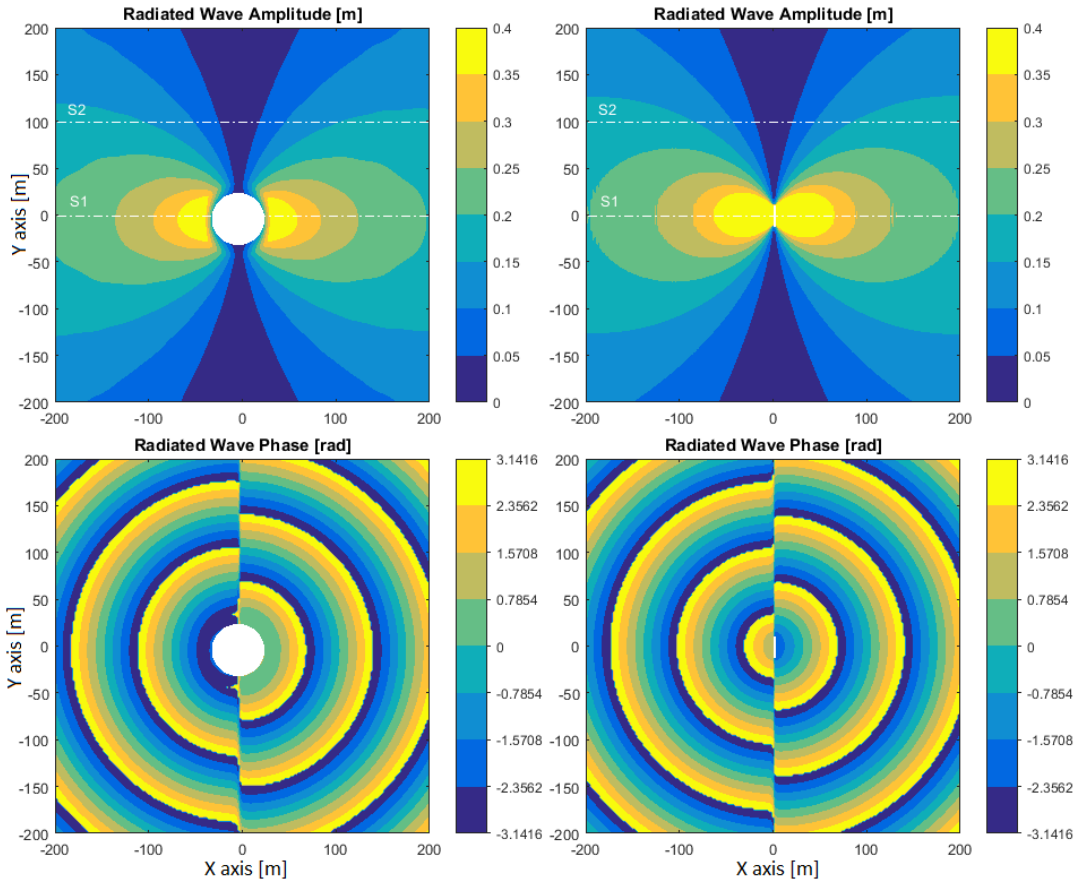

FIGURE 4.9: Radiated wave amplitude and phase for 1 flap obtained in NEMOH (left) and MILDwave with the coupling technique based on the circular wave generation line (right).

4.3.4 Wave generation surface

Due to the small inconsistencies found with the circular wave generation line related to the inner sponge layer reflection, a new method was developed in order to find a consistent way of merging the results from NEMOH into MILDwave. A second version of coupling technique was developed where the internal boundary condition is described in MILDwave by means of a wave generation surface based on the perturbed wave solution from NEMOH. Paper C describes the basics of the technique applied to a single flap and a WEC farm case under regular waves, and then Paper D extended the method to applications where irregular waves and irregular bathymetries were considered.

Set up of the generation surface

The wave generation surface is defined by an area representing the near-field where the perturbed wave solution for the two variables solved by MILDwave (η and Φ) are

imposed at each instant of time based on the results obtained from NEMOH. Each grid cell contained within the wave generation surface is then attributed its corresponding value of free surface elevation and velocity potential. Figure 4.10 shows a sketch representation of this technique. The size and shape of the wave generation surface can be adapted to the geometry of the WEC farm under consideration. A mandatory requirement is that the surface needs to completely surround the WEC farm in order to represent the complete wave energy flux of the perturbed wave.

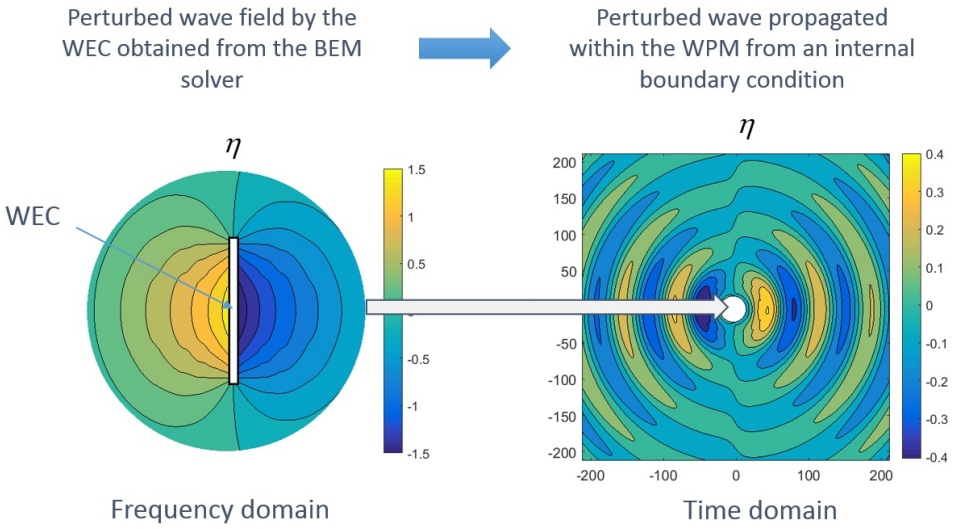

FIGURE 4.10: CT description by means of a wave generation surface.

The perturbed wave solution is obtained from NEMOH in the frequency-domain in terms of wave amplitude A and wave phase φ related to the complex surface elevation by (4.2) and (4.3). These values are then transformed into time-domain variables to be imposed within the wave generation surface area in MILDwave by (4.4) and (4.5). As a consequence of the computational time-staggering in MILDwave between η and Φ , the solution for both variables is imposed with half a time step difference:

$$A(\omega) = |\tilde{\eta}|, \tag{4.2}$$

$$\varphi(\omega) = \arg(\tilde{\eta}), \tag{4.3}$$

$$\eta((n+\frac{1}{2})\Delta t) = A\cos(\varphi - \omega((n+\frac{1}{2})\Delta t)), \tag{4.4}$$

$$\Phi((n+1)\Delta t) = \frac{g}{\omega}A\sin(\varphi - \omega((n+1)\Delta t)). \tag{4.5}$$

Application to perturbed wave for a WEC Farm

The technique was applied to a farm of 5 flaps where the perturbed wave for the whole farm is first obtained from NEMOH and then coupled into MILDwave. In this case the shape of the near-field is rectangular to fit the form of the farm with a 15 m margin between the devices and the border of the wave generation surface, which gives a total size of $60 \times 160\ m$ (x-axis and y-axis respectively). The perturbed wave from NEMOH takes into account all interactions between the 5 flaps and are then input into MILDwave as a wave generation surface of rectangular shape. In this case the perturbed wave from NEMOH was obtained from the superposition of the diffracted wave and the 5 radiated waves corresponding to each device (Section 3.3.2). Figure 4.11 shows the perturbed wave amplitude and phase obtained in NEMOH (left) and MILDwave with the coupling technique (right) for the 5 flaps case.

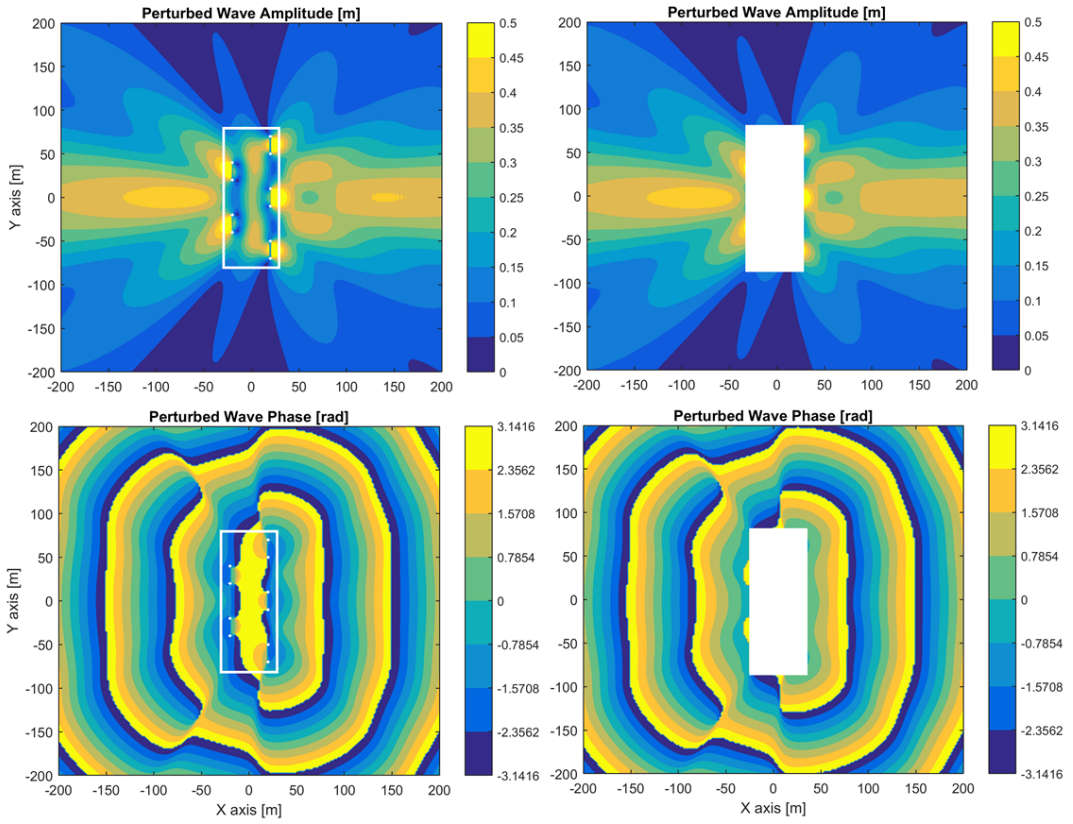

FIGURE 4.11: Perturbed wave amplitude and phase for 5 flaps obtained in NEMOH (left) and MILDwave with the coupling technique based on the wave generation surface (right).

4.3.5 Total wave field

The total wave field is determined by superposing the previous results of the perturbed wave obtained with the coupling technique to the incident wave computed

intrinsically in MILDwave. Figure 4.12 shows the different calculations needed to obtain the total wave amplitude for the case of an 18 flap farm located on a mild-slope bathymetry and is extracted from Section D.9.1 in Paper D. The top plot shows the amplitude for the incident wave, the middle plot shows the perturbed wave obtained with the wave generation surface technique and the bottom plot shows the total wave amplitude from the superposition of both waves. The manner in which the internal boundary for the perturbed wave generation is set up, by forcing the wave solution at each instant of time, allows the plotting of the whole domain including the inner part of the generation surface without any appreciable discontinuity between the near-field and far-field domains.

4.3.6 Irregular waves

Once the regular wave components are computed for the range of desired frequencies in MILDwave the disturbance coefficient K_d representing the irregular sea states disturbance is straightforward to obtain (Section 3.5). Figure 4.13 shows the disturbance coefficient obtained for the case of an incident sea state of T_p = 8 s located on a mild-slope bathymetry. The disturbance coefficient is not dependent on the significant wave height as these calculations remain under the assumption of linear wave theory. The parametrised JONSWAP spectrum was used to represent the wave spectral density distribution of the incident long-crested irregular waves at the offshore boundary, where a peak enhancement factor γ of 3.3 was used. A discretisation of 50 regular waves was considered with wave periods T ranging from 3.5 to 20 s, since the error of the coupling technique increases outside this range (Section D.8.3).

4.3.7 Conclusion

The first version of the coupling technique based on the circular wave generation line gives reasonable performance but the inconsistencies due to the reflection of its inner sponge layer make its application to more complex cases a difficult task, i.e. larger number of WECs or non-circular shapes of the farm. The second version of the coupling technique provides the option of describing the perturbed wave in MILDwave in a consistent way where the same implementation is always applied; imposing the solution at each grid cell composing the wave generation surface based on the solution from NEMOH at the same location. The technique was shown to be consistent for WEC farms of several devices and to be able to adapt its shape to the farm in order to restrict the area where the constant water depth conditions of the BEM solver are assumed.

The coupling technique was applied here only to regular waves in order to demonstrate the accuracy of the method. From the regular waves results it is straightforward to compute irregular sea states considering as many wave components as it is desired.

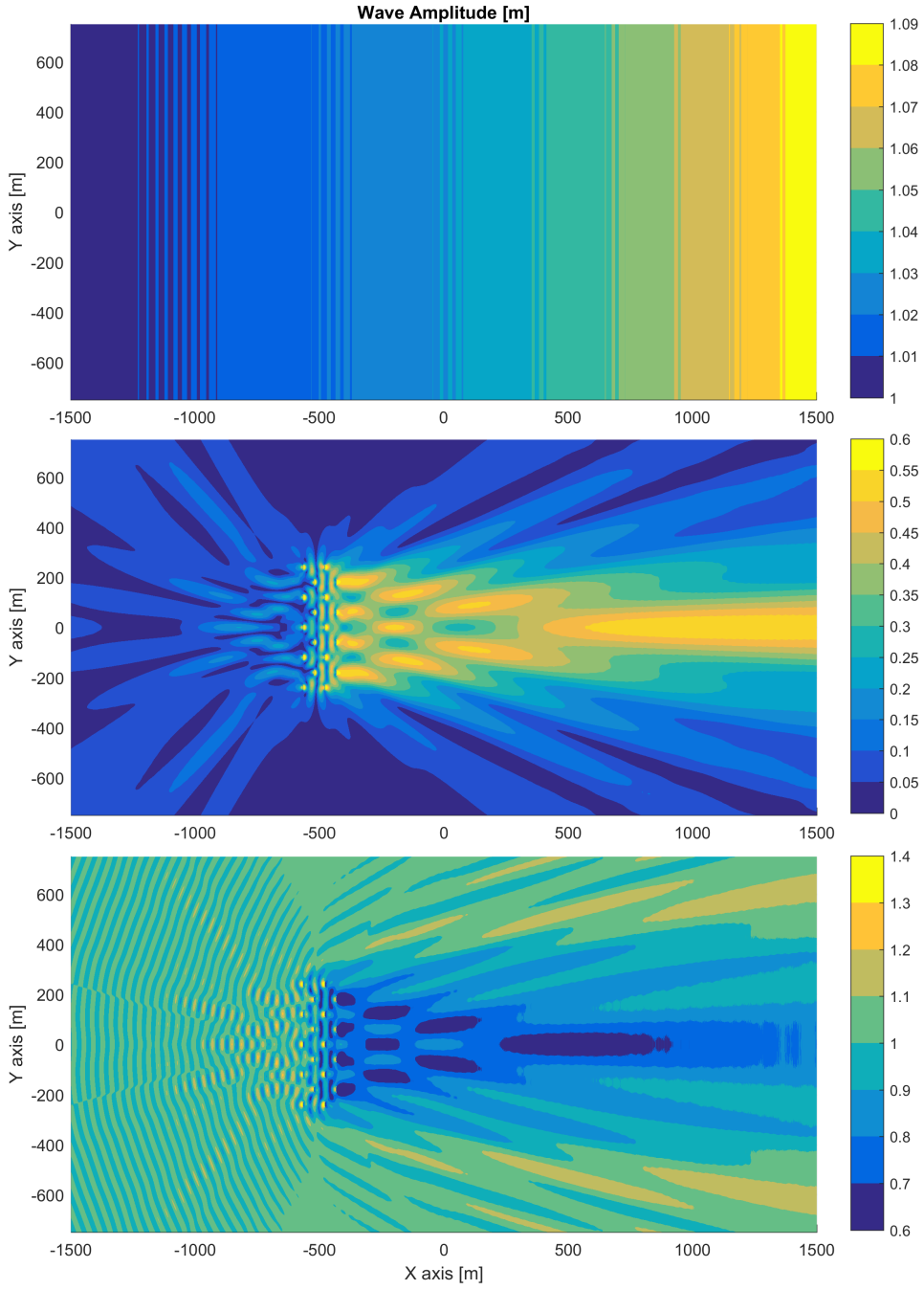

FIGURE 4.12: Amplitude for the incident, perturbed and total wave (top to bottom) obtained from MILDwave results for 5 flaps under an incident wave of $T = 8\ s$.

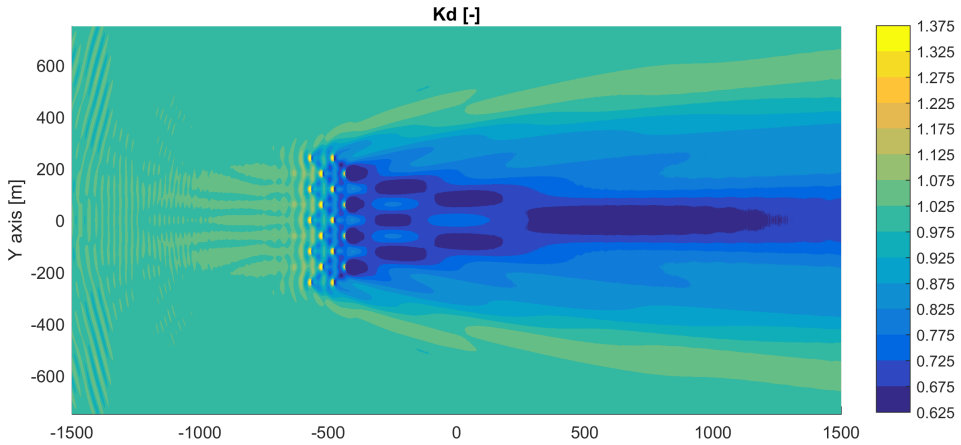

FIGURE 4.13: Disturbance coefficient for a 18 flaps farm on a mild-slope bathymetry for a sea state of $T_p = 8\ s$.

Chapter 5

Results and Conclusion

In this chapter, the main findings of the project are summarised. The accuracy of the methods developed is discussed first together with examples of applications to which they were applied. A synopsis of the work carried out in each publication is then presented, followed by a discussion of the findings, and finally a recommendation of the further work to implement is suggested.

5.1 Errors of Methodologies

Two main methods were applied, the sponge layer technique and the coupling technique, where two stages of development were implemented for the coupling technique based on different set-ups of the internal boundary condition. In all cases the methods aimed at replicating, in MILDwave, the near-field perturbation generated by the WEC in NEMOH. Thus, the error between the perturbation obtained with each technique in MILDwave and the target wave field from NEMOH is described here to validate the representation of the device in MILDwave.

The error is calculated based on (5.1) and (5.2) for the sponge layer technique and coupling technique respectively at each grid cell across the domain. The first method is validated based on disturbance coefficient values for irregular waves, and the second method is validated based on wave amplitude values of regular waves. The sponge layer technique error is non-dimensionalised by the incident significant wave height $H_{s_{inc}}$ and the coupling technique error is non-dimensionalised by the incident regular wave amplitude A_{inc}. Subscripts N and M refer to results obtained from NEMOH and MILDwave respectively,

$$\epsilon_{SLT}(\%) = \frac{K_{dN} - K_{dM}}{H_{s_{inc}}}, \tag{5.1}$$

$$\epsilon_{CT}(\%) = \frac{A_N - A_M}{A_{inc}}. \tag{5.2}$$

Figure 5.1 shows the error obtained throughout the domain for the two methods. Constant water depths of 10 m are assumed in all cases in order to make possible the comparison with NEMOH. The upper plot shows the error for the sponge layer technique where the flap was represented as a group of obstacle cells, and the lower

plots represent the error for the coupling technique using the circular wave generation line set-up (left), and the wave generation surface set-up (right).

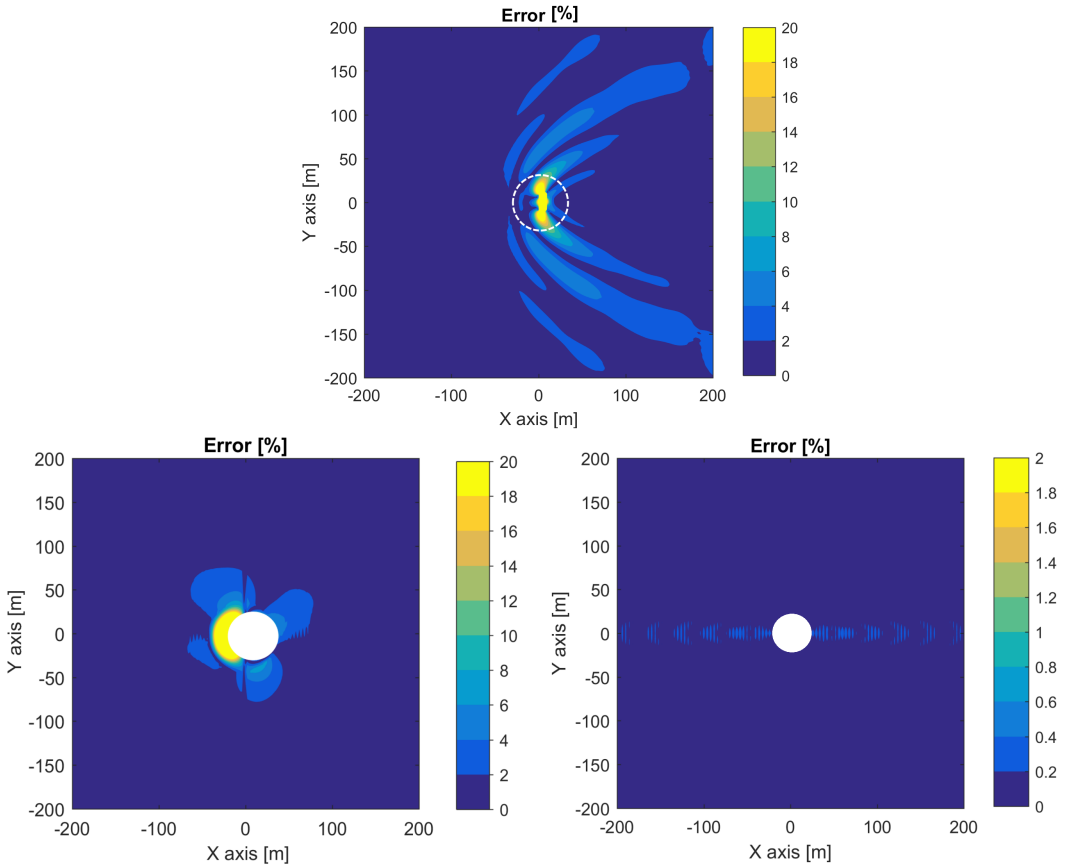

FIGURE 5.1: Error between MILDwave and NEMOH for 1 flap applying the sponge layer technique (top), the coupling technique with circular wave generation line (left), and the coupling technique with wave generation surface (right).

The accuracy of the methods progressively improve, from the sponge layer technique with the highest error in the far-field to the second version of the coupling technique with the lowest errors. If a minimum distance of 30 m from the device is considered the sponge layer technique provides maximum error values up to 10% that remain in the far-field, specifically at the sides. This is due primarily to the radiated wave not being intrinsically represented. However, the results can be seen to match the target values from NEMOH along Section $Y = 0$ (errors below 2%), which represents the results used for the tuning of the obstacles.

The coupling technique using the circular wave generation line set-up gives errors of the same order than the sponge layer technique in the near-field but they disappear rapidly towards the far-field, since the full perturbation is now included, i.e. reflection-diffraction and radiation. Finally the coupling technique using the wave generation surface gives very good agreement and the maximum errors remain below 0.4%. This means that NEMOH predictions are fully coupled in MILDwave without any significant difference when using the coupling technique with a wave

generation surface set-up.

Complementary to this, a comparison was carried out in Paper B assessing the difference between the sponge layer technique and the coupling technique for a regular perturbed wave (Section B.4 and B.7.2). The comparison shows that apart from a difference in wave amplitude at the sides of the WEC and where the sponge layer technique overestimates the perturbed wave, there is an important difference arising from a wave phase shift. The perturbed wave from NEMOH for a flap-type WEC is defined by a phase shift equivalent to approximately half a cycle between the up-wave side and the down-wave side due to the radiated wave. The flap moves first to one side and then to the other side leading to half a cycle difference between the two sides. There is no mechanism to reproduce this effect intrinsically in MILDwave using the sponge layer technique, which strengthens the need to apply the coupling technique to allow for the full representation of the perturbed wave.

5.2 Applications

Both methods can be applied to realistic scenarios including large WEC farms of many devices under irregular waves, and including real bathymetries from specific sites (up to the limit of bed steepness equal to 1/3). The limits of the domain size remain of the order of 1 to 10 km^2 for an average desktop computer (in this case: double core CPU and 8 GB of RAM), but this is expandable by increasing the computational capacities. The methods are limited to low-to-moderate sea states since they are based on linear wave theory. However, the inclusion of dissipation coefficients in the main equations of MILDwave could help to increase these limits allowing for higher sea states to be computed [66].

The sponge layer technique and coupling technique were applied to realistic scenarios in Papers A and D respectively, where irregular waves and changing depths were considered. For the sponge layer technique, the bathymetry was defined by a linear changing depth, and for the coupling technique, a real bathymetry was represented.

The near-shore area located off Annagh Head, west of Belmullet in Ireland where the Atlantic Marine Energy Test Site (AMETS) is located, was considered for the real bathymetry case to which the coupling technique was applied. Figure 5.2 shows the precise location of the domain which is delimited by the rectangle.

Figure 5.3 shows the results obtained for the latter case extracted from Section D.11. A WEC farm composed of 18 flaps deployed in 15 m water, a sea state of $T_P = 8s$, and a real bathymetry were considered as an illustrative example. The top plot shows the bathymetry, the middle plot the disturbance coefficient values, and the bottom plot the K_d difference obtained with a constant water depth chosen to show the importance of considering real bathymetries. The sea-state conditions were defined in such a way that the wave spectral distribution is the same at the

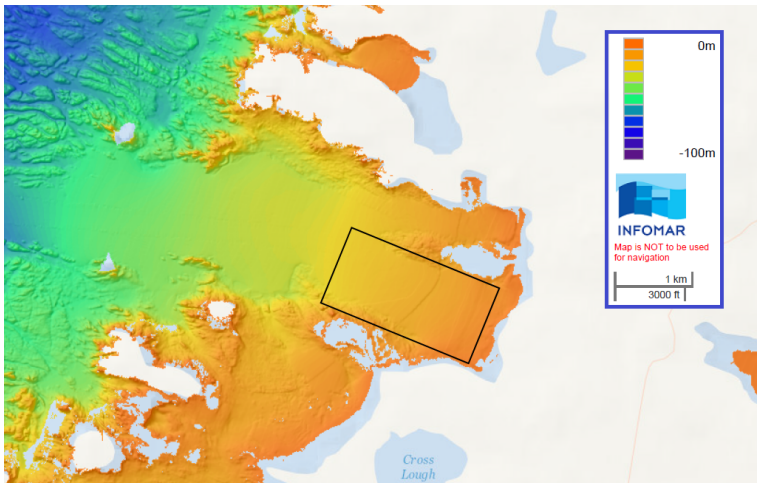

FIGURE 5.2: Map of the area for the considered bathymetry.

location of the farm for both cases: the irregular bathymetry and the constant water depth case.

The flaps were submerged as they were deployed at water depths of 15 m and the flap height is 12 m. As a consequence of their submergence, the disturbance generated on the incoming wave field was lower than for WECs that are surface-piercing, since the reflection and absorption on the waves is lower for submerged flaps. However, considering their disturbance effect is low, the bottom plot shows that the consideration of real bathymetries can make a large difference in the wake effect. The largest differences are about 10%, which would increase significantly if the devices were surface-piercing.

5.3 Summary of Results

The annexes of this thesis present the four main publications completed during this project. For Papers A and B, complementary sections were added after the published versions to complement the published results and clarify their validity. Here the details of the findings obtained in each publication are summarised.

5.3.1 Paper A

The sponge layer technique was described and applied to WEC farm scenarios located on linear changing depths in Paper A. The article describes the implementation of the technique and the tuning of the WEC representation in MILDwave. Once the single flap representation was obtained, the technique was applied to WEC farms of four and nine flaps, assessing their wake effect across a domain of 2000 x 1000 m and where constant water depths were assumed. Sensitivity analyses were conducted where the influence of the peak period and spacing between flaps on the wake effect of the farm was assessed. Finally, a case where the WEC farm is located on top of a mild-slope bathymetry was assessed together with a comparison of the

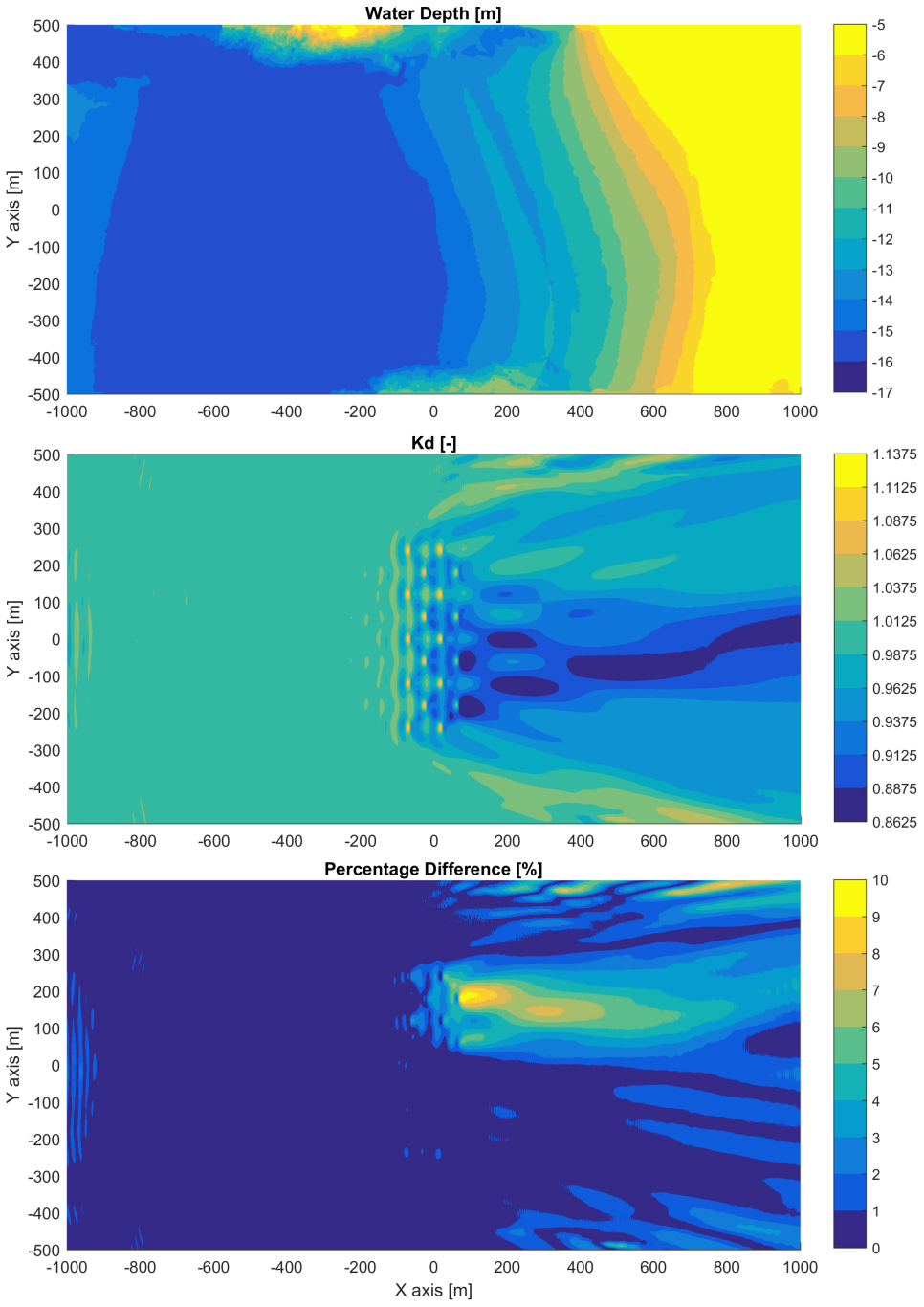

FIGURE 5.3: Real bathymetry case scenario. Top: Water depth. Middle: Disturbance coefficient. Bottom: Percentage difference with constant water depth case.

influence of varying water depths. As an additional content to the published work, a section was added at the end of this paper (Section A.7) where the error from the comparison with NEMOH was assessed for the WEC farm composed of 9 flaps.

The method is relatively simple to apply since it is based on the use of the intrinsic features of the two solvers. The tuning of the obstacle representing the device in the WPM is obtained in an empirical manner by progressively changing the absorption coefficients until the wave field disturbance from the target coincides with that

obtained from the BEM solver. Once an obstacle configuration has been found for a specific sea-state, the representation of the farm is based on a replication of the same obstacles in the domain and only one run is needed to assess its wake effect.

The significant wave height reduction behind the WEC farm tends to not be relevant when applying the sponge layer technique and for the cases considered. The average significant wave height reductions in the lee-side oscillate around 10%, which represents a low value considering the uncertainties involved. However, it is shown in the added section (Section A.7) that the error between the two solvers increases significantly when many devices are considered, since the interactions start playing an important role. This is mainly due to the property that the device is tuned upon an incoming wave propagating along the x-axis and the perturbation caused by each device on the perturbed waves generated by the surrounding devices is not properly represented. Thus, the results from NEMOH show that if all interactions were fully modelled the significant wave height reduction will be higher.

5.3.2 Paper B

The first attempt of applying the coupling technique was conducted in the work presented in Paper B, where the accuracy of the technique was assessed together with a comparison with the sponge layer technique. The intrinsic capability of MILDwave to model the diffraction for a surface-piercing flap was assessed first, showing good agreement except for the up-wave section where flap reflections were overestimated. Then the coupling technique, setting-up the internal boundary as a circular wave generation line, was described. Its accuracy was assessed against NEMOH results and good agreement was found. A comparison between the coupling technique and the sponge layer technique for a regular perturbed wave was assessed, which concluded that the sponge layer technique significantly overestimates the wave amplitude at the sides and does not consider the half-cycle shift for the wave phase between the up-wave and down-wave sides of the flap.

Additional content to the published work was added as a new section at the end of this paper (Section B.7). The added section includes an assessment of the optimal discretisation angle for the set-up of the internal boundary, where the optimal angle discretisation for different sizes of the internal boundary was assessed. It was found that the optimal angle progressively decreases with the radius of the boundary and which is expected, since the larger the circle, the more wave generation points are needed. However, due to the reflection generated by the inner sponge layer, the relation between the optimal angle and the grid cell size was not proportional, leading to gaps in the generation line set-up and thus making the line discontinuous and the set-up not consistent.

Finally, the added section includes error plots from the comparison with NEMOH that were presented in the published sections. These error plots give a better assessment of the accuracy of this first coupling technique version, together with the intrinsic capability of MILDwave to model the diffraction for a flap and to model the

full flap perturbation with the sponge layer technique.

5.3.3 Paper C

The second version of the coupling technique was applied in Paper C, where it was validated against NEMOH predictions for a WEC farm test case and applied to a mild-slope bathymetry for regular waves. The set-up of the internal boundary condition, as a wave generation surface, was described first and then the method was validated both for a single flap and a WEC farm. The comparisons with NEMOH gave satisfactory results since the relative error was remarkably low, i.e. below 0.5%. The method was then applied to a WEC farm located on mild-slope bathymetry, assessing the wake effect for a WEC farm under regular waves.

The work was a preliminary application of the new version of the coupling technique, where the accuracy of the technique was the principal purpose of the publication. It was shown that the method was applicable both to single flaps and to farms of several flaps and that the wave generation surface describing the near-field solution from NEMOH was adaptable in shape. The wave generation surface may be circular or rectangular since it surrounds the WEC farm completely to provide the complete energy flux for the perturbed wave. This allows tightening the near-field to the shape of the farm and therefore reduces the area where the constant water depth assumptions of the BEM solver need to be considered.

5.3.4 Paper D

The same coupling technique as used in Paper C was applied in Paper D but now providing a full description of the method and an application to realistic conditions, where a large WEC farm composed of 18 flaps, irregular waves, and a real bathymetry were considered. The background theory together with the governing equations of the two solvers are detailed first. Then a description of the set-up of the internal boundary as a wave generation surface is described together with the mathematical relations between the main variables obtained from each solver that enables merging of the results. The method was validated again for a single flap and a WEC farm, but convergence analyses of the main numerical parameters involved in the methodology were now assessed to give the optimal range of values to use. Convergence analyses for the time step, grid cell size, wave length and wave generation surface size were conducted and the optimum values provided with a reduction of the error, reaching error values that remained below 0.36%.

The method was then applied to irregular waves by superimposing regular wave predictions for a range of 50 frequencies. The wake effect for a farm composed of 18 flaps and located on a mild-slope bathymetry was assessed for different peak periods and different WEC farm layouts, where the separating distance was also changed. It was found that the higher decrease in the significant wave height occurred for a peak period of $T_p = 8\ s$ with approximate average values of 20% and

maxima of 45%. The significant wave height reduction then progressively diminished to where averages values of 15% and maxima of 30% were found for $T_p = 10\ s$ and average values of 15% and maxima of 25% for $T_p = 12\ s$. However the average reductions values remained constant with the distance towards the far-field in the lee-side and endured across a large area behind the farm. An examination of the separating distance influence was found to be proportional to the significant wave height reduction, as might be expected, where a larger distance leads to a lower decrease. In all cases the wake effect was found to be significant and provided a large reduction area in the lee of the farm.

Finally, the method was applied to a real bathymetry from the near-shore and located close to the Atlantic Marine Energy Test Site (AMETS), demonstrating that the method can be applied to real scenarios. In this case the flap farm was deployed in 15 m water depth, where the devices were submerged and therefore a reduced disturbance on the incoming waves was found, compared to a surface-piercing flaps farm. However, a comparison with constant water depths was included and demonstrated the importance of representing real bathymetries in this type of assessment. The difference was found to be around 10%, which is a significant value, especially considering that with a surface-piercing flap farm, the difference will be higher.

5.4 Discussion

After assessing the method's accuracy (Section 5.1) it is clear that the coupling technique presents a more precise representation of the perturbation generated by the WECs. However, in some cases where the WECs are sufficiently distant enough from each other to reduce their hydrodynamic interactions significantly, the obstacle cell representation can provide a first preliminary assessment and simplify the wake effect calculation for users not familiar with the coupling technique. The complicated aspect of the sponge layer technique remains and this is to find the optimal configuration of the obstacle cells representing the WEC, since once this is completed only one calculation is needed per peak period where irregular waves are generated in the time-domain. The coupling technique needs one calculation per regular wave component, whereas if directional spreading or reflection of waves from the coast are considered the superposition of all components would lead to a larger increase of the number of calculations. Nevertheless, these calculations are achievable in terms of computational requirements given code that automates the process running both solvers: the BEM solver and the WPM for the whole range of components.

The sponge layer technique provides a representation of the flap as obstacle cells that are tuned with NEMOH solutions and where a 3D wave field solution of the wave-body interaction problem is obtained. Tuning the obstacles such that they fully represent the 3D wave pattern from NEMOH remains a difficult task. The tuning is subsequently conducted based on a 2D section of the 3D wave pattern. A later comparison of the results with the target 3D wave pattern from NEMOH allows for

an assessment of the numerical accuracy and therefore to quantify the discrepancies. The error for the 9-flap farm shows that, when interactions with other devices are present, the sponge layer technique presents limitations due to the poor representation of the hydrodynamic interactions, even if the flap was accurately tuned previously as a single device. A solution to this would be to model the whole farm as one single group of obstacle cells and tune it against NEMOH solutions, where the whole farm was modelled considering all interactions. However this method would be valid only for preliminary assessments.

The first version of the coupling technique aimed at achieving the coupling by replicating the technique used in MILDwave to generate an offshore boundary and adapting it to an internal boundary. Errors in the near-field around the device were found and a lack of consistency in the wave generation set-up was encountered. The inner sponge layer reflection was a major factor that did not give a stable wave generation. In addition, the fact of adapting the source term addition method used to generate travelling waves (propagating in one direction) to circular waves (propagating in all directions) made it difficult to consistently describe the generation line as a circle.

A very good agreement was found for the second version of the coupling technique based on the wave generation surface, either for a single flap or a WEC farm. The applications showed the flexibility of the methodology to adapt the area describing the internal boundary to the shape of the WEC farm. Whether described by a circular or a rectangular shape, the internal boundary described as a wave generation surface provides an accurate computation of the perturbed wave in MILDwave. Thus, the version of the coupling technique developed in Paper D is a powerful method and applicable to many types of WEC farms, where the most important environmental phenomena affecting the wave climate in the short term are considered.

It is suggested that the method demonstrated in Paper D may be employed for Environmental Impact Assessments (EIAs). EIAs will be needed as part of the consenting process for the future commissioning of WEC farms composed of a large number of devices and the impact on the wave climate will be an important component of the assessment. Thus, numerical tools providing accurate WEC farm representations in an acceptable computational time will be needed, especially if large domain areas are considered. In addition, these tools can assess the magnitude of the sheltering from a WEC farm on the surrounding marine space, and evaluate if activities such as aquaculture, offshore wind farms, or coastal protection could benefit from its shield effect.

This method remains applicable to low-to-moderate sea states but improvements can be implemented to include linear dissipative terms that will provide a higher accuracy for higher sea states, such as extreme wave conditions. Another possible option is to develop methods where non-linear wave-structure interaction solvers and non-linear phase-resolved WPMs are used, but this will extensively increase the computational time and therefore limit the applications to small domains.

5.5 Conclusion

The development of innovative methodologies was made based on existing methods by merging their features and bringing them together in a manner that fully accounts for the phenomena involved. A wave-structure interaction solver based on a Boundary Element Method (BEM) was used to obtain the solution of the near-field wave pattern surrounding the WEC farm and a Wave Propagation Model (WPM) was employed to asses the far-field propagation of the waves and their transformation towards the outer domain. Both models are based on the linear wave theory and therefore the similarity on the governing equations allows for an easy interchange and comparison of solutions. Two main methodologies were developed. In the first one, the WECs were intrinsically represented as obstacle cells within the WPM and tuned against a target near-field solution obtained from the wave-structure BEM solver. In the second method the near-field solution of the wave-structure BEM solver was described within the WPM at its corresponding location as an internal boundary condition. Wave transformation processes were then assessed in the WPM, based on these two ways of representing WECs and making it possible to quantify wake effects for a WEC farm and its impact on the surrounding wave field.

Together with the objectives defined in Section 1.2, the following achievements have been attained during this project, contributing to the development of the numerical modelling techniques to assess WEC farms wake effects:

- Two numerical methods have been developed to represent WECs in WPMs for realistic environmental conditions. The sponge layer technique is the more straightforward method to apply but presents a lower accuracy when considering many devices; the coupling technique is a more complex method to implement but it proved to be very accurate for all conditions.

- The full perturbation generated by the WECs in the incoming wave field, i.e. the diffraction and radiation phenomena, is fully represented. The coupling technique is shown to be the more accurate technique, since the near-field solution is directly obtained from the BEM solver where both phenomena are fully considered.

- The wave transformation induced by the water depth changes along the domain is modelled in all cases by means of the mild-slope equations and which are the governing equations of MILDwave, the WPM used in this thesis.

- Irregular sea states are computable with both methods based on an incoming wave spectra defined at the offshore boundary. For the sponge layer technique, the irregular waves are directly generated in the time-domain at the offshore boundary while in the case of the coupling technique the irregular waves are computed by superimposition of many regular waves components results. However, the linear wave theory assumptions limit the application of

these methods to low-to-moderate sea states, depending on the non-linearities that are present.

– The method is applicable to changing depths, including real bathymetries, provided the seabed steepness remains below 1/3.

– The computational demand for both methods remains acceptable with an average desktop computer. For the present work, double core CPU and 8 GB of RAM were employed. About an hour is needed with the sponge layer technique and 12 hours with the coupling technique, considering the most complex case presented in this thesis, and with more than 9 WECs and a minimum domain size of 2000 x 1000 m.

– A farm with multiple WECs can be modelled including all hydrodynamic interactions between devices. The sponge layer technique possesses limitations to include WEC farms of many devices when these are relatively close to each other, while the coupling technique is able to deal with as many devices as needed and fully accounts for all hydrodynamic interactions.

5.6 Further Recommended Work

In this last section some suggestions of future work are made to keep continue the improvement of the accuracy of the methods and the wake effect assessment for WEC farms.

The coupling technique was applied by means of in-house scripts combined with intermediate manual steps and access to the source code, meaning that it was not an automated process with one group of in-put files and one group of output files. Thus, the building of a full numerical tool allowing to run the coupling technique as an automated process would be probably the next important task to be implemented. Ideally a full code might be programmed that solves the complete process starting with the wave-structure interaction (with the BEM solver), then the regular waves transformations (with the WPM), and finally the superposition of all regular waves components. Such a tool would provide the user with a simple implementation of the method and make it more accessible to non-expert users.

Another recommendation would be to compare the 3D wave results, obtained from the BEM solver, with CFD solvers in order to assess the importance of neglecting viscous effects. For the case of a flap, vortex shedding will occur at the edges and especially for the reflected-diffracted wave. The appearance of vortex shedding might be less important for the radiated wave since small motion amplitudes were assumed, which decreases the relative flow velocity to the body. For those simulations where significant differences were found, an option might be to apply reduction coefficients to the wave solutions obtained from the BEM solver and improve their accuracy.

The coupling technique was applied assuming incident sea states without directional spreading and based on the near-shore locations of the case studies. However, the same method can be applied to irregular sea-states where waves arrive at the farm with a heading angle and therefore having a wave spectra representation with directional spreading. The only requirement will be to run more regular wave components and therefore a higher computational demand will be needed in time. Once all wave components have been computed, the superposition can be completed in the same way as for the irregular sea states shown in this thesis.

It was mentioned that the application of the methodologies is limited to low-to-moderate sea states and that applying coupling techniques to non-linear solvers might allow for higher sea states to be assessed. This is a difficult task since the computational time will increase with the complexity of the solver, but intermediate solutions might be found. Methods based on a coupling technique between Smoothed-Particle Hydrodynamics (SPH) solvers for the wave-structure interaction part and non-linear phase-resolved WPMs for the wave transformation processes are being developed and could provide a tool to be applied in specific cases where high non-linearities take place and small domains are considered.

Finally, a full validation of these numerical predictions should be made against real data which is difficult to obtain. Wave tank experiments involve significant difficulties coming from reflection issues, and obtaining wave field results from these remains in general less accurate than results from numerical models. Wave measures from the real environment would be the best option to validate numerical models, even though this implies having large scale devices deployed in the sea and a lot of field work which is economically expensive. Therefore, if wave field data for a WEC model deployed in the real environment would be accessible, it would be beneficial to use it for a full validation of these numerical methods.

Bibliography

[1] Intergovernmental Panel on Climate Change, *Climate change 2014: mitigation of climate change*. Cambridge University Press, 2015.

[2] *OceaNET ITN*. [Online]. Available: http://www.oceanet-itn.eu/ (visited on 01/01/2014).

[3] A. F.D. O. Falcão, "Wave energy utilization: A review of the technologies", *Renewable and Sustainable Energy Reviews*, vol. 14, no. 3, pp. 899–918, 2010, ISSN: 13640321. DOI: 10.1016/j.rser.2009.11.003.

[4] D Ross, "Power from sea waves", *Oxford University Press*, 1995.

[5] S. H. Salter, "Wave power", *Nature*, vol. 249, no. 5459, pp. 720–724, 1974.

[6] Scottish Government, *Wave Energy Scotland*. [Online]. Available: http://www.waveenergyscotland.co.uk/ (visited on 01/01/2017).

[7] European Union, *MaRINET2*. [Online]. Available: http://www.marinet2.eu/ (visited on 01/01/2017).

[8] OCEANTEC Energías Marinas S.L., *Oceantec*. [Online]. Available: http://www.oceantecenergy.com/ (visited on 01/01/2017).

[9] Seabased AB, *Sebased*. [Online]. Available: http://www.seabased.com/en/ (visited on 01/01/2017).

[10] Carnegie Clean Energy, *Carnegie*. [Online]. Available: https://www.carnegiece.com/ (visited on 01/01/2017).

[11] J. Falnes, "A review of wave-energy extraction", *Marine Structures*, vol. 20, no. 4, pp. 185–201, 2007, ISSN: 09518339. DOI: 10.1016/j.marstruc.2007.09.001.

[12] *Ocean Energy*. [Online]. Available: http://www.oceanenergy.ie/ (visited on 01/01/2017).

[13] *AW Energy*. [Online]. Available: http://aw-energy.com/ (visited on 01/01/2017).

[14] *Pelamis Wave Power*. [Online]. Available: https://www.pelamiswave.com/ (visited on 01/01/2017).

[15] *Wave Dragon*. [Online]. Available: http://www.wavedragon.net/ (visited on 01/01/2017).

[16] M. Folley, A. Babarit, B. Child, D. Forehand, L. O'Boyle, K. Silverthorne, J. Spinneken, V. Stratigaki, and P. Troch, "A Review of Numerical Modelling of Wave Energy Converter Arrays", in *ASME 2012 31st International Conference on Ocean, Offshore and Arctic Engineering*, Rio de Janeiro, Brazil, 2012, pp. 535–545. DOI: 10.1115/OMAE2012-83807.

[17] M. Folley, *Numerical Modelling of Wave Energy Converters: State-of-the-Art Techniques for Single Devices and Arrays*, Matt Folley, Ed. Academic Press, 2016, p. 306, ISBN: 9780128032114.

[18] C.-H. Lee, *WAMIT theory manual*, 1995. [Online]. Available: http://www.wamit.com/.

[19] I. ANSYS, *ANSYS® Academic Research, Release 16.2*, 2013. [Online]. Available: http://www.ansys.com.

[20] A. Babarit and G. Delhommeau, "Theoretical and numerical aspects of the open source BEM solver NEMOH", in *11th European Wave and Tidal Energy Conference*, Nantes, France, 2015.

[21] B. Borgarino, A. Babarit, and P. Ferrant, "Impact of the separating distance between interacting wave energy converters on the overall energy extraction of an array", in *9th European Wave and Tidal Energy Conference*, Southampton, UK, 2011.

[22] G. Delhommeau, "Seakeeping codes aquadyn and aquaplus", *19th WEGEMT School Numerical Simulation of Hydrodynamics: Ships and Offshore Structures*, 1993.

[23] M. Durand, A. Babarit, B. Pettinotti, O. Quillard, J. L. Toularastel, and A. H. Clément, "Experimental validation of the performances of the SEAREV Wave Energy Converter with real time latching control", in *7th European Wave and tidal Energy conference*, Porto, Portugal, 2007.

[24] O. Thilleul, V. Baudry, P. M. Guilcher, E. Jacquin, A. Babarit, P. Locuratolo, and A. Larivain, "Assessment of Sizing Parameters of a Wave Energy Converters through the Complementary Use of a Linear Potential Code, a Rans and a Sph Solver", in *9th European Wave and Tidal Energy Conference*, Southampton, UK, 2011.

[25] H. Kagemoto and D. K. P. Yue, "Interactions among multiple three-dimensional bodies in water waves: an exact algebraic method", *Journal of Fluid Mechanics*, vol. 166, p. 189, 1986. DOI: 10.1017/S0022112086000101.

[26] J. C. Mcnatt, V. Venugopal, and D. Forehand, "A novel method for deriving the diffraction transfer matrix and its application to multi-body interactions in water waves", *Ocean Engineering*, vol. 94, pp. 173–185, 2014. DOI: 10.1016/j.oceaneng.2014.11.029.

[27] A. Fàbregas Flavià, Francesc Babarit and A. H. Clément, "On the numerical modeling and optimization of a bottom-referenced heave-buoy array of wave energy converters", *International Journal of Marine Energy*, vol. 19, pp. 1–15, 2017.

[28] M. Folley and T. Whittaker, "The effect of sub-optimal control and the spectral wave climate on the performance of wave energy converter arrays", *Applied Ocean Research*, vol. 31, no. 4, pp. 260–266, 2009. DOI: 10.1016/j.apor.2009.10.006.

[29] B. Borgarino, A. Babarit, and P. Ferrant, "Impact of wave interactions effects on energy absorption in large arrays of wave energy converters", *Ocean Engineering*, vol. 41, pp. 79–88, 2012. DOI: 10.1016/j.oceaneng.2011.12.025.

[30] P. Ricci, J.-B. Saulnier, and A. F.D. O. Falcão, "Point-absorber arrays : a configuration study off the Portuguese West-Coast", in *7th European Wave and tidal Energy conference*, Porto, Portugal, 2007.

[31] G. De Backer, M. Vantorre, C. Beels, J. De Rouck, and P. Frigaard, "Power absorption by closely spaced point absorbers in constrained conditions", *IET Renewable Power Generation*, vol. 4, no. 6, p. 579, 2010. DOI: 10.1049/iet-rpg.2009.0188.

[32] A. Babarit, "On the park effect in arrays of oscillating wave energy converters", *Renewable Energy*, vol. 58, pp. 68–78, 2013. DOI: 10.1016/j.renene.2013.03.008.

[33] C. Eckart, "The propagation of gravity waves from deep to shallow water", in *NBS Semicentennial Symposium on Gravity Waves*, Department of Commerce, USA, 1952, p. 165.

[34] J. C. W. Berkhoff, "Mathematical models for simple harmonic linear water waves: Wave diffraction and refraction", PhD thesis, 1976.

[35] I. Warren and H. Bach, "MIKE 21: a modelling system for estuaries, coastal waters and seas", *Environmental Software*, vol. 7, no. 4, pp. 229–240, 1992, ISSN: 02669838. DOI: 10.1016/0266-9838(92)90006-P.

[36] P. Troch, "MILDwave: A numerical model for propagation and transformation of linear water waves", Department of civil engineering, Ghent University, Ghent, Tech. Rep., 1998.

[37] J.-C. Galland, N. Goutal, and J.-M. Hervouet, "TELEMAC: A new numerical model for solving shallow water equations", *Advances in Water Resources*, vol. 14, no. 3, pp. 138–148, 1991. DOI: 10.1016/0309-1708(91)90006-A.

[38] L. Mendes, A. Palha, C. J. Fortes, A. Brito-Melo, and A Sarmento, "Analysis of the Impact of a Pilot Zone for Wave Energy Conversion Offshore Portugal", in *18th International Offshore and Polar Engineering Conference*, vol. 8, Vancouver, BC, Canada, 2008, pp. 401–408, ISBN: 9781880653708.

[39] C. Beels, P. Troch, G. De Backer, M. Vantorre, and J. De Rouck, "Numerical implementation and sensitivity analysis of a wave energy converter in a time-dependent mild-slope equation model", *Coastal Engineering*, vol. 57, no. 5, pp. 471–492, 2010. DOI: 10.1016/j.coastaleng.2009.11.003.

[40] C. Beels, P. Troch, K. De Visch, J. P. Kofoed, and G. De Backer, "Application of the time-dependent mild-slope equations for the simulation of wake effects in the lee of a farm of Wave Dragon wave energy converters", *Renewable Energy*, vol. 35, no. 8, pp. 1644–1661, 2010. DOI: 10.1016/j.renene.2009.12.001.

[41] A. Radder and M. Dingemans, "Canonical equations gravity waves, weakly nonlinear gravity waves", *Wave Motion*, vol. 7, pp. 473–485, 1985.

[42] P. Troch, C. Beels, J. De Rouck, and G. De Backer, "Wake effects behind a farm of wave energy converters for irregular long-crested and short-crested waves", *Coastal Engineering Proceedings*, vol. 1, no. 32, pp. 1–15, 2011, ISSN: 2156-1028. DOI: 10.9753/icce.v32.waves.53.

[43] J. Boussinesq, "Théorie des ondes et des remous qui se propagent le long d'un canal rectangulaire horizontal, en communiquant au liquide contenu dans ce canal des vitesses sensiblement pareilles de la surface au fond.", *Journal de Mathématiques Pures et Appliquées*, pp. 55–108, 1872. [Online]. Available: http://eudml.org/doc/234248.

[44] V. Venugopal and G. H. Smith, "Wave climate investigation for an array of wave power devices", in *7th European Wave and Tidal Energy Conference*, Porto, Portugal, 2007, pp. 1–10.

[45] N. Booij, R. C. Ris, and L. H. Holthuijsen, "A third-generation wave model for coastal regions: 1. Model description and validation", *Journal of Geophysical Research: Oceans*, vol. 104, no. C4, pp. 7649–7666, 1999. DOI: 10.1029/98JC02622.

[46] H. L. Tolman, *User manual and system documentation of WAVEWATCH III. + Appendices.* 2016.

[47] L. H. Holthuijsen, A. Herman, and N. Booij, "Phase-decoupled refraction-diffraction for spectral wave models", *Coastal Engineering*, vol. 49, no. 4, pp. 291–305, 2003. DOI: 10.1016/S0378-3839(03)00065-6.

[48] S. Ilic, A. J. van der Westhuysen, J. A. Roelvink, and A. J. Chadwick, "Multidirectional wave transformation around detached breakwaters", *Coastal Engineering*, vol. 54, no. 10, pp. 775–789, 2007. DOI: 10.1016/j.coastaleng.2007.05.002.

[49] D. L. Millar, H. C. M. Smith, and D. E. Reeve, "Modelling analysis of the sensitivity of shoreline change to a wave farm", *Ocean Engineering*, vol. 34, no. 5-6, pp. 884–901, 2007. DOI: 10.1016/j.oceaneng.2005.12.014.

[50] A. J. Posner, K. O' Sullivan, and J. Murphy, "Economic and Environmental Impact Appraisal of Commercial Scale Offshore Renewable Energy Installations on the west coast of Ireland", *Journal of Coastal Research*, vol. 29, no. 65, pp. 1639–1644, 2013. DOI: 10.2112/SI65-277.1.

[51] H. C. M. Smith, C. Pearce, and D. L. Millar, "Further analysis of change in nearshore wave climate due to an offshore wave farm: An enhanced case study for the Wave Hub site", *Renewable Energy*, vol. 40, no. 1, pp. 51–64, 2012. DOI: 10.1016/j.renene.2011.09.003.

[52] A. Alexandre, T. Stallard, and P. K. Stansby, "Transformation of Wave Spectra across a Line of Wave Devices", 8th European Wave and Tidal Energy Conference, Uppsala, Sweden, 2009, pp. 1–9.

[53] A. Porter, K. Ruehl, and C. Chartrand, "Further development of SNL-SWAN, a validated wave energy converter array modeling tool", in *2nd Marine Energy Technology Symposium*, Seattle, WA, 2014, pp. 1–9.

[54] R. Carballo and G. Iglesias, "Wave farm impact based on realistic wave-WEC interaction", *Energy*, vol. 51, pp. 216–229, 2013, ISSN: 03605442. DOI: 10.1016/j.energy.2012.12.040.

[55] M. Veigas, V. Ramos, and G. Iglesias, "A wave farm for an island: Detailed effects on the nearshore wave climate", *Energy*, vol. 69, pp. 801–812, 2014, ISSN: 03605442. DOI: 10.1016/j.energy.2014.03.076.

[56] J. Abanades, D. Greaves, and G. Iglesias, "Coastal defence through wave farms", *Coastal Engineering*, vol. 91, pp. 299–307, 2014, ISSN: 03783839. DOI: 10.1016/j.coastaleng.2014.06.009.

[57] ——, "Coastal defence using wave farms: The role of farm-to-coast distance", *Renewable Energy*, vol. 75, pp. 572–582, 2015, ISSN: 18790682. DOI: 10.1016/j.renene.2014.10.048.

[58] ——, "Wave farm impact on beach modal state", *Marine Geology*, vol. 361, pp. 126–135, 2015, ISSN: 00253227. DOI: 10.1016/j.margeo.2015.01.008.

[59] J. C. Mcnatt, A. Porter, K. Ruehl, and J. Roberts, "Verification of the SNL-SWAN Spectral WEC-wave Model with Phase-resolved Linear Wave Fields", in *12th European Wave and Tidal Energy Conference*, Cork, Ireland, 2017, pp. 1–10.

[60] K. Silverthorne and M. Folley, "A new numerical representation of wave energy converters in a spectral wave model", in *9th European Wave and Tidal Energy Conference (EWTEC)*, Southampton, UK, 2011.

[61] M. Folley and T. Whittaker, "Spectral modelling of wave energy converters", *Coastal Engineering*, vol. 57, no. 10, pp. 892–897, 2010. DOI: 10.1016/j.coastaleng.2010.05.007.

[62] P. L. Weywada, B. Child, and J. Cruz, "Implementation of a spectral wave model for wave energy converter arrays", in *4th International Conference on Ocean Energy*, Dublin, Ireland, 2012, pp. 17–19.

[63] C. E. Greenwood, D. Christie, and V. Venugopal, "The Simulation of Nearshore Wave Energy Converters and their Associated Impacts around the Outer Hebrides", in *10th European Wave and Tidal Energy Conference*, Aalbord, Denmark, 2013.

[64] E. B. Agamloh, A. K. Wallace, and A. von Jouanne, "Application of fluid–structure interaction simulation of an ocean wave energy extraction device", *Renewable Energy*, vol. 33, no. 4, pp. 748–757, 2008. DOI: 10.1016/j.renene.2007.04.010.

[65] C. Beels, "Optimization of the Lay-Out of a Farm of Wave Energy Converters in the North Sea. Analysis of Wave Power Resources, Wake Effects, Production and Cost", PhD thesis, Ghent University, 2009. [Online]. Available: https://biblio.ugent.be/publication/978565/file/4335143.pdf.

[66] V. Stratigaki, "Experimental study and numerical modelling of intra-array interactions and extra-array effects of wave energy converter arrays", PhD thesis, Ghent University, 2014. [Online]. Available: https://biblio.ugent.be/publication/5664337/file/5664342.pdf.

[67] A. Babarit, M. Folley, F. Charrayre, C. Peyrard, and M. Benoit, "On the modelling of WECs in wave models using far field coefficients", in *10th European Wave and Tidal Energy Conference*, Aalbord, Denmark, 2013.

[68] F. Charrayre, C. Peyrard, M. Benoit, and A. Babarit, "A coupled methodology for wave-body interactions at the scale of a farm of wave energy converters including irregular bathymetry", in *ASME 2014 33rd International Conference on Ocean, Offshore and Arctic Engineering*, San Francisco, USA, 2014, pp. 1–9.

[69] F Charrayre, M Benoit, C Peyrard, A Babarit, H. S.-v. Edf, and P. Paristech, "Modeling of interactions in a farm of wave energy converters taking into account the bathymetry", in *14eme Journées de l'Hydrodynamique*, Val de Reuil, France, 2014.

[70] C. C. Mei, M. Stiassnie, and D. K.-P. Yue, "Scattering by a vertical cylinder with circular cross section," in *Theory and Applications of Ocean Surface Waves: Part 1: Linear Aspects Part 2: Nonlinear Aspects*, World Scientific, 1989, pp. 364–368.

[71] P. M. Ruiz, F. Ferri, and J. P. Kofoed, "Water wave diffraction and radiation by three-dimensional bodies over mild slope bottom", *Ocean Engineering*, vol. 143, no. May, pp. 4–5, 2017, ISSN: 00298018. DOI: 10.1016/j.oceaneng.2017.08.007.

[72] R. P. F. Gomes, M. F. P. Lopes, J. C. C. Henriques, L. M. C. Gato, and A. F. O. Falcão, "A Study on the Wave Energy Conversion by Submerged Bottom-hinged Plates", in *9th European Wave Tidal Energy Conference*, Southampton, UK, 2011.

[73] H. tao Zhao, Z. lin Sun, C. ling Hao, and J. fa Shen, "Numerical modeling on hydrodynamic performance of a bottom-hinged flap wave energy converter", *China Ocean Engineering*, vol. 27, no. 1, pp. 73–86, 2013, ISSN: 08905487. DOI: 10.1007/s13344-013-0007-y.

[74] J. N. Newman, *Marine hydrodynamics*. MIT press, 1977.

[75] G. Thomas, "The Theory Behind the Conversion of Ocean Wave Energy: a Review", in *Ocean Wave Energy: Current Status and Future Prepectives*, 2008, pp. 41–91. DOI: 10.1007/978-3-540-74895-3_3.

[76] N. Booij, "A note on the accuracy of the mild-slope equation", *Coastal Engineering*, vol. 7, no. 3, pp. 191–203, 1983, ISSN: 03783839. DOI: 10.1016/0378-3839(83)90017-0.

[77] M. Brorsen and J. Helm-Petersen, "On the Reflection of Short-Crested Waves in Numerical Models", *International Conference on Coastal Engineering*, pp. 394–407, 1998, ISSN: 08938717.

[78] P. S. Andersen and T. Klindt, "Random Wave Propagation-Based on the Mild-slope Equation: Annex and Appendix", PhD thesis, Aalborg Universitet, 1994.

[79] C. Lee and K. D. Suh, "Internal generation of waves for time-dependent mild-slope equations", *Coastal Engineering*, vol. 34, no. 1-2, pp. 35–57, 1998. DOI: 10.1016/S0378-3839(98)00012-X.

[80] K. Hasselmann, T. Barnett, E. Bouws, H. Carlson, D. Cartwright, K. Enke, J. Ewing, H. Gienapp, D. Hasselmann, P. Kruseman, A. Meerburg, P. Müller, D. Olbers, K. Richter, W. Sell, and H. Walden, "Measurements of wind wave growth and swell decay during the Joint North Sea Wave Project (JONSWAP)", *Dtsch. Hydrogr. Z.*, vol. 8, p. 95, 1973.

[81] S. Astariz, J. Abanades, C. Perez-Collazo, and G. Iglesias, "Improving wind farm accessibility for operation & maintenance through a co-located wave farm: Influence of layout and wave climate", *Energy Conversion and Management*, vol. 95, pp. 229–241, 2015. DOI: 10.1016/j.enconman.2015.02.040.

[82] N. Tomey-Bozo, J. Murphy, P. Troch, A. Babarit, T. Lewis, and G. Thomas, "The modelling of a flap type wave energy converter in a time-dependent mild-slope equation model", in *Renewable Energies Offshore*, 2016, pp. 277–284, ISBN: 9781138626270.

[83] F. Fàbregas Flavià, C. McNatt, F. Rongère, Aurélien Babarit, and A. H. Clément, "Computation of the Diffraction Transfer Matrix and the Radiation Characteristics in the open-source BEM code NEMOH", in *ASME 2016 35th International Conference on Ocean, Offshore and Arctic Engineering*, Busan, South Korea, 2016.

[84] N. Tomey-Bozo, J. Murphy, P. Troch, T. Lewis, and G. Thomas, "Modelling of a flap-type wave energy converter farm in a mild-slope equation model for a wake effect assessment", *IET Renewable Power Generation*, pp. 1–11, 2017. DOI: 10.1049/iet-rpg.2016.0962.

[85] G. Verao Fernandez, P. Balitsky, N. Tomey-Bozo, V. Stratigaki, and P. Troch, "Far-field effects by arrays of oscillating wave surge converters and heaving point absorbers: a comparative case study", in *12th European Wave and Tidal Energy Conference*, Cork, Ireland, 2017.

[86] V. Stratigaki, P. Troch, L. Baelus, and Y. Keppens, "Introducing wave generation by wind in a mild-slope wave propagation model MILDwave, to investigate the wake effects in the lee of a farm of wave energy converters", in *30th International Conference on Ocean, Offshore and Arctic Engineering*, Rotterdam, The Netherlands, 2011, pp. 429–436.

[87] P. Troch and V. Stratigaki, "Phase-resolving wave propagation array models", in *Numerical modelling of wave energy converters : state-of-the-art techniques for single devices and arrays*, M. Foley (Ed.), Ed., Elsevier, 2016, pp. 191–216.

[88] N. Tomey-Bozo, J. Murphy, A. Babarit, P. Troch, T. Lewis, and G. Thomas, "Wake effect assessment of a flap type wave energy converter farm using a coupling methodology", in *ASME 2017 36th International Conference on Ocean, Offshore and Arctic Engineering*, Trondheim, Norway, 2017.

[89] P. Balitsky, G. Verao Fernandez, V. Stratigaki, and P. Troch, "Coupling methodology for modelling the near-field and far-field effects of a wave energy converter", in *36th International Conference on Ocean, Offshore and Arctic Engineering*, Trondheim, Norway, 2017, pp. 1–10.

[90] ——, "Assessing the impact on power production of WEC array separation distance in a wave farm using one-way coupling of a BEM solver and a wave propagation model", in *12th European Wave and Tidal Energy Conference*, Cork, Ireland, 2017, pp. 1176–1186.

[91] T. Verbrugghe, P. Troch, A. Kortenhaus, V. Stratigaki, and A. Engsig-Karup, "Development of a numerical modelling tool for combined near field and far field wave transformations using a coupling of potential flow solvers", in *2nd International Conference on Renewable energies Offshore*, Lisbon, Portugal, 2016, pp. 61–68. DOI: 978-1-138-62627-0.

[92] T. Verbrugghe, V. Stratigaki, P. Troch, R. Rabussier, and A. Kortenhaus, "A comparison study of a generic coupling methodology for modeling wake effects of wave energy converter arrays", *Energies*, vol. 10, no. 11, 2017, ISSN: 19961073. DOI: 10.3390/en10111697.

[93] A. P. Engsig-Karup, H. B. Bingham, and O. Lindberg, "An efficient flexible-order model for 3D nonlinear water waves", *Journal of Computational Physics*, vol. 228, no. 6, pp. 2100–2118, 2009, ISSN: 00219991. DOI: 10.1016/j.jcp.2008.11.028. [Online]. Available: http://dx.doi.org/10.1016/j.jcp.2008.11.028.

[94] T Verbrugghe, B Devolder, J Domínguez, A Kortenhaus, and P Troch, "Feasibility study of applying SPH in a coupled simulation tool for wave energy converter arrays", in *12th European Wave and Tidal Energy Conference*, Cork, Ireland, 2017.

[95] T. Verbrugghe, A. Kortenhaus, P. Troch, and J. M. Dominguez, "A non-linear 2-way coupling between DualSPHysics and a wave propagation model", in *12th International SPHERIC Workshop*, Ourense, Spain, 2017, pp. 121–127, ISBN: 9788469736784.

[96] Marine Institute, *The INtegrated Mapping FOr the Sustainable Development of Ireland's MArine Resource (INFOMAR)*. [Online]. Available: http://www.infomar.ie/ (visited on 01/01/2017).

Appendix A

Paper A

Modelling of a flap type wave energy converter farm in a mild-slope equation model for a wake effect assessment

Published in

IET Renewable Power Generation, IET Digital Library, 2017. ISSN 1752-1416.

Authors

Nicolas Tomey-Bozo[1], Jimmy Murphy[1], Peter Troch[2], Tony Lewis[1], Gareth Thomas[3]

[1]*MaREI Centre (ERI), University College Cork, Haulbowline Road, Ringaskiddy, Ireland*

[2]*Department of Civil Engineering, Ghent University, Zwijnaarde, Belgium*

[3]*School of Mathematical Sciences, University College Cork, Cork, Ireland*

Abstract

It is expected that large farms of Wave Energy Converters (WECs) will be installed and as part of the consenting process it will be necessary to quantify their impact on the local environment. The objective of this study is to assess the impact a WEC farm has on the incoming wave field through the use of a novel methodology. This methodology assesses the changes of the significant wave height surrounding a flap type WEC farm with a special focus on the lee of the farm. A time-dependent mild-slope equation model is employed to solve the propagation of surface waves and their interaction with the devices. The model represents the devices as obstacle cells with attributed absorption coefficients tuned against near-fields obtained from a Boundary Element Method (BEM) solver. The wake effect of the farm is determined by using a step by step approach starting first with an assessment of one device and progressively incrementing to a larger number of flaps. The effect of incident sea states, device separations, and water depth changes on the wake effect of the farm are also investigated. This work shows the potential of a WEC farm to reduce significant wave heights on the lee-side.

A.1 Introduction

Wave energy converters (WECs) transform the incoming waves from the ocean by partially absorbing and partially redistributing the wave energy arriving to the device. Part of the energy is extracted and transformed into electricity while another part is redistributed by a combination of diffraction and radiation phenomena into the ocean. The transformation of the incoming wave energy then leads to a reduction of the wave energy density in the lee of the device. The amount of energy reduction increases with the number of devices allowing for of a large sheltered zone to be created in the lee of the WEC farm. This sheltered zone can be profitable for other marine activities that would benefit from a reduction of the wave energy density in a delimited area. Examples of these activities are offshore wind farms, aquaculture fisheries, or coastal protection projects.

The modelling of WECs to quantify their impact on the wave climate is still a relatively new area of study. Different methodologies have been implemented to attempt to quantify the wave field surrounding a WEC farm but up to date there is not an ideal ready-to-use tool to assess this problem. Boundary Element Method (BEM) solvers based on potential flow have been used to assess the near field effects and farm interactions [1, 2] because of their high suitability to solve wave-body interaction problems. However, BEM solvers present some limitations due to their constant water depths assumption and therefore the absence of wave transformation processes. Wave propagation models, using either phase averaged [3, 4] or phase-resolved models [5, 6], have been applied to study the far field effects in large domains. These models are accurate solvers of wave transformation processes across

large domains and allow the consideration of realistic irregular bathymetries. Their main disadvantage remain the weak capacity of modelling moving bodies and the interaction with waves. An overview of the different methodologies with their advantages and disadvantages can be found in [7].

The most common applications of wave propagation models represent the devices as grid cells with attributed absorption coefficients or source terms. These absorption coefficients or source terms are tuned to match a look up table with reflection and transmission (and absorption inherently) coefficients used as a target to represent the effect of the WEC on the near field. Obtaining the correct target reflection and transmission coefficients is a difficult task as there is no clear procedure on the manner by which they are to be determined. Usually those transmission and reflection coefficients refer to the wave field information along a section line in the wave propagation direction which does not allow for the validation of the 2D wave field perturbation caused by the device. In addition, these coefficients are commonly obtained from tank testing where tank reflection remain an important issue, or from developer look up tables where the source of information remain uncertain due to the general unwillingness from developers to share it.

In this study a time-dependent mild-slope equation model (phase-resolved wave propagation model) is used to simulate the propagation of surface waves through a WEC farm. The target reflection and transmission effect of the WEC on the surrounding near-field is obtained from the wave field solutions calculated in a BEM solver. BEM solvers are regarded as being accurate in the local wave-body interaction problem as they account for all the wave components generated by a moving body [8]. The representation of the target wave reflection and transmission of the device as a complete wave field all around the device allows for the validation of the 2D wave field perturbation created by the presence of the WEC.

The device type selected is a flap type WEC located in shallow waters and subject to wave conditions consisting of irregular long crested waves. The tuning of the flap representation is achieved first by comparing near-field wave solutions from the BEM solver to the wave solutions from the mild-slope equation model. Then, the layout of the WEC farm is designed in an incremental manner by assessing the effect of, first a single flap, then a row of several flaps, and finally two rows of flaps, on the incoming wave field. The flaps are placed at the locations where the wave energy density is higher in order to achieve better energy absorption, thus resulting in a larger impact on the wave field. Finally, the sensitivity of the wake effect to the sea state, the device separation, and the bathymetry are also assessed. The model was setup with a large domain in order to evaluate the wake effect of a flap farm in the far-field and its potential sheltering effect.

A.2 Numerical Tools

A.2.1 Open-source boundary element method solver NEMOH

NEMOH is an open-source BEM solver developed by Ecole Centrale de Nantes [8] and it is used in this work to obtain the near-field surrounding the WECs. NEMOH is based on the linear potential theory and it calculates the perturbed velocity potential generated by the presence of a floating body under an incoming regular wave. This is done by solving the scattering problem with the appropriate set of boundary conditions, which is the well-known linear wave body interaction boundary value problem. The velocity potential $\tilde{\phi}(x, y, z)$ for the perturbed wave is obtained as a 3D solution describing the flow surrounding the body. Then from the potential at the free surface condition $\tilde{\Phi}(x, y)$ where $z = 0$ it is straightforward to obtain the surface elevation $\tilde{\eta}$ as shown in Equation (A.1)

$$\tilde{\eta}(x, y) = \frac{i\omega}{g}\tilde{\Phi}(x, y) \tag{A.1}$$

where ω is the wave frequency and g the gravitational acceleration.

The scattering problem is solved for each wave frequency by dividing the problem into one diffraction problem and one radiation problem per degree of freedom of the moving body. The diffraction problem is computed considering the body is fixed under the presence of an incoming incident wave. The radiation problem is solved by considering a forced motion of the body in calm conditions (absence of waves). The sum of the surface elevation obtained from the diffraction problem and the radiation problems (one problem per degree of freedom) gives the surface elevation for the perturbed wave as shown in Equation (A.2). The solution of the total wave field (Equation (A.3)) is then obtained as a superposition of the surface elevation for the incident wave and the perturbed wave. Details of the equations solved by NEMOH to obtain the perturbed potential solution are described in detail in [8].

$$\tilde{\eta}_p(x, y) = \tilde{\eta}_d + \sum_{n=1}^{6} \tilde{\eta}_r \tag{A.2}$$

$$\tilde{\eta}_t(x, y) = \tilde{\eta}_i + \tilde{\eta}_p \tag{A.3}$$

Tilde (˜) denotes the complex form of the variables and subscripts p, d, r, t, and i refer to the perturbed, diffracted, radiated, total, and incident wave respectively. The complex surface elevation can be expressed as

$$\tilde{\eta} = A_\omega e^{i\varphi} \tag{A.4}$$

where the wave amplitude A_ω and phase φ are the module and argument.

A.2.2 Mild-slope equation model MILDwave

The core of the calculations carried out in this work are implemented using MILDwave, a time-dependent mild-slope equation model developed by Ghent University [9, 10]. MILDwave is a phase-resolved type wave propagation model that solves the propagation of surface waves throughout the domain and the interaction with the obstacles (previously defined) by solving the depth-integrated mild-slope equations of Radder and Dingemans [11]. The velocity potential and the instantaneous surface elevation at the free water surface are the variables solved for each coordinate of the grid (x,y) for each instant t of time by the set of differential equations given in equation (A.5) and (A.6):

$$\frac{\partial \eta}{\partial t} = B_c \Phi - \nabla \Delta (A_c \nabla \phi) \tag{A.5}$$

$$\frac{\partial \Phi}{\partial t} = -g\eta \tag{A.6}$$

where A_c and B_c are the coefficients described in Eqns. (A.7) and (A.8)

$$B_c = \frac{\bar{\omega}^2 - \bar{k}^2 \bar{C} \bar{C}_g}{g} \tag{A.7}$$

$$A_c = \frac{\bar{C} \bar{C}_g}{g} \tag{A.8}$$

with the phase velocity $\bar{C}$ and the group velocity $\bar{C}_g$ for a wave with carrier wave number $\bar{k}$ and carrier angular frequency $\bar{\omega}$. Overbar ($\bar{}$) denotes that the wave characteristic is calculated for the carrier frequency.

Waves are generated in MILDwave at the offshore boundary by using the source term addition method, i.e. by adding an additional surface elevation η^* to the calculated value on a wave generation line for each time step given by equation (A.9) and described in [12]:

$$\eta^* = 2\eta_I \frac{C_e \Delta t}{\Delta x} \cos \beta \tag{A.9}$$

with the water surface elevation of incident waves η_I, the angle of wave rays from the X axis β, the grid size in X direction Δx, the time step Δt, and the energy velocity C_e given by equation (A.10):

$$C_e = \bar{C}_g \frac{\bar{\omega}}{\omega} \sqrt{1 + \frac{\bar{C}}{\bar{C}_g} \left(\left(\frac{\omega}{\bar{\omega}} \right)^2 - 1 \right)} \tag{A.10}$$

The wave generation line is assumed to be parallel to the Y axis in equation (A.9). For the generation of random waves, the peak frequency is used as a carrier frequency in equations (A.7) and (A.8) as the peak frequency is usually lower than the weight-averaged frequency and as the dispersion relation of the model of Radder and Dingemans is more accurate in the high frequency range [12, 13].

Obstacles are defined in MILDwave by grid cells that have attributed absorption coefficients. These absorption coefficients locally affect the surface elevation of the propagated wave which is multiplied by values in the range from 1 to 0. Values equal to 1 represent a water grid cell (no absorption) while values equal to 0 represent a grid cell of a fully reflective obstacle (100 % reflection). Therefore, the wave field reflection and transmission changes depending on the distribution of the absorption coefficients through the set of obstacles cells. Thus, wave energy converters can be represented as obstacle cells with absorption coefficients tuned to represent the target wave reflection and transmission (and absorption inherently).

A.3 Implementation of a Wave Energy Converter

Wave propagation models are used in many engineering studies for determining site specific wave conditions. They can incorporate very large domains and realistic environmental conditions such as irregular bathymetries and shallow water wave transformation processes. However from a renewable energy perspective they do not accurately represent the local wave-body interaction problem when a moving body is considered. Nevertheless wave propagation models can still be the best option when the wake effect for a WEC farm in the far-field needs to be quantified. They can give a satisfactory balance between accuracy and computational time.

A.3.1 Overview of methodology

The solution suggested in this study to accurately model the WEC disturbance on the wave field is to tune the parameters representing the device in the wave propagation model against results obtained from BEM solvers for the near-field. BEM solvers give a complete solution of the local wave-body interaction problem by solving all wave components; the radiated wave generated by the motion of the device for each degree of freedom and the diffracted wave generated by the disturbance of the incident wave due to the presence of a fix body. Thus, whilst remaining under the limitations of the linear water theory, the solution obtained from a BEM solver is considered to be representative of the wave-body interaction phenomena for the near-field. The more the water depth changes with the distance to the device, the smaller is the near-field area surrounding the device where BEM solvers can provide accurate results.

Irregular long crested waves are considered in MILDwave to assess the wake effect generated by a WEC farm. Therefore, the same irregular sea state conditions need to be used as a target for the tuning of the absorption coefficients attributed to obstacle cells representing the device. First a superposition of the regular wave results obtained from NEMOH is computed to obtain the desired target irregular sea states. Then irregular long-crested waves are run in MILDwave and the obstacle cells representing the WEC are tuned against the target irregular wave solutions

computed from NEMOH. Once the accurate configuration of absorption coefficients attributed to the obstacle cells is found, the wake effect of a farm with several devices can be assessed with the same obstacle cell configuration for each device. Finally, it is important to consider that each sea state has its own optimum configuration of obstacle cells and that a tuning of the device representation is needed for every case.

A.3.2 Flap type wave energy converter

The WEC considered in this study is a surface-piercing flap hinged at the bottom of the seabed as shown in Figure A.1. The motion is restricted to pitch and therefore only one degree of freedom is considered. The shaft about which the flap rotates is at the base of the device.

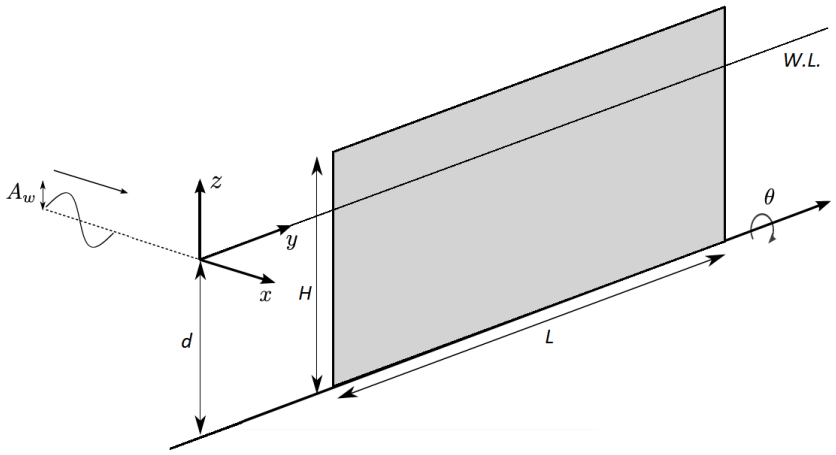

FIGURE A.1: Flap type WEC sketch.

The flap main characteristics are provided in Table A.1 and the parameters θ, $W.L.$, and d represent the angle of pitch motion, the water line level, and the depth respectively.

TABLE A.1: Main characteristics of the flap type WEC.

Parameter	Coefficient	Value	Units
Length	L	20	m
Height	H	12	m
Thickness	t	1	m
Relative density	ρ_r	0.3	-

The amplitude of the angle of motion is calculated based on equation (A.11). This value is used to quantify the radiated wave obtained from NEMOH which is

non-dimensionalised by the amplitude of motion for the corresponding degree of freedom.

$$\theta(\omega) = \frac{A_w \Gamma(\omega)}{-\omega^2(I + A_r) - i\omega(B_r + B_P TO) + H} \tag{A.11}$$

A_w represents the wave amplitude, Γ, the wave excitation moment coefficient, I, the moment of inertia about the Y axis, A_r, the added moment of inertia coefficient, B_r, the radiation damping coefficient, H, the hydrostatic restoring coefficient, and B_{pto}, the Power Take Off (PTO) damping coefficient.

The optimum value of the PTO damping coefficient for each wave frequency is theoretically defined by equation (A.12) as demonstrated in [14]. As irregular sea states are applied in this study, the value of the PTO damping coefficient used is the optimum one for the frequency corresponding to the peak period of the sea state applied.

$$B_{pto} = \sqrt{\left(\frac{H}{\omega} - \omega(I + A_r)\right)^2 + B_r^2} \tag{A.12}$$

A.3.3 Representation in NEMOH

As a first step the wave amplitude corresponding to the total wave solution is computed for each regular wave from the superposition of the perturbed wave obtained from NEMOH and its corresponding incident wave. A domain of 400 x 400 meters is considered as a representation of the near-field surrounding the device. Figure A.2 shows the results obtained for an incident regular wave of $T = 8$ s and $A_\omega = 1$ m. The waves propagate towards the X positive axis for all cases considered for this study.

From the total wave amplitude obtained for regular waves it is possible to compute an irregular sea state which accounts for the perturbation of the WEC. This is done based on the superposition principle of linear water waves along a long range of frequencies representing a wave energy spectrum. The parameterised JONSWAP spectrum described in [5] is used to represent the wave spectral density distribution of the input incident long-crested irregular waves. A peak enhancement factor γ of 3.3 is considered and a discretisation of 100 wave frequency intervals is used.

The relation between the wave spectral density and the amplitude corresponding to each frequency interval is defined by equation (A.13):

$$S(\omega)\Delta\omega = \frac{1}{2} A_w(\omega)^2 \tag{A.13}$$

where S is the wave spectral density and $\Delta\omega$ the increment between frequencies.

A disturbed wave spectrum is define now by equation (A.14) as the local transformation of the undisturbed wave spectrum caused by the presence of the WEC:

$$S_d(\omega) = S_u(\omega) A_{sd}^2(\omega) \tag{A.14}$$

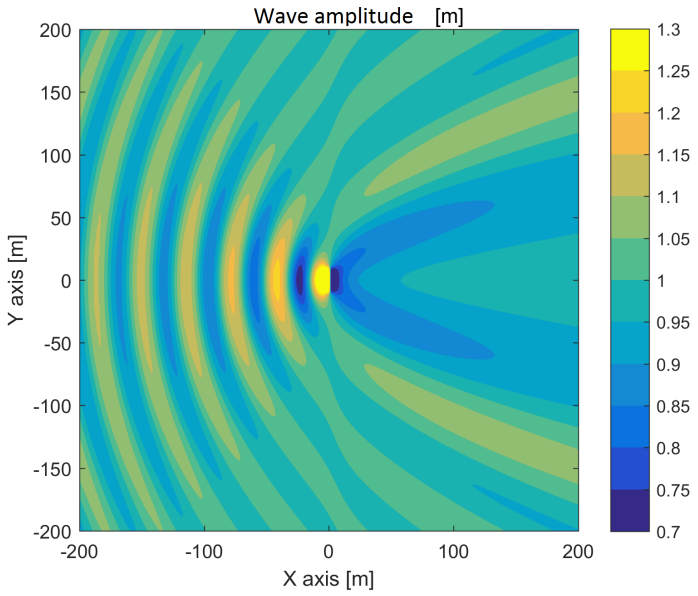

FIGURE A.2: Total wave amplitude for a regular wave of $T = 8$ s and $A_\omega = 1$ m.

where S_d is the disturbed wave spectrum, S_u the undisturbed spectrum, and A_{sd} the disturbed wave amplitude obtained from the total wave amplitude results of each regular wave. Therefore, each grid cell of the domain has a corresponding value of the latest three parameters. In the case of constant water depths the undisturbed spectrum S_u along the whole domain is equivalent to the incident wave spectrum input at the boundary as there is no transformation due to bathymetry changes. Figure A.3 shows the transformation of the wave spectrum for a grid cell located 20 meters on the lee of the device as an example for illustration.

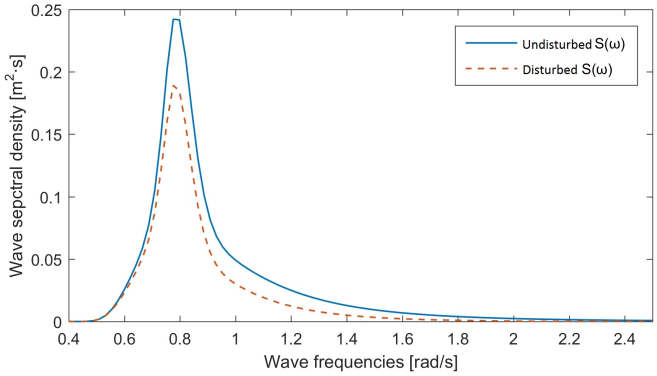

FIGURE A.3: Undisturbed wave energy spectrum vs. disturbed wave energy spectrum (behind the WEC).

The disturbance coefficient K_d defined by equation (A.15) is then used to quantify with a single parameter the disturbed wave spectrum S_d for each grid cell along the domain. H_{sd} represents the significant wave height corresponding to the disturbed wave spectrum and H_{su} the significant wave height corresponding to the

undisturbed wave spectrum.

$$K_d = \frac{H_{sd}}{H_{su}} \tag{A.15}$$

The calculation of the disturbance coefficient enables the plotting of the wave spectrum changes caused by the perturbation of the WEC along the considered domain. Figure A.4 shows the disturbance coefficient K_d obtained along the same domain of 400 x 400 meters for a long-crested irregular sea state with peak period $T_p = 8$ s. Section S, drawn by a dotted line, represents the region where the K_d values are used as a target to tune the absorption coefficients representing the WEC in MILDwave. The disturbance coefficient does not change with the significant wave height of the incident sea state as it is a non-dimensional coefficient and linear waves conditions are assumed. Therefore from now on each sea state is described only by the value of its peak period T_p.

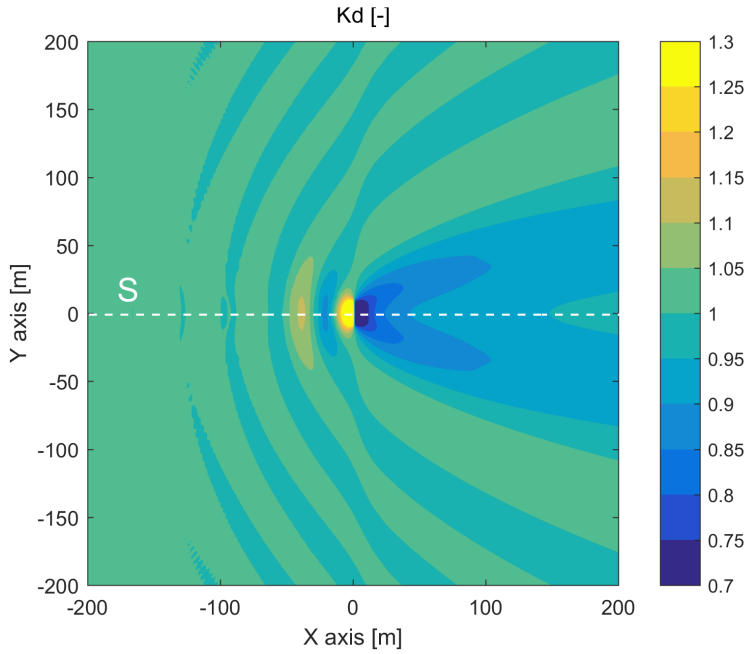

FIGURE A.4: Disturbance coefficient from NEMOH for 1 flap and $T_p = 8$ s.

A.3.4 Representation in MILDwave

Irregular long-crested waves are generated in MILDwave for the same sea state of $T_p = 8$ s and same domain size as done in NEMOH. The absorption coefficients attributed to the obstacle cells representing the flap type WEC in MILDwave are tuned in such a way that the wave field surrounding the device matches the results obtained from NEMOH.

The flap is represented by a group of grid cells occupying the length of the flap and a thickness of 2 grid cells. A grid cell size of 2 x 2 meters is defined for the cases run in this study. The grid cell size has been chosen to obtain consistent results for all

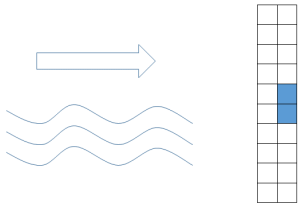

FIGURE A.5: Grid cell discretisation of the flap type WEC.

the different sea states considered based on the guidelines from [10]. Different combinations of absorption coefficients were assigned to the obstacle grid cells to study the effect on the wave reflection and transmission as part of a sensitivity analysis. The aim of this is to achieve the target disturbance coefficient values to properly represent the flap. Figure A.5 shows a sketch of the device grid discretisation where the empty grid cells have the absorption coefficient a set to 0 (fully reflective obstacle) and the coloured grid cells have absorption coefficients a set to a value different than 0 (energy absorbing obstacle).

TABLE A.2: Absorption coefficients configurations

	Absorption coefficient a
Config. 1	0.2
Config. 2	0.3
Config. 3	0.4
Config. 4	0.5

Different values of absorption coefficients are attributed to the coloured cells in order to achieve the target disturbance coefficient distribution along section S. Figure A.6 shows the K_d values obtained along section S from MILDwave for the different configurations displayed in table A.2 together with the target K_d values from the NEMOH wave solutions.

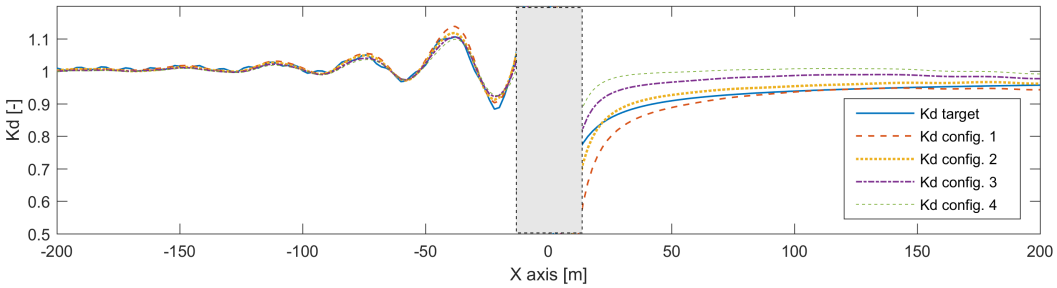

FIGURE A.6: Tuning of the absorption coefficients attributed to the WEC grid cells.

The results obtained for the optimum configuration are shown in the upper plot of Figure A.7 where the K_d values along the whole domain are displayed. Configuration 2 has been selected as the one most accurately representing the flap wave disturbance on the wave field for this sea state. The lower plot from Figure A.7

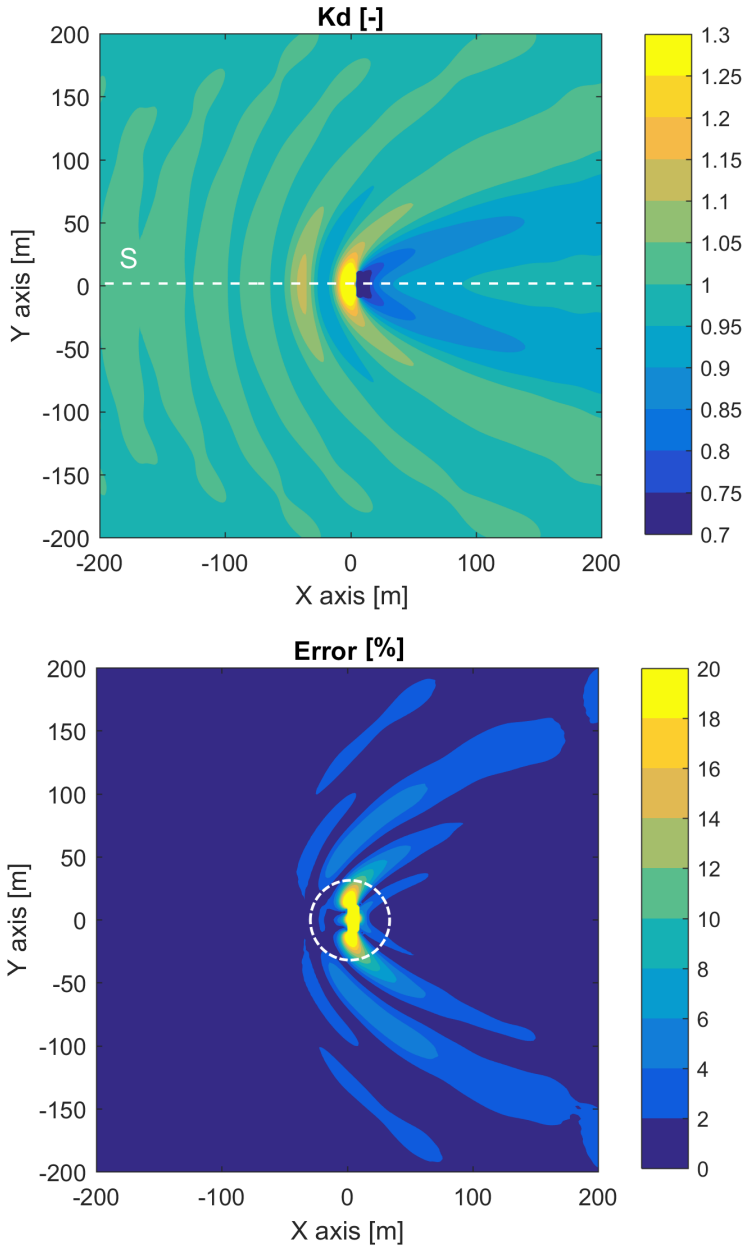

FIGURE A.7: Top: Disturbance coefficient from MILDwave for 1 flap and $T_p = 8$ s. Bottom: Percent error between MILDwave and NEMOH (fig. A.4) for the same scenario conditions.

shows the percent error between the optimum values obtained in MILDwave and the target values from NEMOH as a comparison plot. The error is relatively large in the near-field but gets reduced extremely fast with the distance to the device. At a radius distance higher than 30 meters from the centre of the device (circular dotted line) the error is lower than 10 % and after 50 meters it remains lower than 5%. Thus, the results obtained from modelling the device in MILDwave as a set of obstacle cells show to be representative of the effect of a flap type WEC on the surrounding wave field.

A.4 Wake Effect for a Flap Type Wave Energy Converter Farm

The wake effect for WEC farms composed of several flaps is assessed in this section using MILDwave. A large domain of 2000 x 1000 m is considered and the wake effect is evaluated in the lee of the farm with a focus on the far-field.

A.4.1 Wave energy converter farm with four flaps

A farm of 4 flaps arranged in a line is first considered. The devices are arranged in a row with a separating distance of 3 x L. The row of flaps is located along section $x = -500$ m allowing the disturbance coefficient K_d to be determined along a length of 1500 meters behind the farm. Figure A.8 shows the K_d values obtained for a sea state of $T_p = 8$ s.

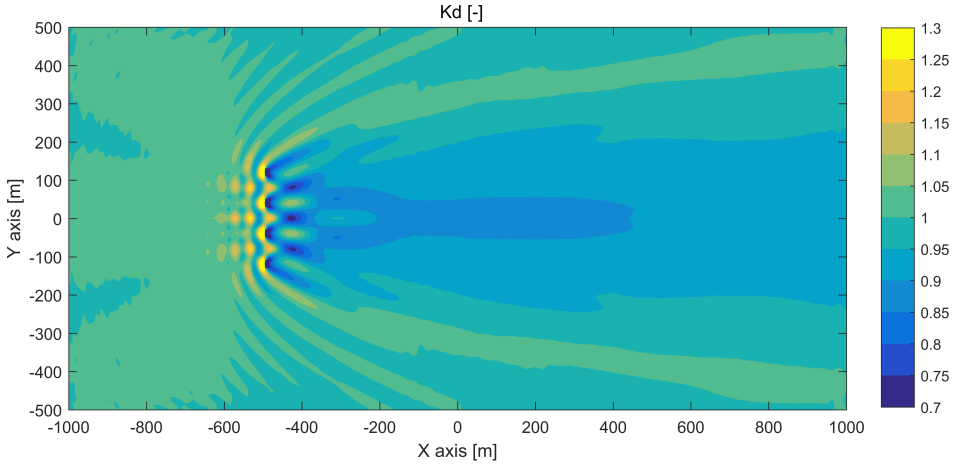

FIGURE A.8: Disturbance coefficient for a 4 flaps farm and $T_p = 8$ s.

Contour lines are plotted in figure A.8 along the zones with same K_d values. The darker is the colour of the area with uniform colour the lower is the value of the disturbance coefficient and therefore the higher is the reduction of the significant wave height. The reduction of the disturbance coefficient remain relatively low for this case scenario with only 4 flaps. The area with K_d values ranged between 0.85 and 0.9 (10-15% of significant wave height reduction) is relatively small and the lee side of the farm is dominated by values ranged between 0.9 and 0.95, which corresponds to a 5-10% of significant wave height reduction.

A.4.2 Wave energy converter farm with nine flaps

The next step was to model a farm of 9 flaps by adding a second row of 5 devices to the previous setup. The second row is located 20 meters behind the first row (with respect to the incoming waves) and the flaps of the second row are centred about the gaps between the flaps of the first row, as it can be intuit from Figure A.9 where the results for this case are shown. The distance in between devices from the second row remain 3 x L as for the first row. This keeps a minimum separating distance

of 30 meters (1.5 L) between the devices from the first and second row due to their misalignment.

The location of the second row has been chosen based on the results from the single row case where the disturbance coefficient K_d is higher and therefore the wave energy density is higher as well. The values of K_d change depending on the location along the domain and the interaction effects of the whole array. Therefore, the locations where a constructive effect on the wave field take place and the disturbed significant wave height increases, are suitable to locate the devices in a attempt to increase the size of the farm. Those spots are exposed to a higher energy density and therefore the WEC is able to extract a higher amount of wave energy. This phenomena is sea state dependent, therefore the devices location needs to be chosen accordingly with the sea state of the site with the highest occurrence probability. The sea state of $T_p = 8$ s is assumed to be the sea state with the highest occurrence probability for this study.

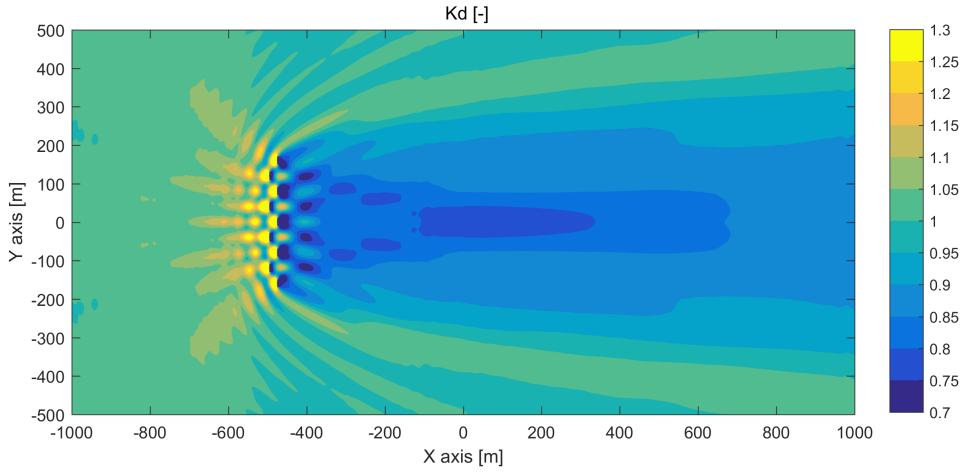

FIGURE A.9: Disturbance coefficient for a 9 flaps farm and $T_p = 8$ s.

As expected, there is significantly lower energy reduction for the 4 flaps farm than for the 9 flaps farm. The higher wave energy absorption and reflection due to the addition of the second row of flaps makes a significant difference in the wake effect. The lowest K_d value obtained for the 4 flaps farm is 0.85 while the equivalent lowest value for the 9 flaps farm is 0.77 considering the fast dissipated near-field results (less than 100 m from the farm) are neglected.

A.4.3 Farm layout influence

Now, the influence of the separating distance in between devices is assessed. The changes in the separating distance leads to important changes in the wake effect due to the amount of wave energy density passing between the flaps. A separating distance of $3L$ was used in the previous case studies and now two additional configurations with a separating distance of 4 and 5 times L are considered. The same

distance of 20 m between rows is kept and the flaps of the second row are centred in the gaps from the front row. A sea state of $T_p = 8$ s is applied in this section.

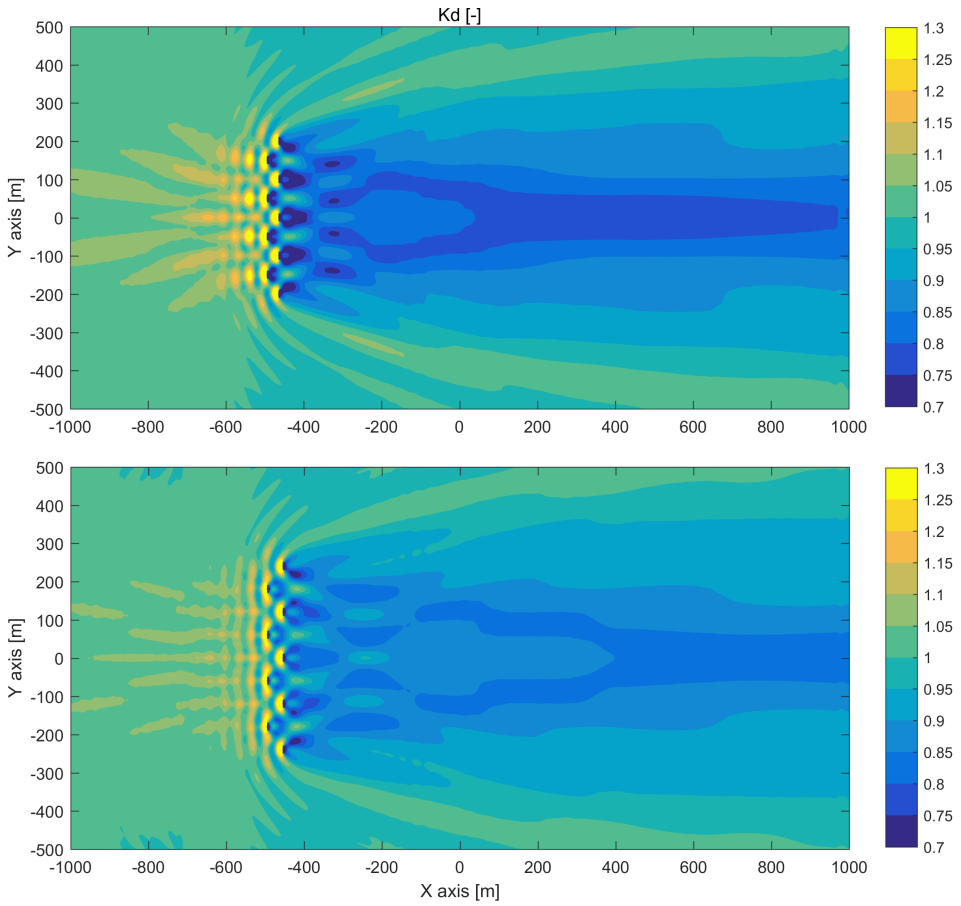

FIGURE A.10: Disturbance coefficient for a 9 flaps farm and $T_p = 8$ s. Top: Spacing in between devices of 4 L. Bottom: Spacing in between devices of 5 L.

Figure A.10 show the disturbance coefficient obtained for the $4L$ and $5L$ cases respectively and can be compared with the results from Figure A.9 where a separating distance of $3L$ was considered under the same incident wave conditions.

It can be seen that the higher reduction of the disturbance coefficient is not achieved with the shortest separating distance of $3L$ as one could logically think but with a separating distance of $4L$. A large area corresponding to the Kd values below 0.75 (equivalent to a 25% of significant wave height reduction) is found for the $4L$ case while a much smaller area corresponding to the same values is found for the $3L$ and $5L$ cases. Therefore the highest sheltering effect is found for the $4L$ case as is the configuration under which the highest reduction of energy density is found. Nevertheless a similar area size is found for the 3 cases (3, 4, and 5 L) if the zone corresponding to the K_d values below 0.9 is considered, which represents only a reduction of 10% in the significant wave height.

From now on, the $3L$ configuration of the 9 flaps farm will be used to assess the influence of the sea state and batheymetry on the wake effect.

A.4.4 Sea state influence

The influence of the sea state in the wake effect is now assessed in this section. A farm composed of two rows and 9 flaps with the same configuration than the last section is considered. Two sea states of $T_p = 6$ s and then a $T_p = 10$ s are considered. The tuning of the absorption coefficients attributed to the obstacle cells representing the flaps has been done again for every sea state. Therefore an optimum configuration of the device representation has been obtained for every sea state.

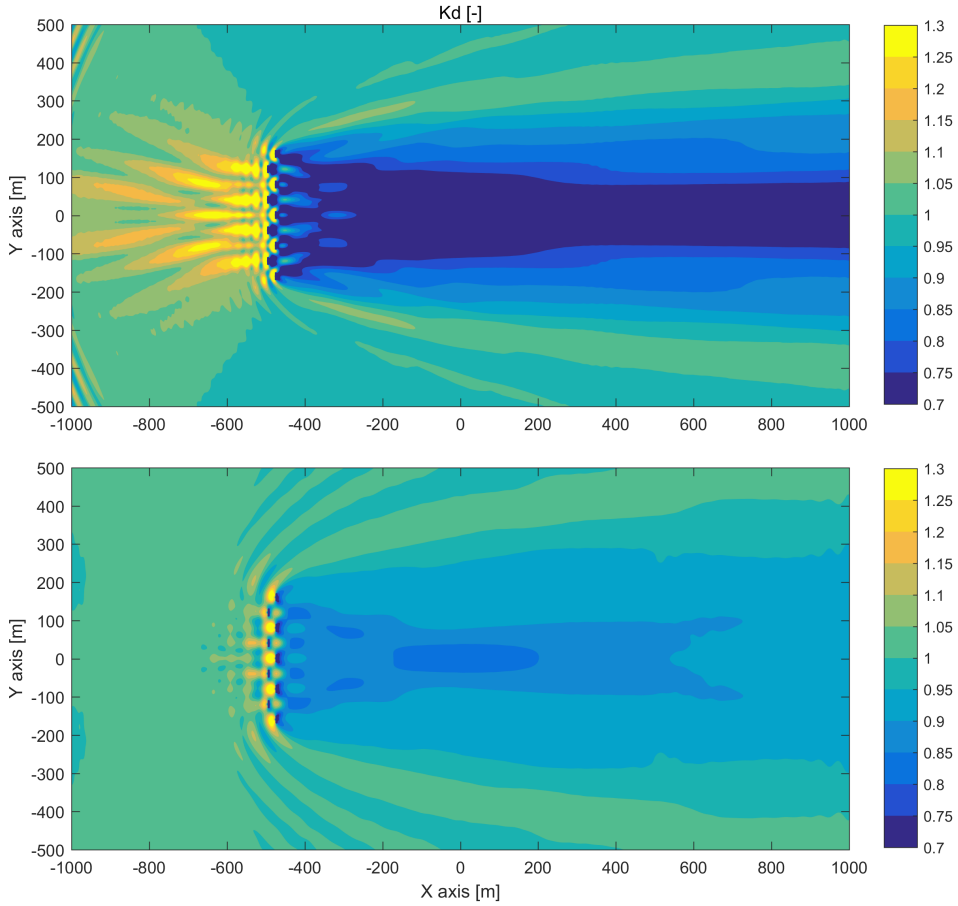

FIGURE A.11: Disturbance coefficient for a 9 flaps farm. Top: sea state of $T_p = 6$ s. Bottom: sea state of $T_p = 10$ s.

Figure A.11 shows the disturbance coefficient obtained for the sea state $T_p = 6$ s and $T_p = 10$ s. A large decrease in the disturbance coefficient is found for the first sea state while no significant difference is found for the second sea state. The reason for such a high disturbance of the farm under the sea state of $T_p = 6$ s is the ratio between the wave length corresponding to the peak period and length of the flaps. The diffraction phenomena becomes significant for ratios between obstacle characteristic length and wave length larger than 0.2 [15]. In this case the characteristic length of the device is 20 meters and the wave length for the peak period is about 50 meters, therefore diffraction effects are important and lead to a much higher wave field disturbance than for the case of $T_p = 8$ s and $T_p = 10$ s.

A.4.5 Changing depth bathymetry influence

When waves propagate from deep to shallow water shoal will occur and the wave height will increase while the waves travel towards decreasing depths. In this section the influence of a changing depth bathymetry on the wake effect of a flap farm is investigated. Then a comparison is made with the constant water depths scenario considering the same farm configuration and sea state. This is done as a step in enhancing the use of this method to real scenarios where there would be a variable bathymetry.

The bathymetry is represented by a constant depth profile along the Y axis and a changing depth profile with a mild-slope along the X axis. A sketch representation of the mild-slope profile is shown in figure A.12. The slope starts at $x = 500$ with 10 meters of water depth and finishes at $x = 0$ with 5 meters of water depth. A dotted line has been drawn on top of next results from figure A.13 in order to represent the section along the domain corresponding to the profile.

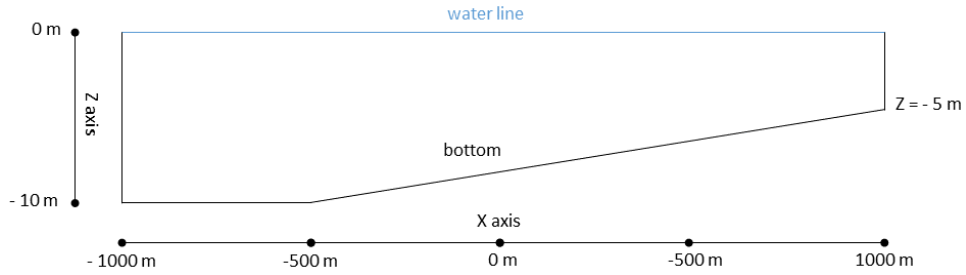

FIGURE A.12: Bathymetry profile along X axis.

First the waves are propagated throughout an empty domain (absence of WEC farm) where the significant wave height get transformed with the shoaling effect. The local significant wave height obtained at each grid cell along the empty domain is then used as the undisturbed significant wave height from the dividing term of the disturbance coefficient shown in equation (A.15). Results of the obtained K_d values are shown in figure A.13 for a state of $T_p = 8$ s.

Now the farm of 9 flaps is modelled and the waves are propagated throughout the domain with the same bathymetry profile from figure A.12. The undisturbed significant wave height used to obtain disturbance coefficient K_d locally for each grid cell is obtained in this case from the significant wave height corresponding to the empty domain case. Thus, when a changing depth bathymetry is considered, an empty domain case needs to be computed first to assess the significant wave height in the absence of WECs in order to evaluate correctly the wake effect of the WEC farm.

The upper plot of figure A.14 shows the disturbance coefficient obtained for the same sea state as the empty domain case. The lower plot shows the percent difference between the K_d values obtained with the mild-slope bathymetry and the case with a constant depth from figure A.9. The output shows good similarity in terms

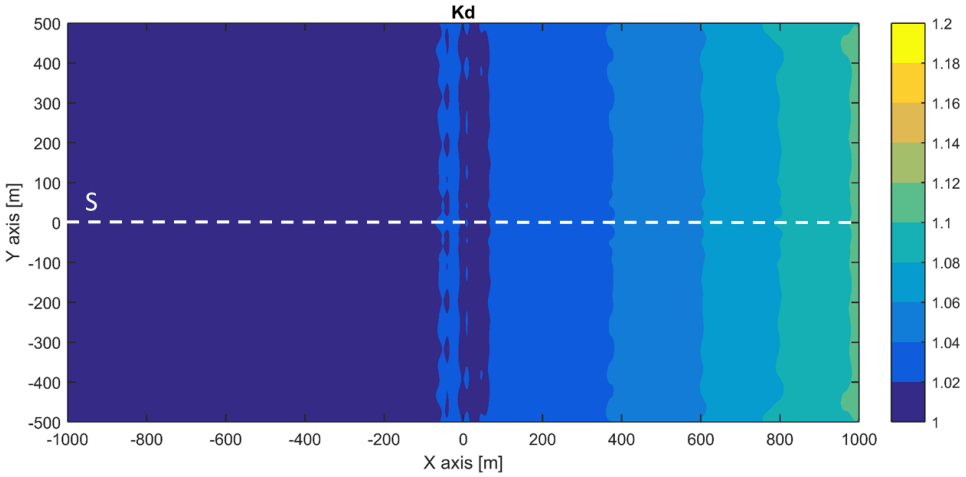

FIGURE A.13: Disturbance coefficient for an empty domain with a mild-slope bathymetry and $T_p = 8$ s.

of the disturbance coefficient areas with the same sheltering provided for both constant water depths or changing bathymetries. The percent difference plot shows that the maximum difference obtained remains bellow 3%, which is a negligible quantity. Therefore, based on this first approach the sheltering effect provided by a flap type WEC farm does not seem to be largely influenced by bathymetries with mild-slopes where the depth decreases progressively towards the wave propagation direction.

A.5 Discussion

The technique employed to represent a wave energy converter in a mild-slope equation model has shown to give an accurate representation of the wave field perturbation generated by a single device. The technique has been verified using output from NEMOH which has shown that the error reduces quickly as the distance from the device increases. Interaction effects between devices can play an important role for cases where the WECs are closely spaced and located at a distance in between themselves shorter than the error dissipation. In this case, a solution can be to represent the multiple device in NEMOH in order to account for the devices interactions in the target wave field, noting that this can be a computational time demanding task. The potential influence of the devices interactions was neglected in this study as a large enough separating distance has been left for the cases considered. However, a validation scenario where a farm of various WECs is modelled in NEMOH and compared against results from MILDwave would allow to define with more precision the minimum distance to leave until interaction effects are completely dissipated.

Following the validation of the single WEC modelling, wake effects of WEC farms were assessed for different scenarios changing the incident sea state conditions, the farm layout configuration, and the bathymetry. The results shown first that adding a second row of devices to a single row farm by blocking the gaps in between devices from the first row leads to a larger sheltered area and to a higher

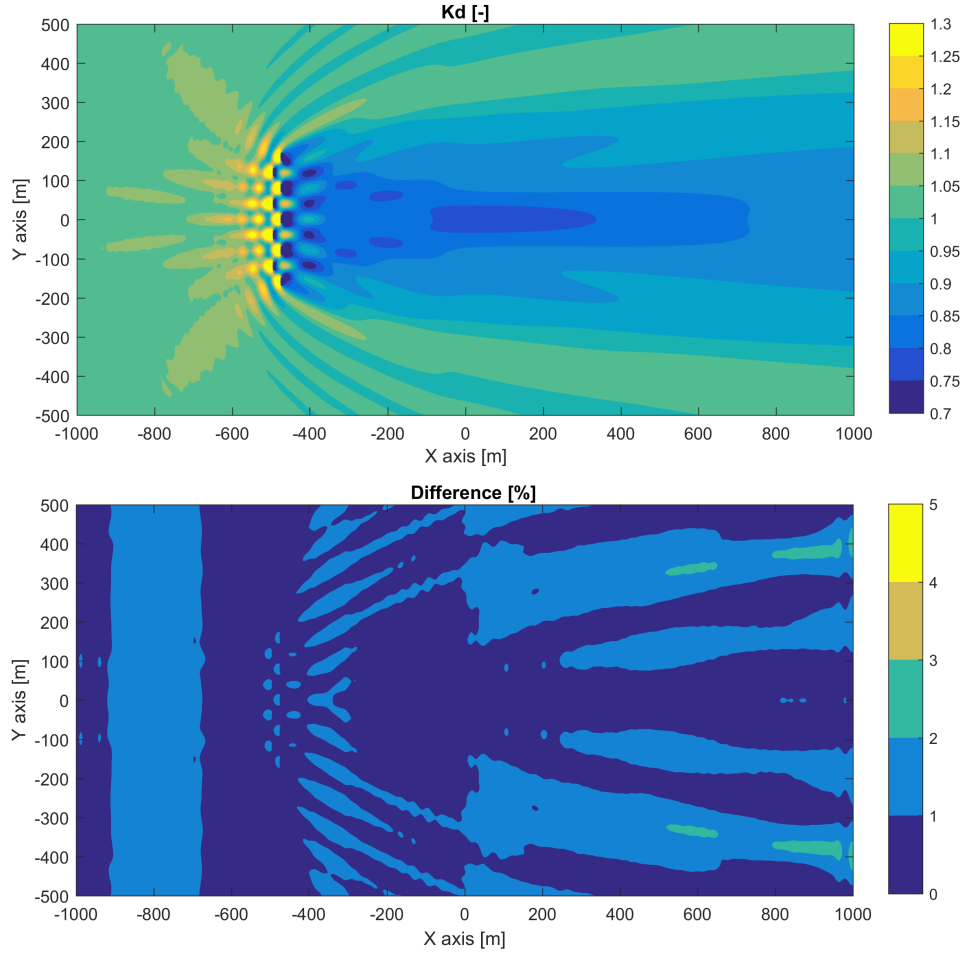

FIGURE A.14: 9 flaps farm and mild-slope bathymetry scenario for a $T_p = 8$ s. Top: Disturbance coefficient. Bottom: Percent difference with constant water depth case from fig. A.9.

significant wave height reduction in the lee of the farm. It is worthwhile to deploy the farms of flap type WECs following a scheme of two rows as it has been shown that the sheltering effect is increased and the devices from the second row can be exposed to higher energy density locations. In addition to this, deploying closely spaced devices in a farm allow for cabling cost reductions.

The influence between the wake effect and the distance separating the devices was proven with the largest reduction of the wave energy density found for the $4L$ spacing distance. The interaction of the individual wake effects of each device in the lee of the farm lead to a higher decrease of the minimum significant wave height values for a specific area. However, if the results are compared with a broader perspective, the areas with K_d values remaining under 0.9 (minimum of a 10 % significant wave height reduction) remain really similar.

The wake effect variability due to the incident sea state for the same farm configuration has been shown to be the most influencing variable. A large reduction of the significant wave height is found for the $T_p = 6$ s compared to the $T_p = 8$ s and $T_p = 10$ s. The lowest K_d value obtained for the $T_p = 6$ s case along the large area of

reduction is 0.62. The large difference between those cases is due to the diffraction phenomena becoming significant for small wave periods, due to the ratio between the wave length of the peak period and the flap length. The sheltered area changes significantly depending of which K_d value is set as the maximum value guaranteed in the area. Large sheltered areas are found for all sea states if a maximum $K_d = 0.9$ (minimum of a 10 % significant wave height reduction) is set as the limit whereas, if the maximum limit is set to $K_d = 0.7$ (minimum of a 30 % of significant wave height reduction), only sea states of $T_p = 6$ s can provide large sheltered areas.

Finally, the influence of the changing depth was assessed and it was found that for a progressively changing depth with a mild-slope the wake effect remains similar. The maximum difference with the constant water depth case was lower than 3%. It is important to notice that no dissipative processes such as wave breaking were applied. Approaching the end of the domain (right hand side) at the shallow water location the wake effect will probably be significantly influenced by wave breaking and this would lead to a higher reduction of the significant wave height at that location and therefore, to a higher difference with the constant water depth case. In addition, a real bathymetry where depth changes irregularly across both X and Y direction will lead do irregular variations in the undisturbed significant wave height along the domain and thus to a different shape of the wake effect.

A.6 Conclusion

It was found that changes in the layout of the WEC farm can lead to much larger significant wave height reductions on the lee side, particularly the distribution of the farm in two rows of WECs. By adapting the layout configuration of the farm to the sea state with the highest occurrence at the deployment location, notable improvements in the significant wave height reduction can be obtained. Achieving large sheltered areas in the immediate vicinity of the WECs, can benefit other marine activities such as offshore wind and aquaculture. For instance, offshore wind farms O&M weather windows can be increased and risks associated with turbines access can be reduced. Already the Floating Power Plant platform has demonstrated the benefit of reduced wave conditions on the lee side for operational activities. Aquaculture farms can benefit from a reduction on the hydrodynamic loads on the structures and increase the weather windows for the feeding activities. The method can effectively demonstrate the far field effects of a WEC array which is of particular concern at sites where there is surfing activity or when the farm is being located in a sensitive environmental area.

Finally as an overall conclusion, the methodology has demonstrated an improvement on the modelling techniques to represent WECs in wave propagation models. The accuracy of the target device reflection and transmission used to tuned its representation in the wave propagation model has been improved compared to previous studies. A 2D representation of the wave field disturbance generated by a WEC

has been used as a target information compared to the usual 1D wave field disturbance information from previous studies. In addition, the results have been validated against the target results with comparison plots for the near-field. Therefore, the methodology can represent realistic scenarios with WEC farms deployed at locations with irregular bathymetries where important wave transformation processes such as refraction, shoaling, reflection, transmission and diffraction intrinsically, occur.

A.7 Added section respect from the published version

This section adds complementary plots and work related to this publication that were not included in the published version. The error of the comparison between NEMOH and MILDwave was done for a single WEC case scenario, and in this section the error is computed for the WEC farm case scenario.

A.7.1 Error for the 9 flaps case

Section A.3 describes the implementation of a flap in MILDwave where Figure A.7 represents the wave solution compared to the NEMOH target wave field. Based on this implementation the wake effect for a farm composed of 9 flaps was then assessed in Section A.4. The 9 flaps were represented by the same obstacle cells configuration related to the corresponding sea state and were replicated along the domain in order to represent a farm of 9 devices. This section shows a comparison of the 9 flaps case modelled in MILDwave for constant water depths in Figure A.9 against the same case modelled in NEMOH where all interactions are taken into account.

Figure A.15 shows the disturbance coefficient obtained in MILDwave (top-left), in NEMOH (top-right), and the error of MILDwave against NEMOH (bottom) for a sea state of T_P = 8 s. The MILDwave solution comes from Figure A.9 where only the area of 1000 x 1000 m surrounding the WEC farm was considered. Then the NEMOH solution was obtained as a superposition of the different wave components where the 9 flaps were modelled intrinsically and therefore all interactions were considered. Each regular wave was obtained based on the diffracted and the radiated wave solution for each device affected by the presence of the surrounding flaps. From the regular waves solution an irregular sea state was computed as a superposition of these in the same way it was done in Section A.3.3 for a single flap.

The error plot from Figure A.15 shows high errors in the near field surrounding the device and specially in the inner part of the farm. The error decreases when moving towards to far-field but still values close to 10% are found in the lee side of the farm and error values close to 20% appear at specific locations in the up-wave area in front of the farm. The aim of this plot is to compare it with the error plot from Figure A.7 where only one flap was modelled in MILDwave and compared against NEMOH. In the case of a single flap, the device is not affected by any neighbouring

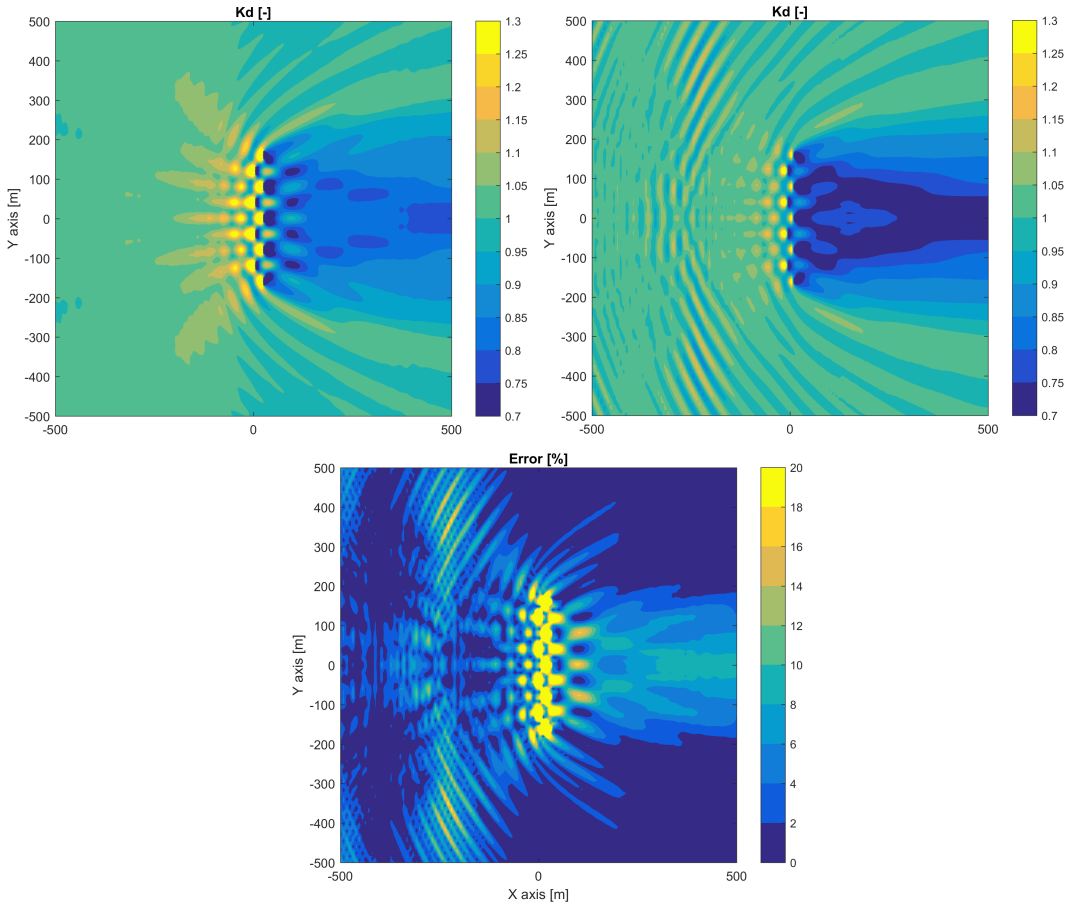

FIGURE A.15: Disturbance coefficient comparison for a 9 flaps farm and a sea state of T_p = 8 s. Top-left: MILDwave results. Top-right: NEMOH results. Bottom: Error difference.

device and therefore the interactions with other devices are not present. The error plot for the case of the 9 flaps farm shows that when interactions with other devices are present the representation of WECs as separated obstacles presents high limitations due to a lower accuracy in the results, even if it has been previously accurately tuned as a single device.

A solution to this would be to model the whole farm as one single group of obstacle cells and tune it against NEMOH solutions where the whole farm has been modelled considering all interactions. When all interactions are properly modelled the disturbance coefficient appear to be much lower down-wave of the farm. Thus, the sheltering effect of a flap type WEC farm has the potential to be be higher than the results assessed in the main body of this publication.

Acknowledgement

The research leading to these results is part of the OceaNET project, which has received funding from the European Union's Seventh Framework Programme for research, technological development and demonstration under grant agreement no

607656.

References

[1] Borgarino, B., Babarit, A., Ferrant, P.: 'Impact of wave interactions effects on energy absorption in large arrays of wave energy converters', Ocean Eng., 2012, 41, pp. 79–88

[2] Mcnatt, J.C., Venugopal, V., Forehand, D.: 'A novel method for deriving the diffraction transfer matrix and its application to multi-body interactions in water waves', Ocean Eng., 2014, 94, pp. 173–185

[3] Smith, H.C.M., Pearce, C., Millar, D.L.: 'Further analysis of change in nearshore wave climate due to an offshore wave farm: An enhanced case study for the wave hub site', Renew. Energy, 2012, 40, (1), pp. 51–64

[4] Astariz, S., Abanades, J., Perez-Collazo, C., et al.: 'Improving wind farm accessibility for operation & maintenance through a co-located wave farm: influence of layout and wave climate', Energy Convers. Manag., 2015, 95, pp. 229–241

[5] Beels, C., Troch, P., De Backer, G., et al.: 'Numerical implementation and sensitivity analysis of a wave energy converter in a time-dependent mild-slope equation model', Coast. Eng., 2010, 57, (5), pp. 471–492

[6] Beels, C., Troch, P., De Visch, K., et al.: 'Application of the time-dependent mild-slope equations for the simulation of wake effects in the lee of a farm of Wave Dragon wave energy converters', Renew. Energy, 2010, 35, (8), pp. 1644–1661

[7] Folley, M., Babarit, A., Child, B., et al.: 'A review of numerical modelling of wave energy converter arrays'. Proc. 31st Int. Conf. on Ocean, Offshore and Arctic Engineering, Rio de Janeiro, Brazil, July 2012, pp. 535–545

[8] Babarit, A., Delhommeau, G.: 'Theoretical and numerical aspects of the open source BEM solver NEMOH'. Proc. 11th European Wave and Tidal Energy Conf., 2015, pp. 1–12

[9] Troch, P., Stratigaki, V.: 'Phase-resolving wave propagation array models', in Foley, M. (Ed.): 'Numerical modelling of wave energy converters: state-ofthe- art techniques for single devices and arrays' (Elsevier, 2016,) pp. 191–216

[10] Troch, P.: 'MILDwave – a numerical model for propagation and transformation of linear water waves'. Internal Report, Department of Civil Engineering, Ghent University, 1998

[11] Radder, A.C., Dingemans, M.W.: 'Canonical equations gravity waves, weakly nonlinear gravity waves', Wave Motion, 1985, 7, pp. 473–485

[12] Lee, C., Suh, K.D.: 'Internal generation of waves for time-dependent mildslope equations', Coast. Eng., 1998, 34, (1-2), pp. 35–57

[13] Lee, C., Kim, G., Suh, K.D.: 'Extended mild-slope equation for random waves', Coast. Eng., 2003, 48, (4), pp. 277–287

[14] Zhao, H.t., Sun, Z.L., Hao, C.L., et al.: 'Numerical modelling on hydrodynamic performance of a bottom-hinged flap wave energy converter', China Ocean Eng., 2013, 27, (1), pp. 73–86

[15] Sarpkaya, T., Isaacson, M.: 'Mechanics of wave forces on offshore structures' (Van Nostrand Reinhold Co., 1981)

Appendix B

Paper B

The modelling of a flap type wave energy converter in a time-dependent mild-slope equation model

Published in

Progress in Renewable Energies Offshore – Guedes Soares (Ed.)

Authors

Nicolas Tomey-Bozo[1], Jimmy Murphy[1], Peter Troch[2], Aurélien Babarit, Tony Lewis[1], Gareth Thomas[4]

[1]*MaREI Centre (ERI), University College Cork, Haulbowline Road, Ringaskiddy, Ireland*

[2]*Department of Civil Engineering, Ghent University, Zwijnaarde, Belgium*

[3]*Ecole Centrale de Nantes – CNRS, 1 rue de la Noé, 44300 Nantes, France*

[4]*School of Mathematical Sciences, University College Cork, Cork, Ireland*

Abstract

The accurate modelling of the wave field distribution around Wave Energy Converters (WECs) has been a relevant subject of research in the recent years. A considerable amount of works has studied arrays of WECs employing methodologies such as Boundary Element Methods (BEMs) based on potential flow or wave propagation models. This study presents an investigation on the modelling of the perturbed wave field by a flap type WEC in a time-dependent mild-slope equation model. The capability of modelling the diffracted wave intrinsically in the mild-slope equation model and the implementation of a coupling technique with a BEM are shown. In the last section a representation of the flap by applying the sponge layer technique is carried out. The understanding of all these techniques with their advantages and disadvantages is relevant for a further development of the wave field modelling. The improvement of the state of the art would allow to quantify more accurately the wake effect of a WEC farm.

B.1 Introduction

Several types of models have been employed up to date to quantify the effect of WECs on the incoming wave climate. BEM based on linear waves are the most common application to solve near field effects and farm interactions (Borgarino et al. 2011). For large domains an extensive use of wave propagation models has been done using either phased averaged models or phase-resolved models (Smith et al. 2012, Beels et al. 2010a). The usual implementation of these models is undertaken by representing the WECs as sink and sources coefficients or as absorption coefficients where their values are calibrated against a device-dependent data base of reflection and transmission coefficients. CFD models have been applied but are seldom used due to their limitations to modelling very local phenomenon. An over-view of this subject can be found in Folley et al. (2012).

As a relatively novel subject of research some studies have developed coupling methodologies in order to improve the accuracy by considering all waves component created by the WEC (Beels 2009, Babarit et al. 2013, Charrayre et al. 2015). The techniques consist of merging the results from BEM solvers into phase-resolved models based on the mild-slope equation. This allows for the combination of the accurate solving at the local scale of the wave-body interaction problem in a BEM with the wave propagation along large domains represented in a mild-slope equation model. Recent applications are capable of solving large grid domains within a relatively low computational time while permitting the representation of irregular bathymetries or dissipation effects such as wave breaking or bottom friction. However up to date only heaving buoys type WECs have been considered which are not the most wave intrusive device.

In this study an investigation on the modelling of a flap type WEC in a time-dependent linear mild-slope model (known as MILDwave) for regular waves is shown. The better understanding of the modelling of the wave energy absorbed by a WEC and the disturbed wave field caused by its presence is the motivation of this work. This will allow for further investigations of the quantification of the wake effect produced by a farm of WECs. The core of the work focuses on the implementation of the flap type WEC by applying various techniques and obtaining the perturbed wave field. First the perturbed wave field is calculated by dividing it into the diffracted component and the radiated component. In order to achieve this objective a combination of the intrinsic MILDwave feature to solve the diffracted wave and a coupling technique with the open-source BEM solver NEMOH (Babarit, A. & Delhommeau, G. 2015) to obtain the radiated wave is applied. A comparison with results obtained unique-ly from NEMOH are presented.

Then a shorter section shows the implementation of the same flap type WEC employing exclusively MILDwave by applying the sponge layer technique (SLT) described in Beels et al. (2010b). This technique consists of a representation of the WEC as a combination of absorption coefficients tuned in such a way that the wave pattern due to reflection and transmission of the wave energy matches specified target values.

B.2 Environment Description

B.2.1 Wave-body interaction problem

NEMOH allows the calculation of the perturbed wave field caused by the presence of the WEC from the perturbed velocity potential obtained by solving the well-known linear wave-body interaction boundary value problem. The perturbed potential is solved by dividing the problem into one diffraction problem and six radiation problems, one for each degree of freedom. Thus the total velocity potential (ϕ_t) can be described as a superposition of the incident potential (ϕ_i) and the solution of the diffracted and radiated potential (ϕ_d and ϕ_r):

$$\phi_t(x, y, z) = \phi_i + \phi_d + \sum_{n=1}^{6} \phi_r \tag{B.1}$$

Then from the potential at the free surface condition the free surface elevation is calculated straight-forward as:

$$\eta(x, y) = \frac{i\omega}{g} \Phi(x, y) \tag{B.2}$$

where ω is the wave frequency, g the gravitational acceleration, and Φ the potential without depth dependence ($z = 0$).

B.2.2 Mild-Slope Equations

MILDwave was developed at Ghent University by Troch (1998) and is based on the depth-integrated mild-slope equations of Radder and Dingemans (1985). This code solves the propagation of surface waves through the domain and the interaction with the obstacles previously defined. The velocity potential $\phi(x, y, t)$ and the instantaneous surface elevation $\eta(x, y, t)$ at the free water surface are the variables solved for each coordinate of the grid (x, y) for each instant of time t by the set of differential equations given in Equation (B.3) and (B.4):

$$\frac{\partial \eta}{\partial t} = B_c \Phi - \nabla \Delta (A_c \nabla \phi) \tag{B.3}$$

$$\frac{\partial \Phi}{\partial t} = -g\eta \tag{B.4}$$

where

$$B_c = \frac{\omega^2 - k^2 C C_g}{g} \tag{B.5}$$

$$A_c = \frac{C C_g}{g} \tag{B.6}$$

with the phase velocity C and the group velocity C_g for a wave with wave number k.

B.2.3 Flap type wave energy converter

The WEC is a surface piercing flap hinged at the bottom of the seabed as Figure B.1 shows and its main characteristics are described in Table B.1.

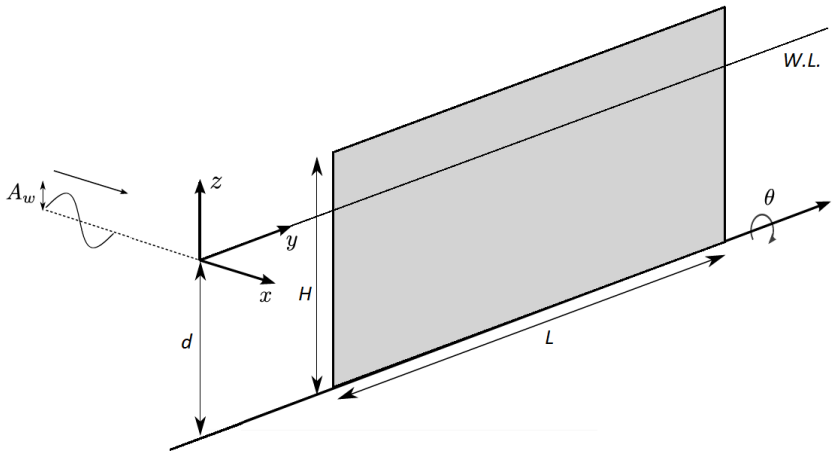

FIGURE B.1: Description sketch of the flap type WEC.

where ρ_r represent the density relative to sea water.

TABLE B.1: Main characteristics of the flap type WEC.

Parameter	Coefficient	Value	Units
Length	L	20	m
Height	H	12	m
Thickness	t	1	m
Relative density	ρ_r	0.3	-

Its motion is restricted to pitch therefore only one degree of freedom is considered. In order to quantify the non-dimensional radiated wave obtained from NEMOH the motion of the flap is calculated as described in Equation B.7:

$$\theta(\omega) = \frac{A_w \Gamma(\omega)}{-\omega^2(I + A_r) - i\omega(B_r + B_{pto}) + (H + K_{pto})} \tag{B.7}$$

where A_w is the wave amplitude, Γ the wave excitation moment coefficient, I the moment of inertia about the Y axis, A_r the added moment of inertia coefficient, B_r the radiation damping coefficient, H the hydrostatic restoring coefficient, and B_PTO and K_PTO the PTO damping and spring coefficient. The PTO coefficients are tuned for each wave frequency as described in Equation (B.8) and (B.9):

$$B_{pto}(\omega) = B(\omega) \tag{B.8}$$

$$K_{pto}(\omega) = \omega^2(I + A_r) - H \tag{B.9}$$

The water depth is considered to be 10 meters and the bathymetry is constant along the whole domain.

B.3 WEC Modelling Accounting for All Wave Components

The perturbed wave field is solved in this section as a sum of the diffraction and radiation components. Only the diffracted wave from the perturbed wave field from a floating body can be intrinsically solved in MILDwave. Thus it is necessary to first show the capability of MILDwave in resolving the diffraction for a surface-piercing flap. Then the radiated wave field is solved in MILDwave by applying the coupling technique with the results obtained from the radiation problem in NEMOH.

All results are compared against the surface elevation obtained from NEMOH and plotted for a domain of $6x6$ wave lengths. The surface elevation is described by the module and phase from its complex form and it is assumed the incident wave propagates towards the X positive axis. For comparison purposes the surface elevation in MILDwave is saved at a certain instant of time t which is a multiple of

the wave period. This allows the comparison to be made with the surface elevation obtained from NEMOH in the frequency domain.

B.3.1 Diffracted wave in MILDwave

The flap is represented in MILDwave as a set of obstacle cells occupying the same length than the de-vice with the absorption coefficient set to 0 (fully reflective obstacle). The diffracted wave is calculated by subtracting the surface elevation obtained in an empty domain (absence of a WEC) to the surface elevation obtained in the presence of the flap.

The diffracted wave field obtained for an incident wave of period 8 s and unit of amplitude is shown in Figure B.2. Left figures are obtained from MILDwave and right figures from NEMOH. The module plots show some discrepancies while the phase plots match entirely. Then Figure 3 shows two sections of the surface elevation module indicated in Figure B.3 as $S1$ and $S2$ in order to facilitate the comparison. Higher values for the MILDwave results appear in the up-wave field of section $S1$ due to a larger reflection. However, for the down-wave field the matching appears to be better. Section $S2$ shows a higher agreement for the sides of the domain.

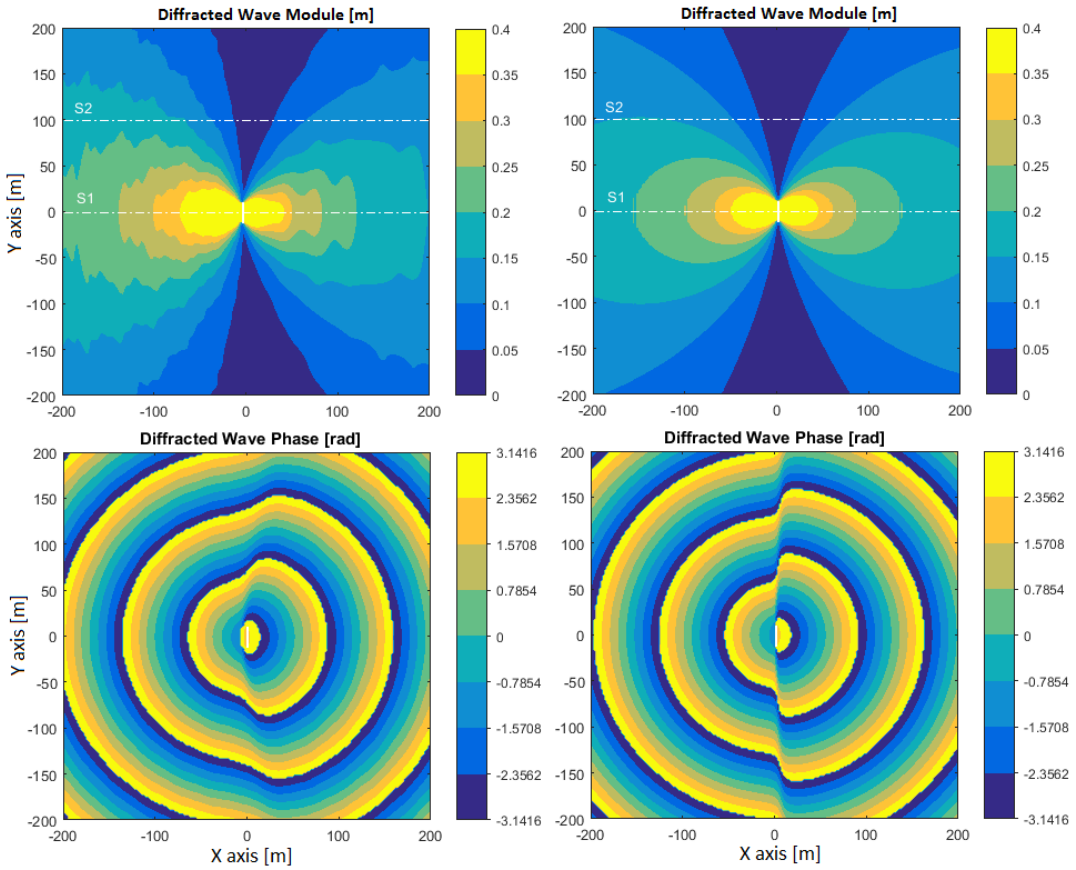

FIGURE B.2: Module (m) and phase (rad) of the complex surface elevation for the diffracted wave. Left figures correspond to results obtained from MILDwave and right figures from NEMOH.

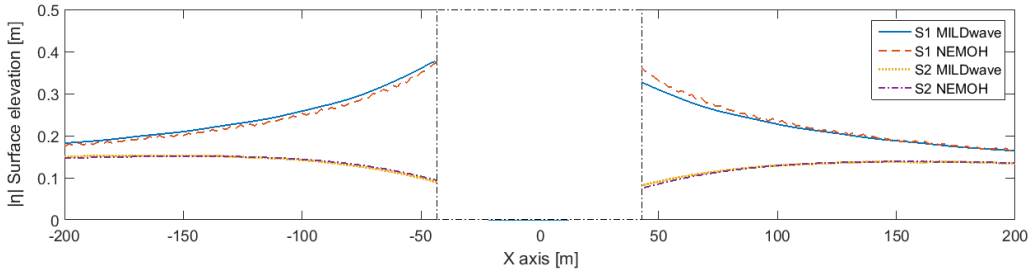

FIGURE B.3: Module (m) of the surface elevation for the diffracted wave for sections $S1$ and $S2$ along the X axis showing results obtained from MILDwave and NEMOH.

B.3.2 Radiated wave with the coupling technique

The propagation of the radiated wave by the flap under an incident wave of period 8s and unit of amplitude is studied in this section. The radiated wave is defined by imposing an internal circular wave generation line surrounding the device at a defined distance from its centre. Then the wave propagates throughout the domain on the same manner as the radiated wave created by the motion of the device. A definition sketch of the methodology is shown in Figure B.4.

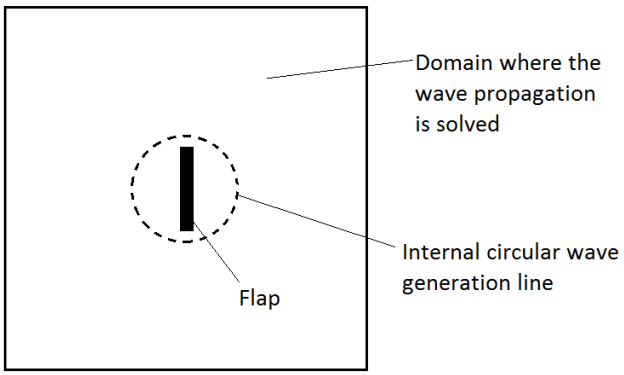

FIGURE B.4: Definition sketch of the coupling technique.

The generation line is defined from the complex surface elevation (module and phase) obtained as a solution of the radiation problem from NEMOH at the location of the circular line. In order to obtain the expected propagation of the radiated wave through the domain a set-up of the internal wave generation line needs to be done as described in Beels (2009).

The generation line is defined by a discretisation of grid generation points i determined by a radius distance r to the centre of the domain (x_C, y_C) and an angle interval Δb as presented in Figure B.5. In each generation point an additional surface elevation is imposed in MILDwave as defined in Equation (B.10):

$$\eta^* = 2|\eta_N|\frac{C_e \Delta t}{\Delta x} \tag{B.10}$$

where $|\eta_N|$ represents the module of the surface elevation obtained from NEMOH, C_e the energy velocity, Δt the time step, and Δx the grid cell size.

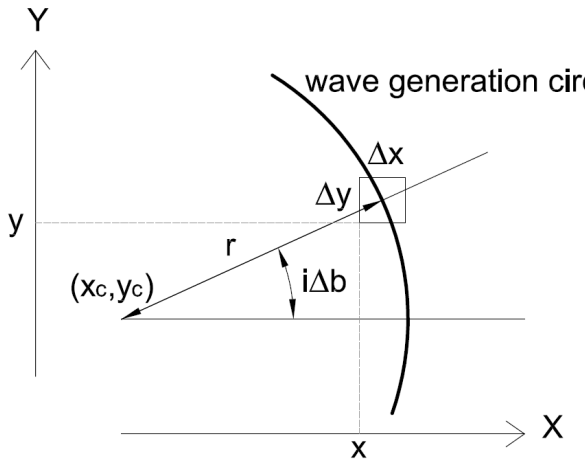

FIGURE B.5: Definition sketch of the internal wave generation line set-up [65].

Taking this into account Figure B.6 shows the radiated surface elevation obtained for a wave generation situated at a 20 m distance from the centre together with the surface elevation obtained from NEMOH. Half a wave length distance from the WEC is needed in order to obtain a stabilised wave field, thus the near field is replaced by a circle covering this surface. Both the module and the phase obtained with the coupling technique show accurate results and match entirely the results from NEMOH. In order to facilitate the comparison Figure B.7 shows the module of the surface elevation for the two sections indicated in Figure B.6 as $S1$ and $S2$.

B.3.3 Total wave field

Some limitations can be found under certain circumstances to solve the diffracted wave intrinsically in MILDwave. The representation of the WEC is limited to a set of cells that have a restricted size according to the considered wave length. Thus, depending on the wave and WEC it might be a more suitable option to apply as well the coupling technique to obtain the diffracted wave field.

The surface elevation for the total wave field (incident + diffracted + radiated) has been calculated considering the two different options to solve the diffracted wave, intrinsically in MILDwave and with the coupling technique. Figure B.8 shows the module of the complex surface elevation for the total wave field for three different wave periods. Left and middle figures represent the solution obtained with the diffracted wave solved intrinsically in MILDwave and employing the coupling technique respectively. Right figures show the solution from NEMOH as a target for comparison.

It is possible to observe that the two techniques give satisfactory results for all wave periods. Slight discrepancies appear down-wave when using the intrinsic feature of MILDwave to solve the diffracted wave. This is partly due to the difficulty of

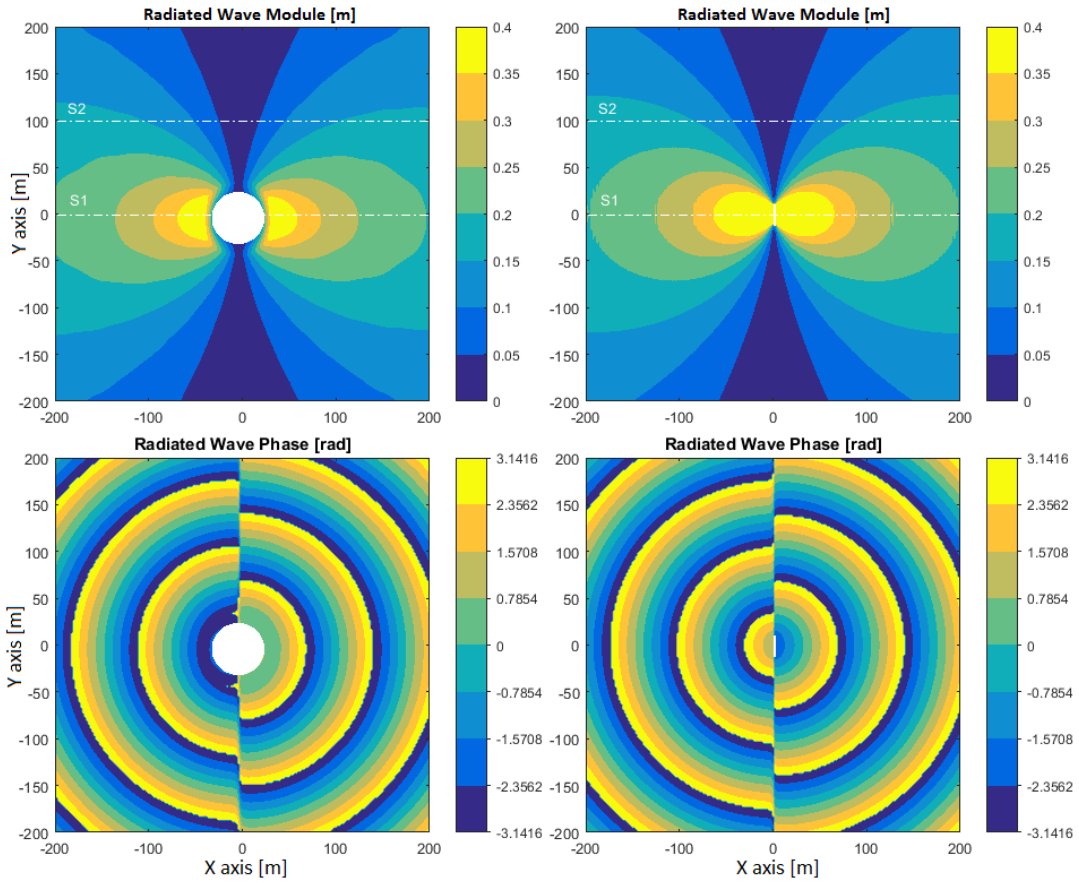

FIGURE B.6: Module (m) and phase (rad) of the complex surface elevation for the radiated wave. Left figures correspond to results obtained from MILDwave employing the coupling technique and right figures to results obtained from NEMOH.

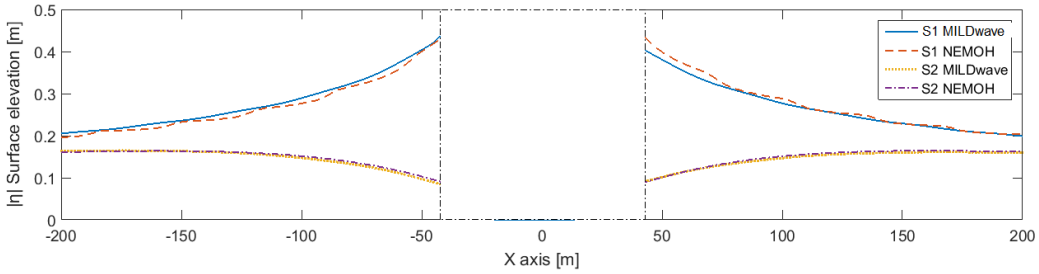

FIGURE B.7: Module (m) of the surface elevation for the radiated wave for sections $S1$ and $S2$ along the X axis showing results obtained from MILDwave employing the coupling technique and results obtained from NEMOH.

representing the one meter thickness of the flap due to the minimum size of the grid cell.

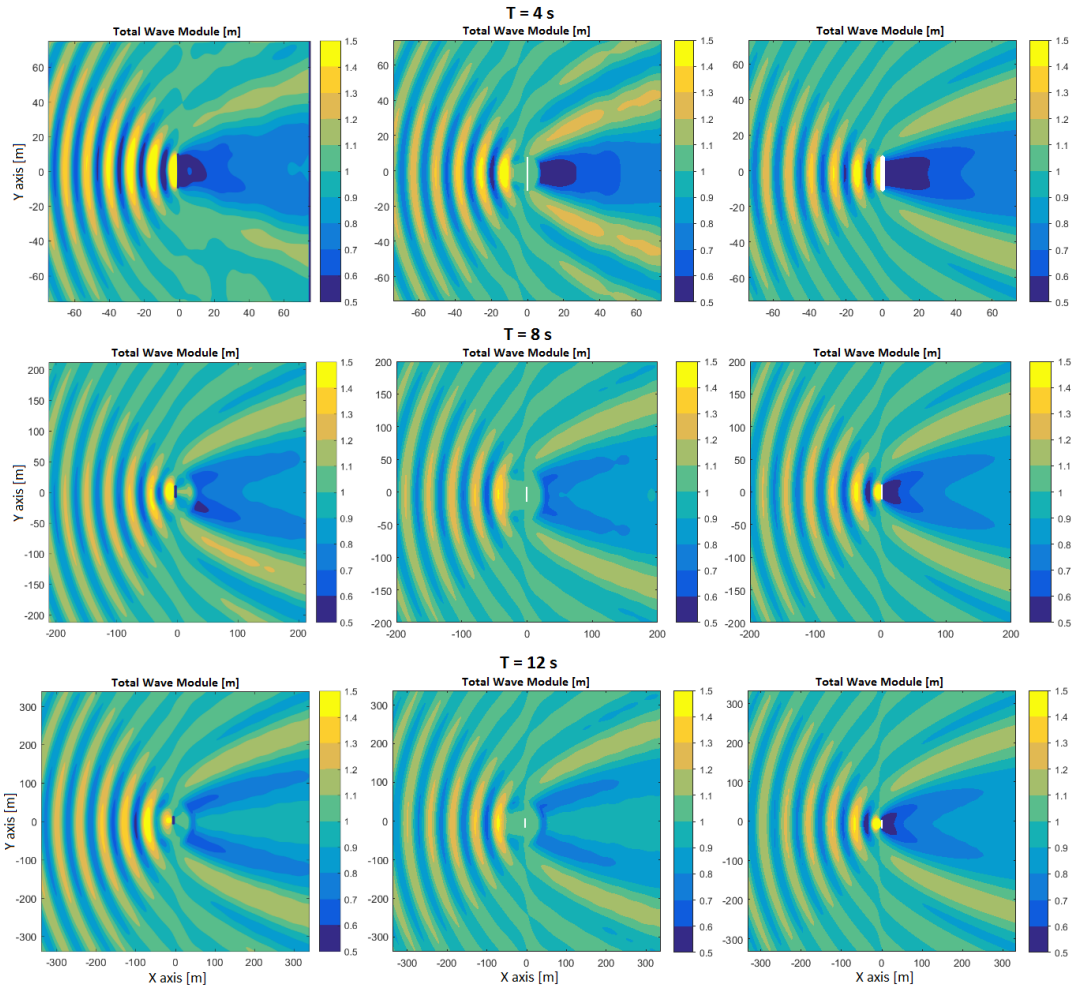

FIGURE B.8: Total wave field for different wave periods (T) accounting for all wave components. Left figures show MILDwave results combining diffraction obtained intrinsically and radiation with the coupling technique. Middle figures show MILDwave results with diffraction and radiation obtained with the coupling technique. Right figures show results obtained from NEMOH.

B.4 WEC Modelling with the Sponge Layer Technique (SLT)

The SLT modelling is achieved by representing the presence of the device as a group of obstacle cells that have an attributed absorption coefficient value. The absorption coefficient locally affects the surface elevation of the propagated wave by multiplying it by values in the range from 1 to 0. Values equal to 1 represents a water cell (no absorption) and then the lower the value the more energy the obstacle absorbs, being 0 a fully reflective obstacle.

The absorption coefficients are tuned in such a way that the perturbed wave field matches the reflection and transmission target values. In this section the target values have been set equal to the disturbed wave field obtained from NEMOH in order to evaluate the difference obtained when accounting for all components (as in the previous section) and when applying the SLT.

The set-up of the SLT requires empirical tuning of the obstacle cells values by

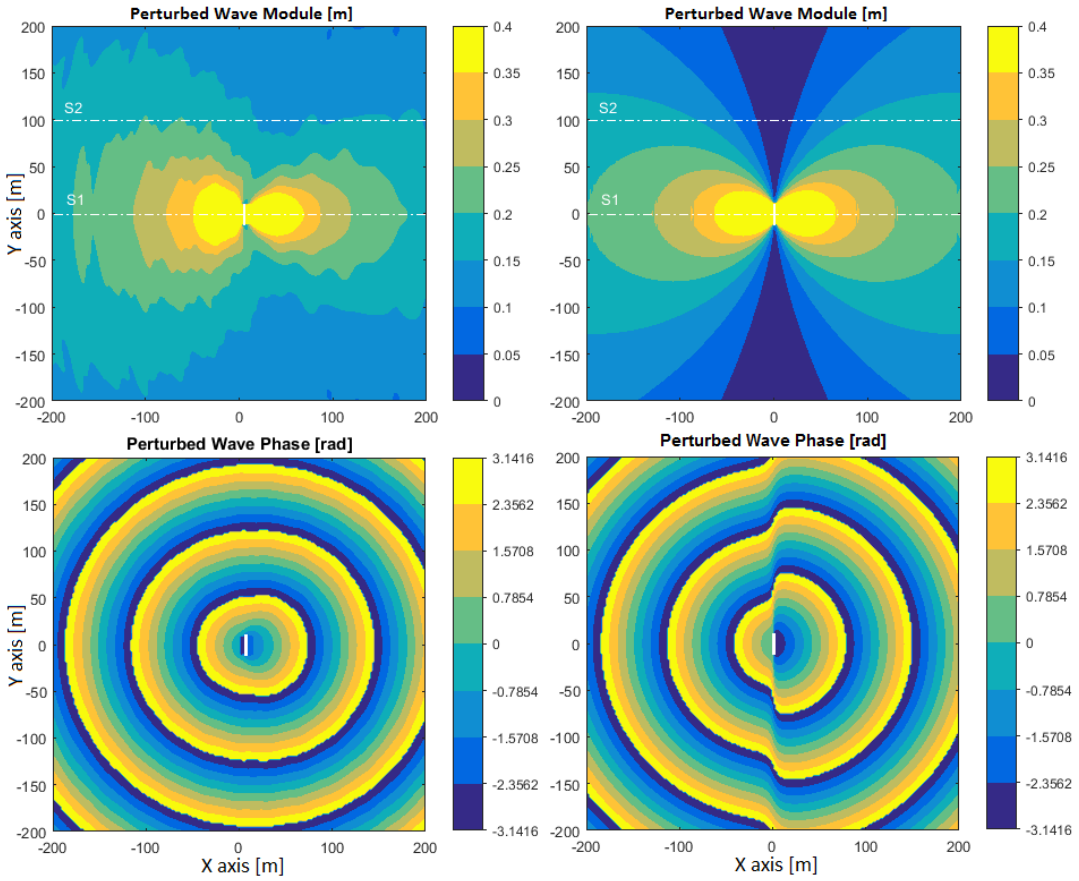

FIGURE B.9: Module (m) and phase (rad) of the complex surface elevation for the perturbed wave. Left figures correspond to results obtained from MILDwave employing the sponge layer technique and right figures results obtained from NEMOH.

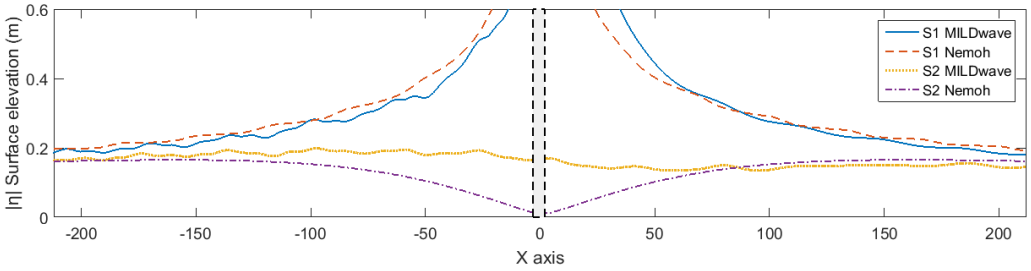

FIGURE B.10: Module of the surface elevation for the perturbed wave for sections $S1$ and $S2$ along the X axis showing results obtained from MILDwave employing the sponge layer technique and results obtained from NEMOH.

changing their distribution function. Figure B.9 shows the surface elevation for the perturbed wave field created under an incident wave of period 8 s and unit amplitude. The perturbed wave field is obtained from MILDwave by applying the SLT (for the left figures) and from NEMOH as a sum of the diffraction and radiation component (for the right figures). The MILDwave plots are obtained by subtracting the surface elevation obtained in an empty domain from the surface elevation obtained

in the presence of the obstacles cells representing the flap. As a first approximation the tuning has been done to reach the target reflection and transmission values of the perturbed wave field along section $S1$. Again Figure B.10 shows the module of the surface elevation for sections $S1$ and $S2$ indicated in Figure B.9 in order to facilitate the comparison of results.

It can be observed that the module matches accurately the target values for section $S1$ but towards the sides of the domain (section $S2$) more discrepancies are found with larger values obtained in the module when employing the SLT. Then the phase of the surface elevation matches the target in the up-wave section while in the down-wave section there is a shift of π radians. This difference is mainly due to the asymmetry in the motion of the flap which is not considered when applying the SLT.

B.5 Discussion

The surface-piercing flap was considered in order to evaluate the performance of MILDwave to compute the diffracted wave, which is theoretically limited to such devices. Nevertheless, a submerged flap can be accurately modelled by solving the complete perturbed wave field applying the coupling technique, in the same way it is was done for the surface-piercing flap.

The coupling technique has shown to provide as accurate results as the ones obtained purely from a BEM. However further work needs to be done to obtain a look up table in order to input the internal wave generation line directly with the right discretisation so as to avoid empirical tuning.

The accuracy of the perturbed wave field obtained from the SLT could be improved with further work in the definition of the absorption coefficients and thus achieve results matching completely the module values and differing only in the phase values.

B.6 Conclusion

Solving the perturbed wave field accounting for all wave components gives a more realistic definition than applying the SLT, particularly for non-heaving devices where there is half a cycle shift in the phase between the sides of the device. However, its application to a farm of several devices and irregular sea states leads to difficult calculations due to the many wave components to consider. Various devices involve accounting for interaction wave components and an irregular sea state for all the present frequencies. An intermediate solution to reduce complexity is to compute all the interaction wave components within the BEM and apply the coupling technique considering the whole farm inside the circular wave generation line.

However, as perturbed waves get dissipated relatively quickly with the distance to the WEC it might be enough to estimate the wake effect with a proper-ly calibrated sponge layer when considering a largely spaced WECs farm. It is still an

open subject of discussion as to which values should be taken as a tar-get for the calibration.

B.7 Added section respect from the published version

This section adds complementary plots and work related to this publication that were not included in the published version. First the optimum angle interval for the discretisation of the wave generation line is investigated and then errors plots are shown for the comparisons from previous Sections B.3.2, B.3.1, and B.4.

B.7.1 Optimum angle interval

Previous Section B.3.2 details how the internal circular wave generation line was described in MILDwave in order to represent the radiated wave generated by the flap. Figure B.5 shows how the generation line was set-up based on a discretisation of the angle interval Δb that depends on the radius distance r defining the circle size. Figure B.11 below shows the work that was carried out to obtain the right value of Δb for the results shown in Figure B.6 where a value of r equal to 20 m was used.

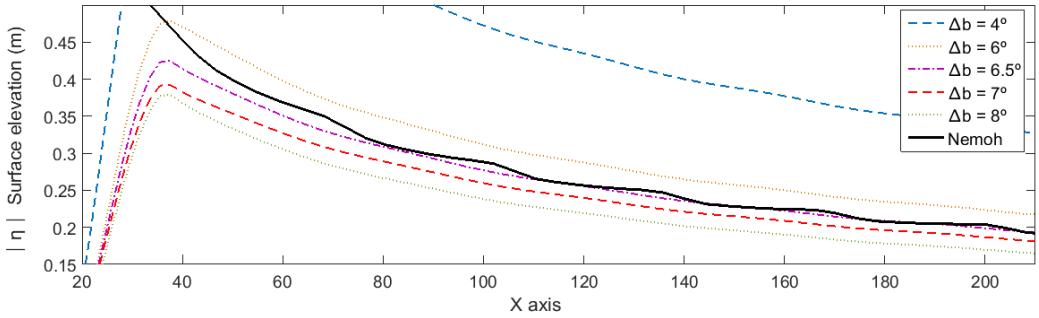

FIGURE B.11: Module of the complex surface elevation for the radiated wave for r = 20 m and several Δb intervals.

The same radiated wave from Figure B.5 was generated using different Δb values with the aim of obtaining the target values from NEMOH. Figure B.11 shows the module of the complex surface elevation obtained in MILDwave along section $Y = 0$ for the same domain of 400 x 400 m and for values of Δb ranging from $4°$ to $8°$. Only half of the domain is shown from X = 20 m to X = 200 m due to the symmetry of the results along section $Y = 0$. The target radiated wave amplitude from NEMOH is represented as a continuous line in the plot. The angle interval Δb equal to $6.5°$ shown to give the best match for the case of r = 20 m and therefore was chosen as the optimal value to generate the radiated wave from Figure B.6.

Figure B.12 shows the optimal angle interval obtained for r values ranging from 15 to 30 m on the same way it was done for Figure B.11. As expected the results show that the larger the radius distance the smaller has to be the angle interval since

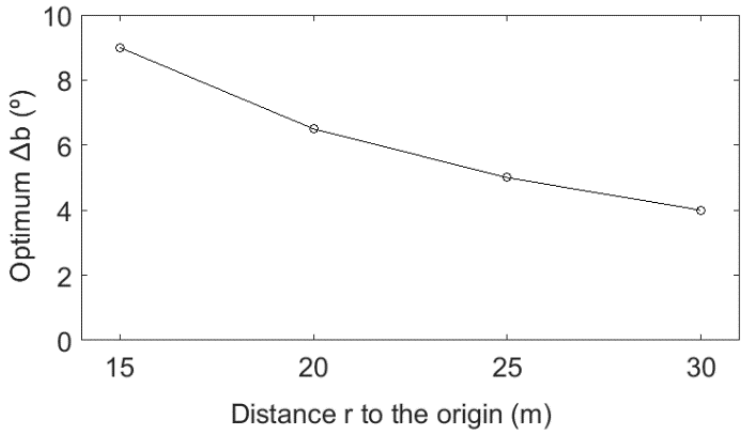

FIGURE B.12: Optimum angle interval Δb defining the circular wave generation line for each distance r to the centre of the domain.

more points are needed to discretise the circular line and replicate the same radiated wave. However, due to the reflection generated by the inner sponge layer the relation between the optimal angle interval and the grid cell size was not proportional. This led to gaps needed in the generation line discretisation making the line not continuous.

B.7.2 Error plots

The plots from this section show the error obtained for the cases shown in Figures B.2, B.6, and B.9 (from Sections B.3.1, B.3.2, and B.4 respectively) where comparisons with NEMOH were carried out for a diffracted wave intrinsically computed in MILDwave, a radiated wave computed with the CT, and a perturbed wave modelling the flap intrinsically in MILDwave with the SLT. The error is calculated based on Equation (B.11) where A_N represents the wave amplitude obtained from NEMOH, A_M the wave amplitude obtained from MILDwave, and A_i the incident wave amplitude which equal to 1 in this case.

$$\epsilon(\%) = \frac{A_N - A_M}{A_i} \tag{B.11}$$

Figure B.13 shows the error between the diffracted wave amplitude obtained intrinsically in MILDwave and the diffracted wave amplitude obtained in NEMOH (see Figure B.2). In this case the flap was modelled as a fully reflective obstacle. The error plot shows a good agreement in the down-wave section with error values below 2% while the up-wave section of the domain presents much higher discrepancies. The results show that for the case of a flap modelled as a group of obstacle cells the diffraction phenomenon is well represented even though the reflection is slightly over estimated.

Figure B.14 shows the percentage error between the radiated wave amplitude obtained in MILDwave and the radiated wave amplitude obtained in NEMOH (see Figure B.6). The radiated wave was obtained in MILDwave by implementing the

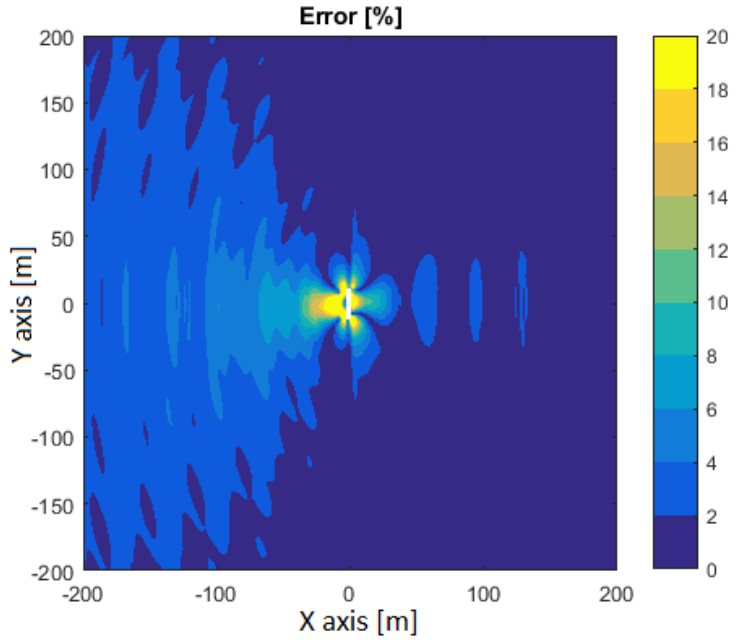

FIGURE B.13: Percentage error between the diffracted wave computed intrinsically in MILDwave, and NEMOH results (see Figure B.2).

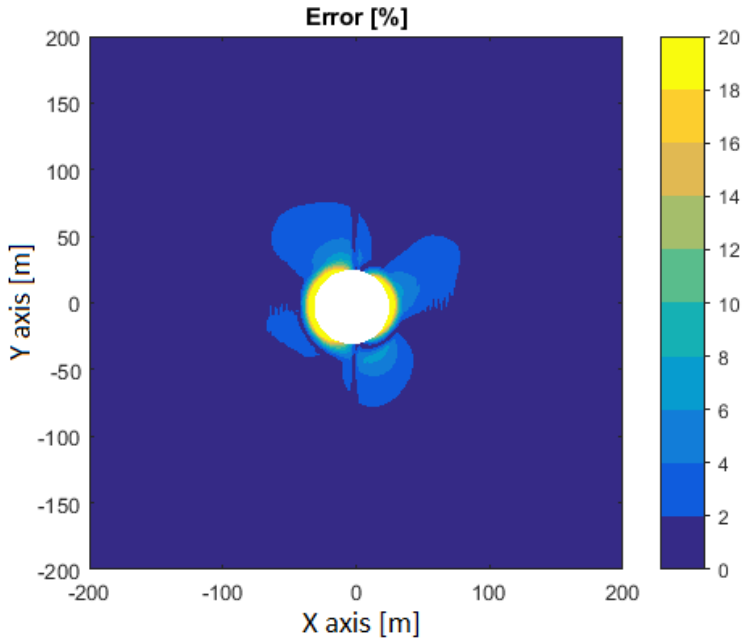

FIGURE B.14: Percentage error between the radiated wave computed in MILDwave with the CT, and NEMOH results (see Figure B.6).

coupling technique described in Section B.3.2. The plot shows a small error that decreases with the distance to the WEC remaining under 4% for a distance higher than 30 m from the boundary (wave generation line). However, still some discrepancies are found and the non-symmetry of the error shows that the coupling technique is

not completely consistent. The way the coupling between the two solvers is implemented in this work still needs some improvements. A more consistent technique is needed for the generation of internal waves (from the centre of the domain towards to sides) to represent the perturbed wave generated by a WEC in MILDwave.

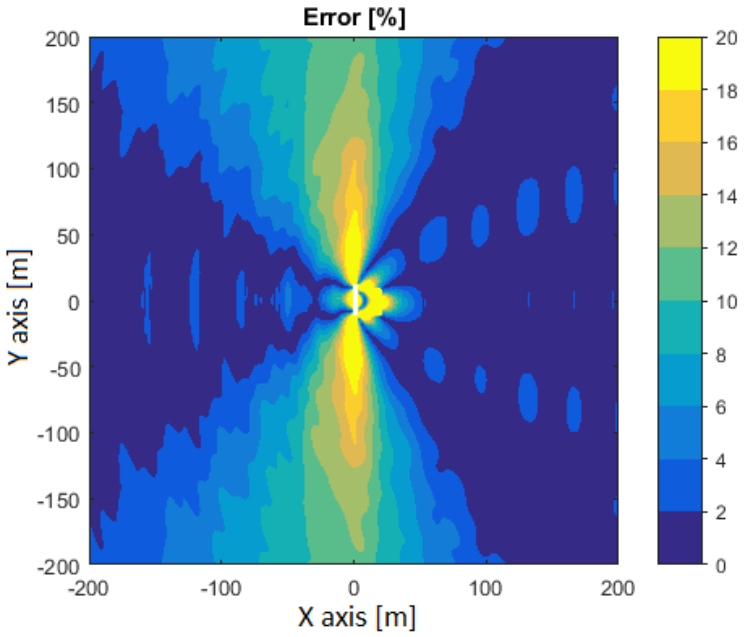

FIGURE B.15: Percentage error between the perturbed wave computed in MILDwave with SLT, and NEMOH results (see Figure B.9).

Figure B.15 represents the percentage error between the perturbed wave amplitude (diffracted and radiated wave) obtained in MILDwave and the perturbed wave amplitude obtained in NEMOH (see Figure B.9). In this case the flap is represented in MILDwave by employing the SLT as it was described in Section B.4. The results from NEMOH along Section $Y = 0$ (S1 in Figure B.9) were used as a target to tune the representation of the device in MILDwave. As expected the results show low errors along section $Y = 0$, however once moving towards the sides of the domain the error become much higher as the difference between NEMOH and MILDwave increases. This difference is mainly caused by the poor representation of the radiated wave generated by the movement of the flap when using the SLT in MILDwave.

Acknowledgement

The research leading to these results is part of the OceaNET project, which has received funding from the European Union's Seventh Framework Programme for research, technological development and demonstration under grant agreement no 607656.

References

Babarit, A., Folley, M., Charrayre, F., Peyrard, C. & Benoit, M. (2013). On the modelling of WECs in wave models us-ing far field coefficients. Proceedings of EWTEC.

Babarit, A. & Delhommeau, G. (2015). Theoretical and numer-ical aspects of the open source BEM solver NEMOH. Pro-ceedings of EWTEC.

Beels, C. (2009). Optimization of the Lay-Out of a Farm of Wave Energy Converters in the North Sea. Analysis of Wave Power Resources, Wake Effects, Production and Cost. PhD Thesis.

Beels, C., Troch, P., De Visch, K., Kofoed, J. & De Backer, G. (2010a). Application of the time-dependent mild-slope equations for the simulation of wake effects in the lee of a farm of Wave Dragon wave energy converters. Renewable Energy, 35, 1644–1661.

Beels, C., Troch, P., De Backer, G., Vantorre, M. & De Rouck, J. (2010b). Numerical implementation and sensitivity anal-ysis of a wave energy converter in a time-dependent mild-slope equation model. Coastal Engineering, 57, 471–492.

Borgarino, B., Babarit, A. & Ferrant, P. (2011). Impact of the separating distance between interacting wave energy con-verters on the overall energy extraction of an array. Pro-ceedings of EWTEC.

Charrayre, F., Peyrard, C., Benoit, M. & Babarit, A. (2015). A coupled methodology for wave-body interactions at the scale of a farm of wave energy converters including irregu-lar bathymetry. Proceedings of ASME. OMAE2014-23457.

Folley, M., Babarit, A., Child, B., Forehand, D., O'Boyle, L., Silverthorne, K., Spinneken, J., Stratigaki, V. & Troch, P. (2012). A Review of Numerical Modelling of Wave Energy Converter Arrays. Proceedings of ASME. OMAE2012-8380.

Radder, A.C. & Dingemans, M.W., 1985. Canonical equations for almost periodic, weakly nonlinear gravity waves. Wave Motion 7, 473–485.

Smith, H., Pearce, C. & Millar, D. (2012). Further analysis of change in nearshore wave climate due to an offshore wave farm: An enhanced case study for the Wave Hub site. Re-newable Energy, 40, 51–64.

Troch, P. (1998). A numerical model for propagation and trans-formation of linear water waves. Department of Civil Engi-neering, Ghent University.

Appendix C

Paper C

Wake Effect Assessment Of A Flap Type Wave Energy Converter Farm Using A Coupling Methodology

Published in

Proceedings of the ASME 2017 36th International Conference on Ocean, Offshore and Arctic Engineering, Trondheim, Norway. OMAE2017-61323.

Authors

Nicolas Tomey-Bozo[1], Jimmy Murphy[1], Aurélien Babarit[2], Peter Troch[3], Tony Lewis[1], Gareth Thomas[4]

[1]*MaREI Centre (ERI), University College Cork, Haulbowline Road, Ringaskiddy, Ireland*

[2]*Ecole Centrale de Nantes – CNRS, 1 rue de la Noé, 44300 Nantes, France*

[3]*Department of Civil Engineering, Ghent University, Zwijnaarde, Belgium*

[4]*School of Mathematical Sciences, University College Cork, Cork, Ireland*

Abstract

It is expected that large farms of Wave Energy Converters (WECs) will be installed and as part of the consenting process it will be necessary to quantify their impact on the local environment. The objective of this study is to improve the state-of-the-art of the methodologies to assess the impact a WEC farm has on the incoming wave field through the use of a coupling methodology. A Boundary Element Method (BEM) solver is used to obtain the near-field wave solution accounting for the wave-body interactions within the array of WECs and a Mild-Slope Equation (MSE) model is used to assess the wave transformation in the far-field. The near-field solution obtained from the BEM solver is described as an internal boundary condition in the MSE model and then propagated throughout the domain. The internal boundary condition is described by imposing the solution of the surface elevation in the area where the farm is located. The methodology is applied to flap type WECs that are deployed in shallow water conditions. The validation of the technique is done first for a single flap and then for an array of 5 flaps. Finally, a mild-slope bathymetry and the influence of the changing depth on the wave transformation is assessed in order to prove the versatility of the method to be applied to real scenarios.

C.1 Nomenclature

η Surface elevation
Φ Velocity potential at the free surface
ω Wave frequency
g Gravitational acceleration
C Phase velocity
C_g Group velocity
k Wave number
ω Angular frequency
η^* Additional surface elevation
Δx grid size in X direction
C_e Energy velocity
A_ω Incident Wave Amplitude
Γ Excitation moment coefficient
I Moment of inertia about the Y axis
A Added moment of inertia
B Radiation damping coefficient
H Hydrostatic restoring coefficient
B_{pto} PTO damping coefficient
θ Amplitude of motion

C.2 Introduction

The presence of Wave Energy Converter (WEC) farms in the ocean will locally affect the wave transformation processes. WECs are designed to absorb part of the incoming wave energy and therefore to reduce the amount of energy density in the leeside of the farm. The quantification of the wake effect generated by a WEC farm will be an important point of the consenting process for the deployment of these technologies. Furthermore, their potential capability to have a sheltering effect on other marine activities taking place on the lee of the farm may open various opportunities. For all these reasons this study aims to improve the state of the art of the methodologies to quantify the wake effect of a WEC farm.

The methodologies employed up to date to quantify the impact of a WEC farm on its surrounding wave field has shown to be missing some features in order to provide a realistic representation of the phenomena. Some studies have used Wave Propagation Models (WPMs) to assess the far-field effect on the lee-side of a WEC farm [1–4] by representing intrinsically the devices as absorption cells or source terms. Others have assessed the near-field wave interactions between devices by using Boundary Element Method (BEM) solvers [5, 6]. Reference [7] summarises and describes in detail all techniques that have attempted to address this problem. WPMs are accurate solvers of the wave propagation throughout large domains considering realistic conditions such as irregular bathymetries and dissipative processes. However, these models do not accurately represent the local wave-body interactions and rely on external lookup tables describing the absorption capacity of the WECs in order to represent them inherently. BEM solvers are the opposite as they provide accurate solutions of the local wave-body solution by solving the well-known boundary value problem but are limited in terms of the constant depth assumptions and the restricted size domains.

A coupling methodology is applied in this study to fulfil the gap between the near-field results obtained from a BEM solver and the wave propagation in the far-field solved in a WPM. The BEM solver employed is the open-source code NEMOH and the time-dependent Mild-Slope Equation (MSE) model MILDwave is used as WPM. An internal boundary condition is described in the MSE model for each regular wave frequency based on the perturbed wave solution obtained from the BEM solver. The propagation of the perturbed wave is then solved throughout the rest of the domain. The superposition of the perturbed wave and the incident wave computed intrinsically in the MSE model allows the computation of the total wave solution. By applying the methodology to a farm of various WECs it enables wave farm wake effects to be assessed.

Previous studies such as [8, 9] have employed similar coupling methodologies where the perturbed wave was calculated for point absorbers WECs. The perturbed wave was solved individually for each device and the wave interactions were calculated within the MSE model. In this study a one-step coupling approach is suggested

where the perturbed wave is computed for the whole farm with the BEM solver and then imposed as a wave generation surface in the MSE model. This allows for the proper calculation of all wave interactions between devices within the BEM solver before applying the coupling technique. In addition, the technical details of the coupling technique are described by defining the way the internal boundary is set up within the MSE model.

In this paper the numerical tools and the main governing equations are first described. The proposed methodology is then outlined by describing the technical set up of the internal boundary that allows for the coupling between the two solvers. The methodology is first validated for a single WEC case consisting of a flap type device. Then the methodology is validated for the case of a WEC farm composed of 5 flap type devices. The total wave field and relative error plots are then computed for both of these cases. Finally, an additional case showing the versatility of the method when applied to large domains and changing depth bathymetries is outlined.

C.3 Numerical Tools Involved

The two hydrodynamic solvers used in this study are described in the following section together with the main governing equations of the problems assessed.

C.3.1 Open-source boundary element method solver NEMOH

NEMOH is an open-source BEM solver developed by Ecole Centrale de Nantes [10] and it is used in this work to obtain the near-field surrounding the WECs. NEMOH is based in the linear potential theory and it calculates the perturbed velocity potential by solving the scattering problem with the appropriate set of boundary conditions as described in [10]. The perturbed velocity potential is obtained as a 3D solution from the well-known linear wave-body interaction boundary value problem. From the potential at the free surface condition $(z = 0)$ it is then straightforward to obtain the surface elevation as shown in Equation (C.1).

The scattering problem is divided into one diffraction problem and one radiation problem per degree of freedom for each wave frequency. The diffraction problem is computed considering the body is fixed under the presence of an incoming incident wave. The radiation problem is solved by considering a forced motion of the body in calm conditions (absence of waves). Then the total solution of the wave field is obtained as a superposition of the incident wave, and the diffracted and radiated wave obtained from NEMOH. Equation. (C.2) describes the superposition in terms of surface elevation:

$$\bar{\eta}(x, y) = \frac{i\omega}{g}\bar{\Phi}(x, y) \tag{C.1}$$

$$\bar{\eta}_t(x,y) = \bar{\eta}_i + \bar{\eta}_d + \sum_{n=1}^{6} \bar{\eta}_r \tag{C.2}$$

Over-bar ($\bar{}$) denotes the complex form of the variable and subscripts t, i, d, and r refer to the total, incident, diffracted, and radiated wave respectively.

C.3.2 Mild-slope equation model MILDwave

The wave propagation model MILDwave is used in this study to solve the wave transformation processes throughout large domains and asses the far-field effects. MILDwave is a time-dependent MSE model developed by Ghent University [11] and is part of the phase-resolved type of WPMs. It solves the propagation of surface waves throughout the domain and the interaction with the obstacles (previously defined) by solving the depth-integrated mild-slope equations of Radder and Dingemans [12]. The velocity potential at the free surface and the instantaneous surface elevation are the variables solved for each coordinate of the grid (x, y) for each instant t of time by the set of differential equations given in Equation (C.3) and (C.4) bellow.

$$\frac{\partial \eta}{\partial t} = B_c \Phi - \nabla \Delta (A_c \nabla \phi) \tag{C.3}$$

$$\frac{\partial \Phi}{\partial t} = -g\eta \tag{C.4}$$

where

$$B_c = \frac{\omega^2 - k^2 C C_g}{g} \tag{C.5}$$

$$A_c = \frac{C C_g}{g} \tag{C.6}$$

Incident waves are generated in MILDwave at the offshore boundary by using the source term addition method, i.e. by adding an additional surface elevation η^* to the calculated value on a wave generation line for each time step given by Equation (C.7) and described in [13]:

$$\eta^* = 2\eta_i \frac{C_e \Delta t}{\Delta x} \cos\beta \tag{C.7}$$

where β represents the angle of wave rays from the X axis and the wave generation line is assumed to be parallel to the Y axis.

C.4 Flap Type Wave Energy Converter

The type of WEC considered in this study is a surface-piercing flap hinged at the bottom of the seabed as shown in Figure C.1. The motion is restricted to pitch therefore only one Degree Of Freedom (DOF) is considered. The shaft about which the flap rotates is at the base of the device. Table C.1 shows the main characteristics of the devices.

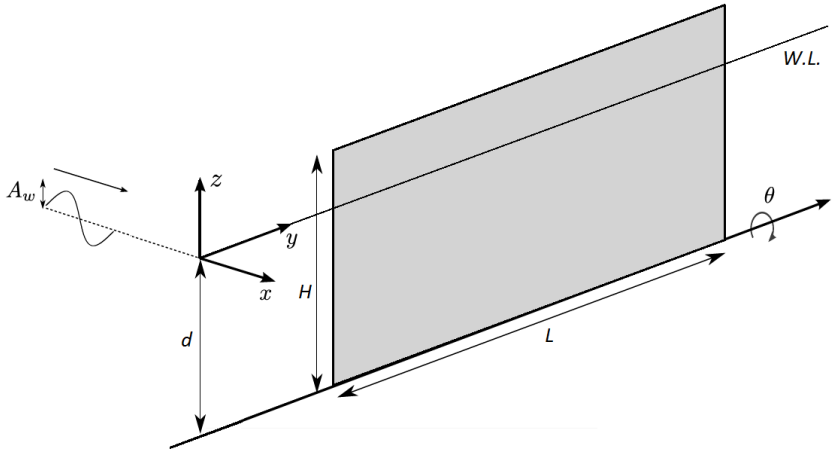

FIGURE C.1: Flap type WEC sketch.

TABLE C.1: Main characteristics of the flap type WEC.

Parameter	Coefficient	Value	Units
Length	L	20	m
Height	H	12	m
Thickness	t	1	m
Relative density	ρ_r	0.3	-

The amplitudes of angle of motion for each device are calculated based on Equation (C.8). The hydrodynamic coefficients Fe, A and B„ are obtained from the BEM solver where Fe represents the excitation force, A the added inertia, and B the radiation damping. The hydrostatic coefficient H and the moment of inertia I are calculated based on the geometry description from Table (C.1). The Power Take Off (PTO) damping coefficient B_{pto} is calculated based on Equation (C.9).

The resultant values of amplitude of motion are used to quantify the radiated wave solution obtained from NEMOH. The surface elevation for the radiated wave is first obtained from the BEM solver in a non-dimensional form relative to a unit of amplitude of motion. In the case of a farm where various WECs are computed within the BEM solver, the terms composing Equation (C.8) are expanded to n dimensions where n represents the number of devices. The expanded form of the equation of

motion takes account for all interactions between WECs and therefore determines the amplitude of motion for each device whilst in the presence of the surrounding moving devices. The same procedure is applied when a larger number of DOF are considered. The dimensions of Equation (C.8) are expanded to n x j where j is the number of DOF of the WEC.

$$\theta(\omega) = \frac{A\Gamma(\omega)}{-\omega^2(I + A_r) - i\omega(B_r + B_{pto}) + H} \tag{C.8}$$

A passive PTO composed of a damper is used in this study. This configuration was chosen to represent a hydraulic PTO which is usually employed for the flap type WECs. Equation (C.9) defines the optimum value of the PTO damping coefficient for a specific wave frequency which is theoretically demonstrated in [14]. In the case of an irregular sea state composed of many wave frequencies a fixed value of the PTO damping coefficient was assigned considering the overall statistics of the sea state instead of an optimal value for each frequency that would be constantly changing in time.

$$B_{pto} = \sqrt{\left(\frac{H}{\omega} - \omega(I + A_r)\right)^2 + B_r^2} \tag{C.9}$$

C.5 Coupling Methodology for a Single WEC

The total wave solution is obtained for each wave frequency from two separate computations. First the incident wave is calculated in MILDwave intrinsically and then the perturbed wave by applying the coupling methodology. A wave generation line is defined at the up-wave boundary for the incident wave computation. Then the incident wave propagates towards the X positive axis across the rest of the empty domain.

For the second computation the perturbed wave is calculated in the BEM solver for the area representing the near-field surrounding the flap. The perturbed wave is obtained from the superposition of the diffracted wave and radiated wave solution. The perturbed wave representing the near-field is then imposed in MILDwave by forcing the solution of the surface elevation at each instant of time within the same near-field area as an internal boundary condition. The internal boundary acts as a wave generation surface that allows waves to propagate throughout the rest of the domain to obtain the far-field solution. The area size and shape of the internal boundary can be adapted in order to restrict as much as possible the area where the limitations of the BEM are imposed (constant water depths and limited wave transformation processes).

Figure C.2 shows a sketch representation of the methodology with the two different waves generated in MILDwave along the whole domain, the incident wave and the perturbed wave. The way the internal boundary condition is described in this study has been modified and improved as compared to the previous study [15]

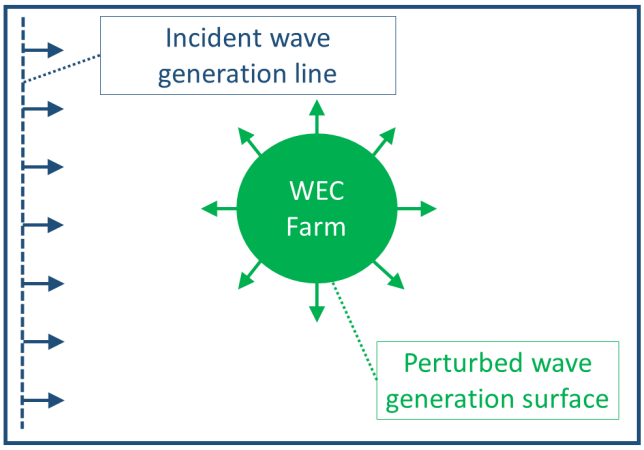

FIGURE C.2: Methodology description sketch

carried out by the same authors. In [15] the internal boundary was input as a circular wave generation line described in the same manner as an incident wave at the offshore boundary is set up, i.e. by adding an additional surface elevation η^* on the generation line for each time step. However, the circular wave generation line presents some limitations; the line discretization depends on the radius of the circle, it is limited to circular shapes, and it needs an inner sponge layer that gives reflection problems.

In this study the internal boundary is described by a wave generation surface that can adapt to the desired shape (as far as it surrounds completely the WECs) and does not need a specific parametrisation, i.e. each grid cell contained within the generation surface is attributed its corresponding surface elevation value from the BEM solver solution at each instant of time.

C.5.1 Near-field from BEM solver

The described methodology is first applied to a single WEC case and constant water depth conditions for validation purposes. The perturbed wave surrounding the single flap is obtained in NEMOH for a domain of 400 x 400 m. The wave results are plotted in terms of wave amplitude and wave phase in order to facilitate the comparison between the frequency domain results from NEMOH and the time domain results from MILDwave. The wave amplitude and phase correspond to the module and argument of the complex form of the surface elevation ($\bar{\eta}$) respectively. Figure C.3 shows the perturbed wave solution across the whole domain corresponding to an incident wave of period of 8 s and an amplitude of 1 m. A circle surrounding the flap delimits the area corresponding to the near-field that is used in the next stage to describe the wave generation surface in MILDwave. In this case a circular area of radius R equal to 20 m is used to delimit the near-field.

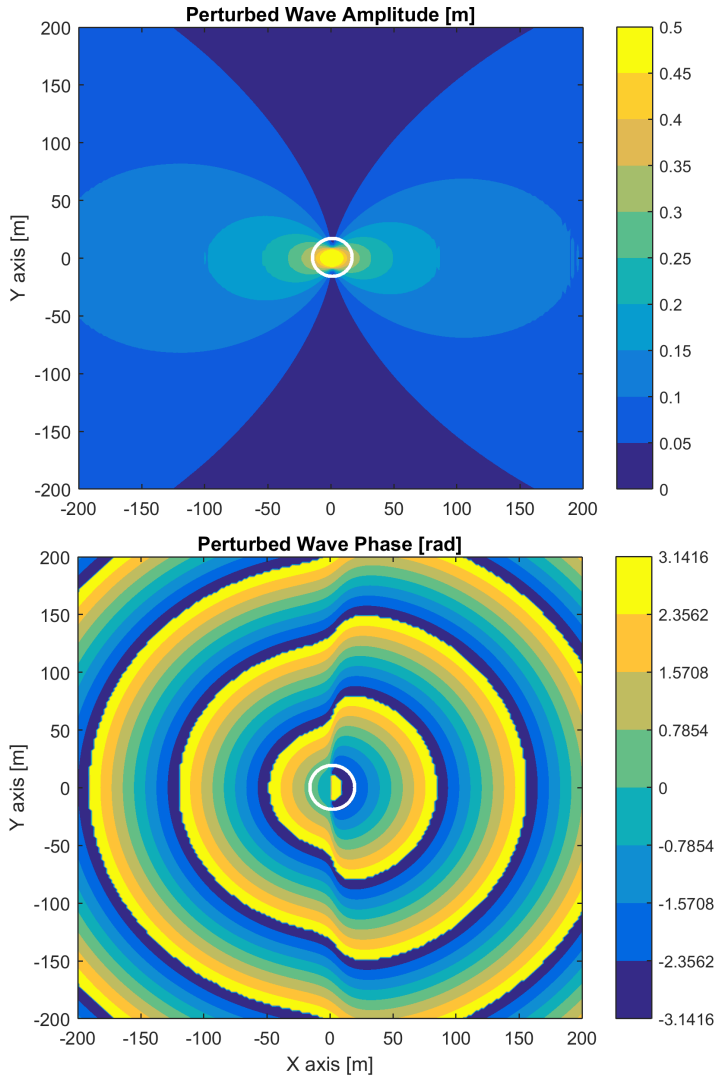

FIGURE C.3: Perturbed wave amplitude and phase from NEMOH solution for a single flap.

C.5.2 Far-field from wave propagation model

The near-field solution of the perturbed wave obtained from NEMOH is now imposed in MILDwave at the same location with respect to the WEC, as a wave generation surface of circular shape with radius r equal to 20 m. The surface elevation solution is imposed in the circular area at each instant of time and propagated throughout the rest of the domain. The same conditions than NEMOH of constant water depths are considered in this case to validate the solution obtained in MILDwave. Figure C.4 shows the far-field wave amplitude and phase obtained in MILDwave for the same domain of 400 x 400 m. The empty disc in the middle of the domain represent the location where the solution is imposed.

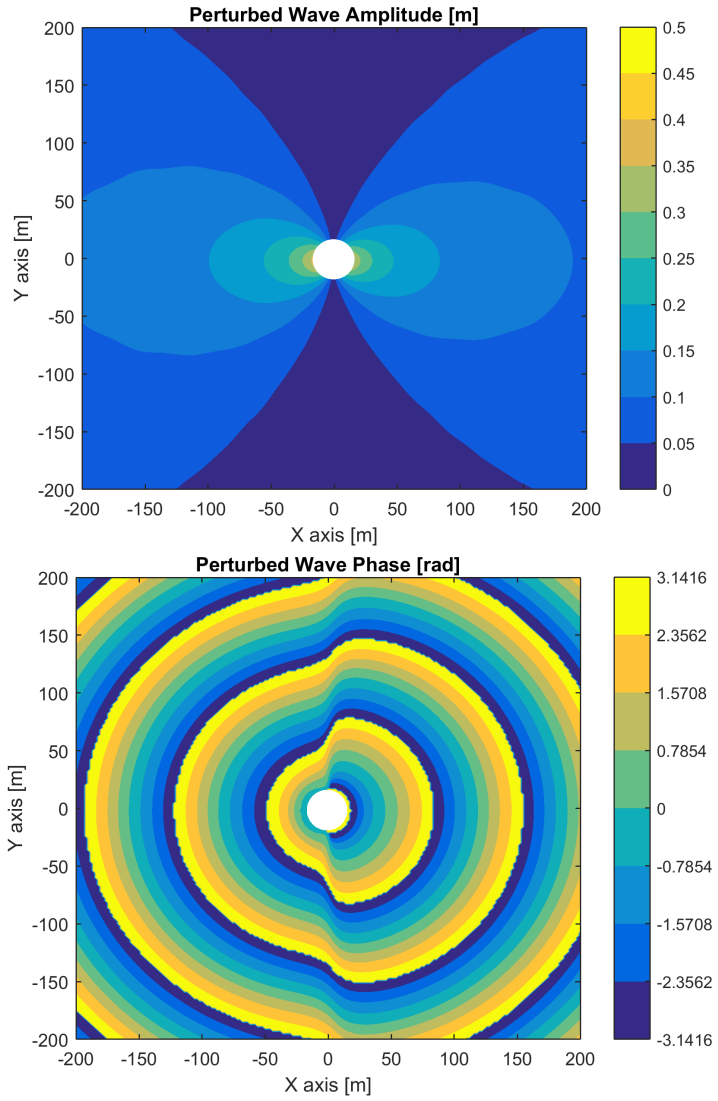

FIGURE C.4: Perturbed wave amplitude and phase from MILDwave solution for a single flap.

Figure C.5 shows the percentage error of the perturbed wave solution from MILDwave respect to the solution from NEMOH. The error is calculated based on Equation C.10 where A_M is the wave amplitude result from MILDwave, A_N the wave amplitude result from NEMOH, and $\bar{A_N}$ the mean value of the wave amplitudes from NEMOH at the boundary between the wave generation surface and the far-field domain solved in MILDwave. The results from NEMOH are considered here as a target solution.

$$\epsilon(\%) = \frac{A_N - A_M}{\bar{A_N}} \tag{C.10}$$

A negligible error is present across the $Y = 0$ section with error values remaining below 4%. Outside this area the error nearly disappears obtaining values that remain under 1%. The error is relatively larger across $Y = 0$ section because wave

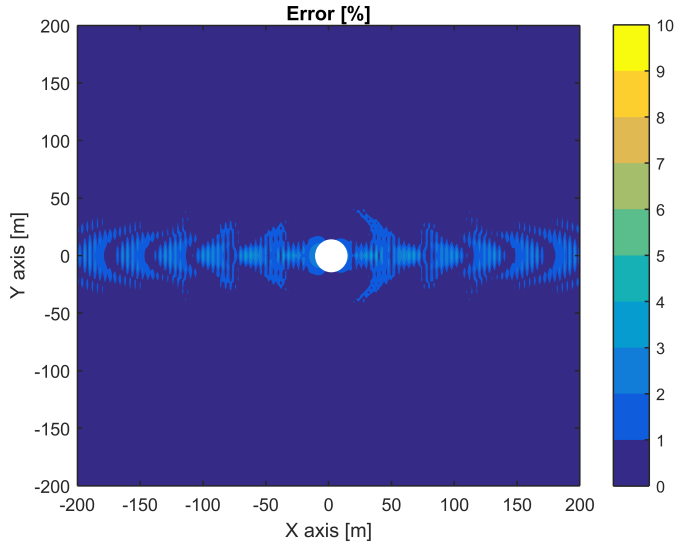

FIGURE C.5: Percentage error between MILDwave and NEMOH solution for a single flap.

amplitude values are larger across this section. The error remains below acceptable values considering that the maximum percentage error of 4% corresponds to an absolute error of 0.0036 m, as the average perturbed wave amplitude is equal to 0.09 m.

C.5.3 Total wave field

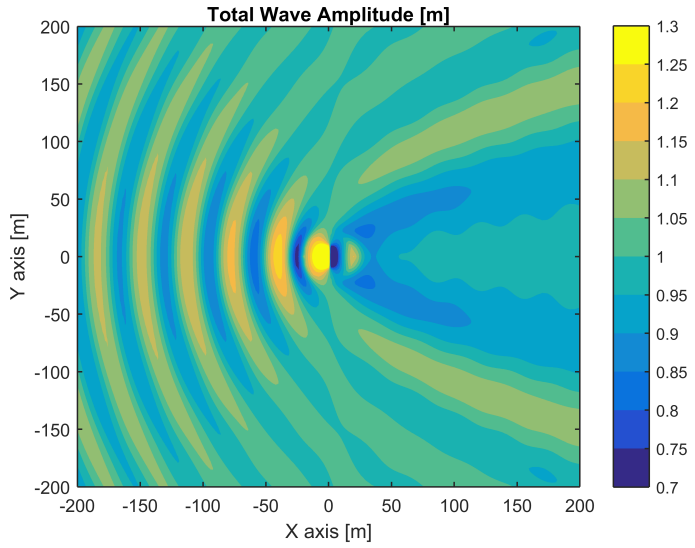

FIGURE C.6: Total wave amplitude from MILDwave solutions for a single flap.

The total wave amplitude obtained as a result of superposing the perturbed wave from Figure C.4 and the corresponding incident wave is plotted in Figure C.6. The

way the internal boundary for the perturbed wave generation is set up (forcing the solution of the wave generation surface) allows us to plot the whole domain including the inner part of the generation surface without any appreciable discontinuity between the near-field and far-field domains.

C.6 Coupling Methodology for a WEC Farm

The next step was the application of the methodology to a farm of 5 flaps in order to prove the versatility of the technique. The same incident wave conditions and constant water depths as previously outlined are considered. The layout of the farm is defined by a separating spacing between devices of 40 m in both X and Y directions with an up-wave row composed of 2 flaps and a down-wave row composed of 3 flaps. The flaps from the down-wave row are staggered respect to the flaps from the up-wave row.

C.6.1 Near-field from BEM solver

The near-field area surrounding the WEC farm is delimited in this case by a rectangular section of 60 x 160 m (X and Y axis respectively). The perturbed wave solution is computed in NEMOH where all interactions are taken into account. Then the perturbed wave solution corresponding to the rectangular area is described as an internal boundary in MILDwave by means of a wave generation surface. In the case of several WECs the perturbed wave from NEMOH is obtained from the superposition of the diffracted wave and the 5 radiated waves corresponding to each device.

The shape of the wave generation surface is adapted to the shape of the WEC farm. In this case the shape of the near-field is a rectangle that fits the form of the farm by leaving a gap of half of the length of a flap (i.e. 10 m). The half flap length distance is left in order to ensure a stable wave generation but the method can be applied with a shorter gap distance. The perturbed wave amplitude and phase obtained from NEMOH are shown in Figure C.7. A rectangle delimits the near-field area which is used to describe the wave generation surface in MILDwave.

C.6.2 Far-field from wave propagation model

The perturbed wave is generated now in MILDwave with the wave generation surface of rectangular shape and propagated throughout the rest of the domain. Figure C.8 shows the far-field solution obtained in MILDwave in terms of wave amplitude and phase. The same domain size as used in Figure C.7 was chosen in order to compare with the target perturbed wave obtained with NEMOH.

The percentage error between the perturbed wave obtained with MILDwave and the perturbed wave obtained with NEMOH is calculated based on Eq. C.10 as it is done for the single flap case. Figure C.9 below shows the values obtained for this error.

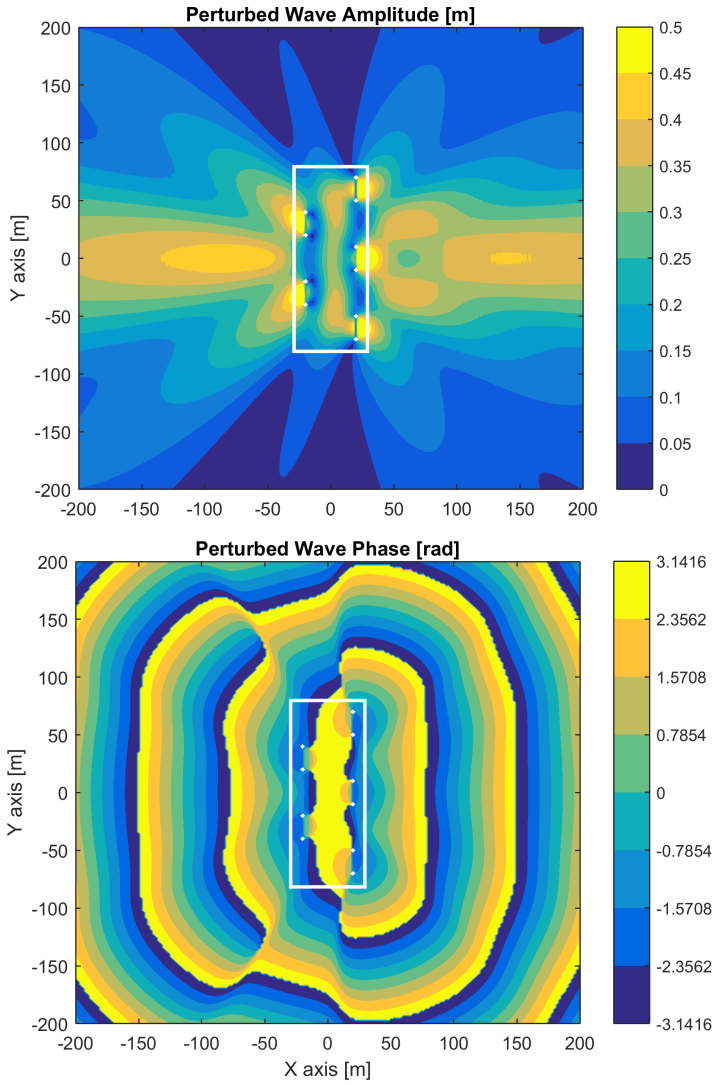

FIGURE C.7: Perturbed wave amplitude and phase from NEMOH solution for 5 flaps.

The maximum error appears along section $Y = 0$ where the wave amplitude is the largest of the domain and remains below error values of 2%. This value can be assumed to be negligible considering a percentage error of 2% corresponds to 0.0055 m of absolute error, as in this case the mean wave amplitude along the internal boundary is 0.27 m. Therefore, a really good agreement is found for both applications of the coupling technique, the single flap case and the case of the 5 flaps farm.

This application case shows the flexibility of the methodology to adapt the area describing the internal boundary. Whether described by a circular surface or by a rectangular surface, the internal boundary allows the computation of the perturbed wave in MILDwave through a coupling technique. The unique mandatory condition is that the surface used to describe the internal boundary condition surrounds completely the WEC farm in order to describe the correct energy flux.

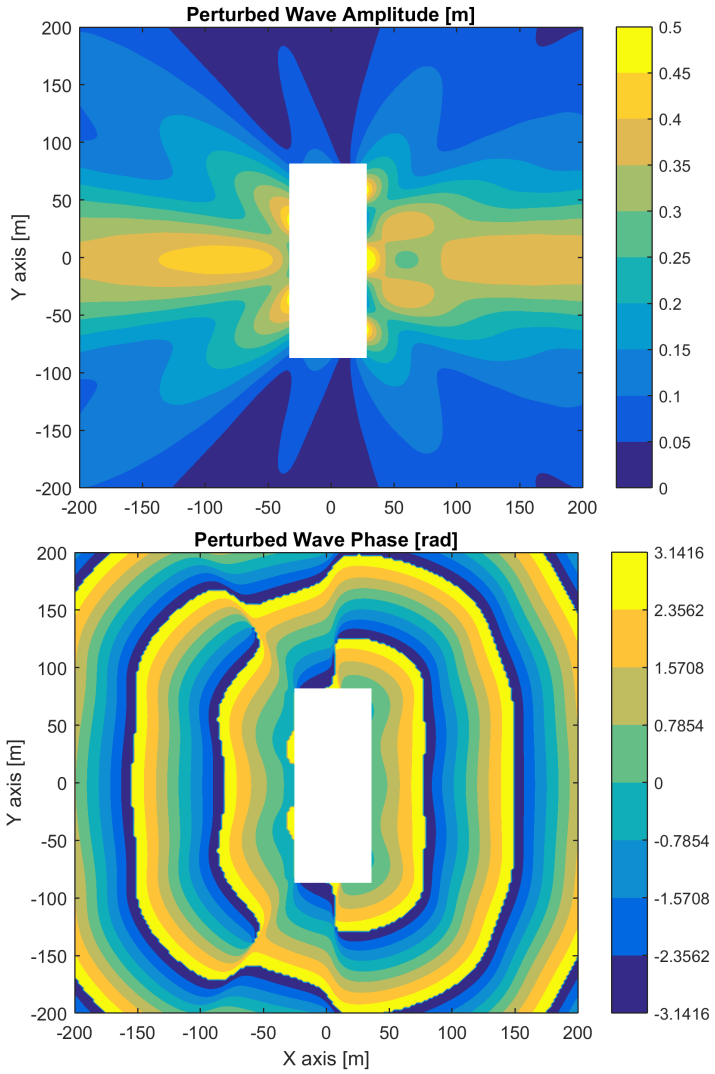

FIGURE C.8: Perturbed wave amplitude and phase form MILDwave solution for 5 flaps.

C.6.3 Total wave field

The total wave field was also obtained for the WEC farm case by superposing the previous results of the perturbed wave to the incident wave computed intrinsically in MILDwave. Figure C.10 shows the wave amplitude obtained along the domain for the total wave. As for the single flap case there is no transition in the results between the near-field where the solution of the perturbed wave is imposed from NEMOH and the far-field domain where the solution is solved by the MSE model. The near-field area surrounding the flaps replicates exactly the same values than the ones obtained in NEMOH due to the way the internal boundary is set up.

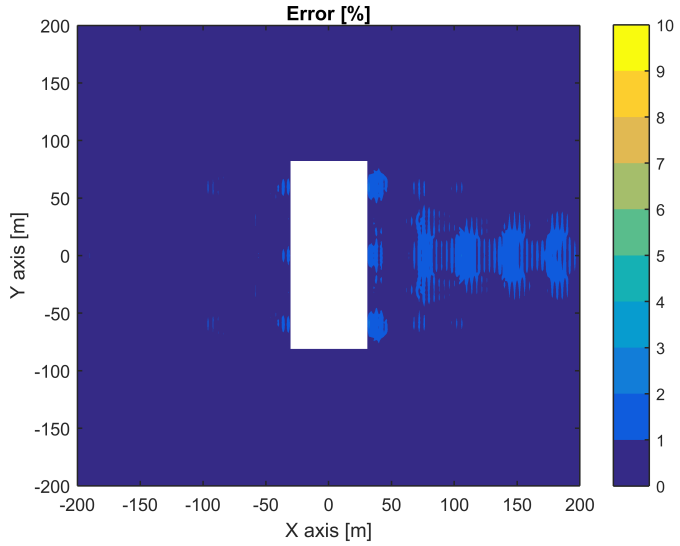

FIGURE C.9: Percentage error between MILDwave and NEMOH solution for 5 flaps.

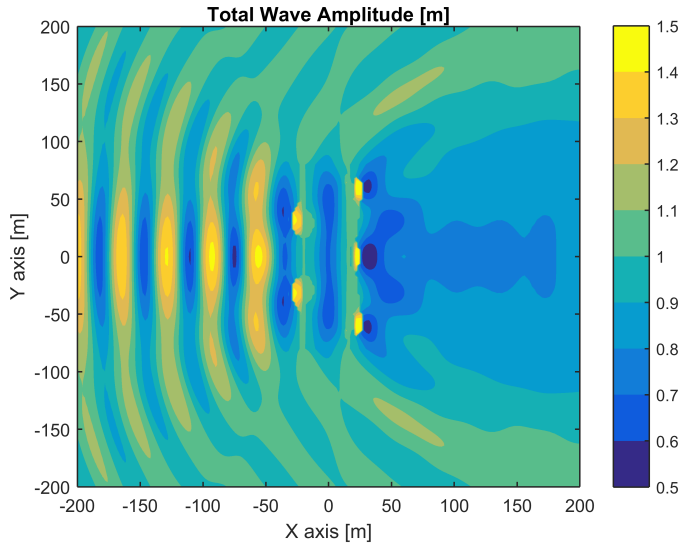

FIGURE C.10: Total wave amplitude from MILDwave solution for 5 flaps.

C.7 Wake Effect of a WEC Farm

Now that the methodology has been validated for small domains where the comparison was possible against BEM solver solutions, the wake effect of a farm of flaps for a large domain is computed in this section. A domain of 1000 x 2000 m (X and Y axis respectively) is chosen which gives a broad perspective of the wake effect in the far-field. The wake effect is quantified by the disturbance coefficient K_d which in the case of regular waves is obtained by dividing the total wave amplitude (presence of flaps) by the incident wave amplitude (absence of flaps) as described in Equation

(C.11).

$$K_d = \frac{A_t}{A_i} \tag{C.11}$$

C.7.1 Wake effect of a WEC farm for constant water depths

First the wake effect is assessed for a constant water depth bathymetry. Figure C.11 shows the disturbance coefficient obtained along the domain. In the case of constant water depths the incident wave amplitude is equal to 1 therefore the disturbance coefficient is equal to the total wave amplitude.

Clear zones with a reduction of the wave amplitude are found along the plot from Figure C.11. An area of 200 x 200 m with values below 0.9 of wave amplitude are found right behind the farm which is equivalent to a 10% of reduction. Obviously this is a simple case for a small farm of 5 flaps that is used to showcase the method. However with a larger number of flaps a larger zone of wave amplitude reduction can probably be found and potentially protect other marine activities located in the leeside of the WEC farm.

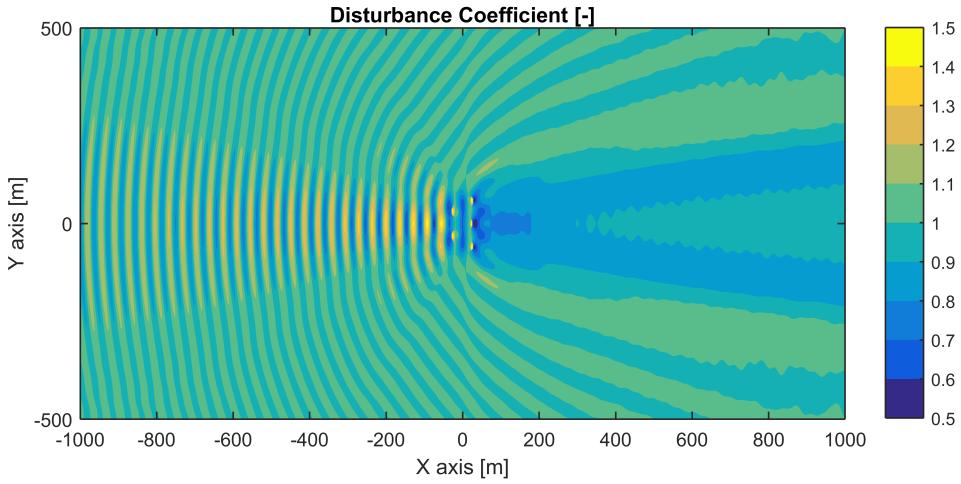

FIGURE C.11: Disturbance coefficient for a large domain with constant water depth.

C.7.2 Wake effect of a WEC farm for a mild-slope bathymetry

A case study with a changing depth bathymetry was run next in order to prove the capability of the method to account for irregular bathymetries. The bathymetry is defined by the constant profile along the Y axis shown in Figure C.12. The profile starts with a constant water depths at the up-wave half section and then a mild-slope at the down-wave half section. The mild-slope starts at the centre of the WEC farm (X = 0 m) with 10 meters of water depth and decreases progressively until 5 m of water depth at X = 1000 m.

Figure C.13 shows three plots; first the incident wave amplitude in the absence of flaps, then the total wave amplitude obtained in the presence of flaps, and finally the disturbance coefficient obtained from the division of the two first plots.

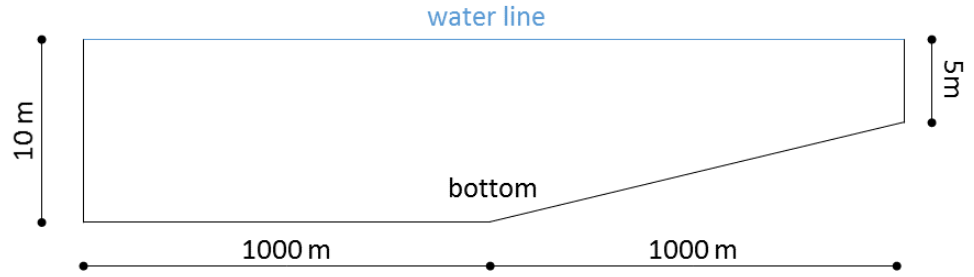

FIGURE C.12: Bathymetry profile sketch.

Comparing the disturbance coefficient plot from Figure C.13 with Figure C.11 only small differences in the wake effect can be observed. Larger differences may be found in the case of a real bathymetry with irregular profiles in both X and Y directions.

C.8 Conclusion

The coupling methodology has shown to give extremely accurate results when comparing the results from the MSE model to the target solutions from the BEM solver. The method has proven to be versatile by tightening the area where the solution of the perturbed wave is imposed to the shape of the farm. This allows the reduction of the area where the limitations of the BEM solvers are assumed.

The methodology remains relatively fast in terms of computational time considering the total calculations for one wave frequency remain less than 10 minutes for the domain size considered in the last section and with a standard computer. The fact of computing all wave interactions within the BEM solver can be demanding in terms of computational time when large WEC farms with many devices are considered. Thus it is the unique way for computing all wave interactions in a farm of WECs within an acceptable computational time. New methodologies are under development to compute wave interactions within an array of WECs based on cylindrical solutions of the perturbed potential from BEM solvers [6, 16]. These methods can increase significantly the calculation time of the perturbed wave for a large array for constant water depths conditions.

It is straightforward to calculate irregular sea states from the regular wave solutions by superposing all wave components that are present in the considered sea state. This allows the proposed methodology to be used to more accurately quantify the impact of a WEC farm has on the wave climate taking account of realistic conditions, i.e. irregular bathymetries, irregular sea states, and wave transformation processes. The impact on the incident wave climate caused by large WEC farms

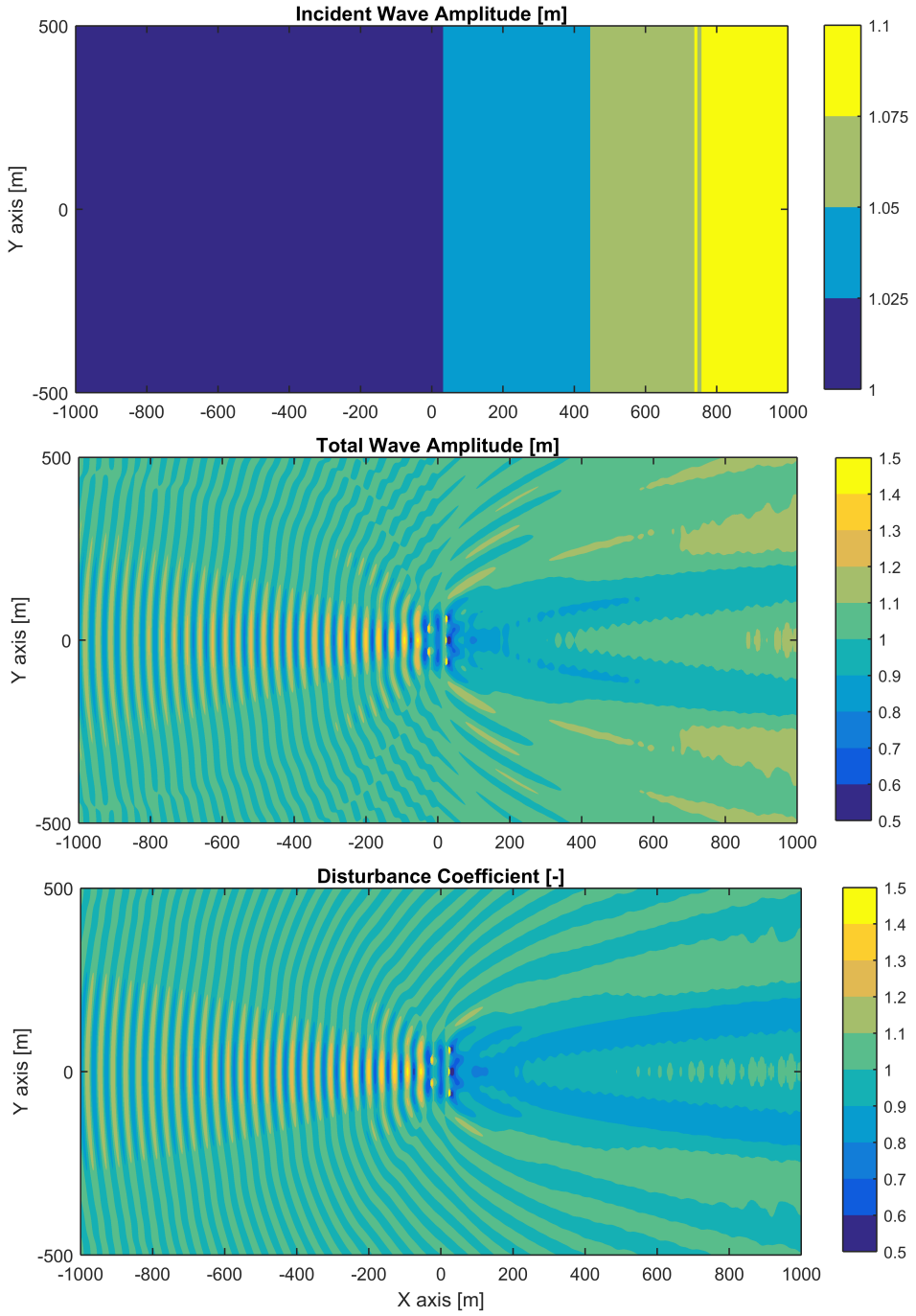

FIGURE C.13: Incident wave amplitude, total wave amplitude, and disturbance coefficient for a large domain with a mild-slope bathymetry.

composed of many devices can be quite significant. Thus it will be mandatory to assess this impact as part of the procedure for the future commissioning of a wave energy farm. In addition, if the assessment finds a WEC farm has a significant sheltering effect, other marine activities sharing the sea space could take advantage of the protected area behind to have calmer water conditions to carry out their tasks.

Acknowledgement

The research leading to these results is part of the OceaNET project, which has received funding from the European Union's Seventh Framework Programme for research, technological development and demonstration under grant agreement no 607656.

References

[1] Beels, C., Troch, P., De Backer, G., Vantorre, M., De Rouck, J.: Numerical implementation and sensitivity analysis of a wave energy converter in a time-dependent mildslope equation model, Coast. Eng., 2010, 57, (5), pp. 471-492.

[2] Beels, C., Troch, P., De Visch, K., Kofoed, J.P., De Backer, G.: Application of the time-dependent mild-slope equations for the simulation of wake effects in the lee of a farm of Wave Dragon wave energy converters, Renew. Energy, 2010, 35, (8), pp. 1644-1661.

[3] Smith, H.C.M., Pearce, C., Millar, D.L.: Further analysis of change in nearshore wave climate due to an offshore wave farm: An enhanced case study for the Wave Hub site, Renew. Energy, 2012, 40, (1), pp. 51-64.

[4] Astariz, S., Abanades, J., Perez-Collazo, C., Iglesias, G.: Improving wind farm accessibility for operation & maintenance through a co-located wave farm: Influence of layout and wave climate, Energy Convers. Manag., 2015, 95, pp. 229-241.

[5] Borgarino, B., Babarit, a., Ferrant, P.: Impact of wave interactions effects on energy absorption in large arrays of wave energy converters, Ocean Eng., 2012, 41, pp. 79-88.

[6] Mcnatt, J.C., Venugopal, V., Forehand, D.: A novel method for deriving the diffraction transfer matrix and its application to multi-body interactions in water waves, Ocean Eng., 2014, 94, pp. 173-185.

[7] Folley, M., Babarit, A., Child, B., et al.: A Review of Numerical Modelling of Wave Energy Converter Arrays, in Proc. 31st Int.Conf. on Ocean, Offshore and Arctic Engineering, Rio de Janeiro, Brazil, July 2012, pp. 535-545.

[8] Babarit, A., Folley, M., Charrayre, F., Peyrard, C., Benoit, M.: On the modelling of WECs in wave models using far field coefficients,Eur. Wave Tidal Energy Conf. EWTEC, 2013.

[9] Charrayre, F., Peyrard, C., Benoit, M., Babarit, A.: A coupled methodology forwave-body interactions at the scale of a farm of wave energy converters including irregular bathymetry, Proceedings of the ASME 2014 33rd International Conference on Ocean, Offshore and Arctic Engineering, San Francisco, USA, June 2014.

[10] Babarit, A., Delhommeau, G.: Theoretical and numerical aspects of the open source BEM solver NEMOH, Proc. 11th Eur.Wave Tidal Energy Conf., 2015, (September 2015), pp. 1-12.

[11] Troch, P. 1998. MILDwave A numerical model for propagation and transformation of linear water waves, Internal Report, Department of Civil Engineering, Ghent University. PMid. 9689969.

[12] Radder, A.C., Dingemans, M.W.: Canonical equations gravity waves, weakly nonlinear gravity wavesWave Motion, 1985, 7, pp. 473485.

[13] Lee, C., Suh, K.D.: Internal generation of waves for time-dependent mild-slope equations, Coast. Eng., 1998, 34, (12), pp. 35-57.

[14] Zhao, H. tao, Sun, Z. lin, Hao, C. ling, Shen, J. fa: Numerical modelling on hydrodynamic performance of a bottomhinged flap wave energy converter, China Ocean Eng., 2013, 27, (1), pp. 7386.

[15] Tomey-Bozo, N., Murphy, J., Troch, P., Babarit, A., Lewis, T., Thomas, G.: The modelling of a flap type wave energy converter in a time-dependent mild-slope equation model, Renewable Energies Offshore (2016), pp. 277284.

[16] Fabregas Flavia, F., McNatt, C., Rongere F., Babarit, A., Clement A.H. Computation of the Diffraction Transfer Matrix and the Radiation Characteristics in the open-source BEM code NEMOH, Proc. 35th International Conference on Ocean, Offshore and Arctic Engineering, Busan, South Korea, June 2016.

Appendix D

Paper D

Wake effect assessment of a flap type wave energy converter farm under realistic environmental conditions by using a numerical coupling methodology

Submitted to

Coastal Engineering

Authors

Nicolas Tomey-Bozo[1], Aurélien Babarit[2], Jimmy Murphy[1], Vicky Stratigaki[3], Peter Troch[3], Tony Lewis[1], Gareth Thomas[4]

[1]*MaREI Centre (ERI), University College Cork, Haulbowline Road, Ringaskiddy, Ireland*

[2]*Ecole Centrale de Nantes – CNRS, 1 rue de la Noé, 44300 Nantes, France*

[3]*Department of Civil Engineering, Ghent University, Zwijnaarde, Belgium*

[4]*School of Mathematical Sciences, University College Cork, Cork, Ireland*

Abstract

Ocean Energy Europe has estimated that 100 GW of ocean energy capacity (wave and tidal) could be deployed in Europe by 2050. Along with the European targets it is expected that large farms of Wave Energy Converters (WECs) will be installed in the sea and, as part of the consenting process for their installation, it will be necessary to quantify their impact on the local environment. The objective of this study is to improve the assessment of WEC farms impact on the surrounding wave field (wake effect) through the use of a numerical coupling methodology. The methodology consists of a Boundary Element Method (BEM) solver to obtain the wave perturbation generated by the WEC farm for the near-field accounting for the wave-body interactions within the farm whilst a Wave Propagation Model (WPM) based on the mild-slope equations determines the wave transformation in the far-field. The near-field solution obtained from the BEM solver is described as an internal boundary condition in the WPM and then it is propagated throughout the WPM numerical domain. The internal boundary is described by imposing the solution of the surface elevation and velocity potential at the free-surface at each instant of time along a line surrounding the WEC farm.

As a case study the methodology was applied to flap type WECs that are deployed in shallow water conditions. The validation of the technique was done first for a single flap and then for a farm of 5 flaps. Once validated, a realistic scenario was assessed by quantifying the impact of irregular sea states composed of long crested waves on a large WEC farm composed of 18 flaps and located on a real bathymetry. The irregular waves were obtained by superposing the regular wave field solutions for all wave frequencies represented in the considered sea state based on the linear water wave theory. Within the limits of this theory these simulations demonstrate the versatility of the methodology to accurately represent the impact of a WEC farm on the surrounding wave climate. The influence of the peak period and the spacing between flaps on the WEC farm wake effect was assessed as well.

D.1 Introduction

The presence of Wave Energy Converter (WEC) farms in the ocean will locally affect the wave climate. WECs are designed to absorb part of the incoming wave energy and therefore to reduce the amount of energy density in the lee side of the farm (wake effect). The quantification of the wake effect generated by a WEC farm is an important consideration in the consenting process for the deployment of these technologies. Furthermore, their potential capability to have a sheltering effect on other marine activities taking place in the lee of the farm may open various opportunities. For these reasons this study aims to improve the state of the art of the methodologies to quantify the wake effect generated by a WEC farm.

Some studies have used Wave Propagation Models (WPMs) to assess the far-field effect on the lee side of a WEC farm [1, 2, 3, 4, 5, 6, 7, 8, 9, 10] by representing intrinsically the devices as absorption cells or source terms. Others have assessed the near-field wave interactions between devices by using Boundary Element Method (BEM) solvers [11, 12]. References [13, 14] summarise and describe in detail all types techniques that have attempted to address this problem. WPMs are accurate solvers of the wave propagation throughout large domains considering realistic conditions such as irregular bathymetries and dissipative processes. However, these models do not accurately represent the local wave-body interactions and rely on external lookup tables describing the absorption capacity of the WECs in order to represent them inherently. BEM solvers are the opposite as they provide accurate solutions of the local wave-body interaction phenomena by solving the well-known boundary value problem but are limited in terms of the constant depth assumptions and the restricted-size numerical domains.

A coupling methodology is applied in this study to bridge the gap between the near-field results obtained from a BEM solver and the wave propagation in the far-field solved in a WPM based on the mild-slope equations. In previous studies such as those by [15, 16, 17, 18, 19, 20] similar coupling methodologies have been developed for point absorber WECs or surging barges for regular wave cases. In this study an improved methodology that uses a coupling technique which has applications to irregular sea states composed of long crested waves is presented. An internal boundary condition is described within the WPM for each regular wave frequency based on the perturbed wave field solution obtained from the BEM solver. The propagation of the perturbed wave is then solved throughout the rest of the domain within the WPM. The superposition of the two separated calculations, the perturbed wave field solved by applying the coupling technique and the incident wave field computed intrinsically, allows the computation of the total wave field for each frequency. The application of the methodology to a farm of various WECs and the superposition of the regular wave field solutions enables the assessment of WEC farm wake effects for realistic scenarios.

This paper presents an extension of the recent work published by the same authors in [21] where a preliminary version of the methodology was described. This study starts with the description of the numerical tools employed and their main governing equations. The proposed methodology is then outlined by describing the technical set up of the internal boundary that allows for the coupling between the two solvers. The coupling technique is validated first for a single-WEC case consisting of a flap type device, and then for a WEC farm composed of 5 devices. In order to validate the methodology the results are compared against BEM solver results by assuming constant water depths and error plots are then computed for both cases. A convergence analysis is carried out to assess the influence of the main numerical parameters on the results and define their optimum values. Then the wake effects for a large WEC farm composed of a large number of devices and located on a real

bathymetry is computed for irregular long crested waves in order to demonstrate the versatility of the methodology when considering real environmental conditions. The influence on the wake effect of the peak period for the considered sea state and the influence of the spacing between flaps are assessed as well.

D.2 Literature Review

The first work to apply a similar coupling technique to WECs was Reference [15]. The BEM commercial solver WAMIT®[22] was used to solve the near-field surrounding the device and MILDwave was used as WPM for the calculation of the far-field results. The internal boundary condition describing the near-field solution in MILDwave was described as a circular wave generation line based on the source term addition method from Equation (D.17) together with an inner sponge layer. The methodology was applied to point absorbers and each device was represented in MILDwave as an single internal boundary. Regular wave results were obtained for a farm of several devices and thus the interactions were calculated within the WPM by means of superposing each wave component.

As a continuation to this work, Reference [16] focused on the improvement of the angle discretisation of the circular wave generation line and the validation against pure BEM solver solutions. Good agreements were found but due to the reflection caused by the inner sponge layer (sponge layer used within the circular wave generation line) it was difficult to obtain completely consistent reference values for the angle discretisation of the circular wave generation line. The author of the current work applied later the same coupling technique to a flap type WEC in [23] and compared the wave field results against the sponge layer technique where the WEC is modelled intrinsically within the WPM as an obstacle. The same small inconsistencies related with the inner sponge layer reflection were found needing to tune the angle discretisation each time a different radius was used for the internal boundary.

The previous aforementioned studies led to more recent works were coupling methodologies have been progressively improved and applied to more complex scenarios making use of different types of solvers. References [9, 21, 24, 25] presented different cases of coupling techniques between the BEM solver NEMOH [26] and MILDwave [27, 19], a WPM based on the mild-slope equations. These studies were applied to point absorber and flap type WEC farms under regular waves and mild-slope bathymetries. The coupling technique applications were based on a description of the near-field perturbation generated by the WEC as an internal boundary where the solution from NEMOH is imposed at the boundary in MILDwave, and therefore there is no need of an inner sponge layer. Then References [28, 29] presented a coupling technique between NEMOH and OceanWave3D [30] to point absorber type WEC farms composed of up to 5 devices and where irregular waves scenarios and changing depth bathymetries were considered for medium-scale domains. Result comparisons with the coupling technique between NEMOH

and MILDwave and experimental data were undertaken showing very good agreements. Finally, references [31, 32] presented a coupling technique application between an SPH (Smooth Particle Hydrodynamics) solver and OceanWave3D for points absorber type WECs under regular waves.

References [17] and [18] adopted a similar coupling methodology between the BEM solver Aquaplus [33] (NEMOH nowadays) and the ARTEMIS module of Open TELEMAC-MASCARET [34], an open-source WPM. The Kochin function approximation was used to describe the fictitious island describing the wave perturbation generated by the WECs in the WPM. The methodology was applied to a farm of point absorber WECs under regular waves. The WECs were represented in ARTEMIS as individually separated internal boundary conditions and the interactions were computed within the WPM.

More recently Reference [20] developed a methodology where the so-called direct matrix method was adapted to the elliptic mild-slope equation. Based on a finite-element method the mild-slope equations were used to solve the effect of the bottom on the waves while the effect of the bodies was represented my means of the diffraction transfer matrices. The method was applied to solve regular waves solutions surrounding truncated vertical cylinders and surging barges that were compared against analytical solutions. The results are promising but the application cases are limited to regular waves.

In this study a one-directional coupling approach per regular wave solution is suggested between the BEM solver NEMOH [26] and the WPM MILDwave [27, 19] where an innovative set-up for the internal boundary is proposed. The methodology is applied to large WEC farms and then complex scenarios replicating real environmental conditions such as irregular sea states, large WEC farms, large domains, and real bathymetry scenarios, are computed in order to showcase the potential applications of the methodology. The internal boundary is defined by a wave generation line which implies that all cells along the line have a solution imposed based on the BEM solver results at the same location. The whole farm is computed within the BEM solver accounting for all interactions between devices and then the perturbed wave solution for the farm is propagated within the WPM. The versatility of the method is proven by adapting the internal boundary in the WPM to the shape of the WEC farm.

D.3 Numerical Tools Employed

Two main phenomena dominate in terms of the wake effect of a WEC farm: the wave-body interaction phenomena (near-field wave pattern) and the wave propagation throughout the rest of the numerical domain (far-field wave pattern). BEMs are selected as an appropriate tool to assess the local wave-body interaction in the near-field due to their high ratio of accuracy to computational time. These solvers are based on linear potential flow theory, thus while remaining below the assumption

of this theory they provide an accurate representation of the wave field surrounding a wave energy converter by solving the scattering problem. There exist solvers that represent the wave perturbation with high accuracy even above the limits of the linear wave theory such as Computational Fluid Dynamics (CFD) solvers but their extremely high computational time demand makes them unsuitable for the application cases presented in this work.

The far-field wave pattern was obtained using a phase-resolving WPM based on the mild-slope equations. These models solve wave-by-wave the propagation of linear water waves in the time domain accounting for the main transformation processes. Some models include dissipative processes such as bottom friction and wave breaking. Coupling the solution from the BEM for the near-field remains theoretically a feasible task due to the similarity in the governing equations between the two solvers. The two hydrodynamic solvers are described in the following section together with the governing equations of the problems assessed.

D.3.1 Linear wave theory

The two models employed in this study are based on the linear wave theory and the applicability of this theory relies on the assumption that we remain within its limits of application. The linear wave theory assumptions are that:

- The fluid is inviscid
- The flow is irrotational, meaning $\nabla \times V = 0$.
- The fluid is incompressible, leading to the continuity equation expressed as $\nabla \cdot V = 0$.

where the irrotationality condition allows describing the flow velocity V as the gradient of the velocity potential ϕ described by Equation (D.1):

$$V(x, y, z) = \nabla\phi \tag{D.1}$$

Equation D.1 together with the incompressibility condition leads to the Laplace Equation:

$$\nabla^2\phi = 0 \tag{D.2}$$

Seeking for a solution of the surface elevation $\eta(x, y, t)$ and velocity potential $\phi(x, y, z, t)$, a group of linearised boundary conditions at the free-surface and sea bottom are described assuming the wave amplitude is small with respect to the wavelength and water depth. The bottom condition ($z = -h(x, y)$) is given by Equation (D.3), and Equations (D.4) and (D.5) describe the kinematic and dynamic condition at the undisturbed free-surface ($z = 0$):

$$\frac{\partial\phi}{\partial z} = 0 \tag{D.3}$$

$$\frac{\partial \eta}{\partial t} = \frac{\partial \phi}{\partial z} \tag{D.4}$$

$$\frac{\partial \phi}{\partial t} + g\eta = 0 \tag{D.5}$$

where g represents the gravitational acceleration and the relation between η and ϕ is given by Equation (D.6)

$$\tilde{\eta}(x, y) = \frac{i\omega}{g}\tilde{\Phi}(x, y) \tag{D.6}$$

with Φ being the velocity potential ϕ at the free-surface condition $(z = 0)$, over-bar ($\tilde{}$) representing the complex form of the variable, and ω the angular wave frequency.

D.3.2 Open-source BEM solver NEMOH

NEMOH is an open-source BEM solver developed by Ecole Centrale de Nantes and is used in this work to obtain the near-field surrounding the WECs. NEMOH obtains the perturbed velocity potential as a 3D solution in the frequency domain from the linear wave-body interaction boundary value problem (or wave scattering problem) assuming constant water depth conditions. The wave scattering problem solves Laplace's equation (Equation (D.2)) assuming a set of boundary conditions composed of the bottom and free-surface boundary conditions described earlier in Equations (D.3), (D.4), and (D.5), and the body and scattering boundary conditions described next by Equations (D.7) and (D.8) respectively:

$$\frac{\partial \phi}{\partial n} = U \cdot n \tag{D.7}$$

$$\lim_{r \to +\infty} \phi_p = 0 \tag{D.8}$$

where ϕ_p represents the perturbed velocity potential generated by the presence of the body, U the velocity of the body when it is assumed to be rigid, n the normal vector to the body surface, and where $r^2 = (x^2 + y^2)$. The body boundary condition needs to be satisfied at the wetted surface of the body for its undisturbed position, describing the non-porosity of the body surface. The scattering boundary condition describes the complete dispersion of the perturbed velocity potential at the infinity of the domain.

The wave scattering problem is divided into one diffraction problem and one radiation problem per degree of freedom of the body motion. Both problems are solved individually for each wave frequency using the Green's function. From the resolution of these problems the diffracted velocity potential ϕ_d and radiated velocity potential ϕ_r are obtained, and the sum of the two solutions gives the perturbed velocity potential ϕ_p.

The diffraction problem is computed considering the body is fixed under the presence of an incoming incident wave velocity potential ϕ_i described by Equation (D.9) at the infinity of the domain and the boundary condition from Equation (D.10) at the body surface:

$$\tilde{\phi_i}(x,y,z) = -\frac{ig}{\omega} A f_0(z) e^{(i(k(x\cos\beta + y\sin\beta) - \omega t - \varphi))} \tag{D.9}$$

$$\frac{\partial \phi_d}{\partial n} = -\frac{\partial \phi_i}{\partial n} \tag{D.10}$$

where A is the corresponding incident wave amplitude, $f_0(z)$ is the depth dependence, k the wave number related to the wavelength by $k = 2\pi/\lambda$, and β the angle of propagation direction with respect to the X axis.

Then the radiation problem is solved by considering a forced motion of the body in calm conditions (absence of waves) assuming the boundary condition from Equation (D.11) for the body surface and assuming the amplitude of the body motion is small with respect to its characteristic length:

$$\frac{\partial \phi_{r,j}}{\partial n} = U_j \cdot n_j \tag{D.11}$$

where j represents each degree of freedom of the body motion.

In order to clarify the way a BEM solver computes the perturbed wave Figure D.1 shows a sketch representation of the scattering problem with the diffraction problem on top and the radiation problem bellow.

Using the principle of superposition the velocity potential for the total wave field ϕ_t in Equation (D.12) is calculated as a sum of the incident velocity potential described in Equation (D.9), and the diffracted and radiated velocity potential:

$$\tilde{\phi_t}(x,y,z) = \tilde{\phi_i} + \tilde{\phi_d} + \sum_{j=1}^{6} \tilde{\phi_{r,j}} \tag{D.12}$$

Then from the velocity potential at the free-surface condition ($z = 0$) it is straightforward to obtain the surface elevation for the total wave field from Equation (D.6).

D.3.3 Wave propagation model MILDwave

MILDwave is used in this study to solve the wave transformation processes throughout large domains and obtain the far-field wave pattern to assess the WEC farm wake effect. MILDwave is a time-dependent mild-slope equation model developed by Ghent University and is a phase-resolving type WPM. The model solves the propagation of surface waves throughout the domain and the interaction with obstacles (previously defined) by solving the depth-integrated mild-slope equations of Radder and Dingemans [35] (Equations (D.13) and (D.14)). These equations describe the

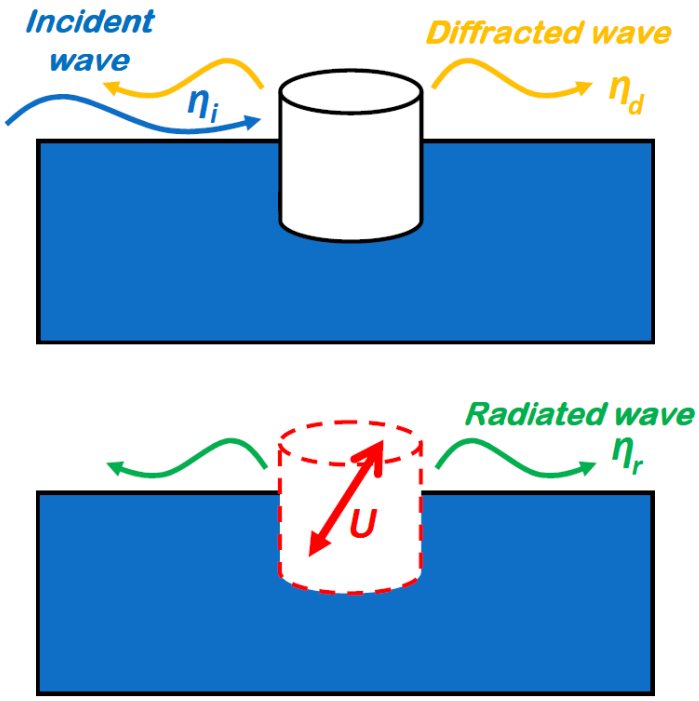

FIGURE D.1: Sketch representation of the diffraction problem (top) and radiation problem (bottom).

transformation of linear regular and irregular waves with a narrow frequency band over a mild slope bathymetry (bed steepness up to 1/3 [36]):

$$\frac{\partial \eta}{\partial t} = B_c \Phi - \nabla \Delta (A_c \nabla \Phi) \tag{D.13}$$

$$\frac{\partial \Phi}{\partial t} = -g\eta \tag{D.14}$$

η and Φ represent respectively the surface elevation and velocity potential at the free-surface level, t represents the time, and g is the gravitational acceleration. The values of B_c and A_c are calculated using Equations (D.15) and (D.16):

$$B_c = \frac{\omega^2 - k^2 C C_g}{g} \tag{D.15}$$

$$A_c = \frac{C C_g}{g} \tag{D.16}$$

with the phase velocity C and the group velocity C_g. The complete derivation of these equations can be found in [15].

A finite difference scheme is used to discretise and solve Equations (D.13) and (D.14) which consists of a two-step space-centred and time-staggered computational grid. The domain is divided in grid cells with dimensions Δx and Δy and central

differences are used for spatial as well as time derivatives. Both η and Φ are calculated in the centre of each grid cell at different time levels, $(n+\frac{1}{2})\Delta t$ and $(n+1)\Delta t$ respectively, where Δt is the time step and n represents the step cycle.

Incident waves are generated in MILDwave at the offshore boundary by using the source term addition method, i.e. by adding an additional surface elevation η^* to the calculated value on a wave generation line for each time step given by Equation (D.17) as described in [37]:

$$\eta^* = 2\eta_i \frac{C_e \Delta t}{\Delta x} \sin\beta \tag{D.17}$$

with η_i the water surface elevation of incident waves derived from Equation (D.6) and (D.9), Δx the grid cell size in X direction, and C_e the energy velocity. The wave generation line is assumed to be parallel to the Y axis.

D.4 Flap Type Wave Energy Converter

D.4.1 Flap description

The flap type WEC is the technology to which the case scenarios are applied since it is a type of WEC perturbing significantly the incoming wave field and thus an appropriate application case to validate the methodology. The flap type WEC is defined as a surface-piercing flap hinged at the bottom of the seabed as shown in Figure D.2. The motion is restricted to pitch therefore only one degree of freedom is considered. The shaft about which the flap rotates is at the base of the device. Table D.1 shows the main characteristics of the flap where the relative density ρ_r defines the density of the WEC compared to the water density. The thickness t is not represented in the sketch since it has a small value compare to the rest of dimensions.

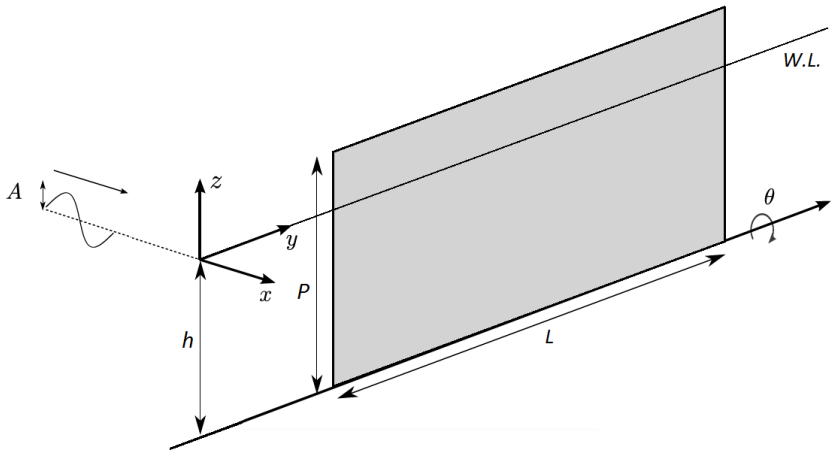

FIGURE D.2: Sketch representation of the flap type WEC

TABLE D.1: Main characteristics of the flap type WEC.

Parameter	Coefficient	Value	Units
Length	L	20	m
Height	P	12	m
Thickness	t	1	m
Relative density	ρ_r	0.3	-

D.4.2 Flap dynamic modelling

The amplitudes of rotation for each flap are calculated based on Equation (D.18) for each angular wave frequency ω. The hydrodynamic coefficients Γ, A_r and B_r, are obtained from NEMOH where Γ represents the excitation force coefficient, and A_r and B_r are the radiation added inertia and radiation damping coefficients. The hydrostatic coefficient H and the moment of inertia I are calculated based on the geometry description from Table (D.1). The Power Take Off (PTO) damping coefficient B_{PTO} is calculated based on Equation (D.19).

$$\Theta(\omega) = \frac{A\Gamma(\omega)}{-\omega^2(I + A_r(\omega)) - i\omega(B_r(\omega) + B_{PTO}) + H} \tag{D.18}$$

The resultant values of the rotation amplitude are used to quantify the radiated wave solution obtained from NEMOH, which is first obtained in a non-dimensional form relative to a unit of rotation amplitude (see Section D.5.2). In the case of a farm where various WECs are considered within the BEM solver, the terms composing Equation (D.18) are expanded to j dimensions where j represents the number of degrees of freedom of body motion (one per device in this case). The expanded form of the equation of motion takes account of all interactions between WECs and therefore determines the rotation amplitude for each device whilst the presence of the surrounding moving devices.

A passive PTO composed of a damper is used in this study. This configuration was chosen to represent a hydraulic PTO which is usually employed for the flap type WECs. Equation (D.19) defines the optimum value of the PTO damping coefficient for a specific wave frequency which is theoretically demonstrated in [38]. In the case of an irregular sea state composed of many wave frequencies a fixed value of the PTO damping coefficient was assigned considering the overall statistics of the sea state instead of an optimal value for each frequency that would be constantly changing in time. Thus, the peak angular wave frequency ω_p of the considered sea state is applied as a fixed optimum value.

$$B_{PTO} = \sqrt{\left(\frac{H}{\omega_p} - \omega(I + A_r(\omega_p))\right)^2 + B_r(\omega_p)^2} \tag{D.19}$$

D.5 Methodology

D.5.1 General approach

The methodology is applied to regular waves that are then post-processed to obtain the corresponding irregular sea state based on a considered incident wave spectrum. Each regular wave solution is composed of an incident wave and a perturbed wave solution that are superposed to obtain the total wave. As a first step the incident wave is solved intrinsically in MILDwave by means of a wave generation line located at the up-wave side of the domain that allows the wave to propagate towards the X positive axis. The incident wave is generated by using the usual source term addition method from Equation (D.17). As a separated calculation, the perturbed wave is obtained by means of a coupling technique that merges the near-field results surrounding the WEC farm from NEMOH into MILDwave as an internal boundary condition that allows for the propagation of the wave towards the rest of the domain.

The perturbed wave is quantified based on the amplitude obtained for the incident wave calculation at the centre of the WEC farm ($X = 0\ m$ and $Y = 0\ m$) and both are synchronised in phase, considering the reference of the incident wave phase been 0 at the same location. Figure D.3 shows a sketch of the methodology representing both calculations, the perturbed wave and the incident wave.

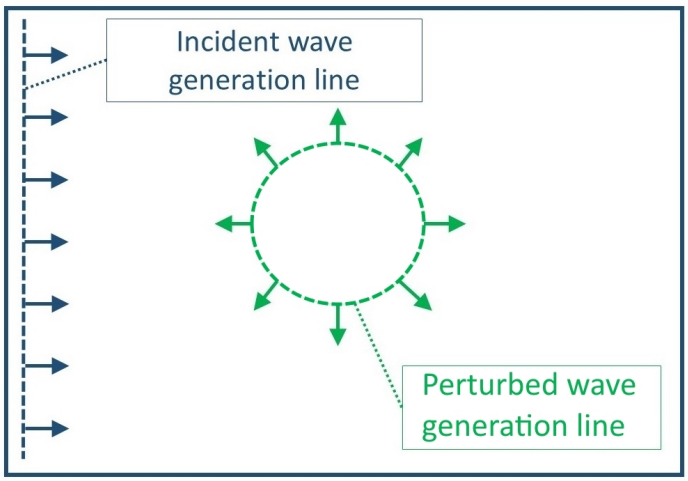

FIGURE D.3: Methodology description sketch.

D.5.2 Coupling technique description

The internal boundary condition is described in this work as a wave generation line where the solution obtained from the BEM solver is imposed at each grid cell along the line surrounding all devices from the WEC farm. As described in Section D.3.3, MILDwave solves the instantaneous surface elevation and the velocity potential at the free-surface for each instant of time. Thus, these two variables are imposed along the wave generation line (black doted line in Figure D.4) at each time step in order

to propagate the wave towards the far-field. The near-field solution is given by the BEM solver and the far-field solution is given by the WPM, as illustrated by Figure D.4.

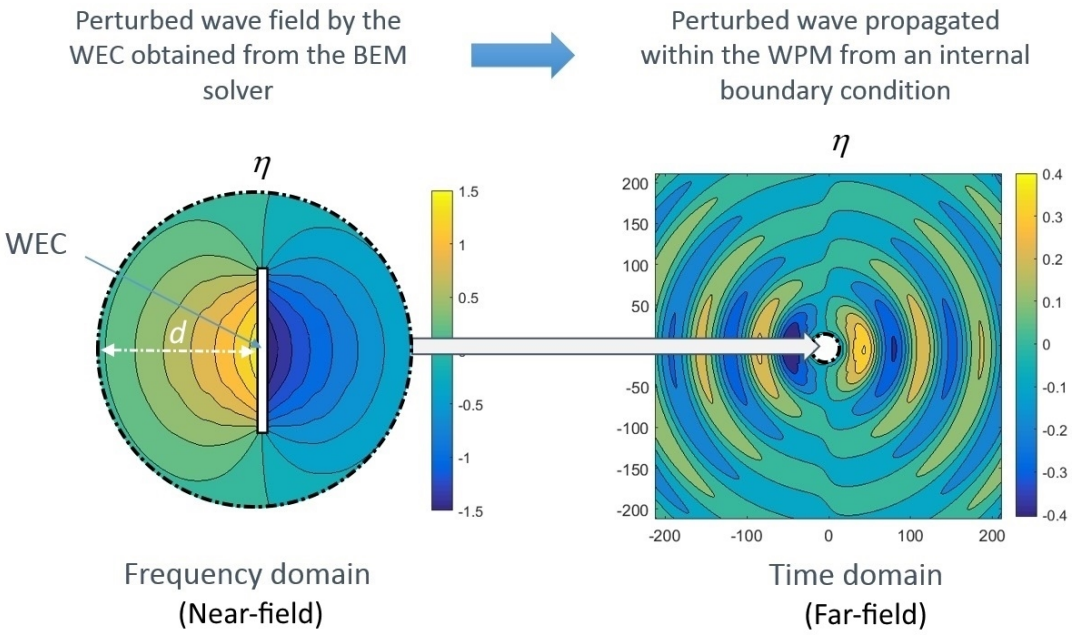

FIGURE D.4: Coupling technique description between the BEM solver and the WPM.

The perturbed wave field solution is obtained from NEMOH in the frequency-domain in terms of wave amplitude A_N and phase φ_N. These are then transformed by Equations (D.20) and (D.21) into the time-domain variables η_{MW} and Φ_{MW} to be imposed in MILDwave at each instant of time at the internal boundary location, i.e. along all grid cells defining the wave generation line. Subscripts N refer to variables obtained from NEMOH and subscripts MW refer to variables imposed in MILDwave. Due to the computational time-staggering in MILDwave between η and Φ, the solution for both variables is imposed with half a time step difference:

$$\eta_{MW}((n+\frac{1}{2})\Delta t) = A_N(\omega)\cos(\varphi_N(\omega) - \omega((n+\frac{1}{2})\Delta t)) \tag{D.20}$$

$$\Phi_{MW}((n+1)\Delta t) = \frac{g}{\omega}A_N(\omega)\sin(\varphi_N(\omega) - \omega((n+1)\Delta t)) \tag{D.21}$$

The size and shape of the internal boundary can be adapted to the geometry of the WEC farm under consideration, even though a minimum margin distance d of 15 m is recommended between the boundary and the centre of the closest device (see Section D.8.4). The mandatory requirement is that the line describing the internal boundary needs to surround completely the WEC farm in order to represent the complete wave energy flux of the perturbed wave.

D.6 Application to a Single WEC Case

D.6.1 Comparison between MILDwave and NEMOH

The methodology was first applied to a single WEC case and constant water depth conditions for validation purposes. Since BEM solvers only consider constant water depth conditions the comparison needs to be done under these conditions. The aim of this comparison is to validate that the same perturbed wave from the BEM solver can be reproduced within the WPM with high accuracy applying the coupling technique by means of an internal boundary. Figure D.5 shows the comparison between the wave field results obtained intrinsically in NEMOH (left) and by applying the coupling methodology in MILDwave (right) for the same domain. The results represent the perturbed wave field solution corresponding to an incident wave period T of 8 s and amplitude A of 1 m across a domain of 400 x 400 m. The wave results are plotted in terms of wave amplitude and wave phase (frequency domain variables) for both solvers results in order to facilitate the comparison between the frequency domain results from NEMOH and the time domain results from MILDwave.

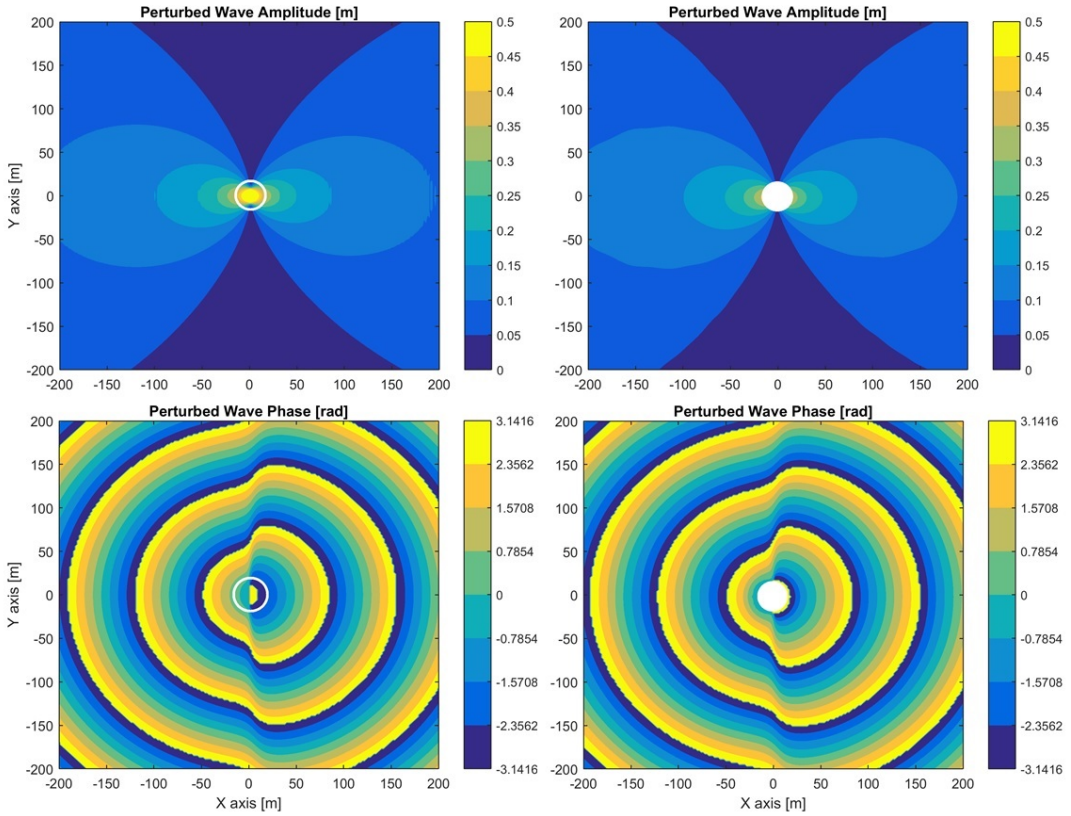

FIGURE D.5: Perturbed wave amplitude and phase obtained in NEMOH (left) and MILDwave (right) for a single flap.

First the perturbed wave field surrounding the single flap is obtained in NEMOH. A circle surrounding the flap delimits the area corresponding to the near-field and far-field (inner and outer domain respectively) and describes the wave generation

line in MILDwave as shown in Figure D.4. In this case a circle of radius equal to 25 m is used to define the line where the solution from NEMOH is imposed in MILDwave, at the same location with respect to the WEC. The surface elevation and velocity potential are imposed along the generation line at each instant of time and propagated throughout the rest of the domain. The empty disc in the middle of the domain represents the location where the solution is given by NEMOH and thus its outer limit represents the internal boundary.

D.6.2 Error between MILDwave and NEMOH

Figure D.6 shows the percentage error between the perturbed wave field obtained from MILDwave and that obtained from NEMOH, relative to the average wave amplitude along the boundary that delimits the near-field and far-field. The error is calculated based on Equation (D.22) where A_M is the wave amplitude result from MILDwave, A_N the wave amplitude result from NEMOH, and $\bar{A_N}$ the mean value of the wave amplitudes obtained from NEMOH all along the boundary line. The results from NEMOH are considered here as a target solution and the comparison is possible due to the constant water depth assumptions of this case scenario.

$$\epsilon(\%) = \frac{A_N - A_M}{\bar{A_N}} \tag{D.22}$$

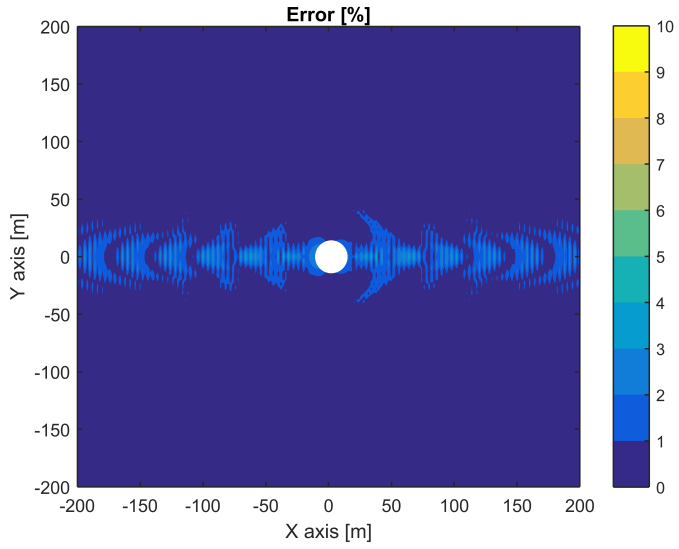

FIGURE D.6: Percentage error between MILDwave and NEMOH results for a single flap

A small error is present across the $Y = 0$ section with overall error values remaining below 4%. Outside this section the error is less than 1%. The error is relatively larger across the $Y = 0$ section zone since the wave amplitude values are larger at this location. The error remains very small and well within acceptable values considering that the maximum percentage error of 4% corresponds to an absolute

difference of $0.0036\ m$, as the average perturbed wave amplitude $\bar{A_N}$ is equal to $0.09\ m$.

D.7 Application to a WEC Farm Case

In this section the methodology is applied to a farm of 5 flaps. The farm is composed of two rows, an up-wave row with 3 flaps and a down-wave row with 2 flaps as illustrated in Figure D.7. The lateral spacing between devices S is $40\ m$ and the spacing between rows R is $40\ m$. The down-wave row of flaps is staggered and placed in front of the gaps from the up-wave row.

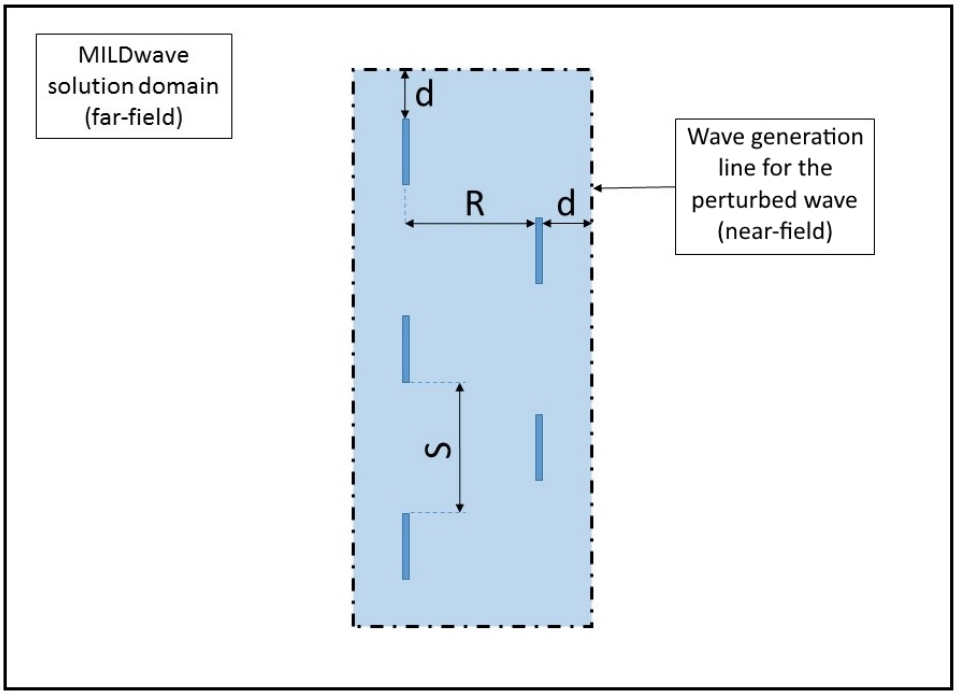

FIGURE D.7: Sketch of the 5 flaps WEC farm layout and the rectangular boundary.

D.7.1 Comparison between MILDwave and NEMOH

The same incident wave conditions ($T = 8\ s$ and $A = 1\ m$) and constant water depths as previously outlined are considered. In this case the shape of the near-field is a rectangle that fits the form of the WEC farm by leaving a margin distance d of 15 m between the boundary and the centre of the closest device. The dimensions of the rectangle are $60 \times 160\ m$ (X and Y axis respectively). The perturbed wave solution considering all interactions was computed in NEMOH and was then inserted into MILDwave by means of wave generation line of rectangular shape surrounding the near-field. In this case the perturbed wave field from NEMOH was obtained from

the superposition of the diffracted wave and the 5 radiated waves corresponding to the motion of each WEC.

Figure D.8 shows the perturbed wave amplitude and phase obtained in NEMOH (left) and MILDwave (right) for the 5 flaps case. The same domain size is used again in order to validate the results with the target perturbed wave obtained from NEMOH assuming constant water depths. A rectangle delimits the near-field and far-field area and describes the location of the boundary between the two solvers. Again, the rectangle is empty for the MILDwave calculation since the near-field solution is given by the results obtained with NEMOH.

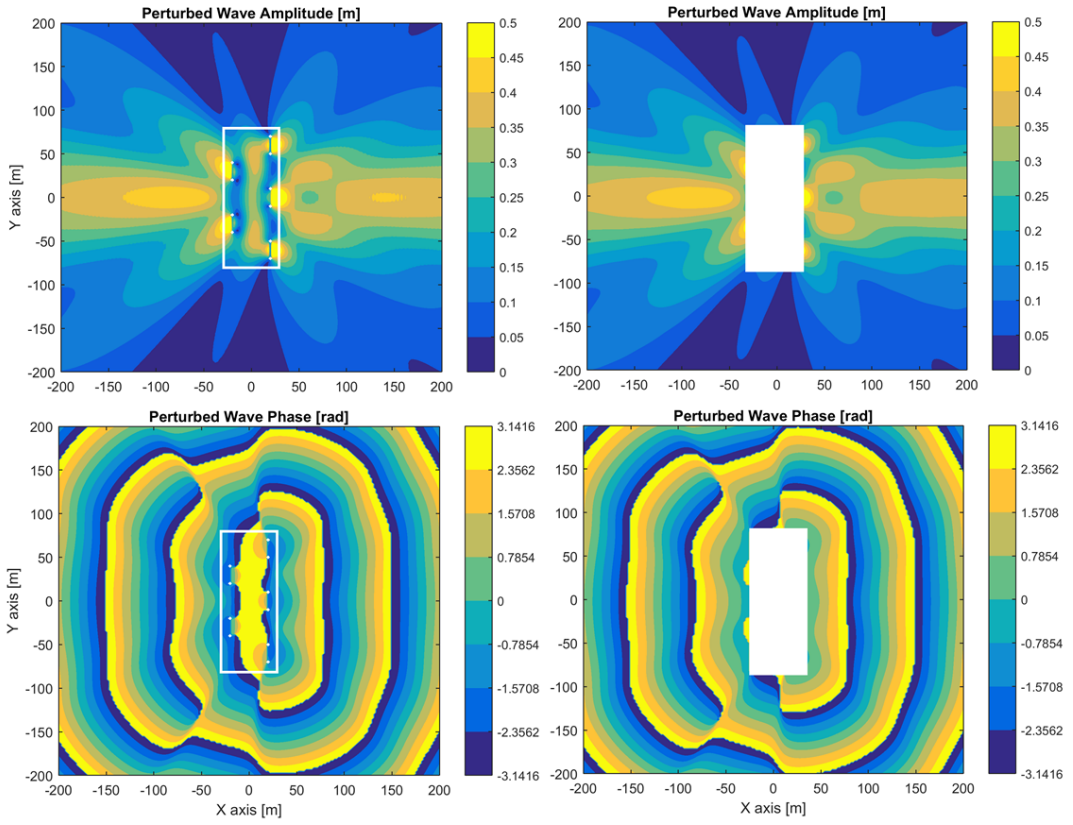

FIGURE D.8: Perturbed wave amplitude and phase obtained NEMOH (left) and MILDwave (right) for 5 flaps.

D.7.2 Error between MILDwave and NEMOH

The percentage error between the perturbed wave obtained from MILDwave and from NEMOH is shown in Figure D.9 along the whole domain. The maximum error appears along section $Y = 0$ with values remaining below 2%. Again the error is larger along this section due to the fact that in this zone the perturbed wave amplitude values are the largest in the domain. The error is small considering a percentage error of 2% corresponds to an absolute difference of $0.0055\ m$, as in this case the mean wave amplitude $\bar{A_N}$ along the boundary corresponds to $0.27\ m$. Therefore, a

very good agreement is found for both applications of the coupling technique, i.e. the single flap case and the 5 flaps case.

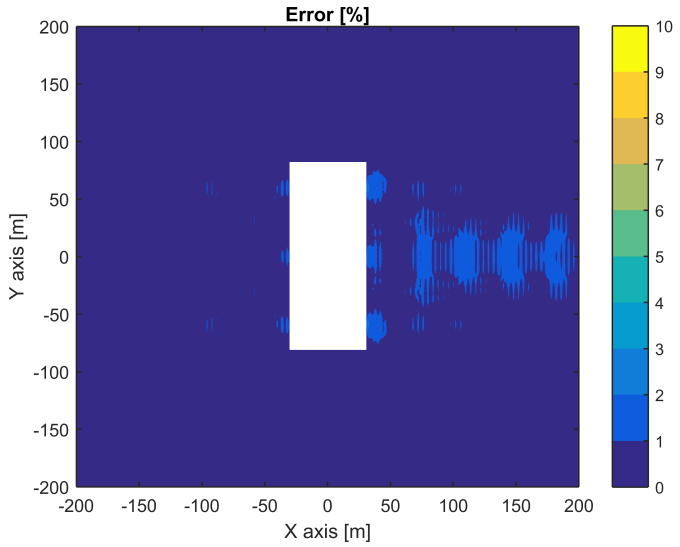

FIGURE D.9: Percentage error between MILDwave and NEMOH results for 5 flaps.

This application case shows the flexibility of the methodology to adapt the near-field area to the shape of the WEC farm. Whether described by a circular or a rectangular shape the internal boundary allows the computation of the perturbed wave in MILDwave with very good agreement.

D.8 Convergence Analyses

Prior to the calculations from Sections D.6 and D.7 convergence analyses were carried out in order to investigate the optimal values of the main numerical parameters involved in the coupling methodology, i.e. grid cell size, time step, wave length limits, and near-field area size. Based on the results from the analyses optimal values were assigned to these parameters in order to find the best match in the comparison between MILDwave and NEMOH. These analyses were carried out based on the single flap case study from Section D.6.

In the following section the details of the analyses are presented in terms of percentage error with respect to the target values from NEMOH. The error is calculated by replacing the dividing term $\bar{A_N}$ from Equation (D.22) by the incident wave amplitude A_i (equal to 1) in order to simplify the comparison between the different analyses. The error values shown in the plots from Sections D.8.1, D.8.2, D.8.3, and D.8.4, represent the maximum error obtained along the domain of 400 x 400 m. The computational cost was not included in the convergence analysis since all calculations remain under a very low simulation cost, of the order of seconds for the cases

considered in this section. Therefore at this stage of the methodology development the priority was given to the error decrease.

D.8.1 Time step

The reference time step value given by the MILDwave developers in order to ensure a stable computation is $\Delta t \leq \Delta x/C$ [27] which represents the Courant-Friedrichs-Lewy criterion. Based on this reference, several cases were run for values of $\Delta t = 0.02\Delta x/C$ to $\Delta t = \Delta x/C$ considering the same regular wave of $A = 1\ m$ and $T = 8\ s$ from previous sections. However above values of $\Delta t = 0.65\Delta x/C$ the calculations became unstable and could not be achieved. The results obtained from the analysis are shown in Figure D.10 where the lowest error obtained was 0.36% remaining relatively constant for all values between $\Delta t = 0.1\Delta x/C$ and $\Delta t = 0.65\Delta x/C$.

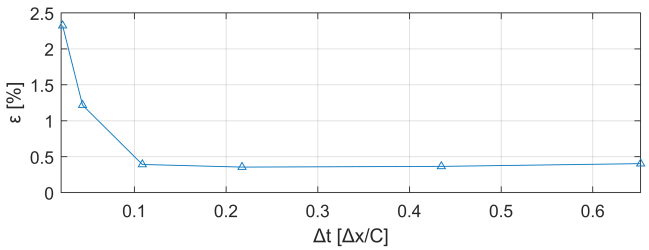

FIGURE D.10: Maximum error vs. time step.

D.8.2 Grid cell size

In the case of the grid cell size the reference values for MILDwave are $\lambda/20 \leq \Delta x \leq \lambda/10$ [27] for non-breaking waves where λ represents the wave length. These values are based on deep water conditions therefore a shift in the recommended range towards lower values can be found when considering shallow water conditions as in the case of this work. In this analysis cases were run for values of $\Delta x = \lambda/140$ to $\Delta x = \lambda/8$ where the same regular wave of $A = 1\ m$ and $T = 8\ s$ was considered. The convergence was obtained for values lower than $\Delta x = \lambda/30$, reaching the minimum error of 0.36% and remaining constant until $\Delta x = \lambda/140$.

D.8.3 Wave length

Following the same reference of $\lambda/20 \leq \Delta x \leq \lambda/10$ for the ratio between the wave length and grid cell size, an analysis of the influence of the wave length on the error was carried out considering a fixed grid cell size. The results obtained are shown in Figure D.12. In this case the error fluctuates considerably due to the influence of the absorption layers at the up-wave and down-wave boundaries of MILDwave that are adjusted in width for each wave period. A convergence was still achieved around values with an average error of 0.8% located between $\lambda = 20\Delta x$ and $\lambda = 90\Delta x$. The

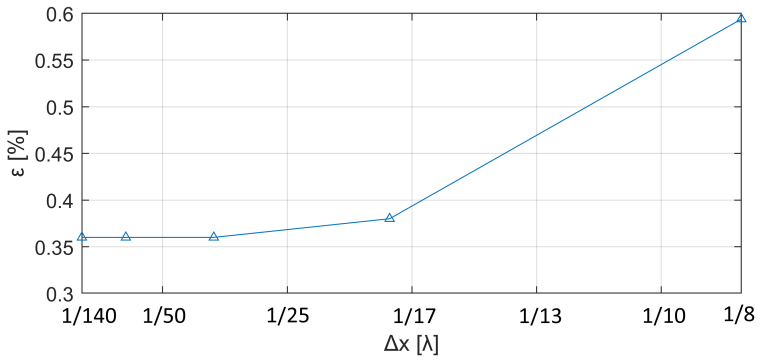

FIGURE D.11: Maximum error vs. grid cell size.

lowest error of 0.36% was found for values close to $\lambda = 35\Delta x$ and this is considered to be the optimal case.

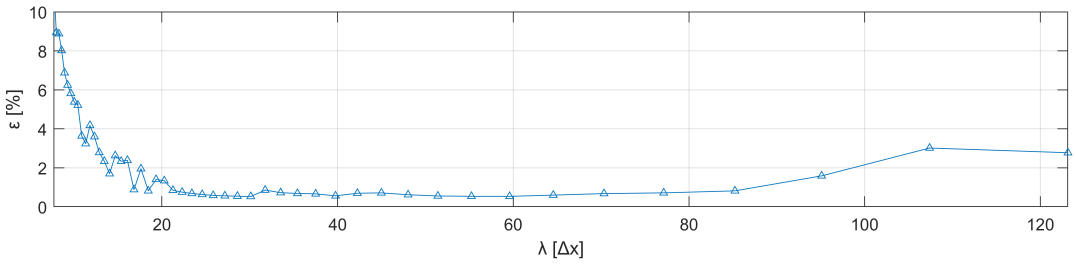

FIGURE D.12: Maximum error vs. wave length.

This analysis proved the importance of considering the wave lengths limits (and therefore wave frequency limits) that can be used with the same grid cell size when running sea states characterised by many different wave frequencies. In the case of irregular sea states composed of a superposition of regular waves, a fixed grid cell size can be applied to a all frequencies if the correct grid cell size is chosen so that all results remain under an error of 1%. This is achievable if the Δx and Δt are chosen to be optimum for the wave length corresponding to the peak wave period T_p of the sea state.

D.8.4 Near-field area size

Here a convergence analysis for the size of the near-field area enclosed by the boundary was achieved in order to find the smallest area that provides a good agreement. The margin distance d, defined as the shortest distance between a device and the boundary, was changed for each case from $d = \lambda/35$ to $d = \lambda/2$. The error clearly converges as d increases reaching an optimum value at $d = \lambda/5$ as shown in Figure D.13. Thus, a minimum margin distance $d = \lambda/5$ needs to be left when defining the size of the near-field area in order to maximise the accuracy of this coupling technique. However, lower values of d are acceptable as well since the error remain below 1% for all cases. It is important to notice that the area corresponding to the

near-field in MILDwave assumes constant water depth conditions and thus the interest on keeping its size as reduced as possible.

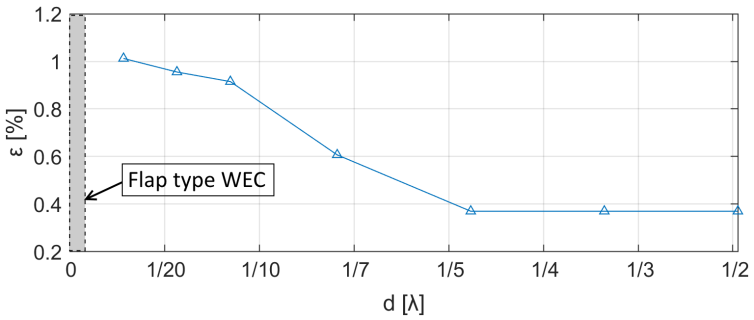

FIGURE D.13: Maximum error vs. near-field area size.

D.9 Wake Effect Assessment for a WEC Farm

The wake effect for a farm composed of 18 flaps was computed in this section using a large domain, irregular long crested waves, and a mild-slope bathymetry. The aim is to demonstrate step by step the calculations carried out to assess the wake effect for a realistic WEC farm case scenario. A domain of 1500 x 3000 m (Y and X axis respectively) was chosen as it gives a greater scope to assess the wake effect in the far-field.

In this case the WEC farm is composed of 4 rows where the first and third row are composed of 4 flaps and the second and fourth of 5 flaps as shown in Figure D.14. The lateral spacing between devices S and spacing between rows R are 100 m and 44 m respectively. The spacings S and R were defined based on the assessment carried out in a previous publication [7] where the WEC farm layout was chosen based on the available wave energy resources, i.e. wave energy density. The centre of the WEC farm is located along section $X = -500$ m and centred with respect to the Y axis at a water depth h of 10 m, which is the constant water depth assumed for the near-field solution in NEMOH.

The farm is located on a changing bathymetry which is defined by a linear mild-slope with the depth decreasing towards the X positive axis direction, the same direction than the wave propagation direction. The bathymetry profile ranges in water depths between 12 and 6 m with a small section where constant water depths are assumed for the WEC farm location as shown in Figure D.15.

D.9.1 Regular waves

Irregular long crested waves are calculated as a sum of the regular waves that compose the sea state, based on the superposition principle from linear water wave theory. The first step is to calculate the total wave amplitude for each regular wave

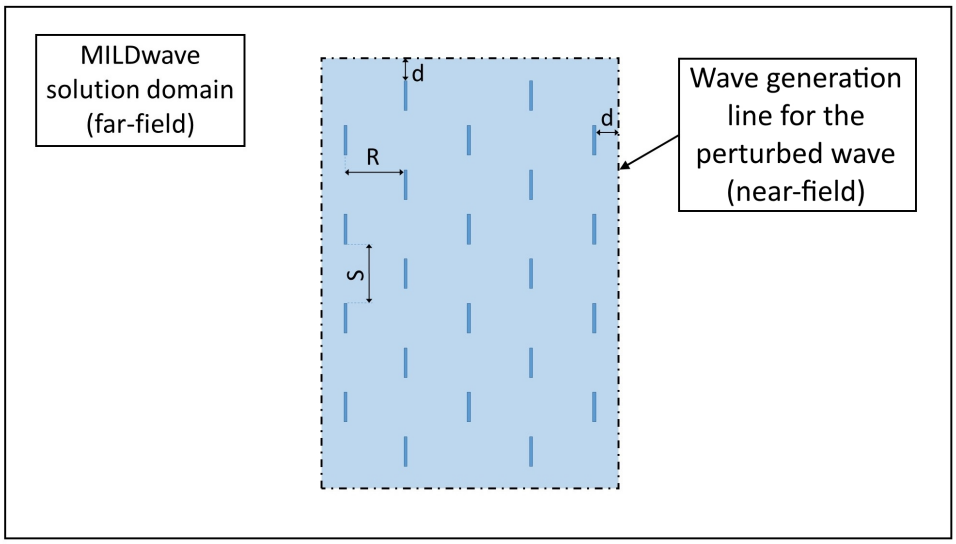

FIGURE D.14: Sketch of the 18 flaps WEC farm layout and the rectangle boundary.

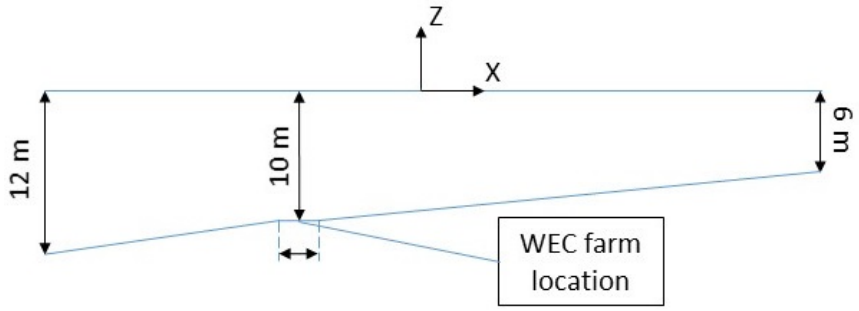

FIGURE D.15: Mild-slope bathymetry profile.

across the whole domain. Each total wave is composed of an incident wave propagated in an empty domain (absence of WEC farm) calculated intrinsically in MILDwave and a perturbed wave created by the presence of the WEC farm obtained by means of the coupling technique. The perturbed wave is computed based on the amplitude and phase of the incident wave solution at the centre of the WEC farm.

Figure D.16 shows the incident, perturbed, and total wave amplitude for an example of a regular wave of $T = 8\ s$ and $A = 1\ m$ on a mild-slope bathymetry. For the case of the perturbed wave plot, the near-field and far-field results are shown together, proving there is no discontinuity between the domain solved by NEMOH and the domain solved by MILDwave.

D.9.2 Irregular waves

Given a specific incident irregular sea state, the local changes in the wave spectral density can be obtained for each grid cell along the domain based on the regular wave solutions. The relation between the wave spectral density and the total wave

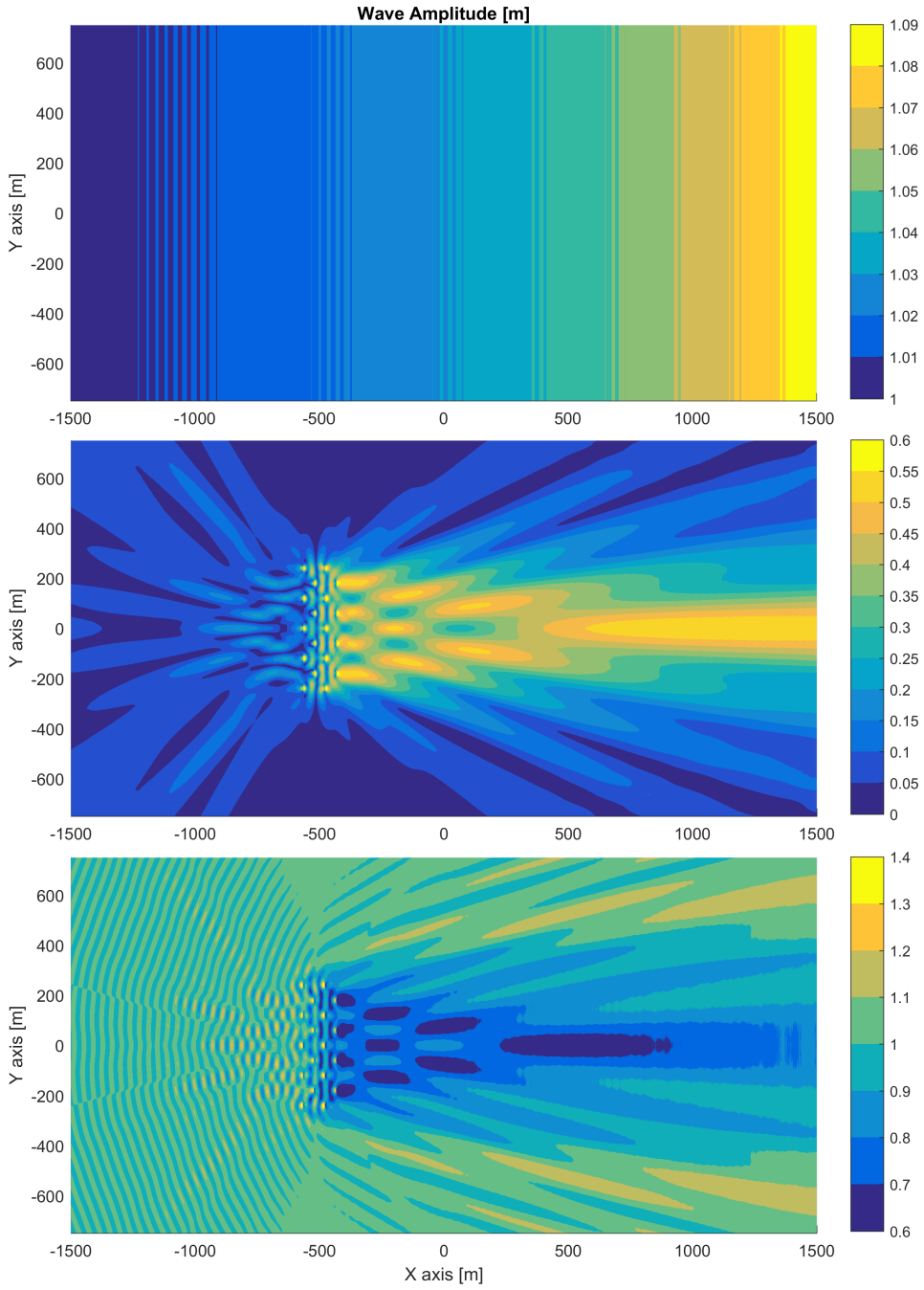

FIGURE D.16: Incident (absence of WEC farm), perturbed (presence of WEC farm), and total wave amplitude for a 18 flaps farm on a mild-slope bathymetry.

amplitude for each frequency interval is defined by Equation (D.23) which allows the determination of the spectral density distribution of the sea state along the frequency range. A range of 50 regular frequencies have been used in this work to discretise the irregular sea states.

$$S(\omega)\Delta\omega = \frac{1}{2}A^2(\omega) \tag{D.23}$$

The wave spectral density S changes along the domain with the water depth h and with the disturbance generated by the WEC farm. Thus, in order to assess the WEC farm disturbance the spectral density distribution is obtained for the undisturbed sea state S_u, in the absence of the WEC farm, and then for the disturbed sea state S_d, in the presence of the WEC farm. In the case of the undisturbed sea state the wave amplitude A corresponds to the incident wave amplitudes for each wave frequency and in the case of the disturbed sea state it corresponds to the total wave amplitude. Figure D.17 shows an example of the change in the wave spectral density due to the presence of a WEC farm for a grid cell centrally located 150 m down-wave of the farm ($X = -350$ m and $Y = 0$ m). From the significant wave height for S_u and S_d the WEC farm disturbance is quantified by the disturbance coefficient K_d described by Equation (D.24).

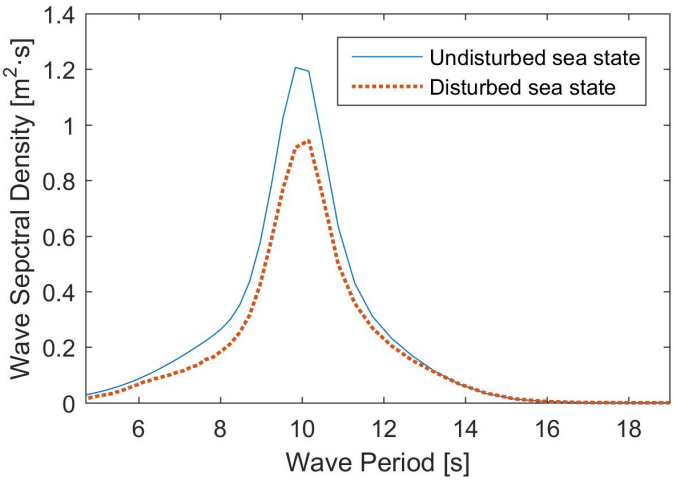

FIGURE D.17: Wave spectral density disturbance at a grid cell point located in the lee side of the farm for irregular waves.

$$K_d = \frac{H_{Sd}}{H_{Su}} \tag{D.24}$$

where H_{Sd} and H_{Su} are the significant wave height for the disturbed and undisturbed sea state respectively at each grid cell of the numerical domain.

The disturbance coefficient can be now obtained for the whole domain to evaluate the disturbance generated by the WEC farm on the surrounding wave field (so-called wake effect). Figure D.18 shows the disturbance coefficient K_d for three incident sea states of peak periods (T_p) of 8 s, 10 s, and 12 s, and significant wave height (H_s) of 2 m. However, due to the linear wave theory assumptions the K_d value is not dependent on the significant wave height and the incident sea state is defined here only by the peak period. The PTO system of each flap has been tuned for every sea state according to Equation (D.19) based on the peak angular wave frequency ω_p.

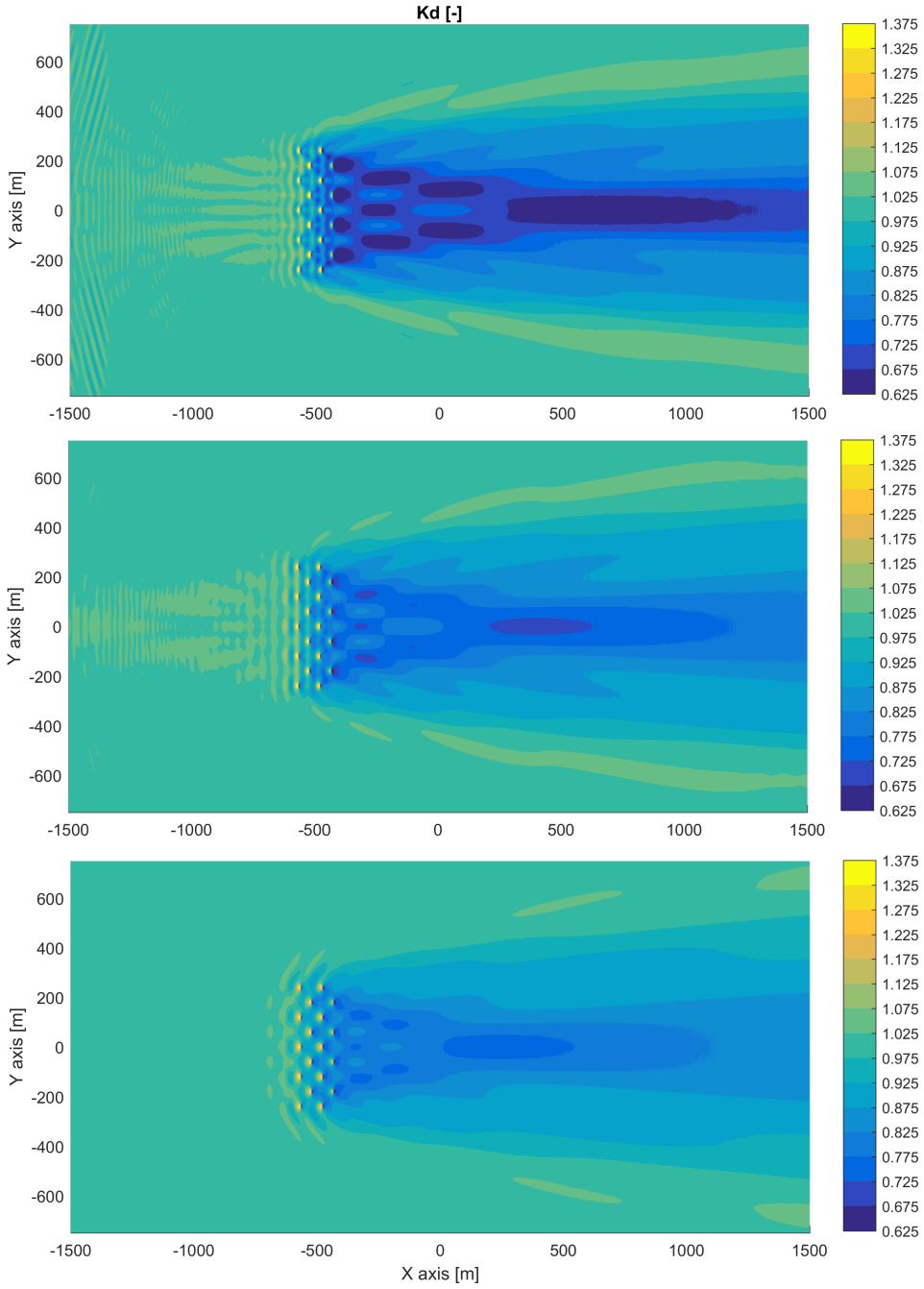

FIGURE D.18: Disturbance coefficient for a 18 flaps farm on a mild-slope bathymetry for sea states of T_p equal to 8 s, 10 s, and 12 s (from top to bottom).

The wake effect for the studied WEC farm shows a large wave height decrease behind the WEC farm that persists into the far field at least until 2 km down-wave from the farm. A large difference is found between the different sea states due to the wave energy absorption capacity of the WECs. The WECs power extraction reaches a saturation at certain sea states depending mainly on the dimensions of the device, instead of keep increasing with the higher energy sea states. Thus, for the same

WEC farm power absorption, the higher the peak period is the less pronounced is the decrease in the disturbance coefficient.

The flap type device was modelled as it is one of the technologies that most affects the incoming wave field. Due to its vertical orientation the device extends through the full water column and acts as a submerged moving barrier. Therefore the wave height reduction is expected to be more significant than for other WEC technologies.

Considering an area in the lee-side of the WEC farm from a minimum distance of 500 m ($X = 0\ m$) behind the farm and up to the far-field, the lowest K_d values are found for the sea state of $T_p = 8\ s$ with minimum values around 0.65 (equivalent to 35% of significant wave height reduction) and average values varying between 0.85 and 0.65 (15% and 35% reduction, respectively). The reduction effect progressively decreases with increasing the peak period, with values ranging between 30% and 10% of reduction for $T_p = 10\ s$, and between 25% and 10% of reduction for $T_p = 12\ s$. If a larger distance was considered in the lee-side of the farm the K_d values will progressively increase towards far-field reaching eventually at a certain point values equal to 1, meaning that the wave energy flux recovers because of diffraction.

D.10 Influence of the WEC Lateral Spacing

The lateral spacing between the WECs of the farm (S) is a significant parameter in terms of the wake effect since it affects the interactions between WECs and thus their wave energy absorption. The larger the lateral spacing is the less each WEC is influenced by the surrounding WECs and therefore the WECs dynamics will be closer to the case of an isolated WEC. Also the diffraction phenomenon is significantly affected by the spacing between WECs, which is quantified by the ratio between the wave length corresponding to the peak period and the shortest lateral spacing between WECs. Thus, changing the lateral spacing can lead to significant differences in the WEC farm wake effect.

Figure D.19 shows the disturbance coefficient K_d obtained for a WEC farm composed of 9 flaps in a single row where S was set to $4L$, $5L$, and $6L$ (L equal to the WEC length) respectively (top to bottom) and a sea state of T_p equal to 8 s. The same mild-slope bathymetry as shown in Figure D.18 was used but the average K_d values obtained in the farm lee-side are smaller since the number of devices and rows is reduced. It is clear that the lateral spacing affects the wave height reduction behind the farm. As expected, the larger the WEC lateral spacing is, the lower is the wave height decrease in the lee-side of the WEC farm. The area in the lee-side of the farm corresponding to K_d values ranging between 0.875 and 0.925 (12.5% and 8.5% wave height reduction respectively) becomes progressively reduced in size by increasing the lateral spacing S and it nearly disappears for the case of $S = 6L$.

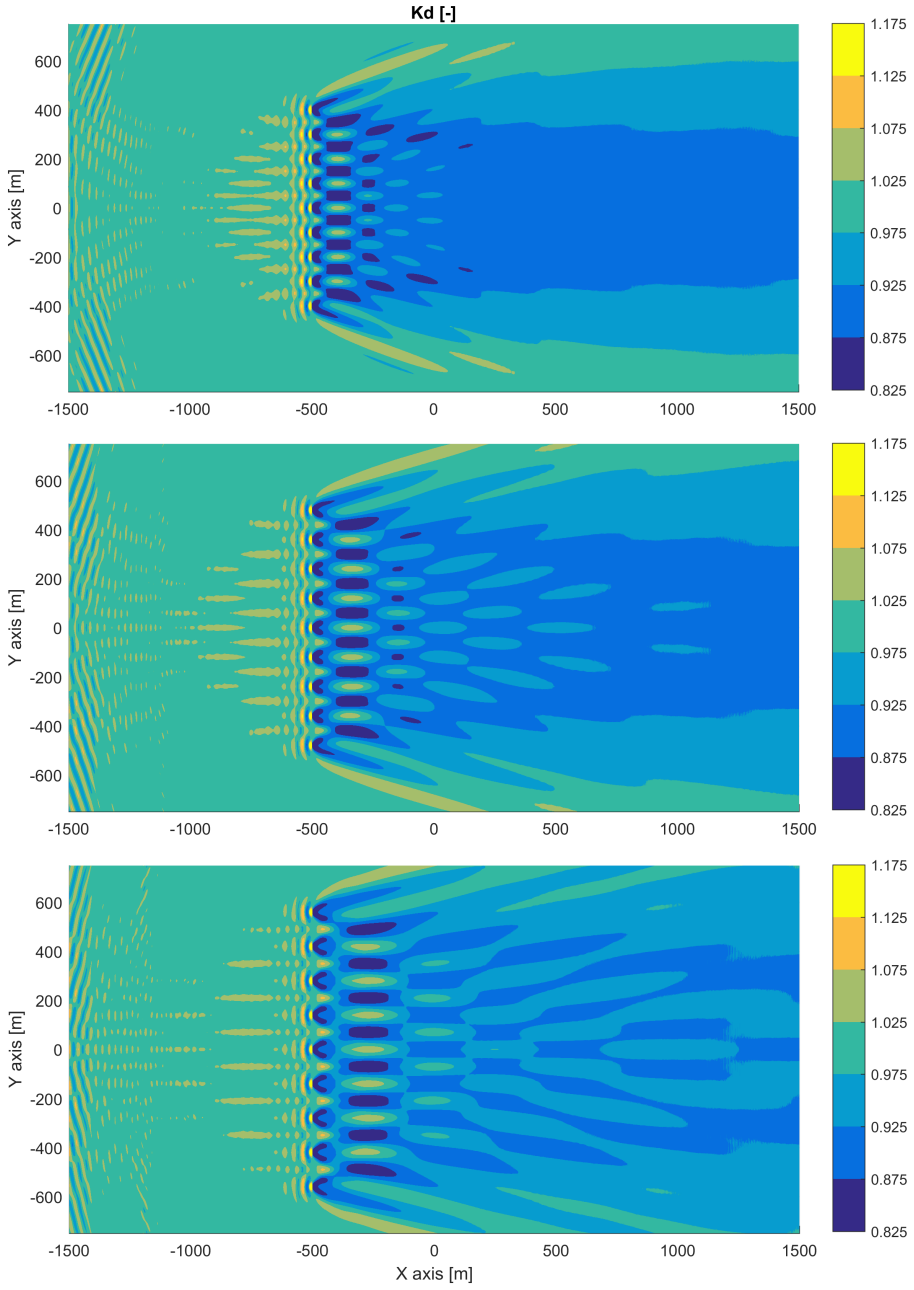

FIGURE D.19: Disturbance coefficient for spacings of $4L$, $5L$, and $6L$ respectively (top to bottom) and sea state of T_p equal to 8 s.

D.11 Real Case Scenario with Irregular Bathymetry

A realistic bathymetry scenario was considered in this section to demonstrate the applicability of the methodology. The bathymetry corresponds to a near-shore area located off Annagh Head, west of Belmullet (Ireland) near the Atlantic Marine Energy Test Site (AMETS). Figure D.20 shows a detailed map of the site (top) where the highlighted rectangular section of 500 x 1000 m defines the area corresponding to considered bathymetry and the general map of Ireland (bottom) shows the location

of the AMETS site. The bathymetry data was obtained from the Integrated Mapping For the Sustainable Development of Ireland's Marine Resource (INFOMAR) programme through their data acquisition platform [39].

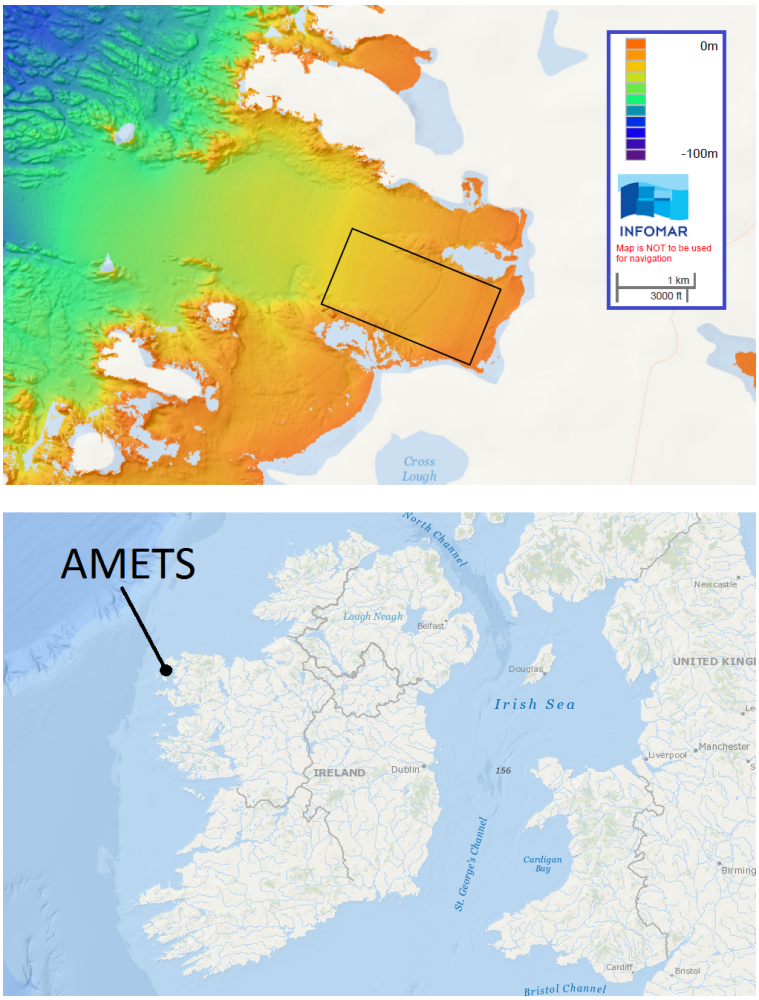

FIGURE D.20: Detailed map of AMETS region with the bathymetry area highlighted (top). General map of Ireland with AMETS location (bottom).

The same WEC farm configuration of 18 flaps was considered but this time deployed at a water depth of 15 m. The flaps are submerged 3 m below the water surface and this reduces their impact on the surrounding wave field. For the site selection it was considered that a minimum distance of 1 km away from the shore was necessary to avoid any problems with near-shore marine activities. In addition, a large area with similar water depth values is necessary for the installation of the WEC farm.

Figure D.21 shows the water depth values (top), the K_d values across the whole domain (middle), and the K_d difference compared to a constant water depth scenario where the same conditions for the WEC farm are considered (bottom). An incident sea state of $T_p = 8\ s$ was considered at the offshore boundary representing

the sea state with the highest occurrence in a year for the AMETS site. For the comparison with the constant water depth case the wave spectral distribution and the water depth were chosen to be the same at the location of the WEC farm, eventually generating a similar wave disturbance on the incoming sea state and where the K_d differences are only due to the different bathymetries.

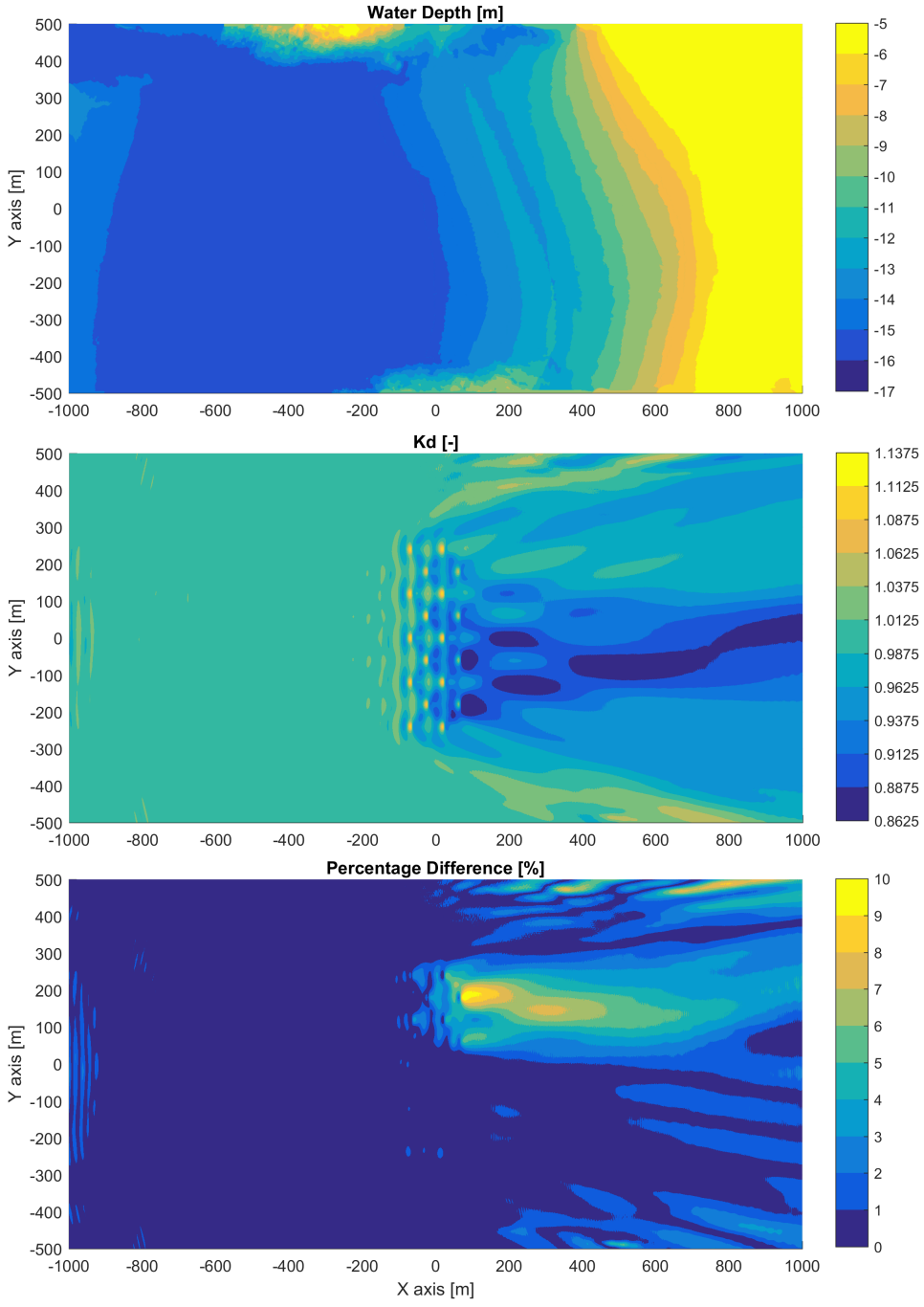

FIGURE D.21: Water depth across bathymetry (top). Disturbance coefficient for 18 flaps on a real bathymetry considering a sea state of $T_p = 8\ s$ (middle). Percentage difference with a constant water depth scenario (bottom).

The lowest K_d values found on the lee-side of the farm are about 0.85 at specific locations. On average the wave height reduction remains around 10%, which proves that for this case scenario the impact of the WEC farm on the surrounding wave climate and near-shore remains low. If a farm composed of surface-piercing flaps such as the one presented in Section D.9 was considered, the impact would be significantly larger. The bottom plot of Figure D.21 shows that differences up to 10% are found for this case scenario, proving the importance of representing real bathymetries when assessing wake effects. Again, if a farm of surface-piercing flaps was considered the difference would be even larger. The asymmetric pattern of the results is a proof as well of the high influence of the bathymetry in the WEC farm wake effect.

D.12 Conclusion

This work has detailed the working principle of a numerical coupling methodology between the wave near-field solution obtained from a Boundary Element Method (BEM) solver and the wave far-field solution from a Wave Propagation Model (WPM). The BEM solver provides with the solution of the perturbed wave field from the WEC farm that is described as an internal boundary within the WPM and then propagated throughout the rest of the domain. The internal boundary consists on a group of grid cells defining a wave generation line where the results from the BEM solver at the same location are imposed at each time step. The solution obtained for the perturbed wave field is then superposed to the incident wave field obtained in the absence of WEC farm in order to obtain the total wave field for each regular wave frequency. Finally, irregular sea states are composed based on the total wave field results from the regular waves ranging within the wave spectral density distribution of the considered sea state.

The presented approach has demonstrated to give highly accurate results when comparing the results to the target solutions from the BEM solver. The technique has proven to be versatile by adapting the internal boundary in MILDwave to the shape and size of the WEC farm. This allows the reduction of the area where the limitations of the BEM solvers are assumed (constant water depths). A convergence analysis for the main numerical parameters influencing the results was undertaken in order to investigate the range of optimal values to be used. This was followed by a sensitivity analysis where the influence of the peak period and the lateral WEC lateral spacing on WEC farm wake effects was assessed. Finally, the wake effect for a 18 flaps WEC farm exposed to irregular long crested waves at a real site was assessed in order to demonstrate the capacity of the methodology to consider real site conditions.

The methodology relies on the linear water wave theory assumptions that remain valid in most of the operational sea state conditions. For the case of sea states where non-linearities become important, higher order wave-structure interaction solvers and wave propagation models are needed. However the implementation of these

solvers will increase the demand in computational time making the computation of large domains such as those considered in this study not feasible by using standard computers. A way to increase the accuracy of the methodology for highly non-linear sea states is to add linear dissipation coefficients to the main governing equations as it was done in [16] to represent wave breaking and in [10] to represent wave regeneration due to the action of wind.

The proposed numerical coupling methodology remains relatively fast in terms of computational time. A limitation in the computational time can occur when obtaining the near-field within the BEM solver for extremely large WEC farms since computing all wave interactions can be computationally demanding. However, currently it is the most practical way for computing all wave interactions within a farm of WECs. New methodologies are under development to compute wave interactions between WECs based on cylindrical solutions of the perturbed velocity potential from BEM solvers [40, 12]. These methodologies can decrease significantly the calculation time of the perturbed wave for a large WEC farm and constant water depths conditions.

The methodology has shown that large WEC farms can have a significant impact on the wave field. Thus it will be important to assess this impact as part of the consenting process for the environmental impact assessment procedure for future commissioning of WEC farms. The development of coupling methodologies such as the one demonstrated in this work will allow the wake effects to be estimated with a much higher precision than with previous methodologies where WECs were represented as obstacle cells or source terms. The methodology enables the quantification of the sheltering effect of a WEC farm and thus to evaluate its impact on the near-shore and the possible synergies with other marine activities sharing the surrounding sea space.

Acknowledgement

The research leading to these results is part of the OceaNET project, which has received funding from the European Union's Seventh Framework Programme for research, technological development and demonstration under grant agreement no 607656. This research has also been supported by the Research Foundation Flanders (FWO), Belgium, Research Project no. 3G029114.

References

[1] C. Beels, P. Troch, G. De Backer, M. Vantorre, J. De Rouck, Numerical implementation and sensitivity analysis of a wave energy converter in a time-dependent mild-slope equation model, Coastal Engineering 57 (5) (2010) 471-492. doi:10.1016/j.coastaleng.2009.11.003.

[2] C. Beels, P. Troch, K. De Visch, J. P. Kofoed, G. De Backer, Application of the time-dependent mild-slope equations for the simulation of wake effects in the lee of a farm of Wave Dragon wave energy converters, Renewable Energy 35 (8) (2010) 1644-1661. doi:10.1016/j.renene.2009.12.001.

[3] H. C. M. Smith, C. Pearce, D. L. Millar, Further analysis of change in nearshore wave climate due to an offshore wave farm: An enhanced case study for the Wave Hub site, Renewable Energy 40 (1) (2012) 51-64. doi:10.1016/j.renene.2011.09.003.

[4] R. Carballo, G. Iglesias, Wave farm impact based on realistic wave-WEC interaction, Energy 51 (2013) 216-229. doi:10.1016/j.energy.2012.12.040.

[5] M. Veigas, V. Ramos, G. Iglesias, A wave farm for an island: Detailed effects on the nearshore wave climate, Energy 69 (2014) 801-812. doi:10.1016/j.energy.2014.03.076.

[6] J. Abanades, D. Greaves, G. Iglesias, Coastal defence using wave farms: The role of farm-to-coast distance, Renewable Energy 75 (2015) 572-582. doi:10.1016/j.renene.2014.10.048.

[7] N. Tomey-Bozo, J. Murphy, P. Troch, T. Lewis, G. Thomas, Modelling of a flap-type wave energy converter farm in a mild-slope equation model for a wake effect assessment, IET Renewable Power Generation (2017) 1-11 doi:10.1049/iet-rpg.2016.0962.

[8] J. C. Mcnatt, A. Porter, K. Ruehl, J. Roberts, Verification of the SNL-SWAN Spectral WEC-wave Model with Phase-resolved Linear Wave Fields, in: 12th European Wave and Tidal Energy Conference, Cork, Ireland, 2017, pp. 1-10.

[9] G. Verao Fernandez, P. Balitsky, N. Tomey-Bozo, V. Stratigaki, P. Troch, Far-field effects by arrays of oscillating wave surge converters and heaving point absorbers: a comparative case study, in: 12th European Wave and Tidal Energy Conference, Cork, Ireland, 2017.

[10] V. Stratigaki, P. Troch, L. Baelus, Y. Keppens, Introducing wave generation by wind in a mild-slope wave propagation model MILDwave, to investigate the wake effects in the lee of a farm of wave energy converters, in: 30th International Conference on Ocean, Offshore and Arctic Engineering, Rotterdam, The Netherlands, 2011, pp. 429-436.

[11] B. Borgarino, A. Babarit, P. Ferrant, Impact of wave interactions effects on energy absorption in large arrays of wave energy converters, Ocean Engineering 41 (2012) 79-88. doi:10.1016/j.oceaneng.2011.12.025.

[12] J. C. Mcnatt, V. Venugopal, D. Forehand, A novel method for deriving the diffraction transfer matrix and its application to multi-body interactions in water waves, Ocean Engineering 94 (2014) 173-185. doi:10.1016/j.oceaneng.2014.11.029.

[13] M. Folley, A. Babarit, B. Child, D. Forehand, L. O'Boyle, K. Silverthorne, J. Spinneken, V. Stratigaki, P. Troch, A Review of Numerical Modelling of Wave Energy Converter Arrays, in: ASME 2012 31st International Conference on Ocean, Offshore

and Arctic Engineering, Rio de Janeiro, Brazil, 2012, pp. 535-545. doi:10.1115/OMAE2012-83807.

[14] M. Folley, Numerical Modelling of Wave Energy Converters: State-of-the-Art Techniques for Single Devices and Arrays, Academic Press, 2016.

[15] C. Beels, Optimization of the Lay-Out of a Farm of Wave Energy Converters in the North Sea. Analysis of Wave Power Resources, Wake Effects, Production and Cost, Ph.D. thesis, Ghent University (2009). https://biblio.ugent.be/publication/978565/file/4335143.pdf

[16] V. Stratigaki, Experimental study and numerical modelling of intra-array interactions and extra-array effects of wave energy converter arrays, Ph.D. thesis, Ghent University (2014). https://biblio.ugent.be/publication/5664337/file/5664342.pdf

[17] A. Babarit, M. Folley, F. Charrayre, C. Peyrard, M. Benoit, On the modelling of WECs in wave models using far field coefficients, in: 10th European Wave and Tidal Energy Conference, Aalbord, Denmark, 2013.

[18] F. Charrayre, C. Peyrard, M. Benoit, A. Babarit, A coupled methodology for wave-body interactions at the scale of a farm of wave energy converters including irregular bathymetry, in: ASME 2014 33rd International Conference on Ocean, Offshore and Arctic Engineering, San Francisco, USA, 2014, pp. 1-9.

[19] P. Troch, V. Stratigaki, Phase-resolving wave propagation array models, in: M. Foley (Ed.) (Ed.), Numerical modelling of wave energy converters: state-of-the-art techniques for single devices and arrays, Elsevier, 2016, pp. 191-216.

[20] P. M. Ruiz, F. Ferri, J. P. Kofoed, Water wave diffraction and radiation by three-dimensional bodies over mild slope bottom, Ocean Engineering 143 (May) (2017) 4-5. doi:10.1016/j.oceaneng.2017.08.007.

[21] N. Tomey-Bozo, J. Murphy, A. Babarit, P. Troch, T. Lewis, G. Thomas, Wake effect assessment of a flap type wave energy converter farm using a coupling methodology, in: ASME 2017 36th International Conference on Ocean, Offshore and Arctic Engineering, Trondheim, Norway, 2017.

[22] C.-H. Lee, WAMIT theory manual (1995). http://www.wamit.com/

[23] N. Tomey-Bozo, J. Murphy, P. Troch, A. Babarit, T. Lewis, G. Thomas, The modelling of a flap type wave energy converter in a time-dependent mild-slope equation model, in: Renewable Energies Offshore, 2016, pp. 277-284.

[24] P. Balitsky, G. Verao Fernandez, V. Stratigaki, P. Troch, Coupling methodology for modelling the near-field and far-field effects of a wave energy converter, in: 36th International Conference on Ocean, Offshore and Arctic Engineering, Trondheim, Norway, 2017, pp. 1-10.

[25] P. Balitsky, G. Verao Fernandez, V. Stratigaki, P. Troch, Assessing the impact on power production of WEC array separation distance in a wave farm using one-way coupling of a BEM solver and a wave propagation model, in: 12th European Wave and Tidal Energy Conference, Cork, Ireland, 2017, pp. 1176-1186.

[26] A. Babarit, G. Delhommeau, Theoretical and numerical aspects of the open source BEM solver NEMOH, in: 11th European Wave and Tidal Energy Conference, Nantes, France, 2015.

[27] P. Troch, MILDwave: A numerical model for propagation and transformation of linear water waves, Tech. rep., Department of civil engineering, Ghent University, Ghent (1998).

[28] T. Verbrugghe, P. Troch, A. Kortenhaus, V. Stratigaki, A. Engsig-Karup, Development of a numerical modelling tool for combined near field and far field wave transformations using a coupling of potential flow solvers, in: 2nd International Conference on Renewable energies Offshore, Lisbon, Portugal, 2016, pp. 61-68. doi:978-1-138-62627-0.

[29] T. Verbrugghe, V. Stratigaki, P. Troch, R. Rabussier, A. Kortenhaus, A comparison study of a generic coupling methodology for modeling wake effects of wave energy converter arrays, Energies 10 (11). doi:10.3390/en10111697.

[30] A. P. Engsig-Karup, H. B. Bingham, O. Lindberg, An efficient flexible-order model for 3D nonlinear water waves, Journal of Computational Physics 228 (6) (2009) 2100-2118. doi:10.1016/j.jcp.2008.11.028.

[31] T. Verbrugghe, B. Devolder, J. Dominguez, A. Kortenhaus, P. Troch, Feasibility study of applying SPH in a coupled simulation tool for wave energy converter arrays, in: 12th European Wave and Tidal Energy Conference, Cork, Ireland, 2017.

[32] T. Verbrugghe, A. Kortenhaus, P. Troch, J. M. Dominguez, A non-linear 2-way coupling between DualSPHysics and a wave propagation model, in: 12th International SPHERIC Workshop, Ourense, Spain, 2017, pp. 121-127.

[33] G. Delhommeau, Seakeeping codes aquadyn and aquaplus, in: 19th WEGEMT School Numerical Simulation of Hydrodynamics: Ships and Offshore Structures, 1993.

[34] J.-C. Galland, N. Goutal, J.-M. Hervouet, TELEMAC: A new numerical model for solving shallow water equations, Advances in Water Resources 14 (3) (1991) 138-148. doi:10.1016/0309-1708(91)90006-A.

[35] A. Radder, M. Dingemans, Canonical equations gravity waves, weakly nonlinear gravity waves, Wave Motion 7 (1985) 473-485.

[36] N. Booij, A note on the accuracy of the mild-slope equation, Coastal Engineering 7 (3) (1983) 191-203. doi:10.1016/0378-3839(83)90017-0.

[37] C. Lee, K. D. Suh, Internal generation of waves for time-dependent mild-slope equations, Coastal Engineering 34 (1-2) (1998) 35-57. doi:10.1016/S0378-3839(98)00012-X.

[38] H. tao Zhao, Z. lin Sun, C. ling Hao, J. fa Shen, Numerical modeling on hydrodynamic performance of a bottom-hinged flap wave energy converter, China Ocean Engineering 27 (1) (2013) 73-86. doi:10.1007/s13344-013-0007-y.

[39] Marine Institute, The INtegrated Mapping FOr the Sustainable Development of Ireland's MArine Resource (INFOMAR). http://www.infomar.ie/

[40] F. Fàbregas Flavià, C. McNatt, F. Rongère, A. Babarit, A. H. Clément, Computation of the Diffraction Transfer Matrix and the Radiation Characteristics in the open-source BEM code NEMOH, in: ASME 2016 35th International Conference on Ocean, Offshore and Arctic Engineering, Busan, South Korea, 2016.